3-D seismic investigation of the diagenesis and deformation of Cenozoic siliceous sediments on the Eastern Atlantic Margin

IRELAND, MARK,THOMAS

3-D seismic investigation of the diagenesis and deformation of Cenozoic siliceous sediments on the Eastern Atlantic Margin

Mark Thomas Ireland

A thesis submitted in partial fulfilment of the requirements for the degree of Doctor of Philosophy at Durham University

Department of Earth Sciences, Durham University

2011

Table of Contents

List of Figures

List of Tables

Abstract

Three-dimensional seismic data from the East Atlantic Margin are used to investigate the diagenesis and deformation of siliceous sediments. Three themes were tackled.

At the Gjallar Ridge, offshore Norway, seismic and well data indicate that diagenesis of siliceous sediments occurs across a zone ~300 m thick. At the top of the zone circular regions, with relief of ~200 m, are interpreted as regions of preferential diagenesis. Below these, regions with a similar size and distribution are attributed to the same cause. The chemistry of formation water expelled transiently through polygonal faults may play a role in their formation. This is the first recognition from seismic data that silica diagenetic transformation zones can be hundreds of metres thick and heterogeneous, as observed at outcrop previously.

On the Mauritanian continental margin layer-bound fault systems deform a probable siliceous succession. Where this succession mantles canyons the majority of faults strike perpendicular to the canyon axes due to increased bedding dip and most are antithetic to bedding dip. Where the bedding dip is greater than ~1°, synthetic faults dip more steeply than antithetic faults, which is the exact opposite that would be expected on a dipping margin. It is hypothesised that the layer hosting the faults has been subjected to simple shear of ~20° or more, rotating the fault planes.

Lastly at the Vema Dome, offshore Norway four submarine slides are identified in siliceous sediments. Each covers an area of ~30 km^2, is up to 600 m thick, with an upper surface topography consisting of a series of arcuate ridges perpendicular to the dip of the slope. The slides are dominated by fold-and-thrust structures, have short transport distances, and unusually low ratios of length to thickness. These characteristics are attributed to deep detachments and the shear strength of siliceous sediments at shallow burial depths.

Declaration

The material contained in the thesis has not previously been submitted for a degree in this or any other institution. The work is entirely my own except where reference is made.

Acknowledgments

Many people over the last three years have helped make my time at Durham and this PhD such an enjoyable experience. First, particular thanks must go to Richard Davies and Neil Goulty, for all their encouragement, support, advice and so many fruitful discussions over the past three years. Most importantly they have always been immensely enthusiastic throughout. All this has undoubtedly helped me with my future career plans. Numerous others, both at Durham University and elsewhere, have provided constructive comments and discussion. Particular thanks should go to: Joe Cartwright, for first introducing me to 3-D seismic data and silica diagenesis; Jonny Imber who I bugged on numerous occasions; Rick Behl and the guys at Occidental Petroleum for a helping put together a thoroughly enjoyable field trip, and those people I had to opportunity to work alongside at Woodside during my internship. Thanks also to Peter Eichhubl, Jonathon Turner and the anonymous reviewers of my papers, as well as the editors.

The following companies and people are thanked for making this research possible. BG Group, for funding my studentship while at Durham, and for their hospitality. Statoil ASA for permission to use the offshore data from Norway shown in this thesis, and permission to publish this. In addition they always showed a genuine interest and enthusiasm for my research, in particular Siv Markussen who has been helpful and engaging throughout. Tullow Oil and Petronas, for permission to use data from offshore Mauritania and for permission to publish this, in particular Alistair Chaney for his input. This research has also used data from the Ocean Drilling Program. Landmark Graphics Corporation provided the seismic interpretation software as part of the LGC University Grant Scheme and Ikon Science provided RockDoc rock physics software. Dave Stevenson and Gary Wilkinson for all their work in supporting the IT systems used over the last three years and the office staff in the Department of Earth Sciences at Durham University.

I'd like to thank all my friends, in particular, Lee, Melv, Marcus, the Daves, Martyn, Joe, JJ for many frivolous times and Jude, Dom, Steve, Ben, Chris, Alan and Rich. A huge thanks to Katie for putting up with me, not just while writing this thesis, but for the last two years, which have been such fun, hopefully there will be lots more adventures to come (like returning to Brazil?!). And last, but not least my family, Jason, Jane, and Rachel, and my Mum and Dad, who have been supportive of everything I have done as far back as I can remember, for which I am very grateful.

1 INTRODUCTION

1.1 RESEARCH CONTEXT

Diagenesis, compaction and deformation are fundamental processes which occur during the early burial of sediment (Chilingar and Wolf, 1988; Kastner *et al.,* 1991; Maltman, 1994; Bjørlykke and Høeg, 1997). In marine environments and particularly regions of high ocean productivity, such as extreme latitudes and equatorial regions, biogenic silica can be an important component of deposited sediment (Gallinari *et al.,* 2002), often termed siliceous sediment (e.g. Bramlette, 1946; Kastner *et al.,* 1977; Keller and Barron, 1983). On the Atlantic margins such sediment are widespread (Fig. 1.1) and can form thick (>500 m) successions covering >10,000 km^2 (e.g. Keller and Barron, 1983). The diagenesis and microstructural properties of siliceous sediment are unique (Bramlette, 1946; Tanaka and Locat, 1999) and result in unusual compaction trends with abrupt changes in sediment properties that coincide with diagenetic changes; both aspects may influence the style of deformation associated with siliceous sediments (e.g. Compton, 1991; Isaacs, 1981; Grimm and Orange, 1997). Three-dimensional (3-D) seismic reflection data provide a novel and powerful tool to investigate the complex shallow burial history of this sediment type.

Diagenesis refers to changes in sediment subsequent to deposition. It covers a wide range of processes that may be physical, chemical or biological which occur as sediment and pore fluids react and attempt to reach equilibrium with changing geological conditions (cf. Berner, 1980). Chemical processes may result in mineral transformations, and includes processes such as dissolution and precipitation which subsequently may affect the mechanical properties of the sediment (Bjørlykke and Høeg, 1997). On passive margins, fluid flow may be strongly affected by chemical processes in the subsurface through mineral dehydration and porosity reduction (Kastner *et al.,* 1991). The factors influencing the rate and timing of the diagenesis in siliceous sediment across large tracts of sedimentary basins are particularly poorly constrained, especially in 3-D.

Deformation and compaction can occur contemporaneously with diagenesis during burial; deformation refers to the change in bulk shape of a body due to an applied force and compaction refers to the permanent reduction in volume (Maltman, 1994). The deformation of sediment has been widely studied and the physical principles that govern this are well

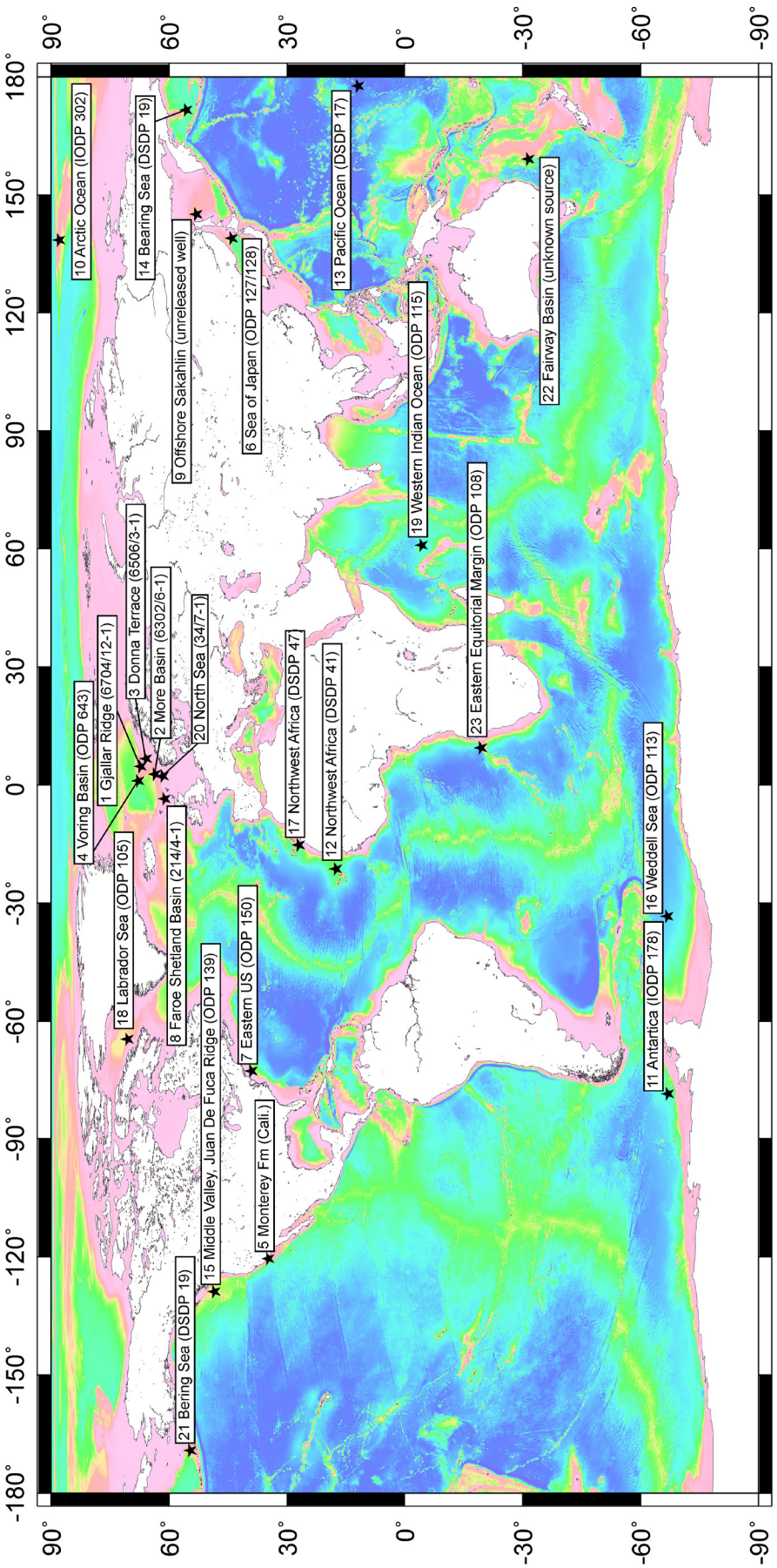

Fig. 1.1 Global location map showing sites of siliceous successions which host the diagenetic transformation of opal-A to opal-CT, confirmed by well data.

established (Maltman, 1994). Compaction, deformation and sediment strength are intrinsically linked and potentially influenced by diagenesis (cf. Maltman, 1994), for example diagenesis can produce an increase in sediment cohesion (Lade and Overton, 1989). Variations in sediment composition and physical properties, as well as external stresses imposed on them result in differing diagenetic, compaction and deformation histories (Bjørlykke and Høeg, 1997). Deformation structures, and their style (e.g. brittle or ductile) and geometry, can reveal information about the early consolidation history of sediment (Allen, 1982).

In the absence of tectonic forces the deformation of sediment is primarily the result of gravity due to vertical loading (compaction) and the imposed shear stress where sediment are on a slope (Maltman, 1994). Shear stresses imposed on sediment due to a slope may results in instabilities, the fundamental principle of slope failure (Maltman, 1994). While much focus is placed on triggering mechanisms for instabilities, there is a need for these to be balanced against preconditioning factors, especially sediment characteristics and stress history (Mosher *et al.,* 2010). The geometry of deformation structures within slope failures can reveal the kinematic history of sediment deformation and therefore record instability (cf. Butler and Turner, 2010). Slope failures are of broad interest in submarine settings because of the widespread occurrence through time and in space, and their often vast scale (Maltman, 1994).

Diagenesis, and to some extent sediment deformation, have traditionally been dominated by outcrop studies at the centimetre to metre scale (e.g. Chilingar and Wolf, 1988; Maltman, 1994). The research in this thesis contributes to the advances made during the last two decades using 3-D seismic reflection data to investigate sedimentary and structural processes which may not always be clearly exposed at outcrop due to scale limitations and difficulties in producing 3-D descriptions from surface exposure (e.g. Cartwright and Huuse, 2005; Davies and Posamentier, 2005).

1.2 RESEARCH OBJECTIVES

This thesis examines the diagenesis and deformation of Cenozoic siliceous sediment at a scale of tens to thousands of meters using 3-D seismic reflection data from the Eastern Atlantic margin. The diagenetic transformation of biogenic silica within siliceous sediment following the path, opal-A → opal-CT → quartz, has been identified over areas of up to 10^4 km^2 using seismic reflection data, which offers a novel method for the study of diagenesis (Davies and Cartwright,

2007). The opal-A to opal-CT transformation is known to result in extraordinary three-dimensional patterns that have been attributed to variations in the rate of the transformation (Davies and Cartwright, 2007).

The diagenesis of siliceous sediment tends to occur in association with other geological phenomena, such as polygonal faults (e.g. Davies and Cartwright, 2002; Volpi *et al.,* 2003; Neagu *et al.,* 2010), submarine slope failures (Davies and Clark, 2006), sandstone intrusions (Davies *et al.,* 2006) and fluid flow and expulsion (Eichhubl and Boles, 2000a; Davies *et al.,* 2008). Such phenomena in siliceous sediment merit investigation where they are observed because of the generic link between them and siliceous sediment and their diagenesis. This thesis will examine the seismic expression of the diagenesis of siliceous sediment and the style of non-tectonic deformation observed in siliceous sediment under the influence of gravitational forces. The main aims of this thesis are to:

1) Test the hypothesis that silica diagenetic transformation zones observed from 3-D seismic reflection data may be thick complex zones.

2) Consider what controls the complexity of silica diagenetic transformation zones using 3-D seismic reflection data and analogue data.

3) Use 3-D seismic reflection data to examine the geometry of layer-bound compaction faults in a siliceous succession on a continental margin.

4) Examine the style of submarine slope failures in siliceous sediment using 3-D seismic reflection data and relate this to the inherent micro structural properties of siliceous sediment.

1.3 SILICEOUS SEDIMENT

Biogenic silica is, and has been produced extensively by phytoplanktonic organisms, such as diatoms (Lisitzin, 1972; Nelson *et al.,* 1995), from the Cretaceous to present day (Laventer, 2009) and possibly as far back as the Devonian (Schieber *et al.,* 2000). The accumulation of biogenic silica generally relates to primary productivity but may vary regionally due to surface temperature (Nelson *et al.,* 1995). The production and deposition of biogenic silica is the result of the transformation of dissolved silicate to particulate skeletal material which in surface waters is estimated to be ~240 ± 40 Tmol (teramoles) of silicon per year at present, with a preservation ratio of 3% (Treguer *et al.,* 1995). Biogenic silica is commonly termed opal-A, where the 'A' denotes it is amorphous, indicating it is non-crystalline (Jones and

Segnit, 1971). The composition of the siliceous sediment on the North Atlantic has been characterized by a number scientific wells and prior to diagenetic alteration is well constrained (e.g. Eldholm and Thiede, 1987b), comprising of varying amounts of diatoms, radiolarians, clay, detrital quartz, sponge spicules and silicoflagellates (Fig. 1.2). Diatoms and radiolarians have a unique test structure, with high intraskeletal porosity (Fig. 1.3 & Fig. 1.5, also Appendix C).

Fig. 1.2 Core photograph from Ocean Drilling Program Leg 104, site 643 (core photos available from http://www.iodp-usio.org/Data_Samples/default.html, accessed 23/09/2010). Depth range is 301.1 – 302.6 mbsf. The composition of the sediment is: 5% detrital quartz, 25% clay, 50% diatoms, 5% radiolarians, 10% sponge spicules and 5% silicoflagellates. Sediment has a porosity of 67%. Scale bar alongside core is in centimetres.

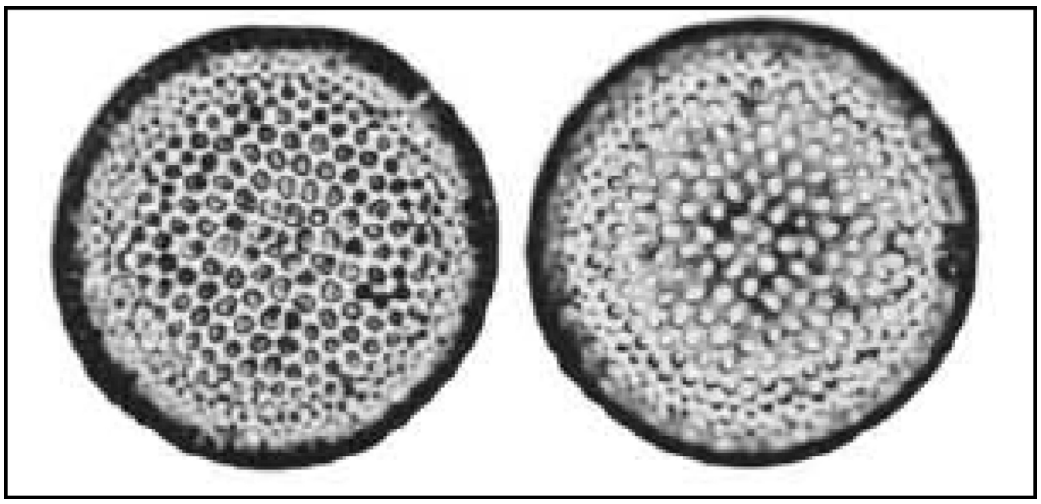

Fig. 1.3 Light microscope image of diatom test, ~25 µm across (~1500x magnification) across species *Thalassiosira oestrupii* in Early Pleistocene sediment on the North Atlantic Margin, from Deep Sea Drilling Project Leg 38, site 348, Vøring Basin (Schrader and Fenner, 1976).

While in many sedimentary successions Deep Sea Drilling Projects (DSDP) and Ocean Drilling Programs (ODP) have established exponentially decaying porosity trends

during compaction (Hamilton, 1976; Huang and Gradstein, 1990; Hurley and Hempel, 1990), the unique properties of biogenic silica mean that these trends may not apply to siliceous successions (e.g. Compton, 1991). During the compaction of this sediment, large volumes of water are also commonly expelled (Eichhubl and Behl, 1998; Eichhubl and Boles, 2000a, 2000b; Davies *et al.,* 2008), due to their high porosity and the potentially significant amounts of structurally bound water within opal-A (Jones and Renaut, 2004).

Much of the present understanding of the chemical systems of the diagenesis of siliceous sediment and the associated compaction and deformation comes from studies of the Miocene Monterey Formation. Over the past 40 years the Monterey formation has been a research area for the upstream oil and gas industry, where it is both a source and reservoir rock in petroleum plays in California, USA (Graham and Williams, 1985). More recently it has been identified as an unconventional hydrocarbon play with enormous production potential (Durham, 2010). Data from the scientific drilling projects of the DSDP, ODP and IODP, have penetrated siliceous sediment globally (Fig. 1.1) and data from these projects complements the studies from the Monterey formation.

1.3.1 DIAGENESIS

The diagenetic changes which accompany siliceous sediment as a function of burial depth were first described by Bramlette (1946). Biogenic silica during burial undergoes polymorphic changes, following the sequence: opal-A → opal-CT → quartz (e.g. Kastner *et al.,* 1977) (Fig. 1.4). The three distinct silica polymorphs, based on the terminology of Jones & Segnit (1971) are: opal-A, a hydrous silica, with a disordered and amorphous structure which make up diatoms and radiolarians tests; opal CT, a metastable disordered hydrous silica with X-ray diffraction similarities to cristobalite and tridymite; stable diagenetic quartz, forming as crystalline quartz.

The opal-A to opal-CT and the opal-CT to quartz transformations are dissolution-reprecipitation mechanisms (Carr and Fyfe, 1958) (Fig. 1.5) and the primary control is temperature (Murata and Larson, 1975). Observations from DSDP and ODP wells and the Monterey Formation, as well as recent investigations using seismic reflection data indicate that temperature is not the only factor which affects the transformations (e.g. Kastner *et al.,* 1977; Isaacs, 1982; Ireland *et al.,* 2010, investigated in Chapter 4). The rate of opal-A to opal-CT transformation is also controlled by the reactive surface area (Steefel and Van Cappellen, 1990); the presence of clays which may inhibit the formation of opal-CT (Fig 1.5); the presence of carbonates, which may promote the precipitation of opal-CT (Kastner

et al., 1977); and factors not related to original sediment composition such as pore water chemistry (Kastner *et al.,* 1977).

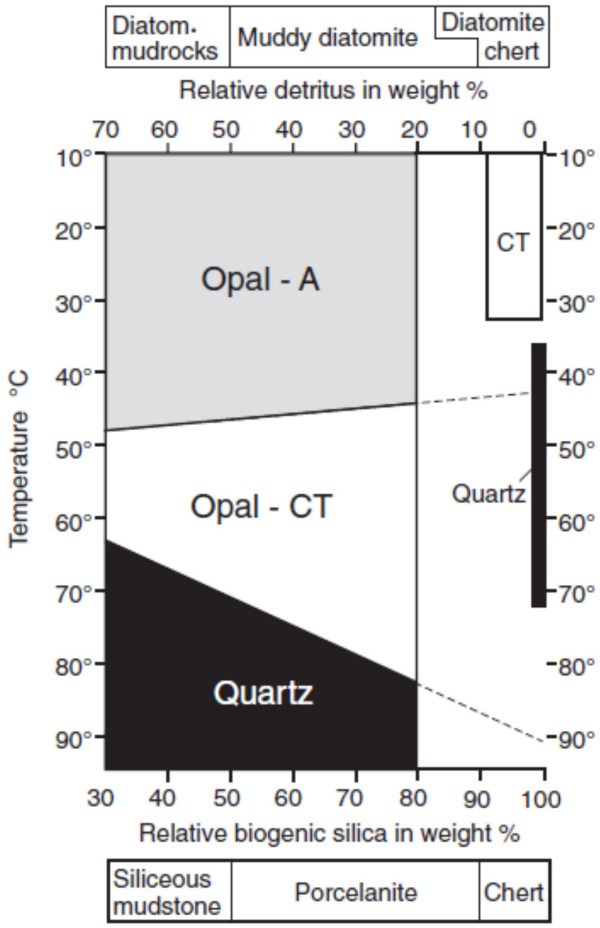

Fig. 1.4 Silica phase diagram for the transformation of opal-A to opal-CT and subsequently quartz. The schematic summarizes the influences of temperature, and relative contributions of detritus and biogenic silica to transformation (From Behl, 2010).

The silica frustules (opal-A) form a relatively incompressible framework and maintain a high porosity relative to detrital, organic, and calcareous components of the rock because of their shape (e.g. Compton, 1991). During the transformations of opal-A to opal-CT and opal-CT to quartz there is significant porosity reduction initially as a result of dissolution of rigid, highly porous silica frustules and precipitation of more crystalline opal-CT (Fig. 1.5) and subsequently dissolution of opal-CT and precipitation of quartz (c.f. Compton, 1991). Transformation of opal-A to opal-CT in siliceous sediment can result in porosity reduction by as much as 30% (Isaacs, 1981; Tada and Iijima, 1983; Meadows and Davies, 2009).

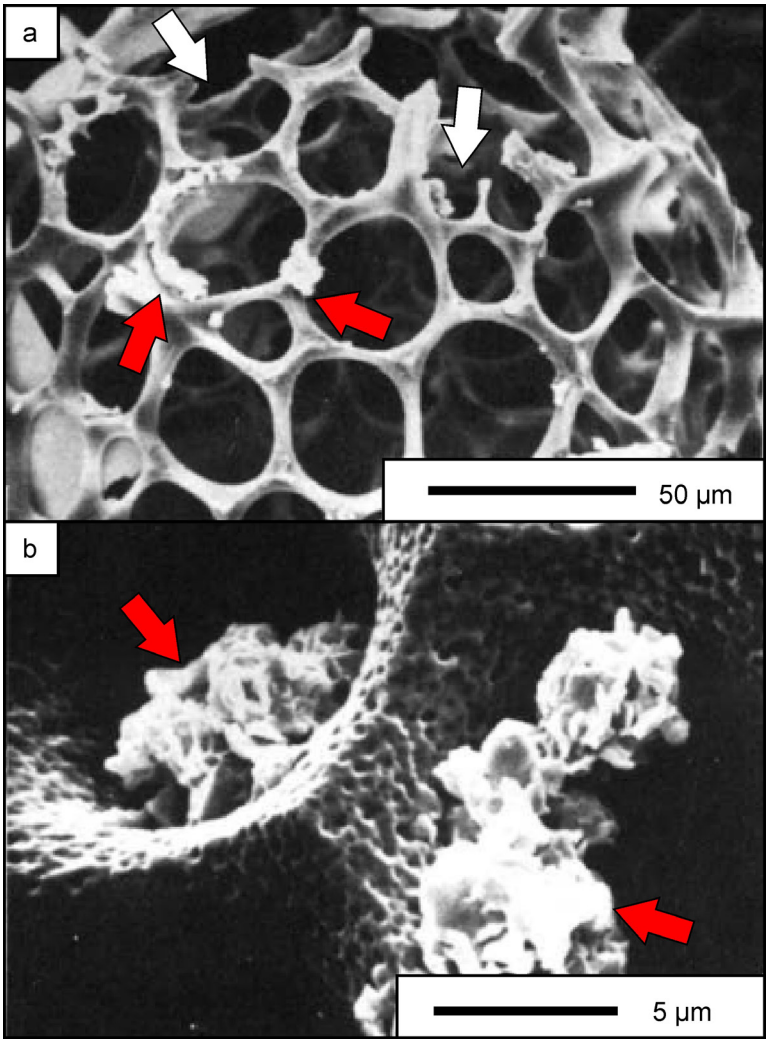

Fig. 1.5 SEM images from Kastner *et al.*, (1977) (a) Early precipitating opal-CT (red Arrows) on the surface of radiolarian test (opal-A) with dissolution of the bars of the test (white arrows) prior to the nodes, and (b) enlargement of opal-CT (red arrows)[1].

This porosity reduction is associated with an increase in the bulk density and typically the P-wave and S-wave velocities (Guerin and Goldberg, 1996), resulting in a large acoustic impedance contrast that can give rise to a seismic reflection event (Fig 1.6) (Hein *et al.,* 1978). Examples have been reported from the Barents Sea (Hein *et al.,* 1978), the Japan Sea (Kim *et al.,* 2007), offshore eastern USA (Guerin and Goldberg, 1996), the North-East Atlantic Margin (Davies and Cartwright, 2002, 2007; Berndt *et al.,* 2004), offshore Sakhalin Island (Meadows & Davies, 2007) and offshore Eastern Australia (Exon *et al.,* 2007). In each of these examples, a single discrete reflection event has been interpreted as

[1] Further images of the microstructure of silica phases can be seen in Appendix C.

corresponding to a narrow transformation interval which is <20 m in thickness (Fig 1.6) (Nobes *et al.,* 1992; Davies and Cartwright, 2002; Meadows and Davies, 2007).

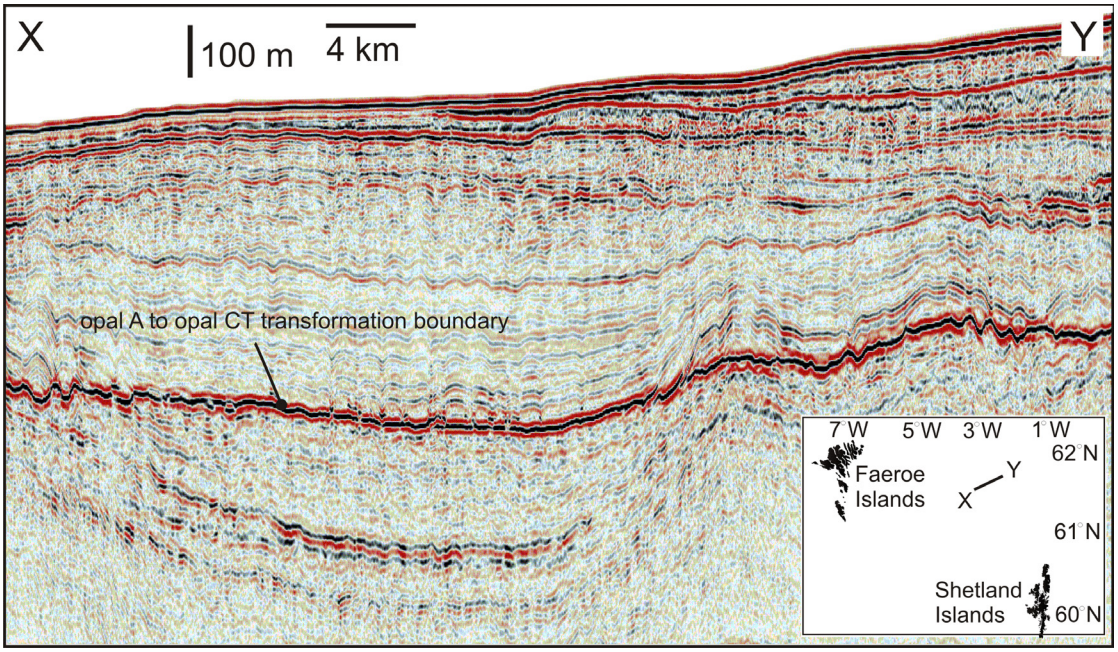

Fig. 1.6 Typical interpretation of a silica diagenetic transformation boundary from seismic reflection data where the reflection interpreted as the opal-A to opal-CT transformation boundary (marked) cross cuts stratal reflections (from Davies and Cartwright, 2002).

At outcrop (Fig 1.7), the zone of transformation is much generally much broader, with a zone of compositionally heterogeneous rocks lying between strata where the silica is uniformly diatomaceous and strata where the silica is uniformly opal-CT (Isaacs, 1981, 1982; Williams *et al.,* 1985). On the North Atlantic Margin, 3-D seismic reflection datasets have identified additional complexities to the previously observed planar cross cutting reflection events (Davies and Cartwright, 2007). Possible causes for these variations will be discussed in Chapter 3 and 4.

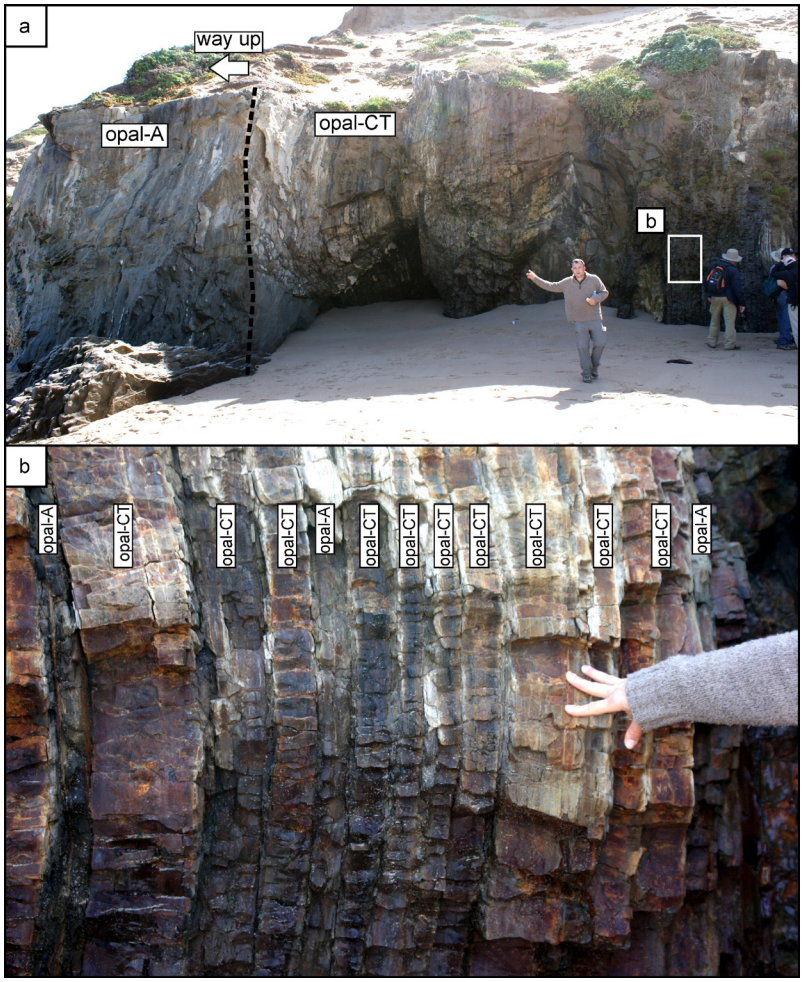

Fig. 1.7 Photos of the Monterey Formation, from the Mussel Rock, near Guadalupe, California. (a) Outcrop in which the slightly more grey coloured sediment to left of the photo are minimally altered diatomaceous sediment (dominantly opal-A), and to the right, the slightly more brown coloured sediment containing opal-CT. The dashed line represents the approximate boundary between different silica phases. (b) Zoom of outcrop, demonstrating the inter-bedded centimetre variability, with untransformed opal-a inter-bedded with opal-CT.

1.3.2 DEFORMATION

The style of deformation observed in sediment will be largely dependent on the stresses applied and the sediment strength. Sediment strength is influenced by the physical cohesion of the grains and the inter-grain friction between them (Maltman, 1994). In addition, pore fluids can support some of the applied load (Maltman, 1994). The silica frustules which make up siliceous sediment result in the sediment having a unique micro-structural framework (e.g. Tanaka and Locat, 1999). The transformation of opal-A to opal-CT and

subsequently opal-CT to quartz are, most likely accompanied by increases in shear strength (c.f. Gross *et al.,* 1997), though there are very few measurements which demonstrate this.

The deformation of siliceous sediment on the Atlantic margin will be significantly influenced by the stresses imposed by gravity because of their position on sloping continental margins and local structural highs. The deformation of siliceous sediment is intriguing, since they do not follow typical compaction trends, nor do they exhibit typical strength profiles (e.g. Volpi *et al.,* 2003). Understanding the deformation of siliceous sediment in the upper 1 km of the sedimentary column on continental margins has implications for slope stability and fluid flow.

Seismic reflection data have revealed that siliceous successions are associated with a number of deformation styles at 10's to 100's m scale, including brittle failure, ductile folding, and hydro-fracturing (e.g. Davies *et al.,* 2006, 2009; Davies, 2005). In this thesis, two particular types of deformation, both which have been imaged widely using seismic reflection data in typically clastic sediments, are investigated:in siliceous sediments, layer-bound faults (often termed polygonal faults) (e.g. Cartwright and Lonergan, 1996), and submarine slope failures (e.g. Haflidason *et al.,* 2004). Neither type of deformation is unique to siliceous sediment, but it is intriguing to investigate such deformation in these sediment to assess the role of sediment type and depositional setting on the style of deformation.

1.3.2.1 SUBMARINE SLOPE FAILURE

The mass movement of sediment can range from the turbulent and rapid movement of grains with fluidal behaviour to the relatively slow movement of coherent masses with discrete internal structural deformation (Martinsen, 1994). In gravitationally-driven deformation on submarine slopes, mobilized layers can range from less than a meter thick, up to hundreds of meters thick (Butler and Turner, 2010). Typically submarine mass movements have clearly distinguishable zones, as summarized in Fig. 1.8. Assessing the morphology and internal structure of submarine slope failures is important to understanding the style of deformation and the kinematics of failure. 3-D seismic reflection data provide the opportunity to image kilometre scale failures, with a resolution of 10's meters. Structures and deformation style can be related to the sediment type, and the physical properties. Low vertical effective stresses caused by elevated fluid pressures as a result of rapid sediment loading is one of the mechanisms responsible for slope instability (Dugan and Flemings, 2000). Recent studies (Volpi *et al.,* 2003; Davies and Clark, 2006; Kristoffersen *et al.,* 2007) have identified the

mass movement of siliceous sediments. The geometry, and kinematics of slope failures within this siliceous sediment may reflect their unique physical properties.

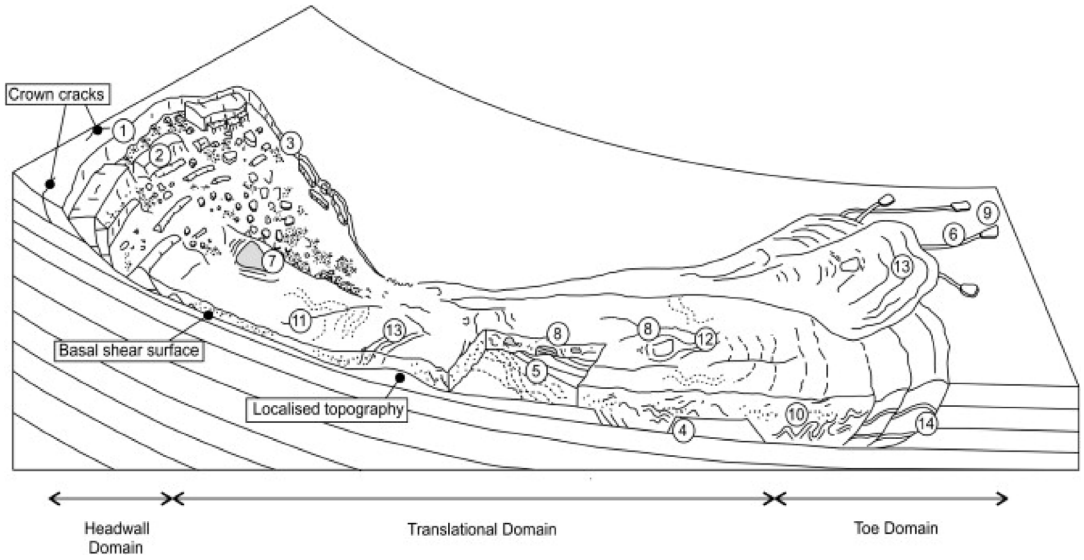

Fig. 1.8 Schematic representation of a submarine slope failure (termed a mass transport complex) and the likely occurrence and associations of kinematic indicators relative to the various domains. (1) Headwall scarp. (2) Extensional ridges and blocks. (3) Lateral margins. (4) Basal shear surface ramps and flats. (5) Basal shear surface grooves. (6) Basal shear surface striations. (7) Remnant blocks. (8) Translated blocks. (9) Outrunner blocks. (10) Folds. (11) Longitudinal shears/first order flow fabric. (12) Second order flow fabric. (13) Pressure ridges. (14) Fold and thrust systems. (from Bull *et al.*, 2009).

1.3.2.2 LAYER-BOUND COMPACTION FAULTS

Layer-bound systems of compaction faults (also termed polygonal faults) found in fine-grained sedimentary units commonly comprise networks of normal faults with random strike directions that form polygonal geometries on bedding planes (Cartwright and Dewhurst, 1998) (Fig. 1.9). Bedding plane geometries of compaction fault systems may depart from polygonal forms due to the influence of external stresses such as basin floor slope (e.g. Higgs and McClay, 1993) and tectonic faults (Hansen *et al.,* 2004). Polygonal fault systems have received a wide variety of interpretations but are generally accepted to be the result of volumetric reduction, with bed-parallel compaction, which complements the heaves on the faults, in addition to vertical compaction (Cartwright and Lonergan, 1996). Laboratory measurements (Bishop *et al.,* 1971) and field data (Goulty and Swarbrick, 2005) suggest that low coefficients of friction on fault surfaces may be an important factor that allows polygonal fault systems to develop (Goulty, 2001, 2002, 2008). Once faults have nucleated

in the fine-grained host sediment, they can continue to grow with increasing overburden stress under laterally confined conditions, provided that the coefficient of residual friction on the fault surfaces is sufficiently low (Goulty, 2008). Layer-bound faults have been identified in the siliceous sediments across the Norwegian Margin (e.g. Hjelstuen *et al.,* 1999; Berndt *et al.,* 2003). Recent studies have documented how the diagenesis of siliceous sediments can influence the propagation and geometry of these layer-bound fault systesm (Davies *et al.,* 2009; Neagu *et al.,* 2010). Geometric analysis of fault systems allows for the potential role of processes such as diagenesis and lithology to be investigated as well as the influence of other external factors such as depositional and stratigraphic setting, gravitational instability, post faulting compaction. The initiation and propagation of polygonal faults due to silica diagenesis are investigated by Shin *et al.,* (2008), Davies *et al.,* (2009) and Davies & Ireland (in review), and is also discussed further in Chapter 7 of this thesis.

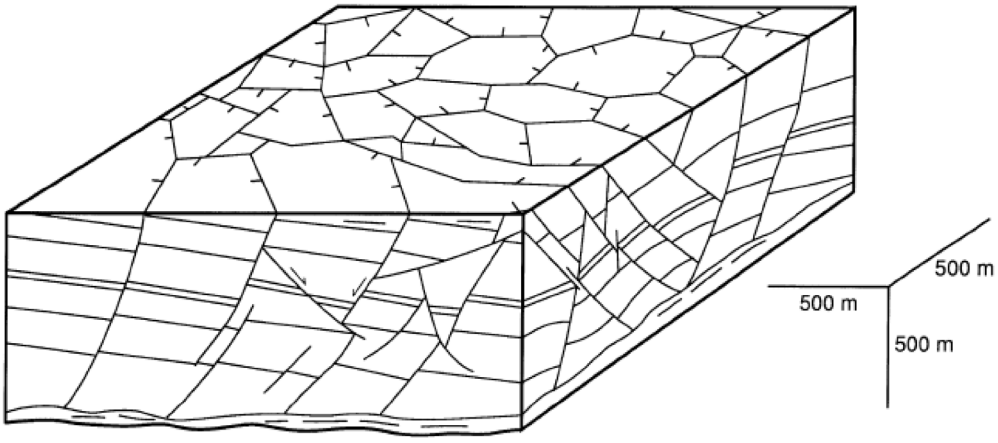

Fig. 1.9 Schematic representation of the geometry of a polygonal fault system, from the North Sea (Fig. 4 from Cartwright and Lonergan, 1996).

1.3.2.3 OVERPRESSURE DEVELOPMENT AND HYDROFRACTURING

The transformations of opal-A to opal-CT and opal-CT to quartz which result in significant porosity reduction and compaction during the burial of siliceous sediments, may consequently, lead to water being expelled at higher rates than would be the case for the mechanical compaction of clastic, non-siliceous lithologies. This release of water is supported by outcrop studies of siliceous sediments that have undergone diagenetic transformation to porcelanite and chert which show evidence for water expulsion and fluid flow in the form of multiple fracture populations, brecciation, and cementation (e.g.

Eichhubl and Behl, 1998; Eichhubl and Boles 2000a, 2000b). Recently 2-D and 3-D seismic reflection data has led to the identification of large scale fluid conduits and pock marks (e.g. Davies *et al.,* 2008), which are interpreted as the result of water expulsion and focused fluid flow emanating from opal-A to opal-CT transformations at burial depths of 200–800 m. For such features to form sealing lithologies must be breached through the initiation and propagation of fractures. This requires the pore pressure to be higher than the sum of the minimal principal stress and the tensile strength of the sediment (Engelder, 1993). Fluid expulsion as a consequence of the diagenetic transformation of silica phases is a potential overpressure generating mechanism (Davies *et al.,* 2008). Davies *et al.,* (2008) calculated for siliceous sediments in the Faroe Shetland Basin that the estimated volumetric rate of water expulsion per unit surface area at the present day from sediments at the opal-A to opal-CT transformation boundary is ~6 $m^3.My^{-1}$ per square meter. Such a volume of water is far greater than that the vertical flux of water at the same depth from compaction of clastic basin fills (Davies *et al.,* 2008). This associated pore fluid expulsion and potential overpressure build-up, particularly in interbedded successions, may result in the 'priming' of siliceous sediments, making them susceptible to subsurface remobilization (Davies *et al.,* 2006) and submarine slope failure (Davies & Clark, 2006).

1.4 GEOLOGICAL SETTING

1.4.1 VØRING BASIN

The tectonic evolution of the outer Vøring Basin is complex (Ren *et al.,* 2003; Moy, 2010) but can broadly be grouped into two stages, (1) the Late Cretaceous rift phase (85 to 65 Ma), during which time extension was predominantly accommodated by upper crustal faulting, followed by (2) depth-dependant lithospheric extension (Kusznir *et al.,* 2005), synchronous with normal fault reactivations, regional uplift, and erosion of the structural highs in the Palaeocene (65 to 55 Ma). Rifting culminated in continental breakup close to the Palaeocene–Eocene transition (*ca.* 55 Ma), at the end of which there was widespread deposition of volcanic units and intrusion of sills and dykes, over a 1 My period (Planke *et al.,* 2005). This thesis focuses on Cenozoic sediment that mantle the Gjallar Ridge and the Vema Dome, 350 km offshore Norway, on the western edge of the Vøring Basin (Fig. 1.10).

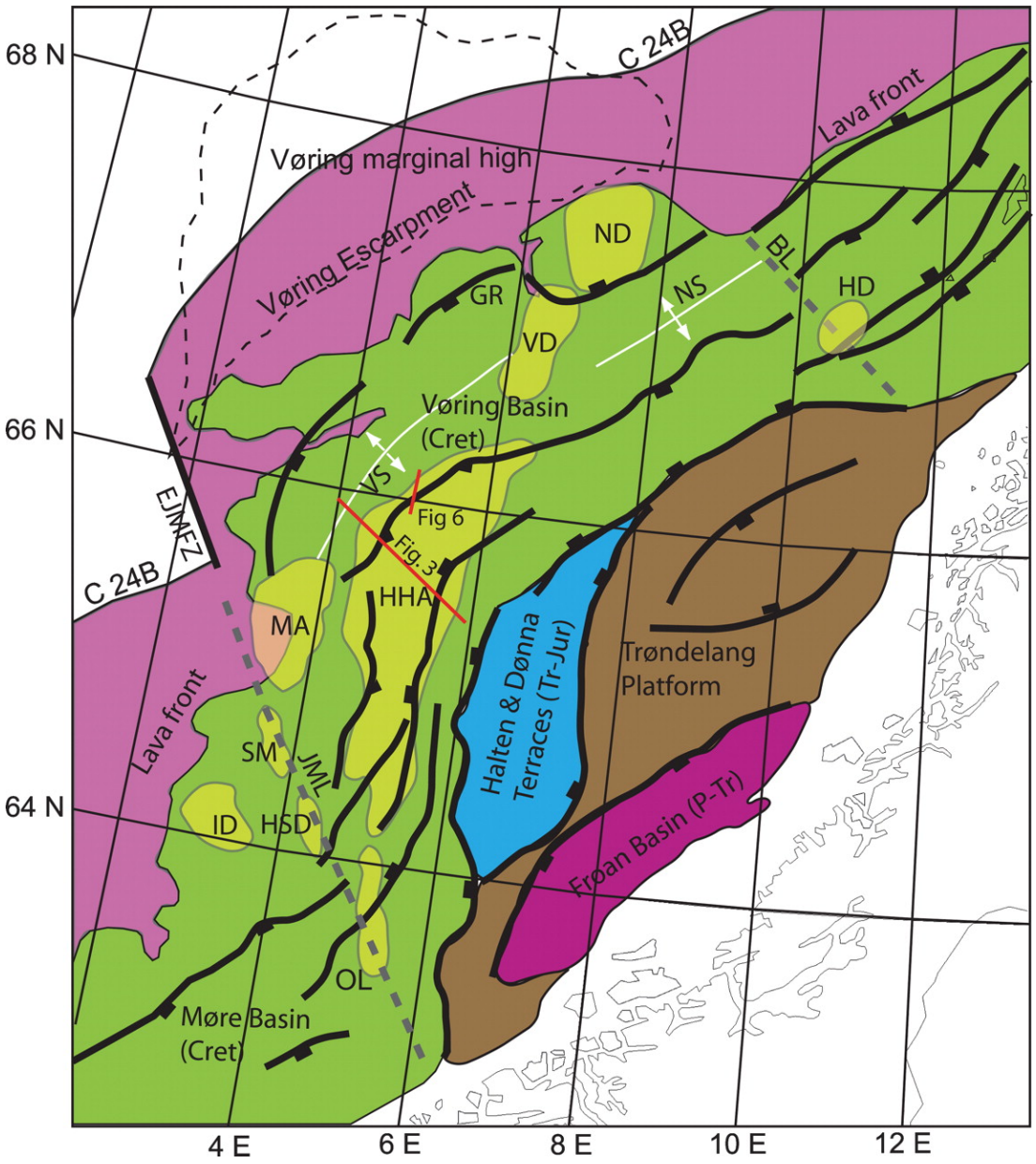

Fig. 1.10 Simplified structural map of mid-Norway. Abbreviations: BL, Bivrost Lineament; EJMFZ, East Jan Mayen Fracture Zone; GR, Gjallar Ridge; HD, Hedda Dome; HHA, Helland Hansen Arch; HSD, Havsule Dome; ID, Isak Dome; JML, Jan Mayen Lineament; MA, Modgunn Arch; ND, Naglfar Dome; NS, Någrind Syncline; OL, Ormen Lange Dome; SM, Souther Modgunn Arch; VD, Vema Dome; VS, Vigrid Syncline (from Doré *et al.*, 2008).

The Gjallar Ridge is an elevated complex of rotated and tilted fault blocks that formed during the Cretaceous (Brekke, 2000). It consists of three structural highs which were gradually uplifted between the Cenomanian and Early Eocene (Lundin and Doré, 1997). The Vema Dome is a pericline which was formed during the Oligo-Miocene and

significantly influenced the final part of basin evolution (Doré *et al.,* 2008). Multiple mechanisms have been proposed for the formation of the Vema Dome (Lundin and Doré, 2002; Mosar *et al.,* 2002; Mjelde *et al.,* 2003). Most recently, the development of the Vema Dome and other dome structures on the Atlantic margin have been suggested as having developed preferentially where the basement is hotter, weaker and therefore more prone to shearing at the relatively low stress levels, with the primary force being development of the Iceland Insular Margin (Doré *et al.,* 2008).

During the Miocene and Early Pliocene, deposition on the outer margin of the Vøring Basin primarily comprised siliceous hemipelagic sediment (Hjelstuen *et al.,* 1999). The interval of interest containing the succession of silica-rich sediment lies 60–800 m below the seafloor. It extends from the base of the Oligocene section of the Brygge Formation to the base of the Plio-Pleistocene Naust Formation. The Brygge Formation belongs to the Hordaland Group (Hansen *et al.,* 2005). The Hordaland Group is overlain by the Lower Miocene to Recent Nordland Group, which is subdivided into the Kai Formation and the overlying Naust Formation. The Brygge, Kai and Naust Formations are laterally extensive across the Norwegian Margin and have been penetrated by over 150 exploration wells (see Appendix C).

1.4.2 MAURITANIAN BASIN

The continental shelf offshore Mauritania is a passive margin on the West African margin. During rifting of the Proto-Atlantic Ocean, Liassic evaporites were deposited in the axes of Triassic-Early Jurassic graben (Vear, 2005). Sediment starvation during the Jurassic allowed the development of carbonate platform complexes, which ceased during the Valangian when a major transgressive event resulted in the deposition of several hundreds of metres of marine shale (Vear, 2005). During the Albian to Turonian, deepwater conditions predominated on the margin with a wide variety of depositional environments represented. The Campanian to the Maastrichtian was a period of relative lowstand during which there was major incision of the continental slope, evident as buried canyons clearly imaged in the seismic data (Vear, 2005). The Oligocene succession on the margin is dominated by deepwater calcarenites and claystones. From the Early Miocene through to the Recent, canyon systems and a large number of channels have traversed the upper slope. On the West African margin, the Neogene succession has a complex depositional history from the Late Miocene to the present day (Schwab *et al.,* 2007). There are numerous slides and mass transport complexes throughout the Neogene succession, and their formation was the

consequence of uninterrupted deposition of sediment in an open-slope environment which gave rise to rapid accumulation of poorly consolidated sediment intercalated with thin weak layers (Antobreh and Krastel, 2007).

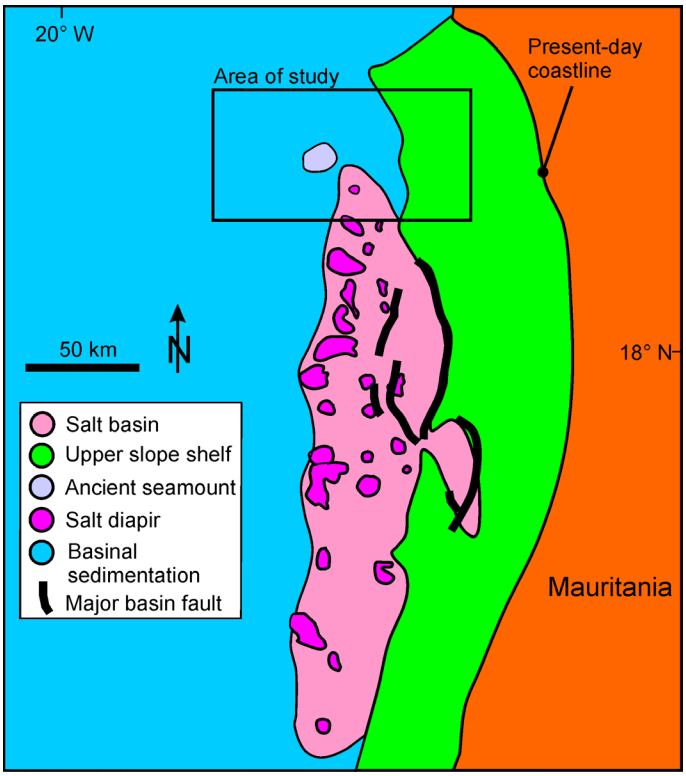

Fig. 1.11 Map of Mauritanian basin, area of study is situated on the northern edge of the extent of the salt basin (after Vear, 2005). Black lines represent basin bounding faults.

1.5 THESIS OUTLINE

Chapter 2 describes the basic principles that underpin interpreting seismic reflection data, the primary mode of investigation in this thesis, and the datasets used.

Chapters 3, 4, 5 and 6 cover the main objectives of this thesis and have been written and prepared as manuscripts that have either been published, accepted for publication or are in review in peer reviewed journals. Each of these chapters therefore contains its own *introduction*, *geological setting*, and *data and methodology* section, which cover some of the points from Chapters 1 and 2.

Chapter 3 investigates the structure of the silica diagenetic transformation zone using 3-D seismic reflection data, incorporating wireline logs and X-ray powder diffraction data. The work in this chapter has been published as: 'Structure of a silica diagenetic

transformation zone: Gjallar Ridge, offshore Norway', in *Sedimentology* (Doi: 10.1111/j.1365-3091.2010.01170.x) (a copy of which can be found in the Appendix C). Over 90% of the final paper is my own work with remaining 10% from the other authors. Contributions by the authors to the manuscript are as follows: Ireland (seismic and well log interpretation, synthetic generation, manuscript and figure preparation) Davies and Goulty (manuscript editing advice) and Carruthers (seismic interpretation).

Chapter 4 describes a potential model for the preferential localization of silica diagenetic transformations and the identification of associated fluid flow conduits. The model is discussed in Chapter 3 but is described in more detail in this chapter, which is based on the published paper entitled 'Influence of pore water chemistry on silica diagenesis: evidence from the interaction of diagenetic reaction zones with polygonal fault systems', in the *Journal of the Geological Society*, (Doi: 10.1144/0016-76492009-049) (a copy of which can be found in the Appendix C). Approximately 50% of this paper is my own work, with Goulty contributing approximately 40 % and Davies 10 %. Contributions by the authors are as follows: Ireland (seismic interpretation, manuscript and figure preparation), Goulty (original idea and manuscript preparation) and Davies (manuscript editing advice). The term 'reaction zone' has been replaced with 'transformation zone' for consistency within this thesis.

Chapter 5 investigates the influence of stratigraphic dip and simple shear on layer-bound fault development in a siliceous sediment located offshore Mauritania. The work in this chapter entitled 'Influence of stratigraphic setting and simple shear on layer-bound compaction faults offshore Mauritania' is in press in the *Journal of Structural Geology* (Doi:10.1016/j.jsg.2010.11.005) (a copy of which can be found in the Appendix C). Over 80% of the final manuscript is my own work, with Goulty and Davies contributing the remaining 20%. Contributions by the authors to the manuscript are as follows: Ireland (seismic interpretation, manuscript and figure preparation), Goulty (manuscript editing advice, mathematical theory), Davies (manuscript editing advice).

Chapter 6 describes fold and thrust dominated slope failures from siliceous successions around the flanks of the Vema Dome. The work in this chapter is based on a manuscript accepted pending corrections in *Marine Geology*. Over 90% of the submitted manuscript is my own work with the other three authors contributing the remaining 10%. Contributions by the authors to the manuscript are as follows: Ireland (seismic interpretation, manuscript and figure preparation) Davies and Goulty (manuscript editing advice) and Moy (seismic interpretation of Vema Dome structure).

Chapter 7 is a synthesis of the conclusions from chapters 3, 4, 5 and 6. It discusses areas of uncertainties, potential analogues, implications and areas for future work.

In Chapters 4, 5 and 6, pronouns referring to the author (myself) appear in the plural form (i.e. *we* replaces *I*) throughout as an acknowledgement of co-author in the manuscripts. The thesis only contains manuscripts for which I am the first author. Davies and Goulty conceived the original project, and in Chapters 3, 4, 5 and 6 all authors listed contributed to the development of the ideas during discussions. In addition to the four main chapters of this thesis, seismic interpretation, the preparation of figures and text and scientific discussions contributed to two additional journal articles on closely related themes: 1) Differential compaction due to the irregular topology of a diagenetic reaction boundary: a new mechanism for the formation of polygonal faults, (2009) Davies, R. J., Ireland, M. T. and Cartwright J. A., *Basin Research* (Doi: 10.1111/j.1365-2117.2008.00389.x) (a copy of which can be found in the Appendix C). 2) Thermal triggering and propagation of polygonal fault arrays by volume reduction reactions in siliceous sediment (accepted), Davies, R. J. and Ireland M. T. *Marine Geology*.

2 DATA & METHODOLOGY

2.1 INTERPRETATION OF 3-D SEISMIC

3-D and 2-D seismic reflection data collected primarily by, or for use by, the upstream oil and gas industry, are typically employed to reduce oil and gas exploration risk, and are increasingly used in collaboration with academic researchers (e.g. Cartwright and Huuse, 2005 and references therein). Primarily, these data allow geoscientists to map subsurface geological structures and stratigraphic features (Sheriff, 2002). Datasets are often extremely large in terms of digital data volume, tens to hundreds of gigabytes and require high power computing hardware and specialist software to interpret them. In this section a description of the fundamental principles of seismic reflection data and the interpretation methods employed in this research are given, along with details of the seismic and well datasets used. A glossary of terms (Appendix A) provides a brief explanation of some of the geophysical terminology used in this and subsequent chapters. The reader is referred to Sheriff (2002) for a further, more comprehensive definitions of terms used in this thesis.

2.1.1 FUNDAMENTALS OF THE SEISMIC REFLECTION METHOD

Reflection seismic uses compressional waves generated at or near the surface (sea surface in marine surveys) by an energy source, that subsequently travel down through the subsurface and are reflected back towards the surface by geological interfaces (e.g. bedding planes) (Bacon *et al.,* 2007). The reflected signals are detected by the receivers and recorded as a function of elapsed time after the source is fired, and the resulting data reveal information about the depth to geological interfaces and changes in rock properties across them (Fig. 2.1) (Bacon *et al.,* 2007). In marine reflection seismic surveys the energy source is typically an array of air guns (a single gun in the case of a vertical seismic profile) towed in various combinations with receivers by a vessel at the sea surface (Fig. 2.1). Marine seismic reflection surveys are the mostly concerned with P-wave reflections, as fluids do not transmit S-waves (Bacon *et al.,* 2007). Fundamental to the seismic reflection method is the property of a layer termed acoustic impedance (Z), which can be defined as:

$$Z = \rho V \qquad \textbf{Eq. 2.1}$$

where ρ is the density of the rock or sediment, and V the velocity of a P-wave through the rock or sediment. Contrasts in acoustic impedance determine the reflection coefficient at normal incidence (Sheriff, 2002). The velocity of a P-wave through an isotropic homogenous solid is controlled by the elastic constants and density of the material (Sheriff and Geldart, 1995). Rocks and sediments are rarely isotropic or homogenous in reality, and as such the velocity of wave will vary depending on composition, porosity, and fluid content, which may all vary in 3-D (Bacon *et al.,* 2007).

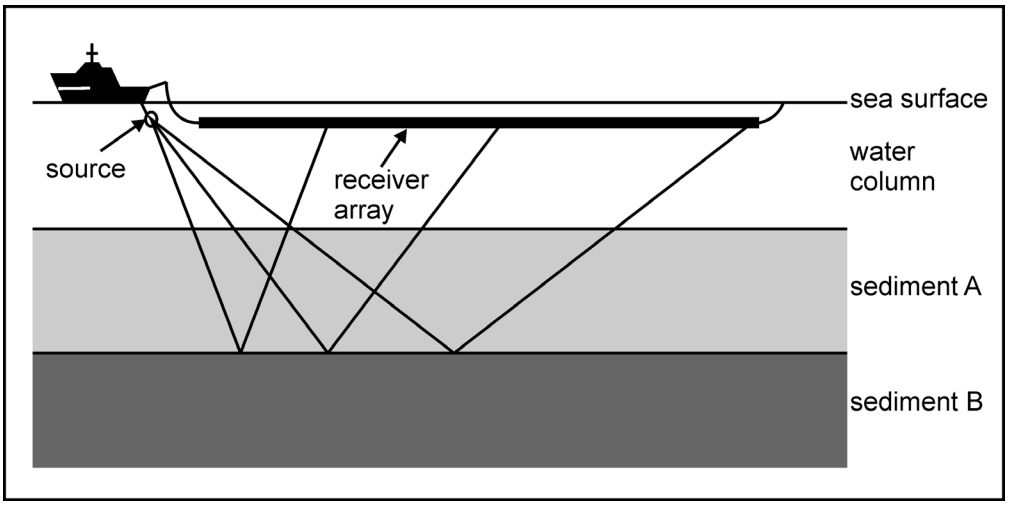

Fig. 2.1 Simplified diagram of marine seismic acquisition. Boat travels through the water emitting sound source. At changes in elastic properties the wave is reflected back, travelling up to the surface where it is recorded by receivers (after Bacon *et al.*, 2007).

Originally seismic data were collected along single 2-D lines, often widely spaced, but it soon became apparent that by acquiring a number of very closely spaced parallel lines of data there is less need to interpolate between lines, which results in a dense coverage of data, a 3-D seismic survey (Bacon *et al.,* 2007). The advantage of 3-D coverage over 2-D coverage is illustrated in Fig. 2.2.

Seismic reflection data provide a first approximation of a cross section beneath the Earth's surface in the case of 2-D data and an imaged volume in the case of 3-D data. Seismic sections are typically displayed with vertical (z) axis in two way travel time (twt) or depth (m) and horizontal (x, y) axis in metres (m) or kilometres (km). Two way time can be converted to depth, but only where accurate information is available regarding the P-wave velocities through

the various rock layers. The seismic data in this thesis are all in time, although, where appropriate, values of time are converted to depth.

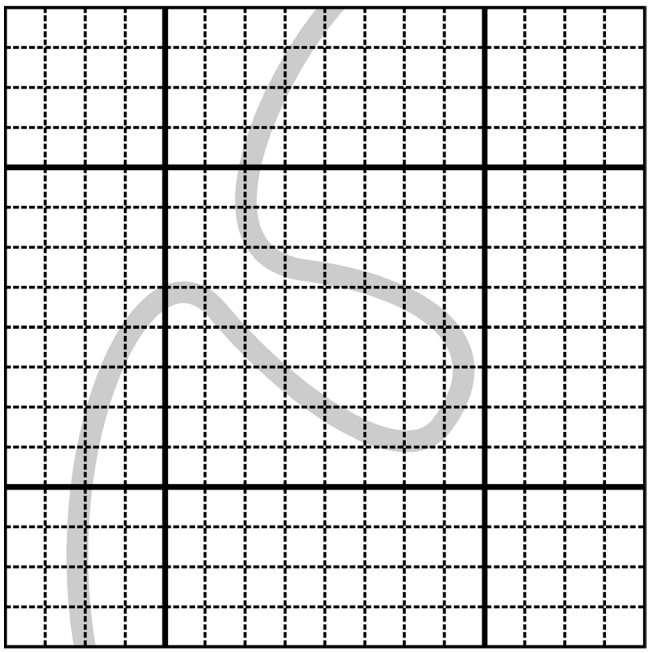

Fig. 2.2 Schematic demonstrating the advantage of a 3-D seismic coverage (dashed lines) over a 2-D seismic coverage (solid lines) when interpreting geological features (a channel in this case - light grey). 2-D data coverage misses the meander loop completely (after Brown, 2005a). No scale implied, but in a typical 3-D survey the line spacing may be 12.5 m.

2.1.2 PROCESSING OF SEISMIC REFLECTION DATA

Prior to the recorded seismic reflection data being interpreted, a number of processing steps are required. The objective of seismic processing is to refine collected data to image the structure of the subsurface, where the fundamental aims are to rearrange the data, filter the data according to specific criteria (e.g. frequency), improve the signal-to-noise ratio, and migrate the data (Bacon *et al.,* 2007). Migration is a key step in the processing, which move data so that they lie in the correct spatial position, rather than their recorded position. The processing of 3-D data may involve many hundreds of algorithms with often more than one method to approach any given problem and can involve trying several of these to achieve the optimal result (Bacon *et al.,* 2007). A comprehensive account of seismic data processing is given by Yilmaz and Doherty (1987) and a typical sequence of steps may be found in Bacon *et al.,* (2007).

Data used in this research were supplied processed, with no requirement for further processing prior to interpretation. Limited information regarding the exact steps carried out during processing of the seismic data are provided in subsequent sections (see 2.2.1, 2.2.2, 2.2.3). Seismic data in this thesis are displayed using the Society of Exploration Geophysists (SEG) normal convention (sometimes referred to as positive standard polarity), where a downward increase in acoustic impedance is displayed as a positive wavelet, and a downward decrease in acoustic impedance is displayed as negative wavelet (Fig. 2.3). A reflection indicating an increase in acoustic impedance or a positive reflection coefficient begins with a downward deflection. For a zero-phase wavelet, a positive reflection coefficient is represented by a central peak. It is important to understand the polarity and processing steps to recognize the limitations of the data and whether misleading artefacts are likely to exist in the processed data (Bacon *et al.,* 2007). As well as primary reflections, raypaths that may return to the surface after incurring more than one reflection in its travel path, are known as 'seismic multiples' (e.g. Sheriff, 1995). Processing attempts to remove such multiple reflections, but ultimately this is not always possible. Multiple reflection events typically have lower amplitudes than primary reflections because of loss of energy at each reflection interface. Multiple reflections often cross cut true stratal reflections.

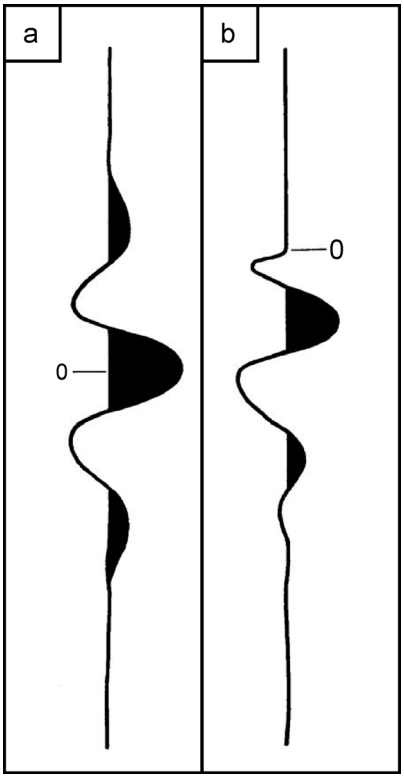

Fig. 2.3 SEG polarity standard. For a positive reflection (a) the centre of a positive symmetrical (zero-phase) wavelet is a peak. (b) a minimum-phase wavelet begins with a trough (from Sheriff, 1995)

2.1.3 RESOLUTION OF SEISMIC REFLECTION DATA.

The horizontal and vertical resolution of seismic reflection data limit the scale of investigation. A key parameter in determining the resolution is the frequency of the wave propagating through the subsurface. In general frequency content decreases with increased depths of penetration due to attenuation of waves, and as such at shallower depths where the frequency content is higher, data resolution is higher. The vertical resolution of seismic data is given by:

$$vertical\ resolution = \frac{\lambda}{4} \qquad \textbf{Eq. 2.2}$$

where λ is wavelength at the dominant frequency. Horizontal resolution of seismic data is improved as a result of migration, which collapses a diffraction hyperbola to a focus whose width will be about half the dominant wavelength (Brown, 2005a). The Fresnel zone defines the collapsed region for perfect migration, but in reality the actual zone may be larger. In the case of 2-D data, migration collapses the Fresnel zone along the line direction only. For 3-D data, migration collapses the Fresnel zone in both the in-line and cross-line directions. The horizontal resolution can be approximated as:

$$horizontal\ resolution = \frac{\lambda}{2} \qquad \textbf{Eq. 2.3}$$

Horizontal resolution is severely degraded by even small errors in migration velocity (Lansley, 2000). In this research the depth of investigation is relatively shallow (generally <1000 meters below sea floor [mbsf]) and sediments have low interval velocities. As a result, the section of interest generally has the highest frequency content and the highest resolution of any part of the data.

2.1.4 SEISMIC REFLECTION INTERPRETATION

Data in this study were interpreted using Landmark Openworks, a Unix-based software package from Landmark Graphics Corporation, mostly used by the upstream oil and gas industry. The SeisWorks package within Landmark Openworks provides seismic interpretation and analysis tools, allowing large volumes of 3-D seismic reflection data, and multiple 2-D seismic reflection lines, to be viewed and interpreted.

Seismic interpretation is primarily concerned with the interpretation of stratigraphic and structural features (cf. Brown, 2005a). The fundamental concepts of interpreting stratigraphic features, termed 'seismic stratigraphy', were described by Vail *et al.,* (1977), based on the principle that seismic reflections follow chronostratigraphic interfaces between beds (see Emery *et al.,* 1996). The interpretation of stratigraphic features generally starts from a well pick (or a distinct stratigraphic reflection in the absence of well data), with the subsequent interpretation being conducted on a series of dip lines and strike lines. Interpretation of features such as faults and folds, which can generically be termed 'structural elements', are best interpreted from lines which intersect the structures perpendicular to their strike direction (Bacon *et al.,* 2007). The application of 3-D seismic reflection data to investigate structural geology is invaluable, as data reveal 3-D geometrical information about structures that would be difficult to identify at the surface (Twiss and Moores, 2007). 3-D seismic reflection data provide significant improvements in the recognition of fault patterns over 2-D data (e.g. Cartwright, 1994; Bacon *et al.,* 2007). Not all reflections in seismic data conform to the seismic stratigraphic 'rules'. Reflections such as those interpreted as a result of diagenetic transformations (e.g. Hein *et al.,* 1978), gas hydrates (e.g. Shipley *et al.,* 1979) and direct hydrocarbon indicators (DHIs) (e.g. Bacon et al. 2007) may all cross cut chronostratigrapic interfaces.

	Amplitude response	**Reflection polarity**	**Conformance with structure**	**Lateral continuity**
Seismic multiple	Generally low amplitude	+ve or –ne	None	Depends on extent of multiple interface
Opal-A to opal-CT transformation boundary	Generally high amplitude	+ve	Not generally, but may be offset by faults	Often extensive ('000s km^2)
Direct hydrocarbon indicator (DHI)	Shows amplitude increase in most case	+ve or –ve	Yes	Relatively low (<100 km^2)
Gas hydrates	Generally low amplitude	-ve	Generally only with seabed	Often extensive

Table 2.1 Characteristics of seismic reflection events that may cross cut stratal reflections.

Silica diagenetic transformations appear on seismic reflection data often as cross cutting reflections which means some of their characteristic may appear similar to multiple seismic reflections, DHIs and gas hydrate reflections in data. Table 2.1 summarises the characteritcs of seismic reflections that may cross cut strata reflections.

To produce an interpretation of the subsurface, the first step is to interpret a horizon on intersecting lines. Typically this process uses an autotracker to guide the user's interpretation of reflections by tracking amplitudes which can be either: i) maximum, ii) minimum, iii) zero crossing.

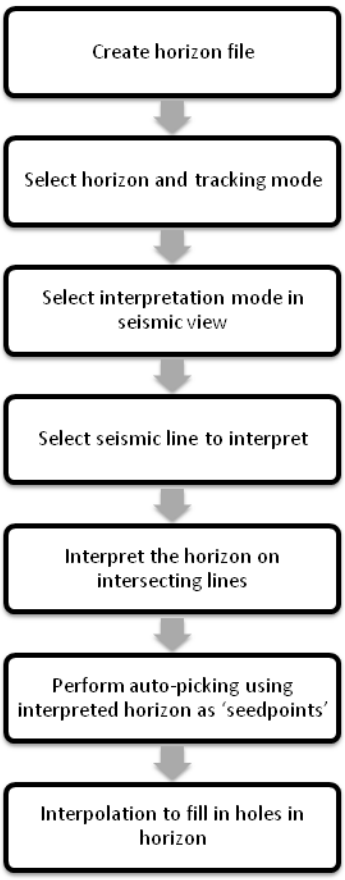

Fig. 2.4 Typical seismic interpretation workflow within Landmark SeisWorks.

The method by which the autotracker searches for the adjacent amplitudes along the reflection to snap to can be either: i) 'auto dip' where amplitude is tracked based on the first and last traces selected by the user or ii) 'autotrack' where the seed point from one trace to the next is used to set track length and direction. In regions of extremely poor seismic imaging the user may specify a 'point to point' interpretation, whereby the user defines the each point. Given the

vast increase in the number of lines 3-D seismic surveys have over 2-D surveys covering a similar area, it would be extremely time consuming and labour intensive for the user to interpret every line as described above. Consequently, interpretation of 3-D data uses automated horizon pickers which use initial interpretations of reflections as 'seed points' and calculates an output horizon from them (Fig. 2.4). The complexity of the reflection being mapped will determine the number of seed points required. For instance, a relatively simple reflection such as the seabed, may only require a coarse grid of seed points (e.g. every 50 in-lines and cross-lines), whereas a more complex reflector such as one which is offset by many faults would require a much finer grid of seed points (e.g. every 5 in-lines and cross-lines). Within Landmark, such auto-picking functionality is provided by the ZAP! 3D package (Landmark, 2005). The method employed in the software searches adjacent traces for picks with similar or identical seismic attributes[1] and where the prospective picks meet user-defined tracking criteria new picks are converted to new seed points (Fig. 2.5). The resulting horizons may be commonly known as 'time-structure' maps, with the depth units being in two way time. Fig 2.4 provides a summarized workflow for the interpretation of seismic reflection data.

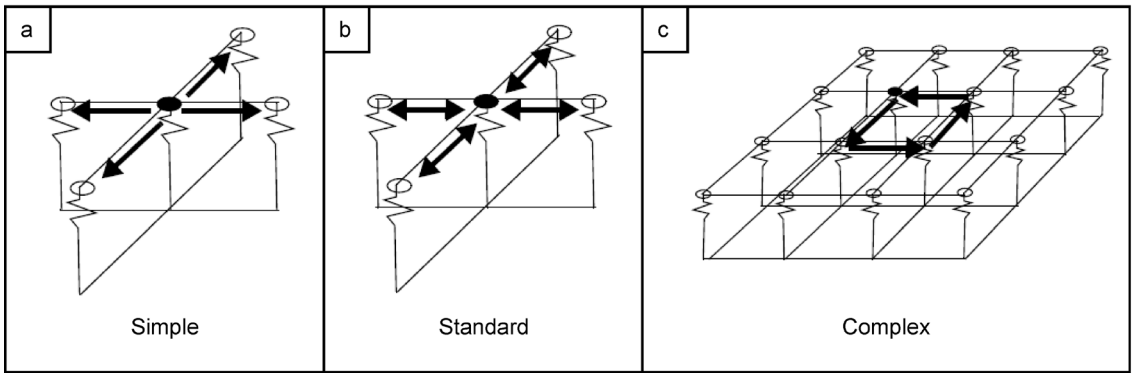

Fig. 2.5 Summary diagram of autopicking methods available within ZAP! 3-D. (a) Simple, where software picks 4 adjacent traces. (b) Standard, where 4 adjacent traces are picked and cross-checks those with the original seed points in the reverse direction. (c) Complex where picks are verified, and cross-checked with all surrounding traces in a tiled surface of a user-specified size (3x3 tile shown). All traces on the specified tile must match before any will be accepted. If all traces tie, each one then becomes the seed point (SeisWorks/3D Horizon Interpretation, Landmark Graphics Corporation, 2005).

[1] Though theoretically an autopicker could pick other seismic attributes, only amplitudes are tracked in this thesis.

2.1.5 SEISMIC ATTRIBUTES AND DERIVATIVES

Seismic attribute is a generic term used to describe calculations or measurements made on seismic traces (Bacon *et al.,* 2007). These attributes are generally calculated from the 3-D seismic volume (although some can be used on 2-D data) and are used to extract further information about the subsurface. In this study the seismic attributes used are amplitude, dip, edge detection and coherency. Seismic attributes are typically best viewed in the horizontal plane. The mathematical calculations for the attributes described below are included in Appendix A where appropriate.

2.1.5.1 HORIZON & TRACE BASED

Seismic amplitude is a measure of "the departure of a wave from zero" (Sheriff, 2002) and may be calculated from an individual reflection event, between two reflection events or by a specified time window around a reflection event. By specifying a referenced window the amplitude across the entire window is calculated. A greater seismic amplitude generally corresponds to a greater increase or decrease in acoustic impedance. In addition to absolute values, the root mean square (RMS) average amplitude, is particularly useful in identifying subtle changes.

Dip is a measure of the magnitude of the time gradient, and constructed by comparing a sample point of a horizon with two adjacent sample points in orthogonal directions and fitting a plane through the three points. The magnitude of dip is in milliseconds per unit distance multiplied by 1000. Individual dip values are not particularly meaningful, but the relative difference between various dip values is very useful in identifying faults (Landmark, 2005).

Edge detection is an image processing technique (e.g. Gonzalez and Woods, 2008) which highlights discontinuities in an image. The method employed within SeisWorks detects differences in *dip* across a horizon, and compares points around a single sample point in an original image, using a 3x3 grid (three samples on either side of a point in both directions).

2.1.5.2 VOLUME BASED

Structure cube is a seismic discontinuity attribute. Where small regions of seismic traces are cut by a fault surface or similar feature, they generally have a different seismic character than the corresponding regions of neighbouring traces resulting in a sharp

discontinuity in local trace-to-trace coherence (Bahorich and Farmer, 1995). Structure cube, developed by Landmark, compares traces in an analysis window with the average trace of the window using weighted correlations, which are sensitive to the relative magnitude of the trace amplitude values (Landmark, 2006). The advantage of such attributes over dip and edge detection is that it does not require the interpretation of horizons by an interpreter or autotracker, though the attribute may be extracted along an interpreted horizon in complex regions. This attribute may be considered similar to coherency type attributes widely described in the geophysics literature (e.g. Bahorich and Farmer, 1995).

2.1.6 WELL-TO-SEISMIC TIE

It is possible, to a first approximation, to calculate the expected seismic response of a given rock or sediment section if treated as a 1-D problem and create a synthetic seismic trace (Sheriff and Geldart, 1995). This enables correlation and matching of well logs and seismic data. Considering the subsurface as a number of layers with their own given acoustic impedance, Z, then the reflection coefficient at (R_n) the nth interface for P-waves at zero-offset is given by the formula:

$$R_n = (Z_{n+1} - Z_n)/(Z_{n+1} + Z_n) \qquad \textbf{Eq. 2.4}$$

where Z_n and Z_{n+1} are the acoustic impedance above and below the interface respectively (Sheriff and Geldart, 1995). Both density and sonic velocity values are required, which can then be multiplied together to generate an acoustic impedance log. A reflectivity curve is then calculated from the impedance log and this is convolved with a wavelet. Either a generic wavelet can be specified or the wavelet can be extracted from the seismic data. In this thesis, the wavelet was extracted, to create an optimum wavelet using the partial coherence matching method of White (1980); this is a statistically robust method. The data from well 6704/12-1 is used to generate a synthetic trace and match this to a 3-D seismic survey from the Gjallar Ridge. This is described and its match to the data is shown in Chapter 3. No well data was available for section of interest for the Mauritania 3-D seismic survey.

2.1.7 COLOUR

Seismic sections and maps (time, depth, or attribute) can be displayed in an almost infinite number of colour bars. Seismic sections in this thesis are displayed using double gradational colour schemes, where there is symmetry of two colours about a centre value, ensuring that both peaks and troughs of seismic data are visible (Brown, 2005a). Horizon maps are shown in a variety of colour schemes; gradational colour spectrums are useful where the interpreter is looking for trends, shapes, patterns and continuity (Brown, 2005a) such as time-structure maps (where a spectrum colour bar is typically used); in other cases gradational colour schemes between two colours, i.e. white and black, or blue and black, are used where the interpreter is looking for contrasts and discontinuity.

2.1.8 3-D VISUALIZATION

Over the past decade the way in which interpreters view seismic data has been changing due to lower cost computer power (Bacon *et al.,* 2007). Data can now be more easily viewed and interpreted in 3-D, where data can be manipulated and viewed from any angle, giving the interpreter a better sense of the three-dimensionality of the data and geological structures. Seismic data were loaded into Landmark's GeoProbe application where data can be visualized in 3-D, providing a more 'interactive' approach to interpretation, and allowing the generation of 3-D images of seismic data and horizon interpretations[2]. This software also allowed for data to be projected onto a flat screen as a stereo pair, with rapid alteration between left and right eye pictures, so that it appears to the viewer as if they are looking at a 'real' 3-D object.

2.2 SEISMIC REFLECTION DATA

This research uses three 3-D seismic surveys. In addition, two 2-D seismic reflection lines have been used to correlate the adjacent Gjallar Ridge and Vema Dome 3-D surveys (see Appendix B). Each 3-D survey covers a different area, and were acquired and processed by different companies. A brief description of each dataset is provided below.

[2] Examples of 3-D visualisation of interpretations can be seen in Fig 4.3, 4.5, 5.5, 6.4 and 7.3.

2.2.1 GJALLAR RIDGE 3-D SEISMIC SURVEY

This survey is located ~200 km offshore mid-Norway in ~1500 m water depth (Fig. 2.6). It covers an area of ~4000 km^2 and has 2223 lines and 3929 traces at a spacing of 12.5 m in both directions. It was provided by Statoil for use by Durham University. The data, originally consisted of two individual 3-D seismic refection surveys, collected separately, which have subsequently been merged into a single seismic volume for interpretation purposes. The data have been processed using a standard sequence of steps including post-stack time migration. The dominant frequency at the depth range 0 – 1000 mbsf is in the range from 40 to 50 Hz, giving a vertical resolution of ~10 m and a horizontal resolution of ~25 m. The data have been zero-phased via wavelet extraction from a nearby exploration well by use of a 2-D tie-line. Decay of seismic amplitudes due to geometric spreading, anelastic attenuation and transmission losses was compensated using a gain ramp during pre-stack processing and automatic gain control (AGC) before post-stack time migration. Seismic horizons mapped in the survey were based on limited shallow correlation to well 6704/12-1 and seismic characteristics. See Appendix B for a list and maps of the key horizons in this thesis.

2.2.2 VEMA DOME 3-D SEISMIC SURVEY

This survey is located ~200 km offshore Norway, in water depths of ~1500 m. It covers an area of ~2500 km^2. The data consists of 2312 lines and 1572 traces, with a 25 m by 25 m spacing. The data were provided by Statoil for use by Durham University. The dominant frequency in the upper 2 seconds twt, the depth of interest in this thesis, is 50 Hz. They have a vertical resolution of ~10 m and a horizontal resolution of ~25 m. The data have not been zero phased and no automatic gain control has been applied. See Appendix B for a list and maps of the key horizons in this thesis.

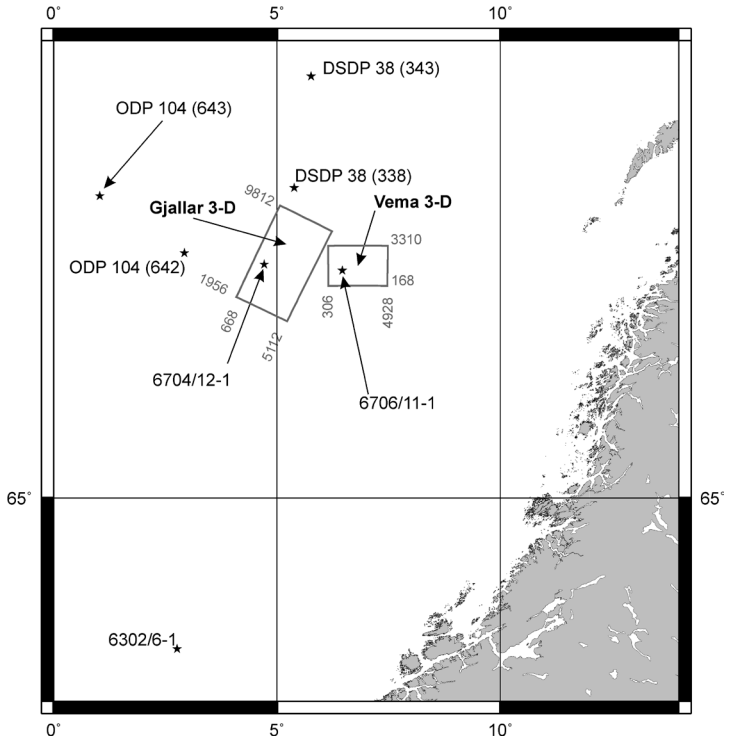

Fig. 2.6 Location map showing the position of the Gjallar Ridge 3-D seismic survey and the 3-D seismic survey that covers the Vema Dome and the Nyk High (grey boxes). Numbers at edge of survey are end line and trace numbers. Location of wells used in this study marked by black stars. See text for details.

2.2.3 MAURITANIA 3-D SEISMIC SURVEY

This survey is located ~100 km offshore of Mauritania in water depths of 300 – 2000 m (Fig. 2.7). It covers an area of approximately 4000 km^2. The data consist of 3481 lines and 5521 traces, with 25 by 25 m spacing. The data was provided by Tullow Oil and Petronas for use by Durham University. Data consist of a single time-migrated three-dimensional (3-D) seismic reflection volume. These data were processed using a standard sequence of steps including multiple suppression and post-stack time migration. The data have a vertical resolution in the Neogene of about 10 m, at the dominant frequency of ~50 Hz,. The processed data have not been zero-phased and have no AGC applied. See Appendix B for a list and maps of the key horizons in this thesis.

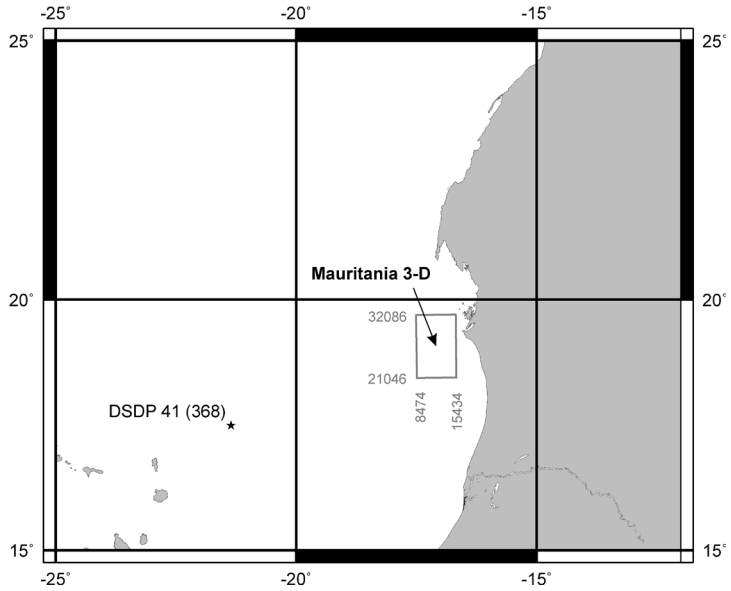

Fig. 2.7 Location map showing the position of the Mauritania 3-D seismic survey (grey box). Numbers at edge of survey are end line and trace numbers. Black star marks well location. See text for details.

2.3 WELL DATA

Seismic interpretation requires knowledge of the sediment and rock types penetrated, to understand seismic wave response, and how the imaged features relate to geological settings. Limited wells are available in the areas studied in this thesis, and these have been correlated where possible the seismic data using either wireline logs or core data. Two sources of well data are used; upstream oil and gas exploration wells and scientific wells drilled by DSDP and ODP.

2.3.1 EXPLORATION WELLS

For the studies from the Gjallar Ridge and Vema Dome, released well data is available from the Norwegian Petroleum Directorate (NPD) and made available to us in electronic format (.las files) by Statoil for integration with seismic reflection datasets within software packages. No core is available in the shallow sections of interest, since the target depths for the exploration wells are generally much deeper. Wireline log data is in some cases available for the shallow section, and this provides important information with regards to the physical properties of the sediments. The location of the wells is shown in Fig. 2.6.

No well data was available for correlation with the 3-D seismic data for the offshore Mauritania area, but the use of a generic depth conversion function which was derived from well data in nearby areas was available. This function was supplied courtesy of Tullow Oil, but the function and the data are commercially sensitive and not included in this thesis. It allows the conversion of TWT to meters (depth) when analysing fault dips in Chapter 5. The validity of this function was verified by comparing interval velocities with data from DSDP 41 (368) (Fig. 2.7)

Exploration wells used in this study are (with lat/lon co-ordinates in brackets):

- *6704/12-1* (4.712626208, 67.12532109) in 1352 m water depth, penetrated a total depth of 4103 m by SAGA Petroleum in 1999
- *6706/11-1* (6.46325, 67.073547) in 1238 m water depth, penetrated a total depth of 4317 m by Den norske stats oljeselskap a.s in 1997
- *6302/6-1* (2.7642975, 63.528893) in 1261 m water depth, penetrated a total depth of 4234 m by Statoil ASA in 2005

Further drilling information on each well is available from the Norwegian Petroleum Directorate at http://www.npd.no/engelsk/cwi/pbl/en/index.htm (accessed 23/09/2010). In Appendix C the depth range of the formations of interest in this study for the above wells. X-ray power diffraction analysis of cuttings from 6302/6-1 were made available from an internal Statoil report.

2.3.2 Deep Sea Drilling Project and Ocean Drilling Program wells

The Integrated Ocean Drilling Program (IODP) and the predecessors, DSDP and ODP, are international marine research programmes that explore the Earth's history and structure as recorded in seafloor sediments and rocks, and monitor subseafloor environments. This study has used data from ODP and DSDP wells, providing invaluable information on sediment composition and physical properties from the relatively shallow depths of investigation which are in general not well sampled by energy exploration. The data used are from the following:

- *DSDP Leg 38*
    - Site 343 (5.764021771, 68.71302507) water depth 3131 m in 1976
    - Site 338 (5.385188109, 67.78436912) water depth 1297 m in 1976
- *ODP Leg 104*
    - Site 642 (2.925944089, 67.22507285) water depth 1281.4 m in 1985

- Site 643 (1.0333, 67.715) water depth 2768.7 m in 1985

- *ODP Leg 112*
  - Site 680 (-11.065, -78.0778) water depth 272 m in 1987
- *DSDP Leg 41*
  - Site 368 (17.5072, - 21.3538) water depth 3366 m in 1979

Logging data can be downloaded from: http://brg.ldeo.columbia.edu/logdb/ (accessed 23/09/2010) and associated reports and citations can be downloaded from http://www.iodp-usio.org/About/default.html (accessed 23/09/2010).

2.4 FIELD ANALOGUES FOR THE SUBSURFACE

To date, the Cenozoic deepwater siliceous sediments from mid-Norway and offshore Mauritania have not been found to be exposed at the surface (outcrop). The Monterey Formation, California, provides arguably the best documented outcrop of the silica diagenetic transformations (see Eichhubl and Behl, 1998). In this thesis several comparisons are drawn between the observed seismic characteristics from the Eastern Atlantic Margin and the Monterey Formation, based mainly on literature, but also field observations. Direct observations allowed informed judgements to be made as to those processes that are comparable, and those which are significantly different. It is important to recognise that the Monterey Formation has experienced a different geological history. Below, Table 1 summarizes the similarities and differences between the Monterey Formation and the siliceous successions offshore the East Atlantic.

The Monterey Formation has been widely studied both in terms of its diagenesis and deformation. Much of the present day understanding of the diagenesis of the Monterey Formation comes from geochemical analysis, particularly, X-ray diffraction, oxygen isotope analysis, in particular from extensive outcrops along the Californian coast from Santa Barbara to Point Conception. The Monterey Formation was deposited between 17.5 Ma and 6 Ma, and the onset of dseposition coincided with rising global sea level (Baron, 1986). Major polar cooling, which began at 15 Ma, postdates the base of the Monterey by more than 2 Ma so is not the main cause for the deposition of diatomaceous sediments which occur in the lowermost Monterey (Baron, 1986). A Later polar cooling in the late Miocene however did, apparently

cause an increased upwelling and deposition of purer diatomites in the upper Monterey (Baron, 1986).

	Monterey Formation	**Kai and Brygge Formation (Norway)**	**Unknown siliceous unit (Mauritania)**
Tectonic setting	Compressional (at plate triple junction)	Passive margin (extensional)	Passive continental margin
Depositional settings	Restricted shelf slope	Basinal deep water	Basinal deep water
Age of siliceous sediments	Miocene to Pliocene	Pliocene to Oligocene	Miocene
Maximum burial depth	~1000 m (but varies along the coast)	1000 m	~1200 m
Diagenetic silica phases identified	opal-A, opal-CT, opal-CT chert, opal-CT chalcedony, quartz	opal-A, opal-CT, quartz	opal-A and opal-CT
Detrital content	10 – 70 %	5 – 75 %	unknown

Table 2.2 Summary of the geological setting and key characteristics of the Brygge and Kai Formations, probably siliceous succession offshore Mauritania and the Monterey Formation which is used as an analogue in this thesis.

The Monterey Formation is a good analogue to the diagenesis and deformation of siliceous sediments because: 1) The formation has undergone for a single burial/exhumation cycle (McCrory *et al.,* 1995). 2) Exposed sections have reached various depths of maximum burial, giving insight into a range of different stages of diagenetic alteration (Isaacs, 1981a). 3) The formation is a currently producing reservoir of hydrocarbons, with wells providing subsurface information on structure and fluid composition. Fig 2.8 shows the lateral relationship between the broad silica phase zones which cut across lithostratigraphic boundaries in the Santa Barbara coastal area.

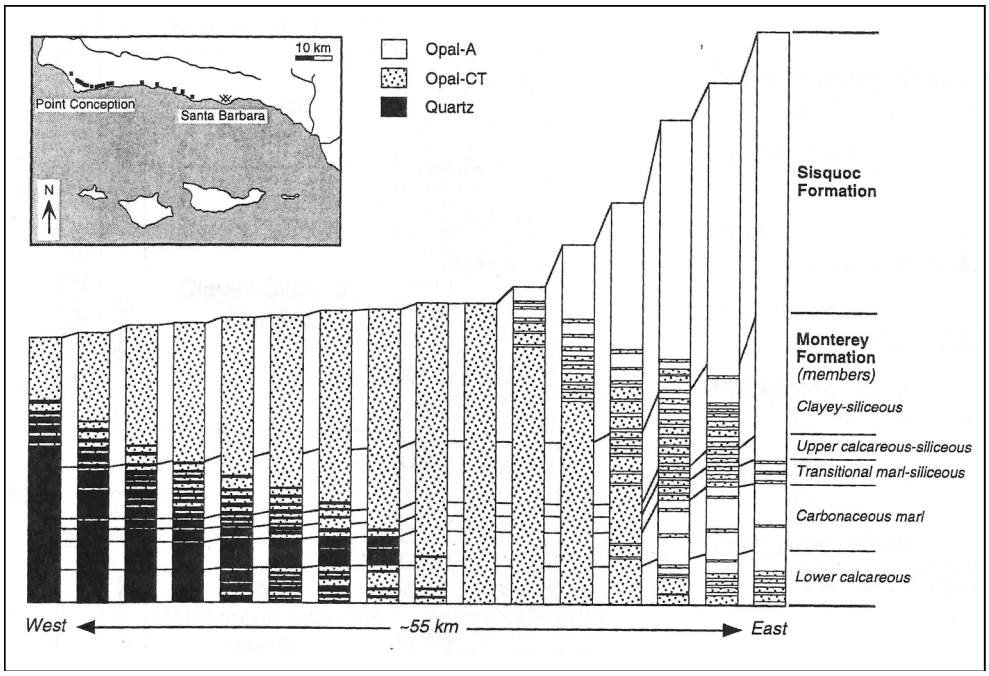

Fig. 2.8 Schematic section from West to East across the Santa Barbara coastal area. Each section represents an equal weight o f rock adjusted in thickness for average porosity differences resulting from compaction during silica phase transformations. At each section there are interbedded and overlapping silica phases, both opal-A and opal-CT and opal-CT and quartz. From Isaacs (1981).

In the Santa Barbara coastal area this broad transition zone in which rocks with contrasting silica phases are interbedded is generally attributed to slight differences in transformation temperatures related to original sediment composition (Isaacs et al., 1981). Reconstructed thermal burial histories of the Monterey Formation which are tied to well data, indicate that these overlapping silica phases can be the direct result of variations in sedimentation rate, temperature over time and original sediment composition.

3 STRUCTURE OF A SILICA DIAGENETIC TRANSFORMATION ZONE: THE GJALLAR RIDGE, OFFSHORE NORWAY

ABSTRACT

Three dimensional seismic data from the Gjallar Ridge were used together with X-ray diffraction data, scientific boreholes and wireline logs to analyse the seismic structure of a silica diagenetic transformation zone. The following features were identified: (a) an interval some 150 to 300 m thick that contains anomalously high amplitude reflections; (b) a strong reflection event at the top of this interval which cross-cuts stratigraphy, interpreted as the transformation boundary between opal-A-rich and opal-CT-rich sediment; (c) amplitude variations on stratigraphic reflections within the interval, attributed to variations in the proportions of opal-A and opal-CT; and (d) a second, deeper, cross-cutting reflection event within the interval, interpreted as the transformation boundary between opal-CT-rich and quartz-rich sediment. The base of the interval containing the anomalously high amplitude reflections is interpreted as a stratigraphic reflection demarcating the base of the silica-rich strata. On a stratigraphic reflection within the interval of high amplitudes, roughly circular regions of anomalously high amplitude with diameters of 0.8 to 2.5 km are separated by lower amplitude regions. This pattern is similar to the cells previously identified at the opal-A to opal-CT transformation boundary and probably results from more complete transformation of opal-A to opal-CT. All of these observations provide the first recognition from seismic data that silica diagenetic transformations are not always narrow boundaries represented by single cross-cutting seismic reflection events, as implied previously, but can be heterogeneous and hundreds of metres in thickness, as observed at outcrop.

3.1 INTRODUCTION

The terms 'transformation zone' and 'reaction zone' are used in geology to refer to the rock or sediment within which mineral transformations take place (Berner, 1980; Ortoleva, 1994). Transformation zones and reaction zones have been described or predicted in many different geological settings at a variety of scales, from microns (Brand and Veizer, 1980) to hundreds of metres (Freed and Peacor, 1989). During burial of sedimentary rocks mineral transformations occur as a result of a variety of chemical processes such as dissolution and precipitation and microbial reactions, and these processes may affect the mechanical properties of the rock (Bjørlykke and Høeg, 1997). Understanding the kilometre-scale variability of a diagenetic transformation zone in sedimentary strata is made difficult because of the scale limitations of well and outcrop data. Using 3-D seismic reflection data allows a transformation zone to be imaged in 3-D at up to sedimentary basin scale.

In this study, the focus is placed on the silica diagenetic transformations that occur during burial of sediment which is rich in amorphous silica of biogenic origin (opal-A). Opal-A is first transformed into the intermediate product of crystalline silica (opal-CT). Subsequently opal-CT transforms to quartz as a result of continued burial. Both stages of transformation occur through dissolution and precipitation (Isaacs, 1982; Williams *et al.,* 1985). These transformations release large quantities of water (Davies *et al.,* 2008) and result in significant changes to the physical properties of the host sediment, often giving rise to a distinctive response on seismic reflection data across areas of ~10^5 km (Davies and Cartwright, 2002; Meadows and Davies, 2007). Discrete seismic reflection events arising from the level where the transformation of opal-A to opal-CT occurs are well documented at the basin scale (Herman, 1972; Tucholke, 1978; Davies and Cartwright, 2002; Davies and Posamentier, 2005). These reflections are reported as single high-amplitude reflection events with positive polarity, corresponding to a downward increase in acoustic impedance (Hein *et al.,* 1978; Davies and Cartwright, 2002, 2007; Meadows and Davies, 2007), and have generally been interpreted as representing the complete transformation of opal-A to opal-CT across a zone with a thickness of a few metres.

The seismic interpretation of a complete silica diagenetic transformation zone is presented here, showing evidence for two transformation boundaries, where opal-A transforms to opal-CT and opal-CT transforms to quartz, and for ongoing transformation of opal-A to opal-CT between those levels. This interpretation constitutes the first recognition from seismic data that silica diagenetic transformation zones can be hundreds of metres in thickness, as observed at outcrop.

3.2 SILICA DIAGENESIS

Opal-A is an important component of ocean sediments (Gallinari *et al.,* 2002) and has been produced by phytoplanktonic organisms, including diatoms (Lisitzin, 1972; Nelson *et al.,* 1995), from the Cretaceous to present day (Laventer, 2009). Within silica-rich sediments the transformations of opal-A to opal-CT and of opal-CT to quartz are major diagenetic changes. The rate of transformation is controlled by the reactive surface area (Steefel and Van Cappellen, 1990); the presence of clays which may inhibit the formation of opal-CT; the presence of carbonates, which may promote the precipitation of opal-CT (Kastner *et al.,* 1977); and factors not related to original sediment composition such as pore water chemistry, temperature and time (Kastner *et al.,* 1977). In regions with high sedimentation rates the transformation of opal-A to opal-CT usually occurs at temperatures of 25°C to 55°C, and transformation of opal-CT to quartz at temperatures of 31°C to 77°C (Pisciotto, 1981). The time for the transformation to complete is highly variable and dependent upon temperature.

Transformation of opal-A to opal-CT in silica-rich sediment can result in porosity reduction by as much as 30% (Isaacs, 1981; Tada and Iijima, 1983; Meadows and Davies, 2009). Transformation of opal-CT to quartz results in further porosity reduction (Compton, 1991). The porosity reduction at each transformation boundary has previously been reported to be associated with an increase in the bulk density and in the P-wave and S-wave velocities (Guerin and Goldberg, 1996), resulting in a large acoustic impedance contrast that can give rise to a seismic reflection event (Hein *et al.,* 1978). Examples have been reported from the Barents Sea (Hein *et al.,* 1978), the Japan Sea (Kim *et al.,* 2007), offshore eastern USA (Guerin and Goldberg, 1996), the North-East Atlantic Margin (Davies and Cartwright, 2002, 2007; Berndt *et al.,* 2004) and offshore Eastern Australia (Exon *et al.,* 2007). In each of these previously reported cases, a single discrete reflection event has been identified and interpreted as arising from a transformation confined to a narrow interval of <20 m in thickness (Davies and Cartwright, 2002; Meadows and Davies, 2007; Nobes *et al.,* 1992). In contrast, work on the Monterey Formation along the Californian coast has shown that there is a broad transformation zone of compositionally heterogeneous rocks lying between strata where the silica is uniformly diatomaceous and strata where the silica is uniformly opal-CT (Isaacs, 1981, 1982; Williams *et al.,* 1985). Examples of broad transformation zones, akin to the Monterey Formation, represented by several discrete seismic reflection events including cross-cutting reflection events associated with both opal-A to opal-CT and opal-CT to quartz transformation in the same succession have not previously been described from 3-D seismic data.

3.3 GEOLOGICAL SETTING

The silica diagenetic transformation zone analysed here is located in Cenozoic sediments on the Gjallar Ridge, 350 km offshore Norway, at the western edge of the Vøring Basin (Fig. 3.1). The ridge is an elevated complex of rotated and tilted fault blocks that formed during the Cretaceous (Brekke, 2000) and consists of three individual structural highs which were gradually uplifted between the Cenomanian and Early Eocene (Lundin and Doré, 1997). During the Miocene and Early Pliocene, deposition on the outer margin of the Vøring Basin primarily comprised biosiliceous hemipelagic sediments (Hjelstuen *et al.,* 1999).

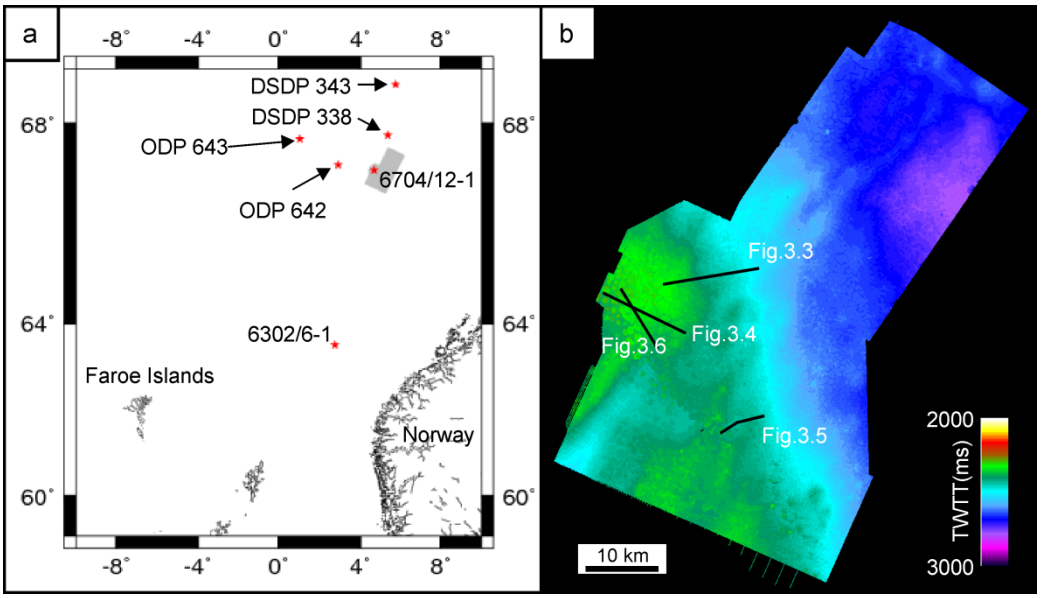

Fig. 3.1 (a) Location map showing wells used in this study (red stars) and the 3-D seismic survey as the area, shaded grey. (b) Two-way travel time map of Horizon 1 across the 3-D seismic survey with the locations of seismic sections shown in subsequent figures.

The interval of interest containing the succession of silica-rich sediment lies within the depth range 60 to 800 m below the sea floor, which is very well imaged by the 3-D seismic volume. It extends from the base of the Oligocene section in the Brygge Formation to the base of the Plio-Pleistocene Naust Formation. The Brygge Formation belongs to the Hordaland Group (Hansen *et al.,* 2005). The Hordaland Group is overlain by the Lower Miocene to Recent Nordland Group, which is subdivided into the Kai Formation and the overlying Naust Formation.

3.4 DATA AND METHODOLOGY

Data have been interpreted from a merged volume of 3-D seismic data that covers an area of ~4000 km^2. The data have been processed using a standard sequence of steps including post-stack time migration. The trace spacing is 12.5 m by 12.5 m, and the dominant frequency at the depths of interest is in the range 40 to 50 Hz, giving a vertical resolution of ~10 m and a horizontal resolution of ~25 m. The data have been zero-phased via wavelet extraction from a nearby exploration well by use of a 2-D tie-line. In the seismic images presented here, the data are displayed so that a black loop corresponds to a positive reflection coefficient associated with a downward increase in acoustic impedance, and a red loop corresponds to a negative reflection coefficient associated with a downward decrease in acoustic impedance. Decay of seismic amplitudes due to geometric spreading, anelastic attenuation and transmission losses was compensated using a gain ramp during prestack processing and automatic gain control (AGC) before post-stack time migration.

The reflection events in the seismic data volume have been correlated to the commercial exploration borehole 6704/12-1. Depth in the well is tied to two-way time (TWT) on the seismic data by a checkshot survey and a sonic log. The density and sonic logs were used to create a synthetic reflection seismogram. First, bad data points with unrealistically low values in the density log were corrected by linear interpolation. A wavelet was extracted from the 3-D seismic volume to create an optimum wavelet using the partial coherence matching method of White (1980). The primary reflectivity obtained from the density and sonic logs was then convolved with the wavelet to generate the synthetic seismogram (Sheriff and Geldart, 1995). The geophysical well logs available provide constraints on the lithologies in the studied succession and on their ages (Hansen *et al.,* 2005).

Results from Ocean Drilling Program (ODP) Sites 642 and 643 and Deep Sea Drilling Project (DSDP) Sites 338 and 343 have been used to demonstrate typical lithologies in the study region based on whole round core descriptions and have been correlated to wireline log responses within well 6704/12-1 (Fig. 3.1). X-ray powder diffraction (XRPD) analysis of samples from well 6302/6-1 (Fig. 3.1) and XRD and diagenetic studies from ODP Site 643 support the seismic observations presented in this paper. Amplitude tracking was used to map the structure of prominent seismic reflections. Where seismic amplitude was extracted as an attribute from a window referenced to a single reflection, the root mean square (RMS) amplitude was used because it is more sensitive than the mean absolute amplitude to extreme values in the data (Brown, 2005a).

3.4.1 WELL TO SEISMIC TIE

Correlation of the synthetic seismogram with the 3-D time-migrated seismic data at the location of well 6704/12-1 is shown in Fig. 3.2. The synthetic seismogram contains an event at 2.33 sec TWT marked Horizon 1, which corresponds to a large step on the density log. This downward increase in density is interpreted as the opal-A to opal-CT transformation boundary although, perhaps surprisingly, there is no corresponding step on the sonic log (Fig 3.2). As a result, there is a large downward increase in acoustic impedance and so the reflection coefficient is positive. The amplitude of this event is much greater than any of the events over an interval of 300 ms in the immediately overlying succession. At 2.52 sec TWT, an event on the synthetic seismogram marked Horizon 2 (Fig 3.2) corresponds to another upward step in density with increasing depth, and is interpreted as the opal-CT to quartz transformation boundary. Overall, the correlation between the synthetic seismogram and the processed 3-D seismic reflection data is good.

Although the sonic log response shows little change at the two silica transformation boundaries where the density steps up, the sonic log appears to be responding normally, giving low velocity values which are consistent with the low saturated bulk densities (Hempel *et al.,* 1989) and fit the interval velocities calculated from the checkshot survey. The P-wave velocities from ODP Site 643 also demonstrate a trend of gradual increase with depth, similar to that observed at 6704/12-1, with no abrupt increase across the transformation boundary (Fig. 3.2). Single extreme values of velocity (in excess of 2500 m s^{-1}) are unsupported by variations in other physical properties and the lithology log. Below 148 mbsf, cores are considerably disturbed and spurious velocity values may be due to flow along the core liner and biscuiting which are both evident in cores (Eldholm and Thiede, 1987b). Over the interval shown in Fig 3.2, there is only one bed where the sonic velocity reaches 2000 m s^{-1}. This bed is located at 2700 ms TWT, below the silica-rich sequence, and gives rise to a strong reflection event on both the synthetic seismogram and the real data. The wireline log responses (density, sonic, natural gamma and resistivity logs) (Appendix A) suggest that it is a thin sand interval surrounded by soft mud.

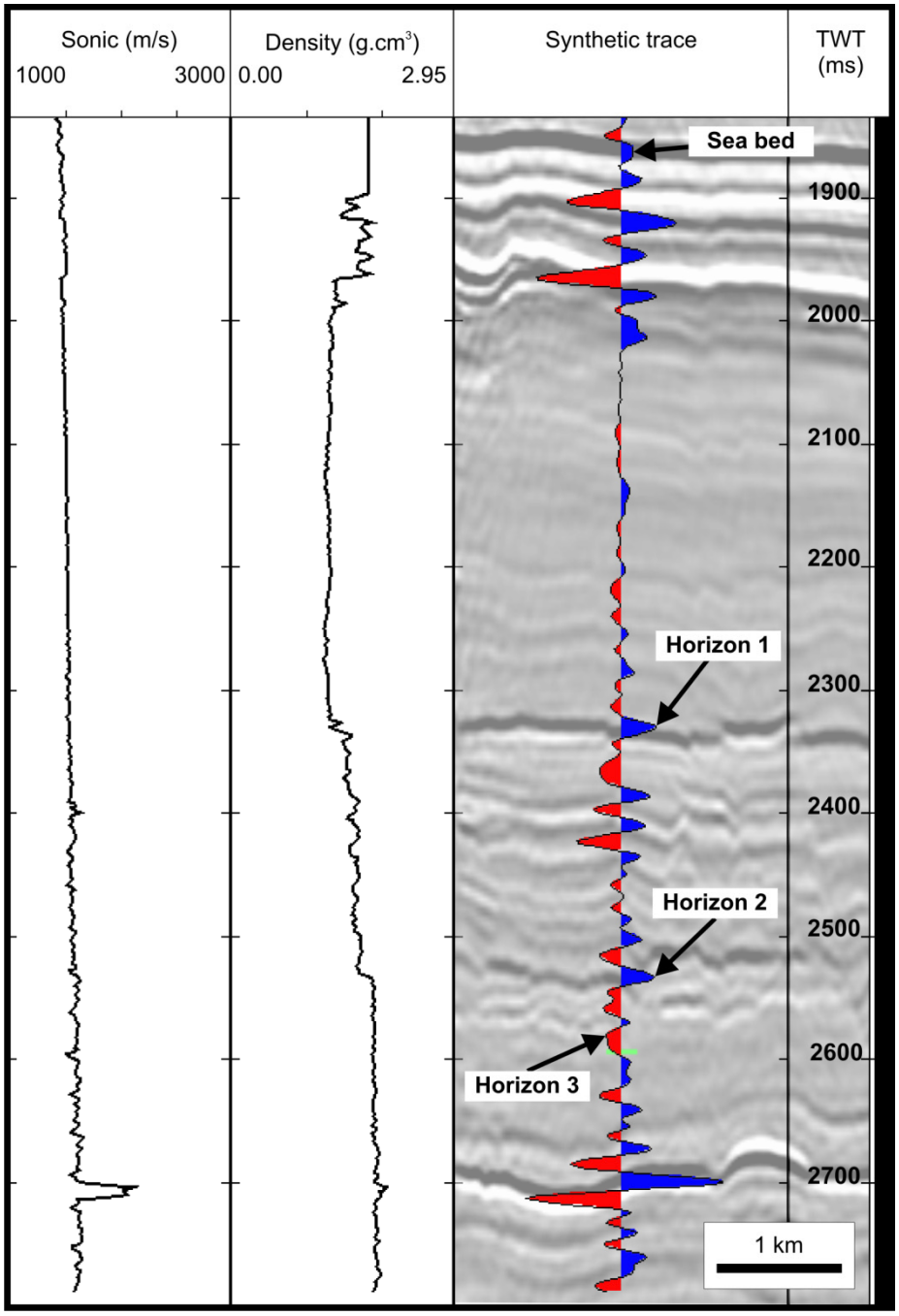

Fig. 3.2 Density and sonic logs from well 6704/12-1 with the synthetic trace generated from the logs overlain on the seismic data at the well location. Blue loops arise from positive reflection coefficients (downward increases in acoustic impedance) and red loops from negative reflection coefficients. On the seismic section, the black loops correspond to positive reflection coefficients and white loops to negative reflection coefficients.

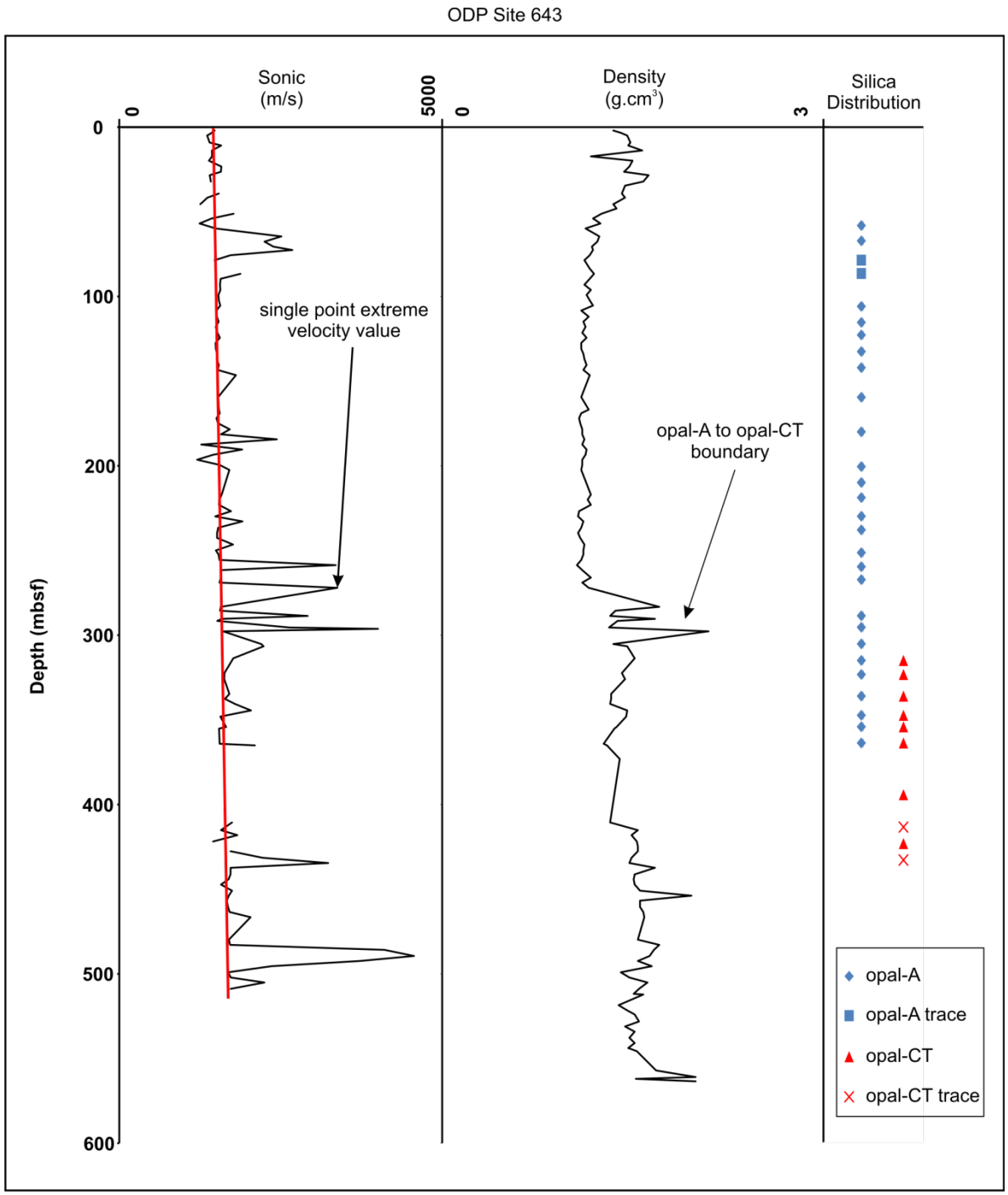

Fig. 3.3 Sonic and density logs from ODP Site 643 with the silica phases present, as determined from XRD data.

3.5 OBSERVATIONS

3.5.1 KEY SEISMIC REFLECTIONS DEFINING THE TRANSFORMATION ZONE

A strong reflection event with positive polarity between 2250 and 2800 ms TWT (depths of 375 to 525 m below the sea bed), marked Horizon 1 in Fig 3.4, cross-cuts stratal reflections and can be tracked across the survey area. This cross-cutting reflection event marks an abrupt change in the seismic response, with the package of reflection events immediately below it being of consistently higher amplitude than the package above. It correlates with an increase in bulk density of ~0.3 g cm^{-3} but no significant change in the sonic log response in well 6704/12-1 (Fig. 3.2). The topography of Horizon 1 varies: over much of the survey area it is near-planar (Fig. 3.4), whilst in areas where it is located close to the upper tips of a polygonal fault system, it comprises a topography of mesas separated by a network of troughs. This array of squat cylindrical protuberances (Fig. 3.5) was first described and termed 'cells' by Davies and Cartwright (2007). These cells are up to 2.7 km wide and 50 to 200 m high, and are each intersected by one or more faults. The cells are predominantly clustered in one area above a major structural horst block in the underlying Mesozoic strata. There are a few smaller cells away from this high, such as the two shown in Figure 3.6a. Depressions have formed in the overburden above the cells, interpreted as the result of compaction within them due to the transformation of opal-A to opal-CT (Davies, 2005; Davies and Cartwright, 2007).

A point of interest concerning the topography on the opal-A to opal-CT transformation boundary is that the exceptional quality of the imaging in these seismic data does not deteriorate below the complex topography at the boundary. This observation attests to the absence of any significant velocity increase across the boundary because the seismic data have only been processed with post-stack time migration, whereas prestack depth migration would generally be required to achieve sharp imaging below a topographically complex boundary associated with a contrast in interval velocity.

Between 2450 and 2900 ms TWT (depths of 525 to 675 m below the sea bed) on Fig. 3.4, and approximately 200 ms TWT (150 m) below Horizon 1, a reflection event with positive polarity, marked Horizon 2, can be tracked through the data volume and corresponds to an abrupt increase in bulk density of ~0.2 g cm^{-3}, and again no significant response in the sonic log at well 6704/12-1. This event is not parallel to Horizon 1 even though it also tends to cross-cut stratal reflection events including the base of the Kai Formation where it passes into the underlying Brygge Formation.

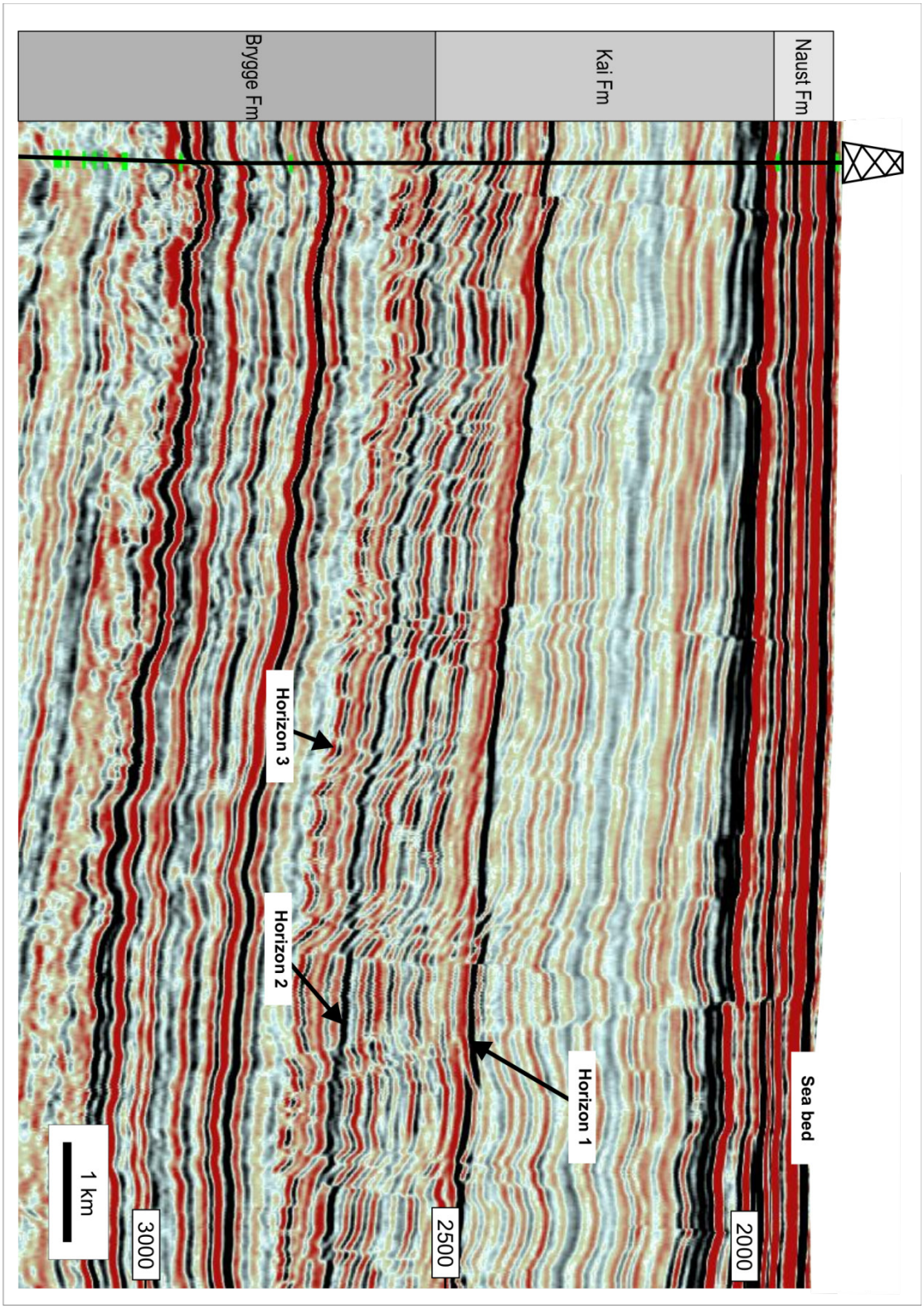

Fig. 3.4 A representative seismic section passing through the location of well 6704/12-1 with simplified lithostratigraphy. Horizons 1, 2 and 3 are described in the text. Vertical scale is TWT in ms.

In some places, it becomes difficult to track because of interference with other reflections. Tracking is most problematic where the stratal reflections have a shallow dip and the cross-cutting nature of Horizon 2 is not so apparent. The high density of faulting, which in places offsets the horizon by up to 40 m, also makes tracking the reflection event difficult. Where Horizon 2 can be seen to clearly cross-cut the stratigraphy, it has a planar topology.

Between 2525 and 3200 ms TWT (depths of 550 to 900 m below the sea bed) (Fig. 3.4), and 200 to 400 ms TWT (150 to 250 m) below Horizon 1, a reflection event of negative polarity, marked Horizon 3, demarcates a boundary between high seismic amplitudes above and low seismic amplitudes below. It is consistently conformable with other stratigraphic reflections, has laterally consistent amplitude, and is offset by polygonal faults with up to 130 m throw. Immediately below Horizon 3 there is a significant reduction in reflection amplitudes.

3.5.2 INTERNAL CHARACTERISTICS OF THE TRANSFORMATION ZONE

The section between Horizons 1 and 3 is characterised by a layered succession of high amplitude reflection events (Fig. 3.4 & Fig. 3.5). There are more variations in the density log from well 6704/12-1 through this succession, including steps of increasing density downwards at Horizons 1 and 2, but the sonic log shows little variation from a smooth trend of gradually increasing velocity with depth. Throughout the succession below Horizon 1 the density is consistently higher than it is above Horizon 1. From the synthetic seismogram in Fig. 3.2 it is clear that greater acoustic impedance contrasts below Horizon 1 are the result of larger variations in the density logs.

Seismic amplitude maps reveal regions of anomalously high amplitudes between Horizons 1 and 3 (Fig. 3.6 & Fig. 3.7). In plan, the high amplitude regions have a circular to elliptical form with one or more faults intersecting them. Their size and distribution in plan is similar to the cells at Horizon 1 (Fig. 3.7). The amplitude anomalies within the section of high amplitude reflections below Horizon 1 are located both in places where Horizon 1 has a planar topology (Fig. 3.6) and where it has an irregular topology (Fig. 3.7). In the amplitude maps, there are examples of junctions between two or more faults coinciding with the locations of the high amplitude regions (Fig. 3.7). The spaitial relationship between the amplitude anomalies and fault junctions has not been statistically quantified, but all high amplitude regions have a fault intersection within their perimeter, and there are no anomalies in which faulting is absent. The lateral variations in amplitude become poorly defined, with increasing depth below Horizon 1a. No evidence of any lateral amplitude anomalies below Horizon 2 has been found.

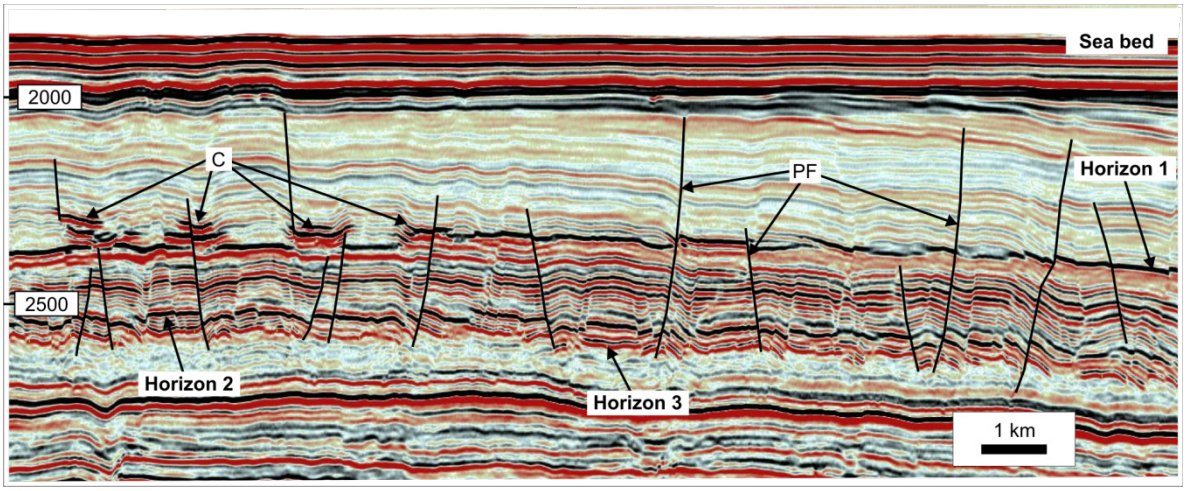

Fig. 3.5 A representative seismic line crossing the area where the topography of Horizon 1 exhibits a cell-like geometry. C — cells; PF — polygonal faults. Vertical scale is TWT in ms

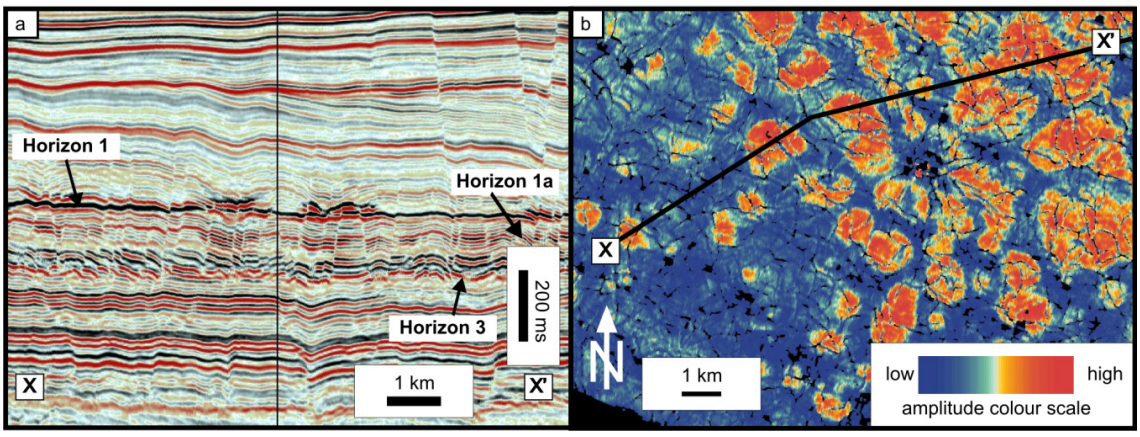

Fig. 3.6 (a) Seismic section through the region of variable amplitude on Horizon 1a. (b) Amplitude map of Horizon 1a showing the location of section in (b).

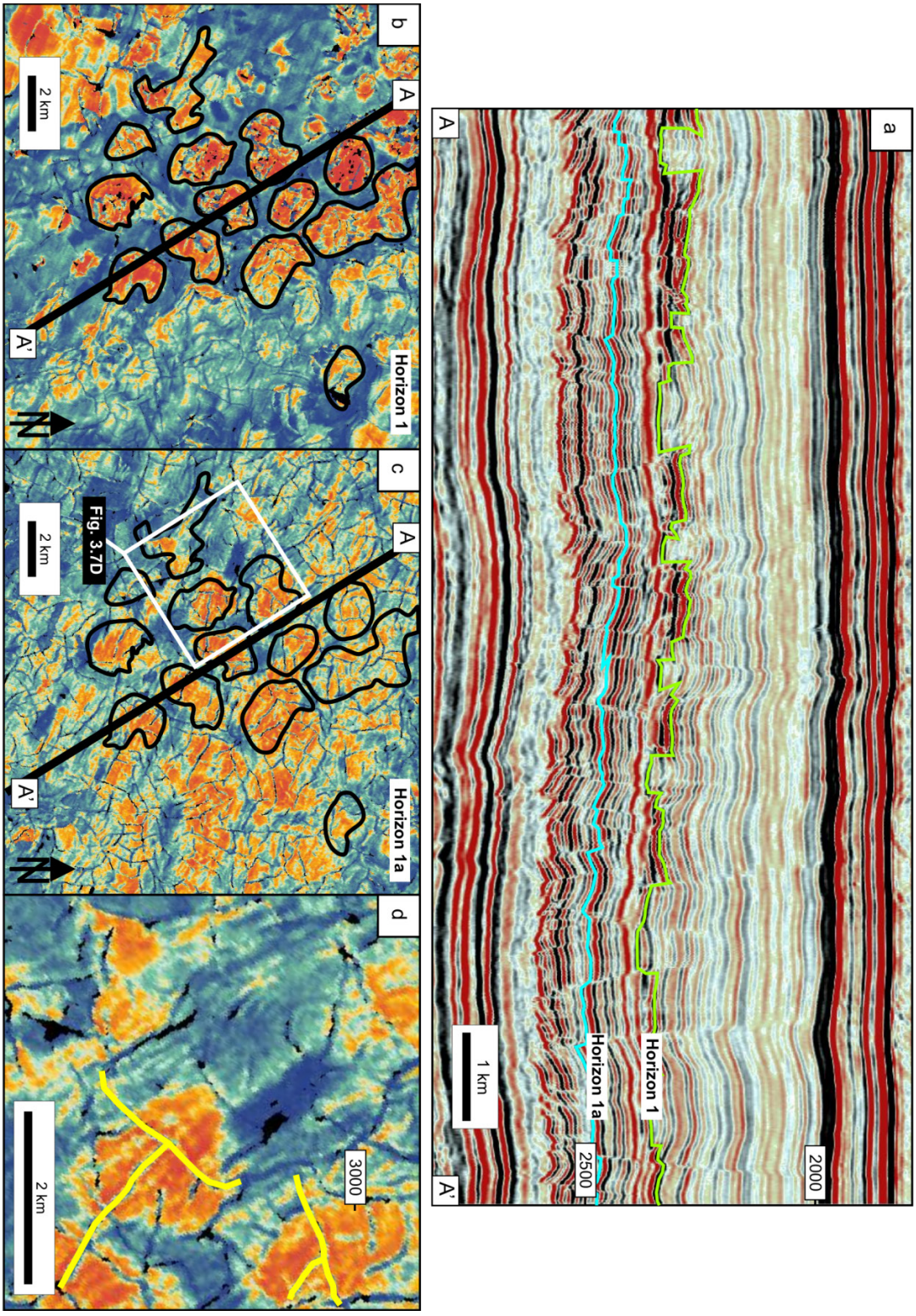
a
A
A'
2000
Horizon 1
Horizon 1a
2500
1 km
b
A
A'
2 km
Horizon 1
N
c
A
A'
2 km
Fig. 3.7D
Horizon 1a
N
d
3000
2 km
low
amplitude colour scale
high

Fig. 3.7 (a) Seismic section through a region where the topography of Horizon 1 is irregular. (b) Map of RMS amplitude from a 50 ms window along stratigraphic reflections above Horizon 1, the interpreted opal-A to opal-CT transformation boundary. (c) Map of RMS amplitude from a 50 ms window along stratigraphic reflections from an interval centred on Horizon 1a, within the interpreted transformation zone. (d) Zoom of amplitude map from the area indicated by the white box in (c), emphasising the near circular planform and the coincidence with polygonal fault junctions (marked in yellow). High amplitudes are shown in orange and low amplitudes in blue. Vertical scale is TWT in ms

In general, where amplitude anomalies are seen to correlate with features in the overburden, they should be treated with caution (Brown, 2005a) in case they are artefacts of seismic processing. The section of interest has a high density of faulting which can produce variations in reflection strength due to common midpoint stacking velocities changing with dip (Sheriff, 2002), but the amplitude changes do not correlate witAs the sonic log in well 6704/12-1 shows no step-like increase in velocity with depth across Horizon 1, focusing effects of seismic waves due to sharp velocity changes can be ruled out as a cause of the amplitude anomalies below. The AGC applied to the data appears to have had a sufficiently long window length not to cause significant artefacts in the amplitude attributes plotted in Fig. 3.6 & Fig. 3.7. The presence of amplitude anomalies below planar topology on Horizon 1 provides reassurance that the anomalies are not artefacts of processing.

3.5.3 LITHOLOGY DESCRIPTION

The lithological and chronological correlations between ODP Site 642 and DSDP Sites 338 and 343 from Laberg *et al.* (2005) have been adopted. Furthermore the lithologies at these sites have been correlated with ODP Site 643 and the information from well 6704/12-1 available from the Norwegian Petroleum Directorate to infer the lithologies and composition of sediments in the study area (Fig. 3.8).

3.5.3.1 Brygge Formation (Age: Eocene - Oligocene)

At ODP Site 642, there are no Oligocene sediments (Fig. 3.8) and Miocene sediments lie unconformably on top of the Eocene succession (Eldholm and Thiede, 1987). The Oligocene sediment thickness decreases from DSDP Site 338 (lower part of Unit 2; 194 to 250 m) to

DSDP Site 343 (Unit 2; 128 to 170 m core depth). Hansen *et al.* (2005) interpreted an upper Oligocene thickness at 6704/12-1 of ~250 m. At ODP Site 642 Eocene volcaniclastic and muddy sediments overly the Eocene basalt (Unit IV). The Eocene sedimentary succession is 115 m thick at DSDP Site 338 (Unit 3) and about 100 m thick at DSDP Site 343 (lower part of Unit 2 and Unit 3) (Eldholm and Thiede, 1987). At well 6704/12-1 there is a thick section of ~374 m of Middle Oligocene to Eocene sediments, identified by Hansen *et al.* (2005) as belonging to the Brygge Formation. At ODP Site 642 Eocene sediments consist of volcaniclastic and altered volcaniclastic muds, sandy muds and sands (Unit IV). At DSDP Site 338 Unit 3 comprises diatom ooze, glauconitic mud and sandy mud, and sandy, calcareous and zeolitic mud (Unit 3). Re-evaluation of dating by Wolf-Welling *et al.* (1997) showed that the lowermost part of Unit 2 is of Oligocene age, while Unit 3 comprises Eocene sediments underlain by Eocene basalts (Laberg *et al.,* 2005). At DSDP Site 343 Unit 2 is a muddy diatom ooze with mud and sandy mud interbeds while Unit 3 is a thinly stratified mud and sandy mud with a turbidite at the base. Unit 2 is of Oligocene age and Unit 3 comprises Eocene sediments (~170 to 270 m depth). These sediments are correlated to the Brygge Formation in 6704/12-1.

3.5.3.2 Kai Formation (Age: Miocene to Pliocene)

At ODP Site 642 Miocene age sediments (lithostratigraphic units II and III) are correlated on Fig. 3.8 to the upper part of Unit 2 and the lowermost part of Unit 1 (54 to 194 m) at Site 338 (Eldholm and Thiede, 1987; Wolf-Welling *et al.,* 1997; Laberg *et al.,* 2005) and to the Miocene succession at DSDP Site 343 (Wolf-Welling *et al.,* 1997). At ODP Site 642 the sediments of Unit II consist of nannofossil oozes with minor diatom–nannofossil oozes and muds, siliceous muds and siliceous oozes, interbedded nannofossil oozes, marly nannofossil oozes, siliceous nannofossil oozes, siliceous muds and siliceous oozes, and siliceous–calcareous oozes with minor siliceous muds and nannofossil oozes. Underlying them are siliceous muds and siliceous oozes of early to middle Miocene age (Unit III). At ODP Site 643 the sediments in units II, III and IV correlate to the Kai formation. They comprise nannofossil oozes, siliceous muds and sandy muds, diatom oozes and mudstones, and minor chalk and siliceous mudstones. At DSDP 338 Unit 2 includes muddy diatom ooze, diatom ooze, and calcareous diatom ooze or muddy diatom ooze, and at DSDP 343 Unit 1 is mud and sandy mud, locally calcareous, with foraminiferal–nannofossil ooze and radiolarian–diatom ooze interbeds. These units are correlated to the sediments of the Kai Formation at well 6704/12-1.

3.5.3.3 Naust Formation (Age: Pliocene to Pleistocene)

The uppermost sediments at each well site consist of a late Pliocene–Pleistocene unit which has a thickness of 82 m at 6704/12-1 (Fig. 3.8). At ODP Site 642 and 643 they comprise interbedded glacial muds and carbonate-rich interglacial sandy muds; at DSDP Site 338 interbedded muds, sandy muds and calcareous ooze with pebbles; and at DSDP Site 343 they comprise muds, which are locally calcareous with pebbles. These sediments are correlated to the uppermost 80 m of sediments in well 6704/12-1, which are identified as belonging to the Naust Formation.

3.5.4 LITHOLOGICAL EVIDENCE FOR DIAGENETIC ALTERATION

The composition of the sediments is highly variable at the centimetre to metre scale, but biogenic silica is common throughout the Kai Formation and the upper part of the Brygge Formation. Typical compositional values for nannofossil oozes are 5 to 20% siliceous material, 60 to 90% nannofossils, 0 to 10% diatoms, 0 to 15% sponge spicules and <5% terrigenous material (Eldholm *et al.,* 1987b). Compositional values for siliceous oozes and muds vary over the ranges 0 to 20% quartz, 0 to 5% feldspar, 10 to 80% clay, 0 to 15% glass, 5 to 50% diatoms, 0 to 50% radiolarians, 5 to 40 % sponge spicules and 0 to 10% silicoflagellates. Diatom oozes can comprise up to 60% diatoms. With increasing depth at ODP Site 643 total biogenic opal content may be up to 75% in some sediments (Eldholm *et al.,* 1987b). ODP Site 642 shows there is an absence of diatoms valves in the lower part of Unit III (Henrich, 1987), and interpreted as due to diagenetic alteration, which was also identified at ODP Site 643 where extensive diagenetic alteration resulted in the opal-A components being totally converted to opal-CT (Henrich, 1987). The sediments from ODP Site 643 of the lower Miocene are highly biogenic siliceous deposits of unit III and lie upon 126 m of monotonous partly siliceous, fossil poor Miocene sediments (Henrich, 1987). Smear slide analysis of the fossil poor mudstones reveal that their fossil content is restricted to a few siliceous manganese-encrusted sponge spicules and diatoms. XRD analysis indicates an almost complete transformation of opal-A to opal-CT (Henrich, 1987), this depth of transformation coincides with an abrupt increase in the density log response (Fig. 3.3). It was also identified that opal-CT lephispheres crystallised in more pure authigenic carbonate bands, while marly layers reveal films of poorly crystallised opal-CT (Henrich, 1987).

A detailed study of the siliceous section through the Brygge Formation in well 6302/6-1 was made available (internal Statoil report). Bulk samples were analysed by XRPD. Despite

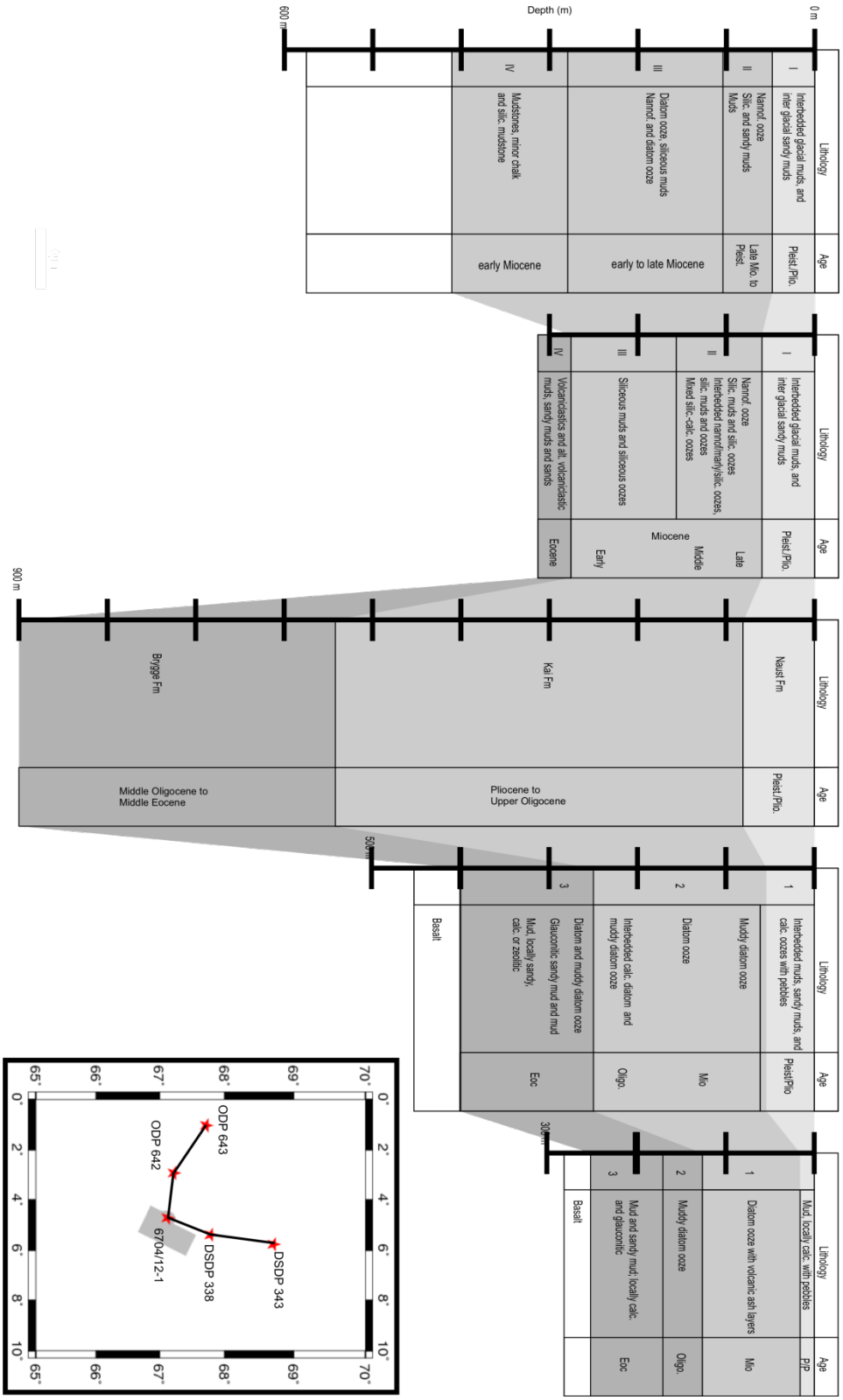

Fig. 3.8 Lithology and chronology adapted from Laberg *et al.* (2005) showing correlation of well 6704/12-1 with ODP Sites 642 and 643 and DSDP Sites 338 and 343.

well 6302/6-1 being located 350 km away from the Gjallar Ridge study area (Fig. 3.1), the same formations are present (Norwegian Petroleum Directorate, 2010) (Appendix C). Here, the Naust Formation is located at depths of 1286 to 2463 m TVDSS, the Kai Formation at 2463 to 2582 m and the Brygge Formation at 2582 to 3223 m. Over the depth range 2700 to 2770 m, opal-A is present in significant amounts (31 to 46%) and opal-CT as very low or trace amounts (Fig. 3.8). At 2780 m depth opal-A and opal-CT are present in approximately equal amounts. Over the depth range 2780 to 2850 m, opal-CT is present in significant amounts (29 to 45%) whereas the amounts of opal-A present are less than 5%. The opal-CT content remains high down to 2970 m depth, below which it drops markedly to values less than 2% below 3000 m depth and zero below 3050 m depth. There is an increase in quartz content with depth from around 12% at 2970 m depth to 27% at 3040 m depth, coinciding with the marked reduction in opal-CT content.

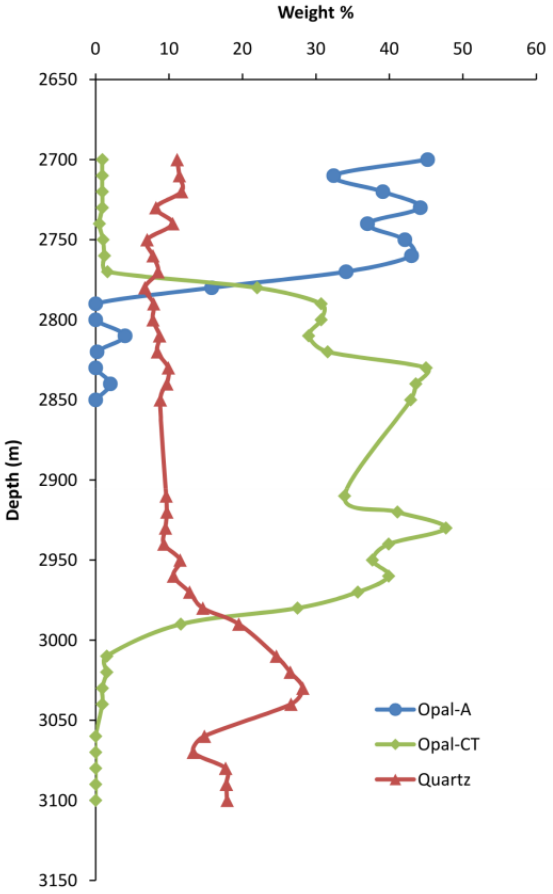

Fig. 3.9 XRPD analysis of bulk samples from well 6302/6-1.

3.6 INTERPRETATION

In this section, the cross-cutting seismic reflections (Horizons 1 and 2 in Fig. 3.4 & Fig. 3.5) are interpreted first and then an integrated interpretation of the whole package of high amplitude reflections is given. In this interpretation reference is given to the inferred lithologies from ODP and DSDP sites, XRPD data and geophysical logs from exploration wells. The density and sonic logs from well 6704/12-1 and the synthetic seismogram (Fig. 3.2) were used to correlate the lithology to the seismic volume. Horizon 1, which has a high-amplitude character and a cross-cutting relationship with stratal reflection events on the seismic data, corresponds to an abrupt increase in measured bulk density in well log 6704/12-1. It is hosted within the Kai Formation. ODP Site 642 and DSDP Sites 338 and 343 indicate that the Kai Formation is likely to have a significant biogenic component, supported by the description from well 6704/12-1 which refers to a 640 m ooze section (Norwegian Petroleum Directorate, 2009). At ODP Site 642 and DSDP Sites 338 and 343 the Kai Formation is an interbedded succession but biogenic silica is significant throughout.

Horizon 1 is interpreted to be the opal-A to opal-CT transformation boundary within the silica diagenetic transformation zone (Fig. 3.10), based on the downward increase in density recorded on the density log and the differential compaction within the depth interval where the cells are located (left side of Fig. 3.5). Differential compaction is evident from the subsidence folds in the overburden. It is ruled out that the reflection could be 1) a direct hydrocarbon indicator (DHI) because of its laterally extensive nature, 2) a gas hydrate because it has the exact opposite polarity (Shipley, 1979), 3) a multiple because its two-way time and dip are not compatible with any plausible multiple raypath. Although the majority of the opal-A is transformed to opal-CT over a narrow depth interval (Fig. 3.9), defined here as the transformation boundary, the proportion of opal-A that has undergone transformation commonly does not monotonically increase with depth through the succession. The XRPD data from the offset well 6203/6-1 (Fig. 3.9) show small, but non-zero, and variable opal-A content to a depth of 60 m below the opal-A to opal-CT transformation boundary (~2780 m depth).

Horizon 2 also has a cross-cutting relationship with the stratigraphy and a high amplitude character, and corresponds to a second abrupt increase in bulk density with increasing depth. This reflection event crosses from the lowermost part of the Kai Formation into the underlying Brygge Formation. Horizon 2 is interpreted to be the opal-CT to quartz transformation boundary (Fig. 3.10). It is definitely not a multiple because its two-way time and dip are not compatible with any plausible multiple raypath, and it cannot be a depositional event because it cross-cuts stratigraphic reflection events. The possibility that it is due to a gas

hydrate is also ruled out because such events are well documented as having negative polarity (Shipley, 1979).

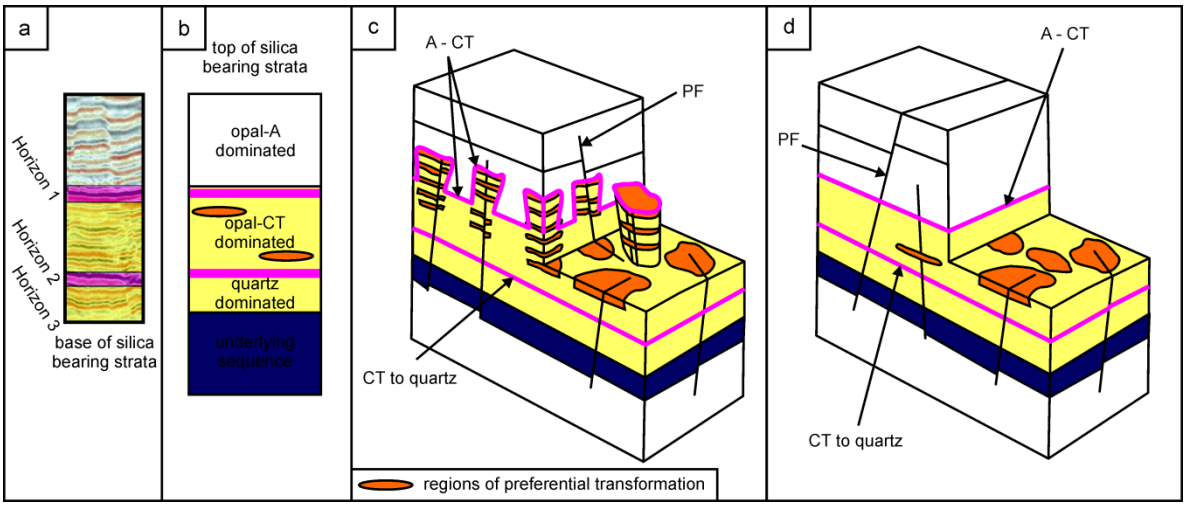

Fig. 3.10 (a) Representative seismic section through the silica diagenetic transformation zone which is indicated by the yellow region. The pink bands represent transformation boundaries. (b) Schematic structure of the silica diagenetic transformation zone in a silica-rich succession. In all three examples, pink lines represent transformation boundaries and yellow regions transformation zones. Orange represents regions of preferential transformation. Cartoons to illustrate the structure of a silica diagenetic transformation zones in regions where the structure has an (c) irregular opal-A to opal-CT boundary and (d) a planar opal-A to opal-CT boundary. A-CT - opal-A to opal-CT transformation boundary. CT-quartz - opal-CT to quartz transformation boundary. PF – polygonal fault..

The bottom-hole temperature in well 6704/12-1 at 4103 m TVDSS is 142°C, and the water depth is 1352 m. The water-bottom temperature in the region has been measured as –0.5°C, using a remotely operated vehicle (Hovland *et al.,* 2005), so the average geothermal gradient is ~51.6°C km^{-1}. This gradient implies a temperature of ~26°C at the minimum depth of Horizon 2, and ~45°C at its maximum depth. This reflector is associated with the change in silica mineralogy from opal-CT to quartz as indicated by the XRPD from well 6203/6-1 between depths of 2970 m and 3000 m. From examination of the Monterey Formation, Pisciotto (1981) showed that opal-A is continually transforming to opal-CT in the upper half of a thick opal-CT zone which is 470 to 750 m in thickness, and that quartz begins to form in the lower half of this zone. Isotopic data for the formation of quartz yielded minimum temperatures of 31 to 62°C and maximum temperatures of 44 to 77°C. This demonstrates that the temperature for transformation of silica phases may overlap, and therefore it could be predicted that across a

zone several 10's to 100's of meters thick that at least two silica phases may be present, as observed in the XRPD data present here.

Horizon 3 is interpreted as the base of the silica-rich succession because it is conformable with other stratal reflection events and there is a substantial reduction in reflectivity below it which implies a substantial lithological change. It lies within the Brygge Formation, which extends into the deeper section by at least 300 ms TWT.

The section of high amplitudes extends from Horizon 1 down to Horizon 3. This character is interpreted as being a consequence of a low acoustic impedance contrast between clay-rich beds and opal-A-rich beds above Horizon 1. Due to transformation of opal-A to opal-CT, there is a higher acoustic impedance contrast below Horizon 1, with the opal-CT-rich beds having higher acoustic impedance. This interval is associated with the depth range 2790 to 2980 m in well 6302/6-1 where XRPD data show varying amounts of opal-A, opal-CT and quartz.

Transformation of opal-A to opal-CT occurs at lower temperature and shallower burial in the purest siliceous sediments (Behl and Garrison, 1994). It is inferred that the clay-rich beds have some silica content, as shown from ODP Site 642 (Eldholm *et al.,* 1987b). The silica in the clay-rich beds may be expected to undergo diagenesis later than that in the silica-rich beds because a greater detrital content relative to the silica content is known to inhibit the transformation rate (Kastner *et al.,* 1977; Williams and Crerar, 1985). This understanding is confirmed by data from ODP Site 643 where crystallised opal-CT lephispheres were identified in more pure authigenic carbonate bands, whereas marly layers contain films of poorly crystallised opal-CT (Henrich, 1987). Thus the whole section of high amplitude reflections between Horizons 1 and 3 is interpreted as representing a silica diagenetic transformation zone. This zone contains interbeds of sediment in which opal-A has undergone variable amounts of transformation to opal-CT and, at greater depths yet possibly overlapping, interbeds of sediment in which opal-CT has undergone variable amounts of transformation to quartz (Fig. 3.9). In well 6302/6-1, the base of the siliceous section is probably at ~3050 m depth, where a decrease in the amount of quartz, absence of opal-CT or opal-A, and increased amounts of clay minerals are indicated by XRPD analysis.

The cells which form the squat cylindrical protuberances in the topography of Horizon 1 (Fig. 3.5) have previously been interpreted as regions in which transformation of opal-A to opal-CT has taken place earlier (Davies and Cartwright, 2007). The amplitude maps in Figures 6B and 7C show similar cell patterns in plan view, but on stratigraphic horizons below Horizon 1, as identified by Ireland *et al.* (2010) (see Chapter 4). These amplitude variations in

stratigraphic reflection events are attributed to the same cause: the circular zones of higher amplitude represent locations where more complete transformation of opal-A to opal-CT has taken place in the silica-rich beds. Ireland *et al.* (2010) (Chapter 4) pointed out that the cells on Horizon 1 have formed around the upper tips of polygonal faults, and that there are one or more faults intersecting each circular region of higher amplitude found on stratal reflection events below Horizon 1. They suggested that the preferential advance of the opal-A to opal-CT transformation boundary at the cells is due to transient expulsion up the faults of pore water released by the opal-CT to quartz transformation. In this model the water is inferred to have a greater magnesium and hydroxyl concentrations than the water it displaces around the upper fault tips, which promotes opal-A to opal-CT transformation at lower temperature so the transformation zone advances more rapidly through those zones. The circular zones of higher amplitude along the stratigraphic reflection events such as Horizon 1a in Figures 6 and 7 are interpreted as regions of more complete transformation of opal-A to opal-CT. This interpretation requires that not all the opal-A converts to opal-CT at Horizon 1, which implies a broad transition zone of opal-A-rich and opal-CT-rich beds like that found in the Monterey Formation on the Californian coast (Isaacs, 1981, 1982; Keller and Isaacs, 1985).

3.7 DISCUSSION

3.7.1 TRANSFORMATION ZONE CHARACTERISTICS

The silica diagenetic transformation zone at the Gjallar Ridge described here is characterised seismically by a clear cross-cutting reflection event of positive polarity from the opal-A to opal-CT transformation boundary; a zone of relatively bright stratal reflection events, some of which exhibit enhanced amplitudes corresponding to cells at the opal-A to opal-CT transformation boundary; and a deeper cross-cutting reflection event of positive polarity from the opal-CT to quartz transformation boundary. Vertical and horizontal amplitude variations in the seismic reflection data provide evidence of heterogeneity within the fine-grained succession of the transformation zone. The interval of high amplitude reflections must correspond to an interbedded succession with relatively large vertical contrasts in acoustic impedance.

The more subtle, kilometre-scale lateral variations in reflection amplitude on stratal reflecting horizons within the transformation zone emphasize complexity in the extent of diagenetic alteration. The rate of transformation of opal-A to opal-CT depends on temperature, time and the composition of both the host sediments and the pore fluid (Kastner *et al.,* 1977). Ireland *et al.* (2010) (Chapter 4) have proposed that the cell structures identified at the opal-A to

opal-CT transformation boundary owe their existence to variations in pore fluid composition due to transient expulsion of pore water up polygonal faults. The lateral variations in reflection amplitude on stratal reflecting horizons are interpreted here as representing variations in the extent of transformation of opal-A to opal-CT. The circular regions of higher reflection amplitude are in a sense 'fossilized cells' because they are located in places which would have been cells when the silica transformation zone was at a deeper level in the succession.

While there is a possibility that mass transport of silica may occur at a small scale, such as between adjacent beds (Vanderborght *et al.,* 1977), the possibility that the cells and circular amplitude anomalies within the transformation zone are caused by advection of silica is discounted for two reasons. First, the solubility of silica is so low that unrealistically large volumes of water would be needed to transport sufficiently large amounts of dissolved silica (Ireland *et al.,* 2010, Chapter 4). Second, the differential compaction that occurs at the levels of the cells clearly indicates greater compaction within the cells than outside them in the same stratigraphic interval. Above chert bodies formed by silicification along faults that had previously formed in diatomite within the Monterey Formation, the exact opposite compaction pattern to that at the Gjallar Ridge is observed because the chert is relatively incompressible compared to the surrounding diatomite and with burial the diatomite is compressed around the rigid chert (Behl and Garrison, 1994)(also see Fig. 7.2).

The cross-cutting reflector marked as Horizon 2 in Figures 2, 4 and 5 is interpreted as the opal-CT to quartz transformation boundary. Opal-CT to quartz boundaries have previously been interpreted on seismic reflection data (Pegrum *et al.,* 2001; Meadows and Davies, 2007) and proven via well sampling from the Fylla area, Greenland (Pegrum *et al.,* 2001). The opal-CT to quartz reflection is not always parallel to the opal-A to opal-CT transformation boundary, most likely because of variations in geothermal gradient, lithology and pore water composition. A tendency for the cross-cutting reflection events due to silica phase transformations to be parallel to unconformities has been noted (Davies and Cartwright, 2002; Meadows and Davies, 2007). It has been suggested (Ireland *et al.,* 2010, see Chapter 4) that during a hiatus the magnesium concentration in the pore water around the opal-A to opal-CT diagenetic transformation boundary drops, due to the absorption of magnesium into clay minerals and possibly by dolomitization. On reburial, the reduced magnesium concentration in the pore water around the former opal-A to opal-CT transformation zone means that a higher temperature has to be reached before this transformation recommences.

Without core or cuttings, it is not possible to quantify the amounts of the three silica minerals through the transformation zone on the Gjallar Ridge. But the XRPD and XRD analysis of nearby wells has been used through the same formations to show that the

transformation does indeed occur across hundreds of metres of strata, as inferred from the seismic data presented here. The strong cross-cutting reflection of Horizon 1 indicates that there must be a substantial change in silica phase at this depth, and is in agreement with the XRPD results which show that most of the transformations of opal-A to opal-CT and of opal-CT to quartz occur across narrow depth ranges of ~30 m (Fig. 3.9). Observations presented here show that the transformation continues through a much wider zone than interpreted previously from seismic reflection data from the Vøring Basin (Davies and Cartwright, 2007). This interpretation implies a similarity to the broad silica transformation zone found in the Monterey Formation on the Californian coast (Isaacs, 1981, 1982; Keller and Isaacs, 1985).

3.7.2 DEFINING A TRANSFORMATION ZONE

Using geophysical criteria from 3D seismic reflection imagery is a novel method to identify the structure of a two-step silica diagenetic transformation zone (Fig. 3.10). Clear seismic characteristics define these transformation boundaries and the ongoing transformation of residual opal-A to opal-CT in the transformation zone, but identification of the base, where transformation of opal-A through to quartz is complete, is more problematic. The XRPD data from well 6302/6-1 show no opal-CT below 3050 m TVDSS, 50 m below the opal-CT to quartz transformation boundary, but this depth is interpreted to be the base of the section which was originally rich in biogenic silica because the overall silica content (all quartz) below this depth is greatly reduced.

To identify a transformation zone it is suggested that a number of key criteria should be met (Table 3.1). Seismic reflections, geophysical logs and XRPD data are used to define the extent of the transformation zone, but it is recognized that with more data of different types the limits of the transformation zone may be identified at the same depths

The data presented here highlights the complexity of silica diagenetic transformation zones observable in seismic reflection data, and also show how the physical properties of the sediment are affected by the transformation of opal-A to opal-CT, and then to quartz. Although previous authors (Guerin and Goldberg, 1996) have said that the strong acoustic impedance contrast between opal-A-rich sediment and opal-CT-rich sediment is the result of an increase in both bulk density and sonic velocity, wireline log data from the Gjallar Ridge show no abrupt increase in sonic velocity at either transformation boundary indicating that the acoustic impedance contrasts at the transformation boundaries are primarily due to density increases.

	Top	Internal	Base
Essential seismic observation	Strong high	Anomalously high	
	Amplitude reflection	Seismic amplitudes	
Preferred seismic observation	Cross cutting reflection	Discrete seismic unit	Seismic reflector coinciding with lithological change
	Deformation in overburden	Patterns	Distinct change in seismic response below strong amplitude reflection
	Associated with patterns	Lateral or vertical variations in seismic amplitude	
		Evidence of other reflections due to diagenesis	
Preferred well log or outcrop observations	Associated with deformation in the overburden	Co-existence of silica phases	Diagenetic changes are indistinguishable from the natural background variability (Nobes *et al.,* 1992)
	Sharp response in well log	Evidence of secondary transformations	
	Changes in rock properties	Deformation associated with alteration (Eichhubl & Behl, 1998)	
	Sufficient burial temperature.		

Table 3.1 Suggested list of criteria that should be met in order to identify a complete transformation zone from seismic reflection data.

3.8 CONCLUSIONS

Here , the term transformation zone has been adopted for the volume of sediment in which silica diagenetic transformations occur, and the seismic characteristics of a silica transformation zone at the Gjallar Ridge has been described. The most distinctive and diagnostic feature is the opal-A to opal-CT transformation boundary, which is a strong reflection event of positive polarity that cross-cuts stratal reflections. In places, a second strong reflection coefficient that also has positive polarity and cross-cuts stratal reflections is observed

around 200 ms deeper, and is interpreted as the opal-CT to quartz transformation boundary. Reference to XRPD data in offset well 6302/6-1 and XRD data from ODP Site 643 confirms that these transformation boundaries mark changes in the dominant silica phase over depth intervals of a few metres, although complete transformation from one phase to another takes place over depth intervals of around 100 m or more. The third obvious seismic characteristic is the greater amplitude of the reflection events from the opal-A to opal-CT transformation boundary down to the base of the silica-rich succession compared to the overlying beds. It is inferred that there is a much greater acoustic impedance contrast between interbeds of higher and lower silica content following the transformation of opal-A to opal-CT. An interesting feature of the silica diagenetic transformation zone is the lack of significant change in the sonic velocity across either transformation boundary, which implies that the acoustic impedance contrasts giving rise to the cross-cutting reflection events are essentially due to changes in density.

A remarkable feature of the opal-A to opal-CT transformation boundary across one part of the Gjallar Ridge is the development of the irregular topography consisting of individual cells of 1 to 2 km diameter and up to 200 m in height. A viable hypothesis for their formation is that the transformation boundary has preferentially advanced around the upper tips of polygonal faults because of flushing by magnesium-rich pore water expelled transiently up the faults (Ireland *et al.,* 2010, Chapter 4). A subtle seismic characteristic is the variation in seismic amplitude along stratigraphic reflections below the opal-A to opal-CT transformation boundary. Where amplitudes are greater this is interpreted as evidence of more complete transformation of opal-A to opal-CT. These amplitude variations are the first seismic evidence that a silica transformation zone involves more gradual transformation of silica from one phase to another than has been implied by previous observations of individual cross-cutting reflection events. Thus the seismic data from the Gjallar Ridge confirm that the transformation of opal-A to opal-CT and of opal-CT to quartz occurs across a zone up to 300 m in thickness, and is not confined to the two narrow depth intervals giving rise to the cross-cutting reflections, although the rate of transformation is clearly enhanced at those two transformation boundaries. These seismic observations are consistent with the XRPD data and with the observations reported from outcrops of the Monterey Formation.

4 INFLUENCE OF PORE WATER CHEMISTRY ON SILICA DIAGENESIS: EVIDENCE FROM THE INTERACTION OF DIAGENETIC TRANSFORMATION ZONES WITH POLYGONAL FAULT SYSTEMS

ABSTRACT

3-D seismic data from the north-east Atlantic margin have revealed opal-A to opal-CT transformation zones hosted in Oligo-Pliocene strata as bright reflection events which cross-cut stratigraphic reflections. In some areas, the topographic relief at the top of the transformation zone has an extraordinary geometry comprising roughly circular flattish regions, spaced 1–3 km apart, separated by networks of steep-sided troughs or ridges with a relief of up to 200 m. Here we show that these topographic structures formed around the upper tips of polygonal faults, and that remnants exist at deeper stratigraphic levels below the opal-A to opal-CT cross-cutting reflection. Furthermore, we deduce that the chemistry of formation water expelled transiently through the polygonal faults must have played a key role in their formation. Within silica-bearing successions, the transformation of opal-A to opal-CT is followed by the transformation of opal-CT to quartz at greater depth. The opal-CT to quartz transformation releases magnesium which is known to promote opal-A to opal-CT transformation at lower temperatures. Consequently, we suggest that when the opal-A to opal-CT transformation zone nears the top of the polygonal fault system, it advances more rapidly through strata flushed by pore water that is richer in magnesium.

4.1 INTRODUCTION

Three-dimensional (3-D) seismic reflection data from the north-east Atlantic margin have revealed extraordinary topographic structures at opal-A to opal-CT transformation zones hosted in Oligo-Pliocene strata (Davies and Cartwright, 2002, 2007; Davies, 2005). The structures comprise either roughly circular flat-topped regions with relief of up to 200 m, spaced 1–3 km apart and separated by a network of troughs, or circular to polygonal depressions of 1–2 km diameter lying within a network of ridges that have elevations of 10–50 m. Here we put forward a model for the formation of these structures, based on further analysis of seismic reflection data from the Gjallar Ridge and the Faeroe-Shetland Basin (Fig. 4.1). Our model fits published observations from outcrops, boreholes, and laboratory experiments. It may also explain why the transformation zones are commonly observed to lie parallel to late Neogene unconformities, rather than to the seabed.

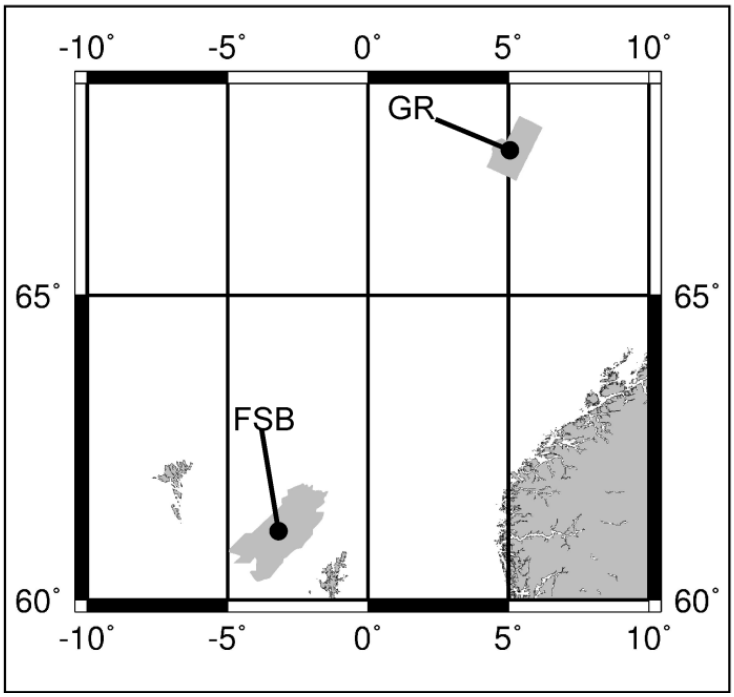

Fig. 4.1 Location map for study areas on the north-east Atlantic margin. GR – Gjallar Ridge survey area, FSB – Faeroe-Shetland Basin survey area.

Silica diagenetic transformations occur during the first 1000 m of burial of biosiliceous sediment. Initially, opal-A (biogenic silica) dissolves and precipitates as opal-CT (crystalline silica), and opal-CT subsequently recrystallizes to quartz (Isaacs, 1982; Williams *et al.,* 1985).

The transformation of opal-A to opal-CT in silica-rich sediment may reduce porosity by as much as 30% (e.g. Isaacs, 1981; Tada, 1991), releasing large volumes of pore water and resulting in a large acoustic impedance contrast which can give rise to a seismic reflection event that cross-cuts stratigraphy (Hein *et al.,* 1978). Analysis of 2D and 3-D seismic data has provided evidence for a variety of fluid flow conduits above transformation zones, indicative of water expulsion from the transformation zones and transient upward flow (Davies *et al.,* 2008).

The rate of transformation of opal-A to opal-CT depends on temperature and time, but is also strongly affected by the composition of the host sediments and the pore fluid (Kastner *et al.,* 1977). It is reduced by the presence of clays and increased by the presence of carbonates. Of particular significance for our model, opal-CT lepisphere formation is aided by the precipitation of nuclei containing magnesium hydroxide as an important component (Kastner *et al.,* 1977; Williams and Crerar, 1985).

4.2 GEOLOGICAL BACKGROUND AND DATA

In the Vøring Basin offshore mid-Norway, the silica diagenetic transformation zone is located in a sequence of Miocene sediments which mantles the Gjallar Ridge (Fig. 4.1). The top of the transformation zone is marked by a strong reflection event that cross-cuts stratigraphic reflections and, in places, has a remarkable topography (horizon A in Fig. 4.2). The Gjallar Ridge is a complex of tilted fault blocks that formed during the Cretaceous (Brekke, 2000). During the Miocene and Early Pliocene, deposition on the outer margin of the Vøring Basin was dominated by biosiliceous hemipelagic sediments (Hjelstuen *et al.,* 1999). The stratigraphy of the section of interest extends from the base of the Lower Miocene Brygge Formation to the top of the Kai Formation. Well 6704/12-1 recorded a total of 640 m of ooze section (Norwegian Petroleum Directorate, 2009), and provided limited calibration of the diagenetic transformation of opal-A to opal-CT.

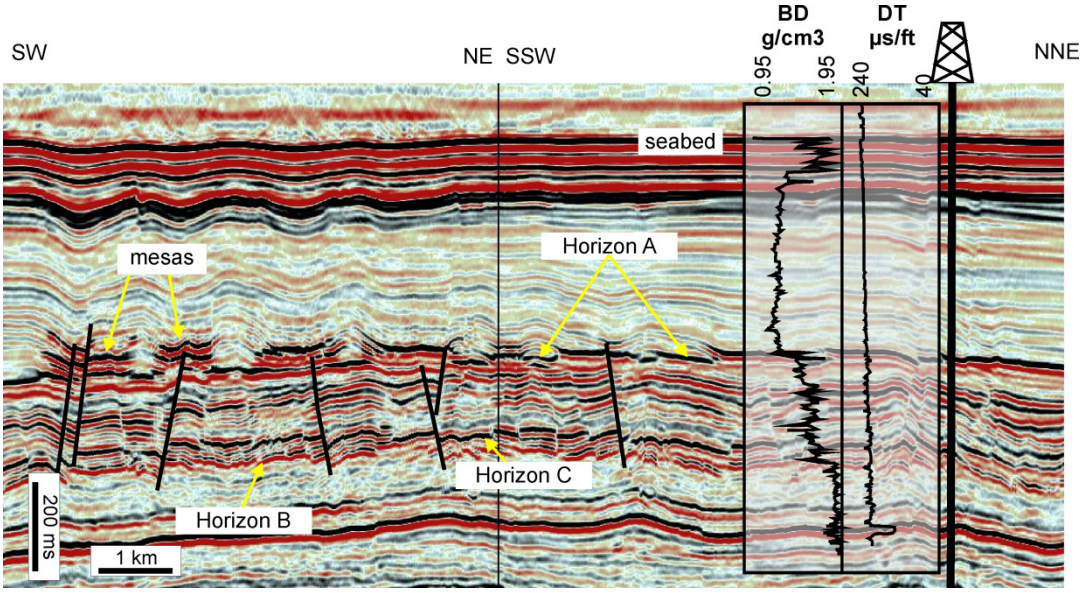

Fig. 4.2 Representative seismic section from the area on the Gjallar Ridge where the topography of horizon A comprises circular mesas separated by a trough network. Some polygonal faults are marked. Sonic and density logs from well 6704/12-2 are overlain. See text for interpretation of labelled horizons.

The Faeroe-Shetland Basin (Fig. 4.1) is a semi-confined deep water basin that overlies a Mesozoic and lower Cenozoic rift basin. The silica diagenetic transformation zone is located in a sequence of Oligo-Miocene age sediments, and is also marked by a strong reflection event with a geometrically patterned topography over a wide area (Fig. 4.3). Some data from well 214/4-1 are available to calibrate the seismic data. A remotely operated vehicle collected cuttings deposited on the seabed, with samples obtained from a depth range spanning the regional high-amplitude reflection event shown at the top of the data cube in Fig. 4.3. Davies and Cartwright (2002) used these samples and regional two-dimensional seismic data to show that the high-amplitude reflection event arises from an opal-A to opal-CT diagenetic front. Biostratigraphic analysis of samples taken from above and below the front showed that the interval is lower Oligocene to Pliocene in age, and that the opal-A to opal-CT transformation is hosted in silt and sand-grade sediment that contained abundant diatom valves prior to transformation.

We have used 3-D seismic data from surveys across the Gjallar Ridge and in the Faeroe-Shetland Basin to investigate the origin of the geometrically patterned topographic structures at the top of the silica diagenetic transformation zone. The processed seismic data are

of high quality with a vertical seismic resolution of 10-20 m in the uppermost 1000 m of sediment. The seismic images shown here are displayed so that a black loop denotes a positive acoustic impedance contrast and a red loop a negative acoustic impedance contrast.

4.3 OBSERVATIONS

4.3.1 TOPOGRAPHIC STRUCTURES

In both study areas (Fig. 4.1), images of the opal-A to opal-CT transformation on 3-D seismic data exhibit structures of similar scale, but the form of the relief in each area is approximately the inverse of the other. On the Gjallar Ridge, the flat-topped circular regions of higher elevation, or 'mesas', are separated by a network of narrow troughs. In the Faeroe-Shetland Basin, a network of steep-sided narrow ridges separates circular depressions. The spatial association of these topographic structures with polygonal fault systems was noted by Davies (2005) and Davies & Cartwright (2007).

On the Gjallar Ridge, a strong reflection event with positive polarity located 300–500 m below the seabed (horizon A in Fig. 4.2) cross-cuts stratal reflections and has previously been interpreted as marking the transition from opal-A to opal-CT (Davies and Cartwright, 2007). This reflection event marks an abrupt change in the seismic response, with the package of reflection events immediately below it being of consistently higher amplitude than the package above. On the density log from well 6704/12-1, which is overlain on the seismic section in Fig. 4.2, horizon A correlates with an increase in bulk density of ~0.3 g cm^{-3} at ~500 m depth below the seabed. In places, the topography of horizon A has the mesas/trough network relief, with mesas up to 2.7 km in diameter and 50–200 m in height located around the upper tips of faults in a polygonal fault system. Most mesas are centred over one or more faults, and some are bounded by faults. Depressions have formed in the overburden above the mesas as a result of differential compaction due to the conversion of opal-A to opal-CT (Davies, 2005), and subsequently faults have formed on the margins of depressions and crests of the anticlines in the overburden (Davies *et al.,* 2009). Though the faults in the overburden were termed polygonal faults by Davies et al. (2009), they do not form a complete interlinked fault network with a polygonal planform geometry. They have clearly formed in association with the folding of the overburden due to differential compaction across the opal-A to opal-CT transformation zone, and so are a consequence of the topography at the top of the transformation zone, not a cause of it.

At ~700 m below the seabed, a reflection event of negative polarity (horizon B in Fig. 4.2) demarcates a boundary between high seismic amplitudes above and low seismic amplitudes below. Horizon B is located near to the lower tips of the faults in the polygonal fault system and has laterally consistent amplitude. It is parallel to stratigraphic reflections, and is interpreted as a stratigraphic reflection demarcating the base of the silica-rich sequence. At ~650 m below the seabed, a reflection event of positive polarity (horizon C in Fig. 4.2) conforms to stratigraphy here, but cross-cuts stratigraphy in other places within the 3-D seismic volume. It correlates with a second abrupt increase in bulk density in well 6704/12-1 (Fig. 4.2), and is interpreted as marking the boundary between opal-CT and quartz.

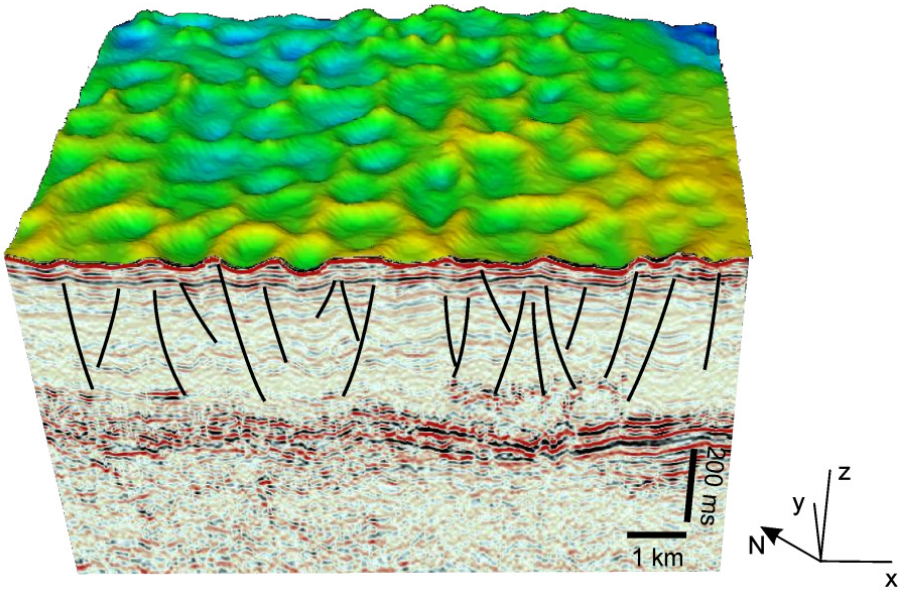

Fig. 4.3 Representative seismic cube from the area in the Faeroe-Shetland Basin where the topography of the opal-A to opal-CT reflection event comprises circular to polygonal depressions lying within a network of ridges.

In the Faeroe-Shetland Basin, the reflection event at the top of the opal-A to opal-CT transformation zone has developed a relief consisting of a polygonal network of ridges ~50 m in height which separate roughly circular to polygonal depressions of 1–2 km in diameter (Fig. 4.3). Polygonal faults mapped below the transformation zone show a reasonable correspondence with the location of the ridges on the transformation zone, allowing for fault dip (Davies, 2005). We therefore infer that the ridges lie directly above the upper tips of the faults. The spatial association of polygonal fault systems with the geometric patterns in the topography

of the opal-A to opal-CT transformation zones in the Faeroe-Shetland Basin and the Gjallar Ridge area indicates that factors controlling their development are related.

4.3.2 AMPLITUDES OF STRATIGRAPHIC REFLECTIONS

Figure 4a is another section from the Gjallar Ridge 3-D seismic data volume where the opal-A to opal-CT transformation zone is represented by a strong reflection event (horizon A) that cross-cuts stratigraphy. Here the upper boundary of the transformation zone is almost planar with only two circular mesas at an elevation of some 20 m above the regional level. At a depth of 60–120 m below horizon A, a stratigraphic reflection event with positive polarity (horizon D in Fig. 4a) can be tracked through the data volume locally. The seismic amplitude map for horizon D (Fig. 4.4b) reveals regions of anomalously high amplitude which have circular to elliptical shapes in plan, with one or more faults intersecting them. Their size and distribution in plan view is almost identical to the mesas at horizon A nearby (Fig. 4.2).

The fact that the amplitude anomalies on horizon D are evident underneath planar topography on horizon A suggests that they represent real variations in acoustic impedance and have the same root cause. We interpret the higher amplitudes along horizon D as regions of more complete conversion of opal-A to opal-CT. This interpretation requires that not all the opal-A converts to opal-CT at horizon A, which implies a broad transition zone of opal-A-rich and opal-CT-rich beds like that found in the Monterey Formation on the Californian coast (Isaacs, 1981, 1982; Keller and Isaacs, 1985). Nobes et al. (1992) also found opal-A present below the main opal-A to opal-CT diagenetic boundary in silica-rich sediment of Late Miocene/Early Pliocene age in the Sea of Japan.

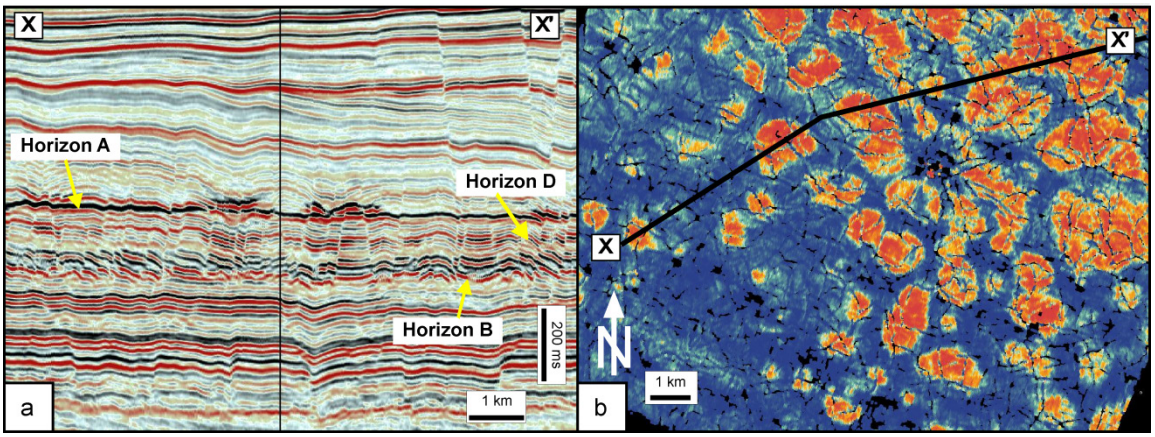

Fig. 4.4 (a) Seismic section from the Gjallar Ridge where the topography of horizon A is approximately planar. (b) Amplitude map of horizon D showing circular regions of high amplitudes in red and low amplitudes in blue. Black line is location of section in A.

4.3.3 FLUID EXPULSION FEATURES

Fig. 4.5 shows 3-D volumes from the Gjallar Ridge 3-D seismic volume where we have interpreted a number of features as direct evidence of fluid expulsion. A segment of the horizon slice for horizon A around one of the circular mesas is shown in Fig. 5a. A coherency volume (Fig 4.5b and c) highlights discontinuities in the seismic data as dark shades and continuous regions as bright blue. This seismic attribute reveals small circular dark zones near the centre of the mesa (Fig. 4.5b) and similar features can be identified in other mesas across the 3-D volume. We interpret them as sections through pipes, as described by Berndt et al. (2003) where the bedding has been disrupted so that the coherence between adjacent traces in the seismic cube is very low. A deeper time slice (Fig. 4.5c) shows that the pipes are located directly above the upper tips of polygonal faults. On vertical sections the pipes can only be recognised as minor disturbances in seismic reflections.

A second region of the Gjallar Ridge seismic volume reveals pockmarks on a stratigraphic horizon (Fig. 4.5d) which are circular in planform and have a V-shaped morphology in section (e.g. Hovland and Judd, 1988). These pockmarks are also located above the upper tips of polygonal faults and constitute evidence of transient fluid expulsion at a palaeo-seabed. Similar evidence for fluid flow up fault planes has been identified from the Faeroe-Shetland Basin, where amplitude anomalies tracking faults indicate that fluid flow occurred up the faults from the level of the opal-A to opal-CT transformation zone to the

contemporaneous seabed (Davies *et al.,* 2008). Other examples of seismic images of fluid flow pathways associated with faults in soft sediments have been published by Berndt et al. (2003) and Gay and Berndt (2007).

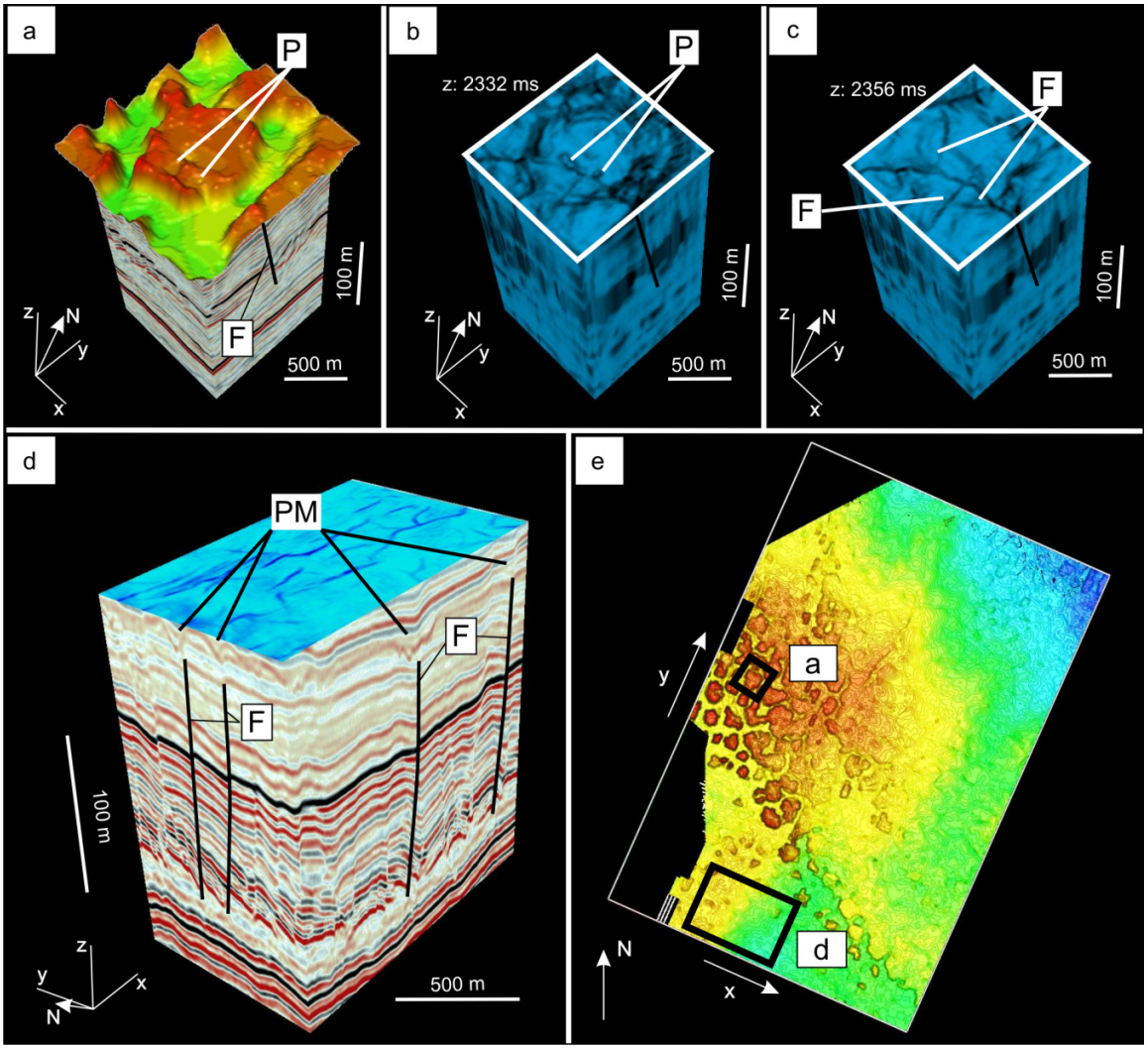

Fig. 4.5 3-D visualizations of seismic data from the Gjallar Ridge. F – faults, P – pipes, PM – pockmark. (a) Horizon slice at the opal-A to opal-CT transformation zone surface around a mesa, showing an underlying fault cutting the seismic data volume. (b) Coherency type attribute for part a seismic cube capped by the time slice at 2.332 s, showing small circular pipes. (c) Coherency type attribute for the same seismic cube capped by a deeper time slice at 2.356 s, showing faults intersecting below the pipes and the mesa feature. (d) Seismic cube with coherency time slice at the top surface. Above the marked faults on the sides of the cube, pockmark features can be seen. (e) Portion of the two-way time map for the cross cutting reflection interpreted as the main opal-A to

opal-CT transformation zone. Red is shallowest and blue is deepest. Rectangles indicate the areas of the horizon slice in (a) and the time slice in (d).

4.4 MODEL FOR FORMATION OF TOPOGRAPHIC STRUCTURES

We point out here that the mesas and ridges have only been found around the upper tips of polygonal faults, which strongly suggests that the chemistry of water expelled up the fault planes has a key role in their formation. Chemical controls on the transformation of opal-A to opal-CT were investigated by Kastner et al. (1977). Noting that the rate of transformation is increased in carbonate sediments and reduced in clay-rich sediments relative to pure siliceous oozes, they inferred either the presence of a 'catalyst(s)' within the carbonate system and/or the presence of inhibitor(s) in clay-rich sediments. In laboratory experiments, they found that the presence of magnesium and a source of hydroxyl enhance the transformation of opal-A to opal-CT, and suggested that nuclei with magnesium and hydroxyl ions in the proportion ~1:2 attract silanol groups to act as sites of opal-CT nucleation and subsequent growth of opal-CT lepispheres. Williams & Crerar (1985) have since described how open framework silica polymers form and flocculate to produce opal-CT in pore waters containing abundant cations.

In our model, we assume that a polygonal fault system has developed at shallow depth in a succession of sediments that are rich in biogenic silica before any transformation of opal-A to opal-CT takes place (Fig. 4.6). As the sediments compact and the faults grow, pore water is expelled episodically up the faults (e.g. Gay and Berndt, 2007; Goulty, 2008) and dissipates by horizontal and vertical flow through the beds around the upper fault tips. It may be inferred from the disruption in the sediment bedding exhibited by the fluid-escape features (Fig. 4.5) that the flow is transient. The estimated volumetric rate of water expulsion per unit surface area from an opal-A to opal-CT transformation zone is ~6 $m^3.My^{-1}$ per square meter, which is far greater than that the vertical flux of water due to compaction of typical clastic sediments (Davies *et al.,* 2008). These large volumes of fluid released during the transformation CT, means that enhanced fluid flow up

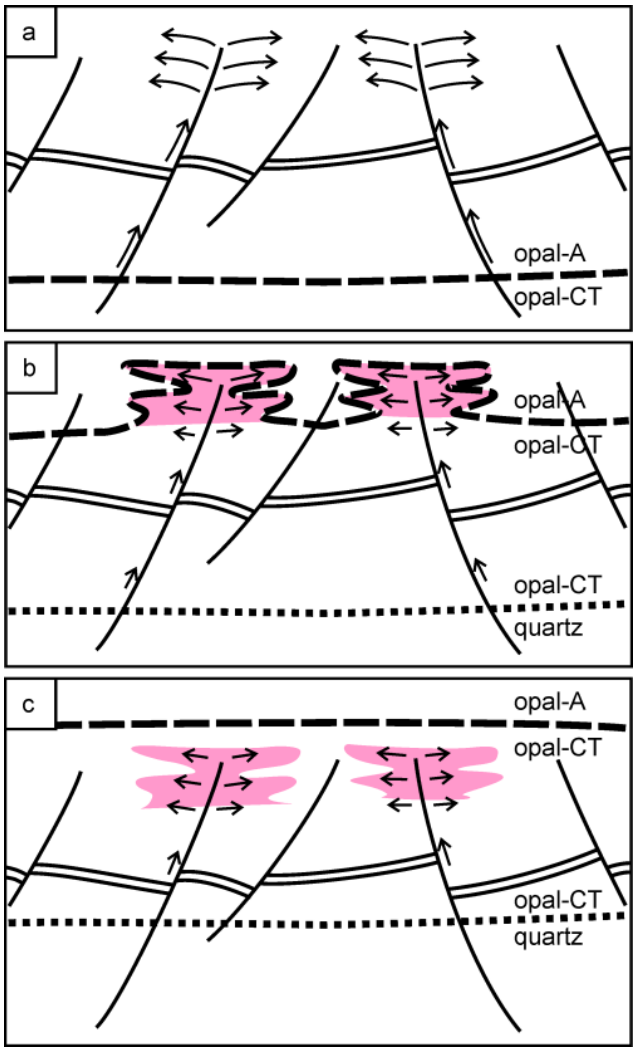

Fig. 4.6 Development of patterns at the opal-A/opal-CT transformation zone during ongoing burial, as seen in section. (a) Opal-A/opal-CT transformation zone has reached the base of a succession of silica-rich sediment cut by a polygonal fault system. (b) Opal-A/opal-CT transformation zone has advanced preferentially in the flushed regions (pink) where magnesium-enriched water released by opal-CT/quartz transformation continues to invade. (c) Opal-A/opal-CT transformation zone has annealed after advancing above the flushed regions (pink) which now become deeper buried regions of preferential transformation imaged as high amplitude anomalies on seismic reflection data, where there is ongoing invasion by magnesium-enriched water released by opal-CT/quartz transformation. Single solid lines—fault planes. Double solid line—arbitrary stratigraphic horizon. Heavy dashed line—main opal-A/opal-CT transformation zone. Heavy dotted line—main opal-CT/quartz transformation zone. Arrows—pathways for fluid expulsion from both transformation zones.

the fault planes occurs once transformation has started in the faulted succession of silica-rich sediment (Fig. 4.6a). Following further burial, opal-CT at the base of the silica-rich succession begins to transform to quartz (Fig. 4.6b), giving up magnesium in the process (Kastner *et al.,* 1977). Smaller quantities of water, now enriched in magnesium, are released by the dissolution of opal-CT and can flow up the fault planes. This water may flow away from the upper fault tips along the bedding, where horizontal permeabilities are greater than vertical permeabilities, into the regions where mesas will subsequently develop, as on the Gjallar Ridge (Fig. 4.2). Alternatively, local hydrofracturing of the sediment may allow it to flow preferentially upwards, and subsequently outwards, into regions where ridges will subsequently form, as in the Faeroe-Shetland Basin (Fig. 4.3). Again, we would expect such flow to be transient. When the transformation zone reaches the vicinity of the upper fault tips, it advances more rapidly through the flushed zones (Fig. 4.6b) because the increased concentrations of magnesium and hydroxyl in the pore water promote opal-A to opal-CT transformation at lower temperature (Kastner *et al.,* 1977). As burial proceeds, the opal-A to opal-CT transformation zone moves up above the upper fault tips, and the reflection event anneals to follow the approximately planar isotherms (Fig. 4.6c). At this final stage, more complete transformation of opal-A has occurred in the regions around the upper fault tips where invasion by magnesium-enriched water released by the transformation of opal-CT to quartz continues to invade the formation: hence the enhanced amplitudes of stratigraphic reflection events in these regions (Fig. 4.4b).

4.5 DISCUSSION AND CONCLUSIONS

The hypothesis that the topographic structures of ridge and trough networks at the top of silica diagenetic transformation zones only form where fluids have been expelled from the upper tips of polygonal faults is testable: it is open to falsification by the discovery this type of structure where there is no spatial association with polygonal faults. Assuming that patterns do form due to the flushing of the regions above fault tips where cells or ridges at higher elevations develop across the transformation zones (Figs 4.2 & 4.3), candidate mechanisms are mass transport of silica by advection; perturbation of isotherms due to advective or convective heat transport; and changes in pore water chemistry in the flushed regions (cf. Davies and Cartwright, 2007).

The possibility that the reflection amplitude variations observed along stratigraphic horizon D (Fig. 4.4b). and the cells and circular amplitude anomalies around the upper tips of polygonal faults are caused by advection of silica is discounted for two reasons. First, the

solubility of silica is so low that unrealistically large volumes of water would be needed to transport sufficiently large amounts of dissolved silica. The main zone of opal-A to opal-CT transformation gives rise to a near-planar reflection event cross-cutting stratigraphy (horizon A in Fig. 4.4a) which probably approximates an isotherm. We infer that isotherms in the underlying sequence are parallel to horizon A. The amplitude variations along the underlying stratigraphic reflections around horizon D (Fig. 4.4b) do not correlate with topographical variations, and so are not caused by the increase in temperature with depth. It seems likely that the structural highs along horizon A (Figs 4.2 and 4.3) have the same root cause as the high-amplitude regions along stratigraphic horizon D (Fig. 4.4b), given the remarkable similarity in geometry, size and distribution, and lateral variation in pore water chemistry appears to be the only plausible mechanism that can explain them.

The topographic structures imaged in the Vøring Basin (Figs 4.2 & 4.4) and Møre Basin (Davies and Cartwright, 2007) are circular regions of shallower opal-A to opal-CT conversion that are cut by faults or bounded by faults. In these cases, the faults appear to have fed conduits of limited lateral extent for fluid flow, which in some places may be focused along fault intersections, as deduced by Eichhubl & Boles (2000). In the Faeroe-Shetland Basin (Fig. 4.3), shallower opal-A to opal-CT conversion has occurred in the polygonal ridge network. The ridges are located above the upper tips of polygonal faults, and we infer that fluid has been expelled upwards along the length of the faults rather than through laterally restricted conduits.

Although individual beds that are particularly rich in opal-CT (porcellanite beds) or quartz (chert beds) would be brittle, polygonal faults in soft mud-rich sediments may not provide permanently open conduits for steady fluid flow, but would provide higher permeability pathways which fluids could exploit. We expect that upward fluid flow along fault planes would be transient, and might occur in association with small displacements on the faults. The transient nature of fluid flow would help to make the magnesium available as a catalyst for opal-CT formation instead of contributing to dolomite precipitation.

Increased magnesium concentration is not the only factor that could be responsible for catalysing the precipitation of opal-CT at shallower depths and lower temperatures. More generally, increased alkalinity due to the presence of other cations helps to flocculate silica particles by forming positively charged hydroxyl complexes (Williams and Crerar, 1985). Successions rich in biogenic silica commonly have a significant calcium carbonate component, comprised of foraminifers, calcareous bioclasts and nanofossils (Eldholm *et al.,* 1987a). Carbonate tends to precipitate with upward water flow in spite of its reverse solubility with

temperature because the reduced concentration of carbon dioxide in aqueous solution, due to degassing at lower pressure, increases carbonate solubility, and this effect tends to outweigh the temperature effect (Eichhubl and Boles, 2000). Therefore the expelled water that has flushed the regions around the upper fault tips of polygonal faults could also have increased alkalinity due to enhanced calcium concentration.

Davies & Cartwright (2002) noted that the cross-cutting seismic reflection event due to opal-A to opal-CT transformation in the Faeroe-Shetland Basin appears to be fossilized, because it is parallel to an overlying early Pliocene unconformity rather than to the seabed. We speculate that the parallelism is another manifestation of pore water chemistry acting as a control on silica diagenesis. During active burial of a thick silica-rich succession, the depth and temperature where opal-A to opal-CT transformation occurs are reduced because of the increased magnesium concentration in upwardly transmitted pore water released by the ongoing transformation of opal-CT to quartz below. During the hiatus represented by the unconformity, exhumation results in cooling and the arrest of diagenesis. Magnesium in the pore water between the two main silica diagenetic transformation zones is slowly taken up by transformation of residual opal-A to opal-CT, and possibly by absorption into clay minerals. On reburial, the reduced magnesium concentration in the pore water around the former opal-A to opal-CT transformation zone means that a higher temperature has to be reached before transformation recommences. We are currently seeking a means of testing this hypothesis.

The novel aspect of this paper is that a chemical control has been identified as the mechanism responsible for generating diagenetic patterns at the kilometre scale. The seismic data show that the structural fabric provides pathways for fluid flow, resulting in lateral variations in pore water chemistry that affect the silica transformation rate. Although it is not possible to provide a definitive description of the chemical transformations involved without additional well data, the model we propose is consistent with all the seismic evidence and laboratory studies of silica diagenesis.

5 INFLUENCE OF STRATIGRAPHIC SETTING AND SIMPLE SHEAR ON LAYER-BOUND COMPACTION FAULTS OFFSHORE MAURITANIA

ABSTRACT

We have used three-dimensional seismic data to examine the geometry of layer-bound compaction faults on the Mauritanian continental margin. The faults deform a fine-grained Neogene unit which mantles buried canyons. Above the canyons, most layer-bound faults strike perpendicular to the canyon axes, whereas between the canyons the faults are omni-directional and intersect bedding planes in polygonal patterns. On the flanks of a large structural high, faults also strike perpendicular to the slope direction, displaying a concentric pattern. Faults that show preferential alignment are located in areas with increased bedding dip, and most aligned faults are antithetic to the bedding dip. Where the bedding dip is greater than ~1°, the synthetic faults dip more steeply than the antithetic faults. This discovery was unexpected because the stress tensor due to the effect of gravity on a dipping margin would cause the antithetic faults to form with steeper dips, which we show theoretically. We hypothesise that the layer hosting the faults has been subjected to simple shear of ~20° or more, with the top of the layer displaced downdip by ~100 m relative to its base. A potential application of these, and similar, observations is to assess slope stability on continental margins.

5.1 INTRODUCTION

Sediments are subject to body and surface forces, including gravity, from the time of deposition and their response to these forces depends on their mechanical properties and the magnitudes of the forces (Maltman, 1994). Numerous authors have identified that depositional slopes can influence the development of faults in sediments (e.g. Crans *et al.,* 1980; Higgs and McClay, 1993; Kobayashi *et al.,* 1998; Victor and Moretti, 2006). The geometry of extensional fault systems is also affected by the presence of low friction substrates which act as basal detachments (e.g. Morley and Guerin, 1996). Of particular relevance to the observations reported here, Stewart and Argent (2000) showed that the kinematics of synthetic versus antithetic fault arrays dictate that synthetic fault arrays must branch onto a basal detachment, whereas faults within antithetic arrays may die out downwards.

Layer-bound systems of compaction faults found in fine-grained sedimentary units commonly comprise networks of normal faults with strike directions that form polygonal geometries on bedding planes (Cartwright and Dewhurst, 1998). Bedding plane geometries of compaction fault systems may depart from polygonal forms due to the influence of external stresses such as basin floor slope (e.g. Higgs and McClay, 1993) and tectonic faults (Hansen *et al.,* 2004). Here we describe layer-bound faults from the Neogene succession offshore Mauritania (Fig. 5.1). Layer-bound fault systems deform a deep marine succession that overlies several kilometre-wide canyons. We document changes in the planform geometry of fault systems above the canyons and on the flanks of a large structural high, and interpret them with reference to the kinematic model of Stewart and Argent (2000) for the development of synthetic and antithetic fault arrays. We then consider the distribution of dips within these layer-bound fault systems in the light of a theoretical analysis of the stress state induced by gravity acting on a dipping margin. In two areas where the continental margin is dipping and both antithetic and synthetic faults are present, we infer that the host layer has undergone a significant amount of simple shear deformation.

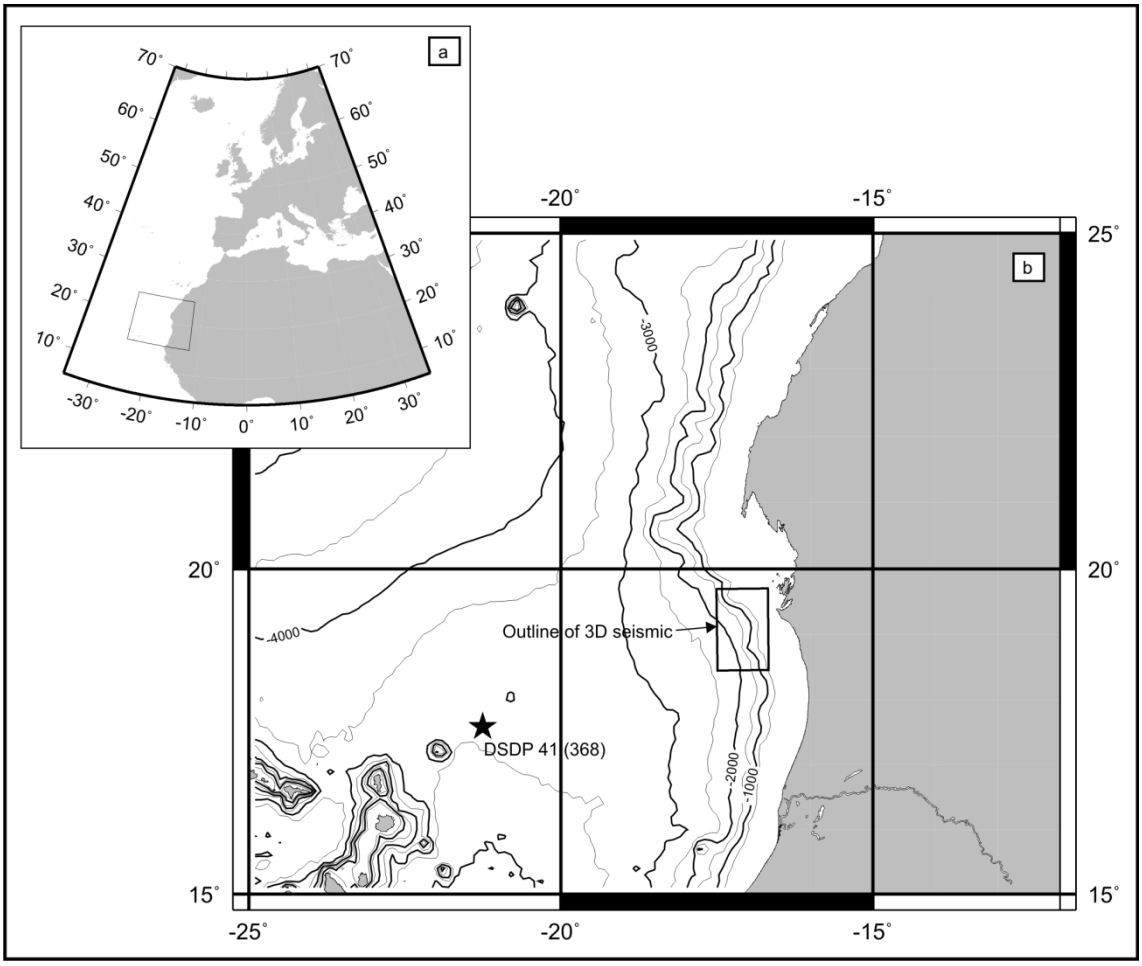

Fig. 5.1 Location map showing (a) the position of Mauritania on the West African margin and (b) the location of the 3-D seismic survey with bathymetry contoured in metres below sea surface. The star marks the position of DSDP 41 (site 368).

5.2 LAYER-BOUND COMPACTION FAULTS

Factors common to layer-bound systems of normal faults are that they have only been found sediments that were deposited in low-energy settings, that are dominantly composed of very fine-grained lithologies such as smectitic claystones, siliceous or carbonate oozes and chalks, with high porosity and extremely low permeability (Cartwright and Dewhurst, 1998). Such systems have developed over large areas of passive margins and over some intracratonic basins, commonly with the faults cutting stratigraphic horizons in a crudely polygonal geometry. These so-called polygonal fault systems have been identified in more than 50 sedimentary basins world-wide (Cartwright and Dewhurst, 1998). They are widespread on the North Atlantic Margin (Lonergan *et al.,* 1998; Clausen *et al.,* 1999; Lonergan and Cartwright, 1999; Gay and Berndt, 2007; Hustoft *et al.,* 2007), and other notable studies have focused on polygonal fault

systems found in Australia (e.g. Watterson *et al.,* 2000), offshore Canada (Hansen *et al.,* 2004) and offshore West Africa (Gay *et al.,* 2004). Polygonal fault systems are thought to have resulted from volumetric reduction with bed-parallel compaction, which complements the heaves on the faults, in addition to vertical compaction (Cartwright and Lonergan, 1996).

Layer-bound polygonal systems of normal faults are an intriguing phenomenon because purely uniaxial compaction of clastic sediments generally does not result in brittle shear failure (Goulty, 2008). Consequently, their very existence in layer-bound sequences that have not undergone tectonic extension seemed paradoxical when they were first identified on three-dimensional (3-D) seismic data (Cartwright, 1994). Laboratory measurements (Bishop *et al.,* 1971) and subsurface data (Goulty and Swarbrick, 2005) provide evidence that low coefficients of friction on fault surfaces are the key factor that allows polygonal fault systems to develop (Goulty, 2001, 2002, 2008). Once faults have nucleated in the fine-grained host sediments, they can continue to grow with increasing overburden stress under laterally confined conditions, provided that the coefficient of residual friction on the fault surfaces is sufficiently low.

A small number of layer-bound compaction fault systems have been described where the typically ordered polygonal pattern is disrupted (e.g. Higgs and McClay, 1993; Hansen *et al.,* 2004). Layer-bound faults from the Moray Firth with a dominant dip direction shelfwards were attributed to downslope gravity sliding, triggered by tilting (Higgs and McClay, 1993). Lonergan and Cartwright (1999) studied polygonal faults in the Alba Field, and noted that the density of faulting in the mudrocks was reduced above the reservoir and that 18% of the faults at one horizon had strike directions within a 10° range, parallel to the slope direction. They suggested that stress heterogeneities associated with the change in lithofacies from sand to mud and stress field alterations associated with the compactional draping were responsible for these observations. Hansen et al. (2004) identified that the presence of tectonic faults influenced the organisation of nearby polygonal fault systems, giving rise to orthogonal intersections between the two sets.

5.3 EFFECT OF SEAFLOOR SLOPE ON FAULT GEOMETRY

In sedimentary basins where the strata are horizontal, one principal stress axis is vertical and the other two principal stress axes lie in the horizontal plane. In tectonically passive settings, the maximum effective stress σ'_1 is vertical, and stress is isotropic in the horizontal plane. If any normal compaction faults are initiated, there is no preferred strike orientation (Fig. 5.2a). Where the strata are dipping, with bedding planes parallel to the dipping seafloor, the effect of

gravity modifies the effective stress tensor as shown in Fig. 5.2b: σ'_1 is increased compared to the case of horizontal strata, and plunges in the downslope direction at a steep angle; the intermediate principal effective stress σ'_2 lies in the strike direction of the strata; and the minimum effective stress σ'_3 is reduced and plunges gently in the upslope direction, orthogonal to σ'_1 (Mandl, 1988, p.121). The preferred strike direction of any normal compaction faults that are initiated is now parallel to the strike of the strata, in the direction of σ'_2. Furthermore, if the faults are antithetic, dipping in the upslope direction, the fault dip is increased; and if the faults are synthetic, dipping in the downslope direction, the fault dip is decreased.

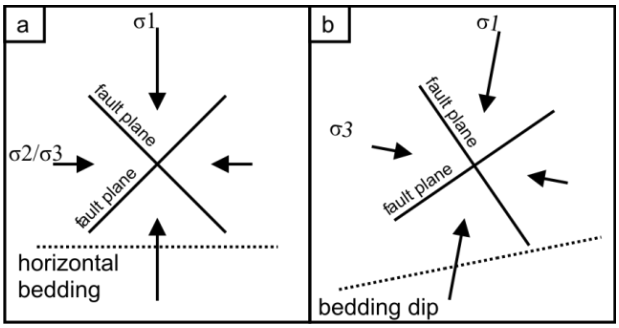

Fig. 5.2 (a) Effective stresses acting within a tectonically passive basin where the bedding is horizontal. (b) Maximum and minimum effective stresses acting within a tectonically passive basin where the bedding dips to the left.

Here we derive the Terzaghi effective stress tensor (Terzaghi, 1943) due to gravity acting on plane-parallel beds of sediment below a planar dipping seafloor, and give a numerical example to illustrate the expected effect on the relative attitudes of any synthetic and antithetic compaction faults that may be initiated in the sediment.

We consider the effective stresses acting on a bedding plane at a general point Q (Fig. 5.3). The algebraic symbols used are defined as follows:

g gravitational acceleration,

h perpendicular depth of Q below seafloor,

K constant,

X,Y,Z Cartesian axes with X-axis downslope parallel to the seafloor, Y-axis in the strike direction, and Z-axis perpendicular to the seafloor,

θ dip of the bedding and the seafloor,

ρ_b average bulk density between Q and the seafloor,

ρ_w density of seawater,

σ'_1 maximum principal effective stress,

σ'_2 intermediate principal effective stress, and

σ'_3 minimum principal effective stress.

The effective stress tensor at Q is calculated by considering the effect of gravity on the sediment between Q and the seafloor. The vertical force of gravity acting on unit cross-sectional area of the bedding plane through Q exceeds the hydrostatic pressure by $(\rho_b - \rho_w)gh$ and, assuming no overpressure is present, the excess force per unit area may be resolved into a normal effective stress $(\rho_b - \rho_w)gh\cos\theta$ acting in the Z-direction and a shear stress $(\rho_b - \rho_w)gh\sin\theta$ acting in the X-direction.

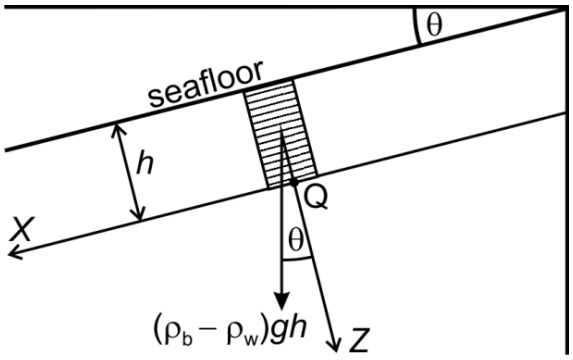

Fig. 5.3 Effect of gravity at a general point Q in plane parallel sedimentary layers below a dipping seafloor. The algebraic expression is the difference between the vertical gravitational force acting on unit cross-sectional area of the bedding plane through Q and the hydrostatic pressure at Q.

We assume that the sediment compacts uniaxially, in the direction of the maximum principal stress, the principal effective stresses maintain the same relative magnitudes during compaction, and the strains in the X-Y plane are zero. Then the stress in the X-Y plane must be isotropic, and the normal effective stresses acting in the X-direction and the Y-direction may be expressed as $K(\rho_b - \rho_w)gh\cos\theta$. Provided that the bedding dip is small, it is reasonable to assume that K is approximately equal to the coefficient of earth pressure at rest, which may be taken as a constant for a given lithology (Mayne and Kulhawy, 1982). Furthermore, the Y-

direction is a principal stress direction because there are no shear stresses acting in the X-Y and Y-Z planes. Now we need to determine the magnitudes and directions of the principal effective stresses acting in the X-Z plane.

The two-dimensional effective stress tensor referred to (X,Z) coordinate axes is

$$(\rho_b - \rho_w)gh\begin{pmatrix} K\cos\theta & \sin\theta \\ \sin\theta & \cos\theta \end{pmatrix} \quad \textbf{Eq. 5.1}$$

The eigenvalues of this tensor are the maximum and minimum principal effective stresses, and the corresponding eigenvectors define their directions. They may be found by a standard procedure for square matrices (Stroud and Booth, 2007). The maximum principal effective stress is

$$\sigma'_1 = (\rho_b - \rho_w)gh\left[(1+K)\cos\theta + \sqrt{(1-K)^2\cos^2\theta + 4\sin^2\theta}\right]/2, \quad \textbf{Eq. 5.2}$$

plunging basinwards at the angle

$$\arctan\left\{\left[(1-\mathrm{K_0})\cos\theta + \sqrt{(1-K)^2\cos^2\theta + 4\sin^2\theta}\right]/2\sin\theta\right\} + \theta, \quad \textbf{Eq. 5.3}$$

and the minimum principal effective stress is

$$\sigma'_3 = (\rho_b - \rho_w)gh\left[(1+K)\cos\theta - \sqrt{(1-K)^2\cos^2\theta + 4\sin^2\theta}\right]/2, \quad \textbf{Eq. 5.4}$$

plunging shelfwards at the angle

$$\arctan\left\{2\sin\theta\,/\left[(1-K)\cos\theta + \sqrt{(1-K)^2\cos^2\theta + 4\sin^2\theta}\right]\right\} - \theta, \quad \textbf{Eq. 5.5}$$

The intermediate principal effective stress is in the Y-direction and has magnitude

$$\sigma'_2 = K(\rho_b - \rho_w)gh\cos\theta. \quad \textbf{Eq. 5.6}$$

As a numerical example, suppose that $K = 0.7$, a typical value for the coefficient of earth pressure at rest in clay (Mayne and Kulhawy, 1982), and $\theta = 3°$. The maximum principal effective stress plunges basinwards at 83.4°. The minimum principal effective stress is 1.3% less than the intermediate principal effective stress and plunges shelfwards at 6.6°. If synthetic

and antithetic normal faults form under these stress conditions (Fig. 5.2), it is to be expected that the dips of the antithetic faults would be 13° steeper than the dips of the synthetic faults.

5.4 GEOLOGICAL SETTING

Vear (2005) provided an excellent account of the petroleum plays of the Mauritanian continental margin, and placed them in their wider geological context. The continental shelf offshore Mauritania (Fig. 5.1) is a passive margin with significant oil and gas discoveries at Chinguetti and Banda. On the West African margin, deepwater channelised systems are an important petroleum play, with turbidite complexes representing exploration targets and proven reservoirs. During rifting of the Proto-Atlantic Ocean, Liassic evaporites were deposited in the axes of Triassic-Early Jurassic graben. Sediment starvation during the Jurassic allowed the development of carbonate platform complexes, which ceased during the Valangian when a major transgressive event resulted in the deposition of several hundreds of metres of marine shale. During the Albian to Turonian, deepwater conditions predominated on the margin with a wide variety of depositional environments represented. The Campanian to the Maastrictian was a period of relative lowstand during which there was major incision of the continental slope, evident as buried canyons clearly imaged in the seismic data. The Oligocene succession on the margin is dominated by deepwater calcarenites and claystones. From the Early Miocene through to the Recent, canyon systems and a large number of channels have traversed the upper slope.

The layer-bound fault systems investigated here lie within Neogene strata. On the West African margin, the Neogene succession is generally thin, but offshore Mauritania it is significantly thickened with complex deposition from the Late Miocene to the present day (Schwab *et al.,* 2007). There are many slides and mass transport complexes throughout the Neogene succession, and their formation was the consequence of uninterrupted deposition of sediment in an open-slope environment which gave rise to rapid accumulation of poorly consolidated sediment intercalated with thin weak layers (Antobreh and Krastel, 2007). Canyon systems and smaller channels cross and incise the slope at numerous stratigraphic levels throughout the Neogene succession. These canyons may be filled with bathyal turbidites (Vear, 2005) and, they may, have fed basin-floor fan systems further offshore. Schwab et al. (2007) have identified contourite drifts deposited in channel pathways that can be confused with turbidity current channel levees, and when these deposits become buried they may be even more difficult to distinguish due to loss of seismic resolution with increasing depth.

5.5 DATABASE AND METHODOLOGY

Data have been interpreted from a single time-migrated 3-D seismic reflection volume that covers an area of 4000 km^2 in water depths of ~500-2500 m (Fig. 5.1). These data were processed using a standard sequence of steps including multiple suppression and post-stack time migration. The survey has a bin size of 25 m × 25 m and the data have a vertical resolution (given by one quarter of the wavelength at the dominant frequency) in the Neogene of about 10 m. The processed data have not been zero-phased. In the seismic sections shown, a reflection event consisting of a red loop followed by a blue loop represents an increase in acoustic impedance downwards.

A generalised depth conversion function, derived from unreleased velocity data in several wells across the Mauritanian margin, was used to convert fault heights from time (ms) to depth (m), and to calculate the dip angle for the faults. Deep Sea Drilling Project (DSDP) velocity data provide further corroboration for the depth conversion, with velocities in the Recent to Neogene clays and claystone lithologies of DSDP Leg 41, Site 368 ranging from 1430 to 2460 m s^{-1} (Trabant, 1977). Assuming an average velocity of 2000 m s^{-1} between the seafloor and the infilled canyons, the seismic sections are displayed here with a vertical exaggeration of ~1.5 over that interval.

Seismic attribute maps were used for the interpretation of faults on selected horizons. We used edge detection and coherency (e.g. Brown, 2005a) as the primary method of imaging the faults, as shown by the examples in Fig. 5.4a and b, but for clarity in this and subsequent figures we show fault trace maps interpreted from these seismic attributes, as in Fig. 5.4c. Fault dips were calculated from the horizontal and vertical offsets of upper and lower tips at the middle of fault traces on vertical seismic sections oriented perpendicular to the strike of the fault. The regional seismic stratigraphy, which is described in more detail in the next section, is relatively well constrained, although we cannot rule out local variations in the lithology because we have no well data in the area covered by the 3-D seismic survey.

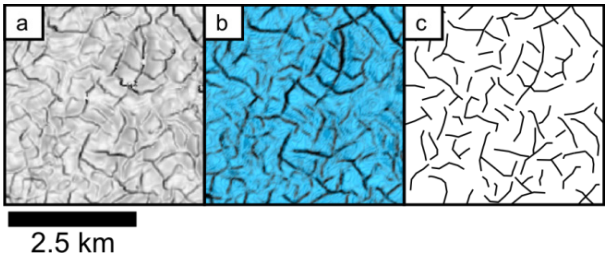

Fig. 5.4 Horizon slices generated during the interpretation: (a) edge detection map, dark colours highlight spatial differences on the interpreted horizon; (b) coherency volume, dark colours are discontinuous regions, and blue continuous; and (c) interpreted fault traces picked from (a) and (b).

5.6 SEISMIC OBSERVATIONS

5.6.1 Regional structural elements

Structural elements that can be recognised on the margin include deep-rooted Mesozoic faults associated with rifting of the proto-Atlantic and shallow collapse faults associated with the ascent of salt diapirs and folding of the overburden. However, only the structural high of the Khop Structure, discussed below, affects the layer-bound fault systems in this study, and there is no evidence of faults that penetrate through the whole Palaeogene succession to cut both Mesozoic and Neogene strata.

In the southern portion of the survey, the dips of the Neogene strata are significantly steepened beyond the regional dip by a large structural high, the Khop Structure (Fig. 5.5). The structure is ~6 km high, ~60 km in diameter at its base, and ~10 km in diameter at its top. The top is irregular with several circular mounds which protrude up to ~200 m above the top of the main structure. The eastern flank is steeper (maximum dip ~14°), and the western flank is gentler (maximum dip ~6°). The structure has poor internal reflectivity. Reflection events around 4 s two-way time onlap the structure, which suggests an Early Cretaceous age. The origin of the structure is uncertain, but a possibility includes a buoyant serpentinite body, mobilised and emplaced diapirically from the upper mantle (cf. Bonatti, 1976). Such serpentinite bodies have been found along large, tectonically active fracture zones which intersect the Mid-Atlantic Ridge (Miyashiro *et al.,* 1969). The circular mounds at the top of the structure are interpreted as carbonate pinnacle reefs (e.g. Elvebakk *et al.,* 2002). Apart from the large excursions from the regional dip due to the Khop Structure, there are local departures due to major periods of canyon incision of the slope.

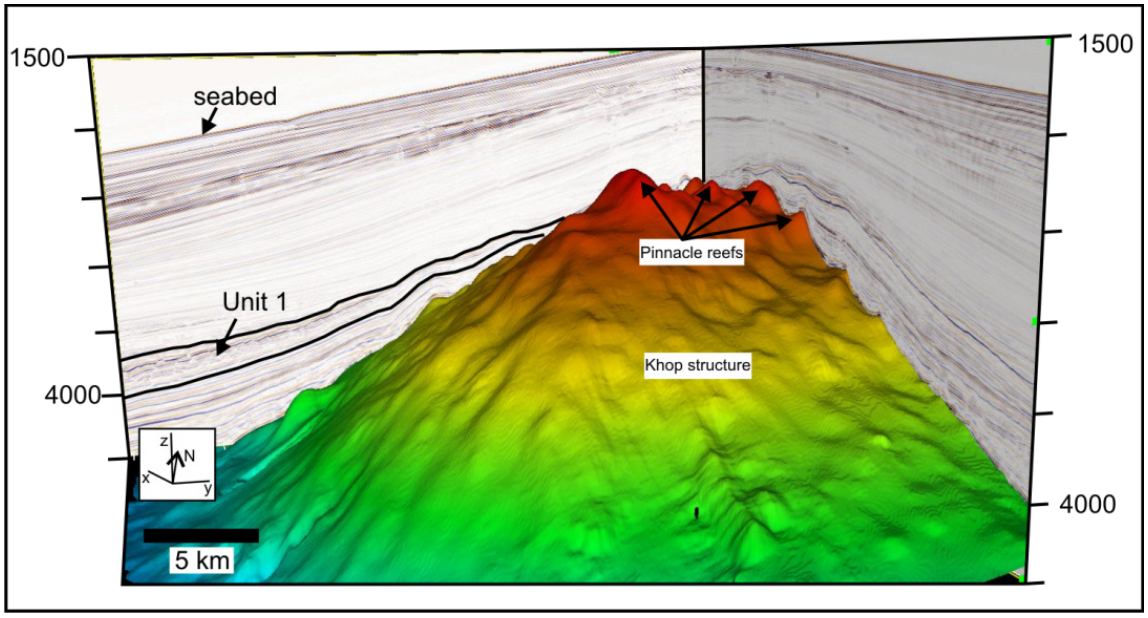

Fig. 5.5 3-D visualisation of the Khop Structure. The interpreted upper surface of the structure is coloured by two-way time (red shallowest, blue deepest). Unit 1 is the faulted interval. Vertical scale is two-way time in milliseconds.

5.6.2 Neogene elements

The section marked 'Unit 1' in Fig. 5.6 is 200–400 m thick and its top and base are marked by reflection events of positive polarity. The unit is characterised by a layered succession of relatively high-amplitude reflection events that are offset by many faults with throws of up to 70 m. Based on the seismic character of Unit 1 and its position within the existing stratigraphic framework, this unit is interpreted as deepwater sediment, mostly likely consisting of hemipelagic siltstones and mudstones and siliceous shales. There is evidence for Unit 1 having a significant biogenic silica component on the basis of a strong reflection with positive polarity that cross-cuts stratigraphic reflections (Fig. 5.6c), and thus has a character consistent with an opal-A to opal-CT transformation boundary (e.g. Davies and Cartwright, 2002). DSDP Leg 41 also encountered siliceous sediments of a similar age (Riech and Roesch, 1977). Direct hydrocarbon indicator (e.g. flat spot), gas hydrates and seismic multiple have been ruled out because the characteristics is not consistent any of these.

Below Unit 1, a succession of planar parallel reflections is commonly truncated by channel features, interpreted as deepwater canyons (Fig. 5.6). Within them, the seismic reflectivity is relatively poor. The canyons traverse the survey area from north-east to south-west (Fig. 5.7). The observed canyon geometries, abrupt incision of the slope, the westward

decrease in slope gradient and locally occurring slumping and gravity-driven deformation indicate that during the Neogene the setting was mid-slope. Eastward is more proximal, and there is evidence to support an upper slope setting, including canyon and channel amalgamation and cannibalisation (e.g. Bouma, 2004). Depositional elements such as channel bodies can generally be mapped out using a variety of amplitude analysis techniques (Brown, 2005), but the identification of internal features within the canyons is difficult here because of the poor reflectivity, which may be due to the high structural dips and complex stacking patterns within the canyons (e.g. Santos, 2000).

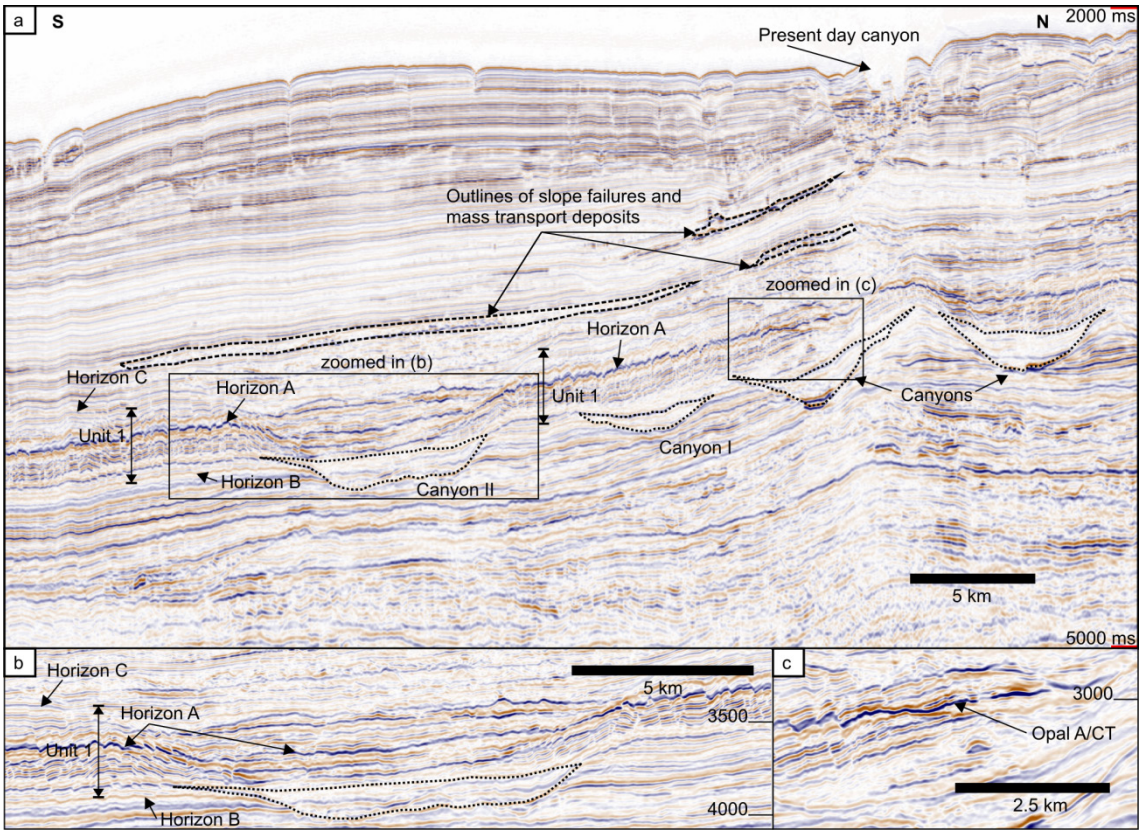

Fig. 5.6 (a) Representative S–N seismic line showing examples of kilometre-wide canyons which incise the margin, and the overlying Unit 1. Horizon A is the horizon used to interpret fault traces, Horizon B marks the base of Unit 1, and Horizon C marks the top of Unit 1. (b) Zoom to show truncation of seismic reflections by canyon incision and detail of Unit 1. (c) Zoom to show detail of the opal-A/CT reflection where it is prominent. Vertical scale is two-way-time in milliseconds. The vertical exaggeration is ~4× in (a) and ~1.5× in (b) and (c).

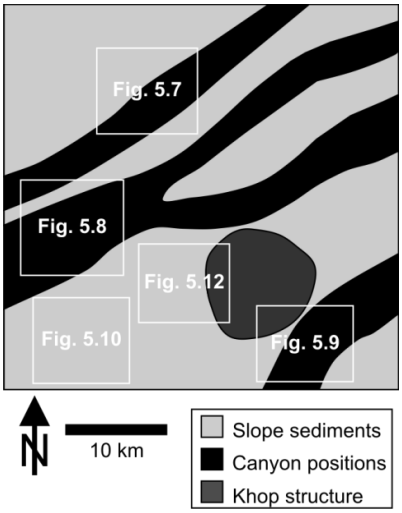

Fig. 5.7 Line drawing showing the positions of the canyons (in black) which traverse the 3-D seismic survey area within the Neogene succession. The positions of the fault maps shown in subsequent figures are outlined in white.

We have examined the deformation of Unit 1 associated with three canyons in particular, termed canyons I–III. Canyon I has low sinuosity and in cross-section has a maximum width of 5 km, a maximum depth of 300 m, and truncates stratigraphic reflections (Fig. 5.8). Canyon II has low sinuosity, a maximum width of 8 km, and a maximum depth of 300 m. Upslope it consists of two individual segments that amalgamate, both truncating stratigraphic reflections (Fig. 5.9). Canyon III also consists of two individual segments which amalgamate. Its course has been deflected around the southern margin of the Khop Structure. It has a maximum width of 4 km and a maximum depth of 250 m (Fig. 5.10). All three canyons are considered contemporaneous. The three canyons all incise the slope and we have measured the dip of the base of each canyon to be steeper than the incised stratigraphy. These dips are 3° at the base of Canyon I, 2.5° at the base of Canyon II, and 3° at the base of Canyon III. The dip of the strata adjacent to the canyons is <1° (e.g. Fig. 5.11). Unit 1 was deposited after canyons I and II had been infilled, but forms the fill for Canyon III, where the canyon was bypassed during sandy deposition and later filled during transgression (e.g. Vear, 2005).

5.6.3 General seismic characteristics of layer-bound fault systems

Layer-bound fault systems intensely deform Unit 1. The faults are exclusively normal faults with most likely dip-slip displacements, although it cannot be ruled out that there is some component of oblique slip. Maximum throw values of the faults are in the range 10–100 m, but

mostly are in the range 30–70 m. The lower tips of the faults mostly appear to terminate at Horizon B, given the limits of seismic resolution, and the upper tips of many faults are around Horizon C, but some clearly extend above (Fig. 5.6). The maximum throw of the faults tends to occur around Horizon A. Faults are either planar or slightly listric in cross-section. There are no observable changes in fault-plane dip at the inferred opal-A to opal-CT transformation boundary (e.g. Neagu *et al.,* 2010). This may be due to the fact that the porosity drop due to silica diagenesis is only small (<10 %) and therefore does not result in a measurable change in fault plane dip. Most faults have mapped segment lengths of 300–2500 m. The planform is polygonal across large areas, but not everywhere. The fault systems exhibit dramatic changes in the distribution of strike directions to a dominant single orientation above canyons I, II and III.

5.6.4 Layer-bound faulting above canyons

Faults which deform Unit 1 above Canyon I are dominated by a single direction of fault dip, antithetic to the dip of the slope (Fig. 5.8a). The faults are all normal faults, and typically maximum throws are ~12 m. Faults imaged on vertical seismic sections are generally linear with dips ~30°, assuming an interval velocity of 2000 m s-1 for Unit 1. In planform, the fault segments have linear to curvilinear traces and are 300–2500 m long (Fig. 5.8c). The planform distribution of faults is dominated by parallel to sub-parallel segments, oriented NW–SE and spaced 200–400 m apart. Because of the strong dominant fault trend, fault intersections are uncommon. Above the margins of the canyon, a second fault population is observed, with a dominant NE–SW trend parallel to the canyon axis (Fig. 5.8c). The faults which are perpendicular to the canyon axis tend to terminate close to the faults along the margins of the canyons.

Faults which deform Unit 1 above Canyon II are also dominated by a single direction of fault dip, antithetic to the dip of the slope (Fig. 5.9a). The faults are all normal faults, and typically maximum throws are ~20 m. Fault traces are slightly concave to the hanging wall and have dips ~35°, again assuming an interval velocity of 2000 m s^{-1}. The planform distribution of faults is dominated by parallel to sub-parallel segments spaced 400-1500 m apart. The dominant orientation of the faults is NW–SE (Fig. 5.9c), perpendicular to the canyon axis. Because of the strong dominant fault trend, fault intersections are uncommon. Adjacent faults may overlap, and in some instances link laterally along trace. Above the margins of Canyon II there are sets of faults with a dominant NE–SW trend parallel to the canyon axis (Fig. 5.9c), similar to those observed above the margins of Canyon I but fewer in number. Again the faults

which are perpendicular to the canyon axis tend to terminate against the faults above the margins of the canyons.

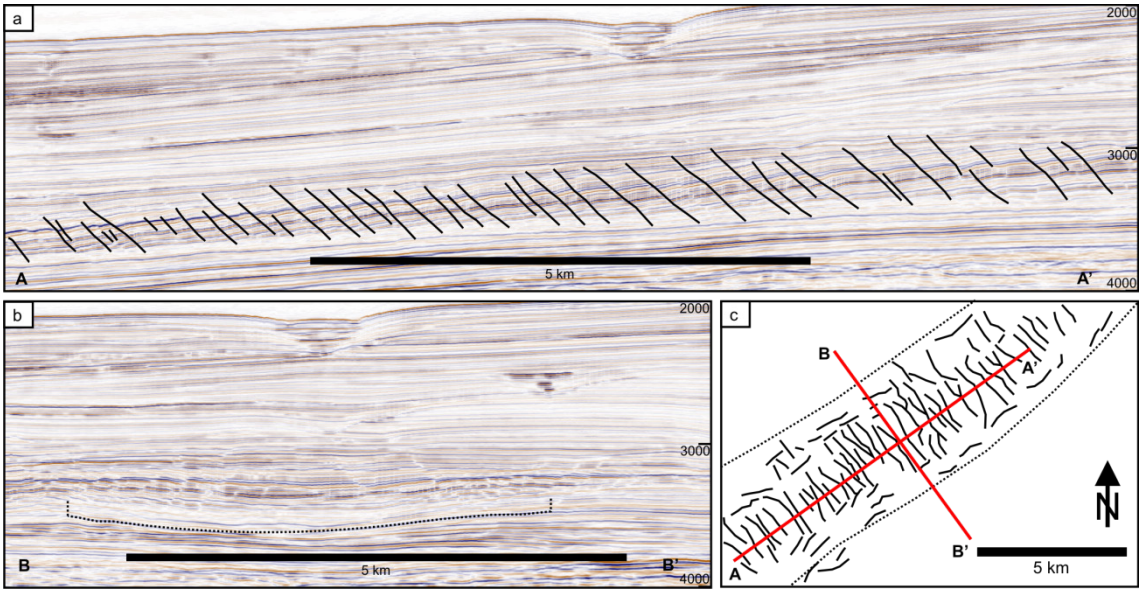

Fig. 5.8 Representative seismic sections from Canyon I (a) along the axis of the canyon, showing a domino array of antithetic faults, and (b) perpendicular to the canyon axis. (c) Fault trace map showing the two dominant fault trends above the canyon. Canyon base and margins are marked by dotted lines. Vertical scale in (a) and (b) is two-way time in milliseconds.

Fig. 5.9 Representative seismic sections from Canyon II (a) along the axis of the canyon, showing a domino array of antithetic faults, and (b) perpendicular to the canyon axis. (c) Fault trace map showing the two dominant fault trends above the canyon. Canyon base and margins are marked by dotted lines. Vertical scale in (a) and (b) is two-way time in milliseconds.

Canyon III has been infilled by Unit 1, indicating that this canyon was bypassed or abandoned and not filled with sandy sediments. A significant difference in the faulting of Unit 1 here is that in cross-section the faults are both antithetic and synthetic relative to the bedding dip (Fig. 5.10a). The faults are all normal faults, with a maximum throw of ~15 m. Faults are more noticeably listric than those that deform Unit 1 above canyons I and II. Measurements of fault dips reveal that antithetic faults and synthetic faults have markedly different fault dips. Antithetic faults have a gentler dip of ~30°, while synthetic faults have a steeper dip of ~40°. In planform, the faults are regularly spaced and orientated WNW–ESE, which is again perpendicular to the canyon axis (Fig. 5.10b). Reflection events tend to bend down towards the fault plane on the hanging wall side, and curve up towards the fault plane on the footwall side (Fig. 5.10a). There are faults trending NNE–SSW along the canyon margins, including along the line of amalgamation of the two canyon segments, but fewer than seen above the margins of Canyon I.

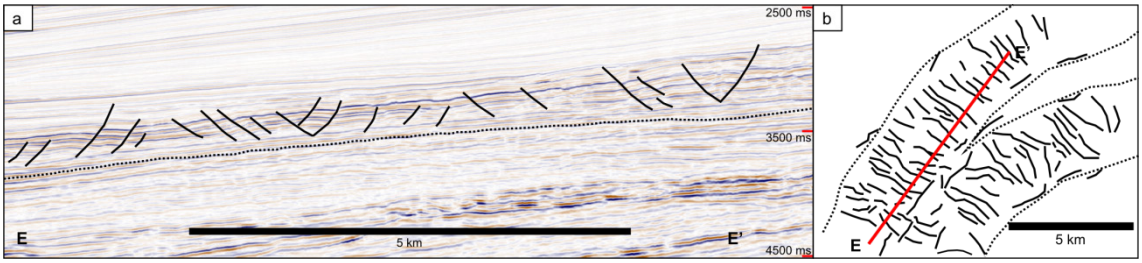

Fig. 5.10 (a) Representative seismic section from Canyon III showing synthetic and antithetic faults. (b) Fault trace map showing the dominant fault trends. Canyon margins are marked by dotted lines. Vertical scale in (a) is two-way time in milliseconds.

5.6.5 Layer-bound polygonal fault systems

Where Unit I does not overlie canyons, the faults display no preferred orientation in map view (Fig. 5.11). The faults are all normal faults, and typically throws are ~30 m. Examination of fault dips reveals distinct changes depending on the direction of fault dip relative to the slope. Within ~10 km of the Khop Structure, where the bedding dip is between 1° and 1.5°, the antithetic faults have gentler dips of around 35° and the synthetic faults have steeper dips of around 40°, whereas at greater distances the antithetic and synthetic faults have similar dip distributions (Fig. 5.12). At fault planes, reflection events may curve down into the fault plane on the hanging wall side, and curve up into the fault plane on the footwall side. The planform distribution of faults is polygonal, with cell diameters in the range 200–1000 m. Fault intersections are commonly orthogonal or at high angles (Fig 5.11c).

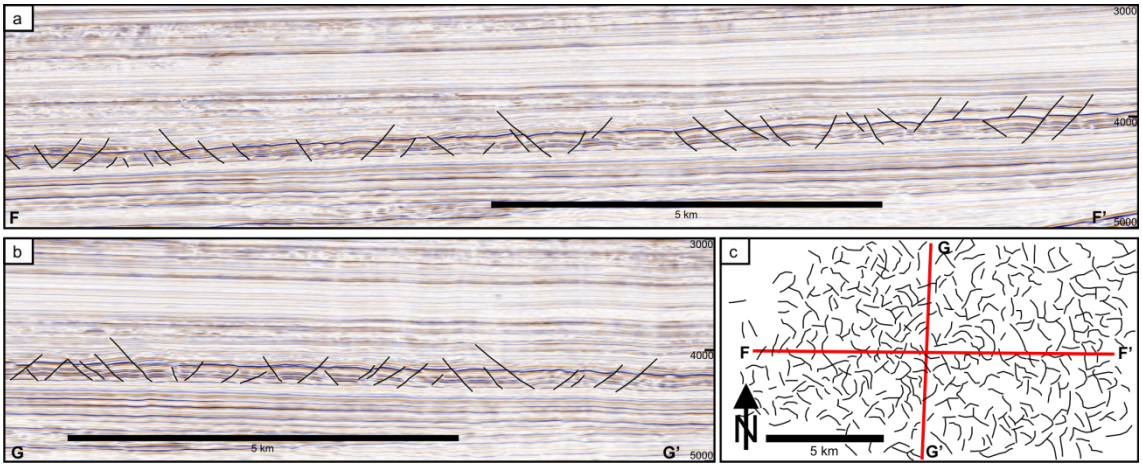

Fig. 5.11 **Representative seismic sections from a polygonally faulted area: (a) section containing the dip direction of the slope; and (b) section along the strike of the slope. (c) Fault trace map. Vertical scale in (a) and (b) is two-way time in milliseconds.**

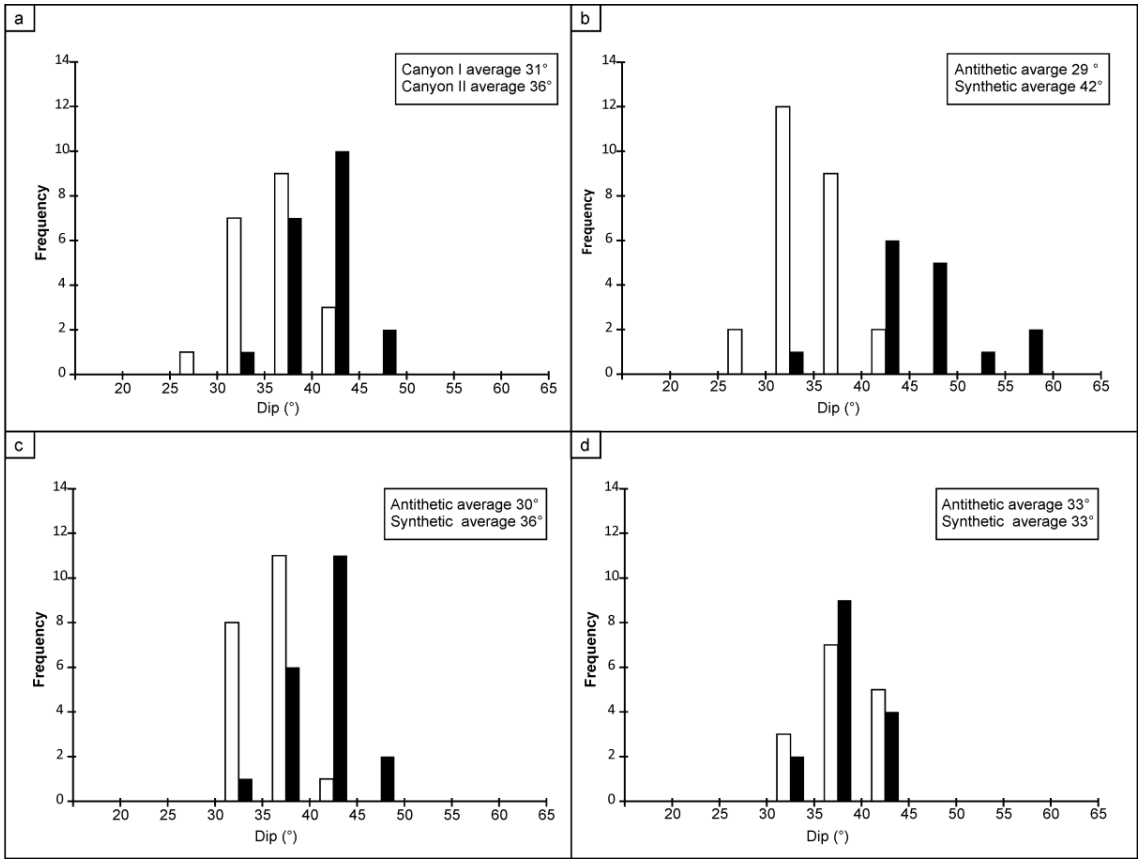

Fig. 5.12 **Histograms of fault dip for: (a) antithetic faults in canyons I (white bars) and II (black bars); (b) antithetic (white bars) and synthetic (black bars) faults in canyon III; (c) antithetic (white bars) and synthetic (black bars) polygonal faults within 10 km of the Khop Structure, with strike directions within 20° of the strike of the slope; and (d) antithetic (white bars)**

and synthetic (black bars) faults in the polygonal fault systems more than 10 km from the Khop Structure, with strike directions within 20° of the strike of the slope.

5.6.6 Layer-bound faults on the flanks of the Khop Structure

Where Unit 1 drapes the flanks of the Khop Structure (Fig. 5.5), faults show a concentric map pattern around the structure (Fig. 5.13a). The faults have a linear to curvilinear traces with lengths in the range 1–3 km. This concentric pattern is located at distances of ~5 km from the centre of the structure, where the bedding dip is ~10°. In section, the faults are antithetic relative to the slope (Fig. 5.13c) and they have very low dip angles of ~20°.

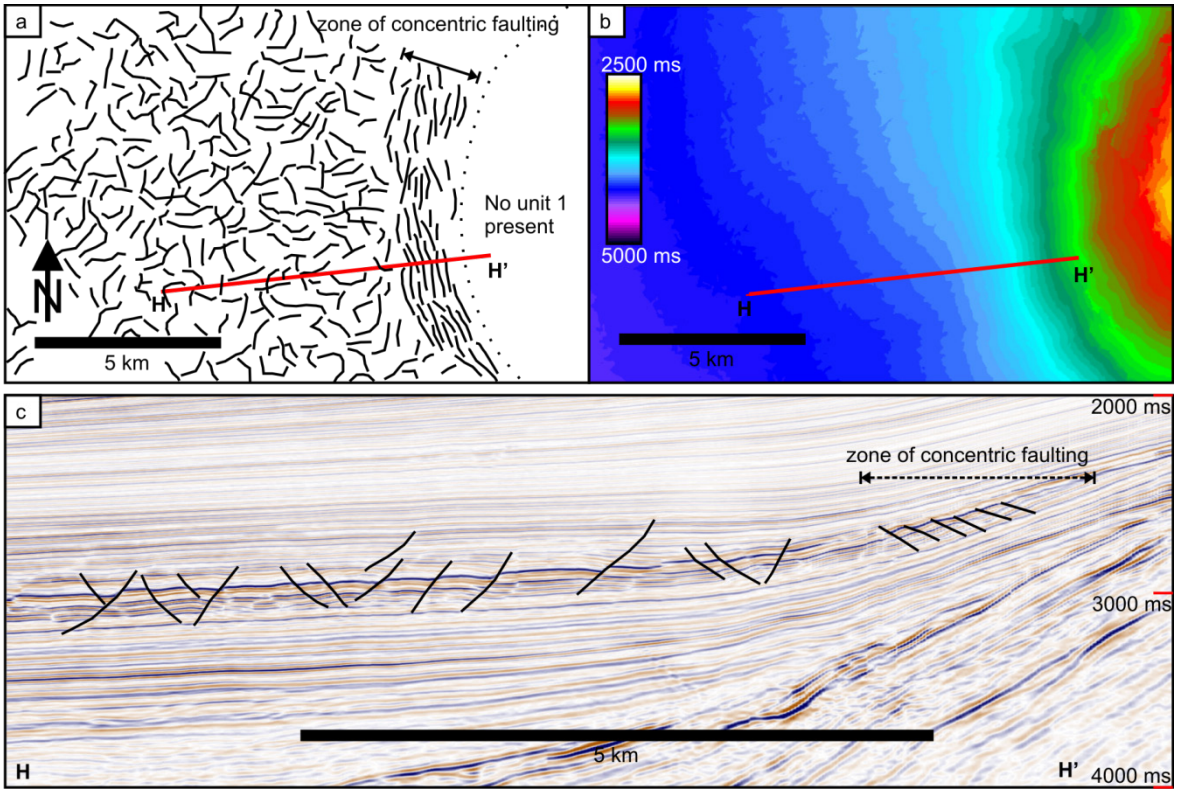

Fig. 5.13 (a) Fault trace map of Unit 1 close to and on the western flank of the Khop Structure. (b) Time structure map for Horizon A. (c) Seismic section along the profile H–H' marked in (b).

5.7 INTERPRETATION

5.7.1 Overview

The layer-bound fault systems described here show varying fault patterns and dip distributions. These variations are interpreted to relate to the 1) presence of underlying stratigraphic elements, i.e. the canyons, 2) variations associated with changes in lithology, and 3) changes in the dip of the bedding. The regional dip measured across the 3-D seismic survey is between 0.5° and 3°, generally decreasing basinwards, except on the flanks of the Khop Structure where the dip exceeds 10° in places. Where reflection events curve down into the fault plane on the hanging wall side and curve up into the fault plane on the footwall side, this is interpreted primarily as drag along the fault plane. On the hanging wall side some of this apparent curvature may be due to hanging wall growth fault migration in response to footwall collapse along the fault (e.g. Imber et al., 2003). The fault kinematics and influence of stratigraphic and structural elements and dip on the fault systems are described in the following sections.

5.7.2 Aligned arrays versus polygonal arrays

Layer-bound faults above and within canyons and on the flanks of the Khop Structure show preferential orientations and do not display the typical polygonal planform pattern of most layer-bound fault systems (e.g. Cartwright and Lonergan, 1996). The stress field can therefore not be isotropic in these areas. On the steep flanks of the Khop Structure, the bedding dip is significantly greater (~10°) than the regional dip, and the alignment of the faults is parallel to the strike of the slope. Since the Khop Structure is approximately circular, the fault pattern is concentric. This observed alignment of faults is in accordance with the previous work on the preferential alignment of layer-bound fault systems (e.g. Higgs and McClay, 1993) which has shown that stratigraphic dip of a few degrees results in the intermediate principal effective stress being orientated in the strike direction. The direction of fault dip will again be determined by the nature of the substrate. An alternative explanation for the development of concentric normal faults on the flanks of diapiric structures could be that they are extensional faults caused by intrusion, but such faults would be synthetic to the bedding dip (e.g. Stewart, 2006), not antithetic as observed here. Furthermore, sedimentary onlap (Fig. 5.5), indicates that the deposition of Unit 1 post-dates the emplacement of the Khop Structure.

Aligned faults above canyons I and II and within Canyon III are perpendicular to the axes of the canyons. Canyons are major erosional features in deepwater settings (Reading, 1998) and, as a result of their incision, the canyon infill has locally greater dip than the same beds adjacent to the canyons. This increased bedding dip again appears to be the key factor in the alignment of the faults. It is not necessarily the case that only compaction faults with strike directions in this orientation were initiated, but clearly only those faults with this orientation have developed to a seismically resolvable scale. Some of the faults above the margins of the canyons dip towards the canyon axes, while others are antithetic. We attribute their alignment to local horizontal anisotropy induced by some combination of monoclinal drape of the faulted layer across the canyon margins and differential compaction (e.g. Carver, 1968; Cosgrove, 1999; Davies *et al.,* 2009). It is difficult to arrive at a more specific interpretation because of the limited extent and inconsistent dips of these fault subsets.

5.7.3 Synthetic versus antithetic faults

The fault systems above canyons I and II contain only antithetic domino faults. In such a system, a basal detachment can be ruled out as this would favour the development of faults synthetic to the slope (e.g. Stewart and Argent, 2000). In the case of antithetic faulting, the upper parts of fault blocks are allowed to move some distance downdip, through rotation of fault blocks about their lower tips, while remaining in continuity with the upper layer which can also move downdip (Fig. 5.14a). Where Unit 1 is faulted within Canyon III, faults are both antithetic and synthetic. In this case, there must be a detachment at the base of the faulted interval, which is most likely a fine grained sediment, possibly hemi-pelagic deposited after canyon abandonment (Fig. 5.14b).

The concentric faults on the steepened flanks of the Khop Structure are all antithetic to the slope. In the case of faults being aligned by increased bedding dip, there is no detachment so faults are pinned at the lower tips, as in canyons I and II.

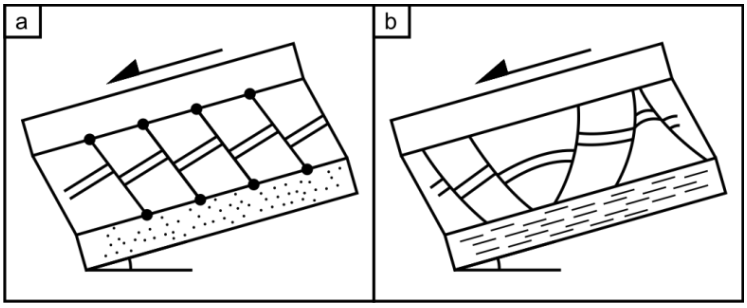

Fig. 5.14 Cartoons of (a) antithetic faults where there is no basal detachment, and (b) antithetic and synthetic faults where there is a detachment present (after Stewart and Argent, 2000).

5.7.4 Evidence for simple shear from fault dips

Histograms of fault dip show that the dips of the faults above Canyon I are smaller than those above Canyon II (Fig. 5.12a), although the bedding dip of ~2° above Canyon I is greater than that above Canyon II where it is ~1°. Furthermore, the concentric faults on the flanks of the Khop Structure have extremely low fault dips (<25°) even though the bedding dip is ~10°, i.e. the fault dips are much gentler than might be expected given that an increase in bedding dip should cause antithetic faults to dip more steeply via passive rotation. In the case of Canyon III, the dips of the synthetic faults are steeper than those of the antithetic faults (Fig. 5.12b). The same observation is true for the polygonal faults within 10 km of the concentric faults on the Khop Structure (Fig. 5.12c), but not for the polygonal faults at greater distances (Fig. 5.12d). The contrasting fault dips in Fig. 5.12b and c cannot be explained by a rotation of the principal stresses, because the effect of downslope gravity traction is to induce exactly the opposite effect on the dips of synthetic and antithetic faults. As shown in Section 3 and Fig. 5.2, where the bedding is dipping an antithetic fault would form at a steeper dip than the synthetic fault. So we infer that the dips of all these faults have been modified by something other than compaction perpendicular to the bedding since the faults first developed.

There are two possible reasons why the synthetic faults are observed to dip more steeply than the antithetic faults. Either the antithetic faults formed earlier than the synthetic faults and have subsequently undergone more compaction, or the antithetic and synthetic faults formed contemporaneously and were subsequently rotated. We can discount the first hypothesis because some antithetic faults terminate onto synthetic faults, indicating that in some cases the antithetic faults are younger. There are also examples of the opposite situation, where synthetic faults terminate onto antithetic faults, indicating that in some cases the syntithetic faults are younger. We therefore infer that synthetic and antithetic faults developed contemporaneously. Therefore we interpret the significantly gentler dips of the antithetic faults in comparison to the

synthetic faults as being the result of simple shear (e.g. Ferrill *et al.,* 1998). The interpretation of simple shear also explains why the dip of domino arrays of antithetic faults above Canyon I, above Canyon II, and on the flanks of the Khop Structure become progressively smaller as the bedding dip increases. A greater amount of simple shear due to the downslope component of gravity acting on the overburden is to be expected where the bedding dip is greater, and therefore a greater magnitude of passive rotation of the fault planes.

The amount of displacement across the faulted interval due to simple shear may be estimated in the case of the aligned faults within Canyon III, where both antithetic and synthetic faults are present. The average dip of the antithetic faults is 30°, the average dip of the synthetic faults is 40°, and the thickness of the faulted interval is about 300 m. The dip of the strata within Canyon III is 3°, as in the case of the numerical example given at the end of Section 5.3. If we also assume that the constant $K = 0.7$, so that σ'_1 is inclined at 6.6° to the vertical (Section 5.3), and that the initial dips of the fault planes were at angles of 60 ± 6.6° (i.e. symmetrically disposed with respect to the direction of σ'_1), then we can estimate the displacement due to simple shear in the downslope direction. The calculation is a lengthy exercise in trigonometry, so we present the results in graphical form in Fig. 5.15. The lateral displacement across the faulted interval, of 300 m thickness, due to simple shear is approximately 125 m, corresponding to simple shear of approximately 23°. There are uncertainties in this estimate because we do not know the value of *K*, nor the initial dips of the antithetic and synthetic faults. Nevertheless, it seems reasonable to infer that the amount of simple shear that has taken place is around 20° or more.

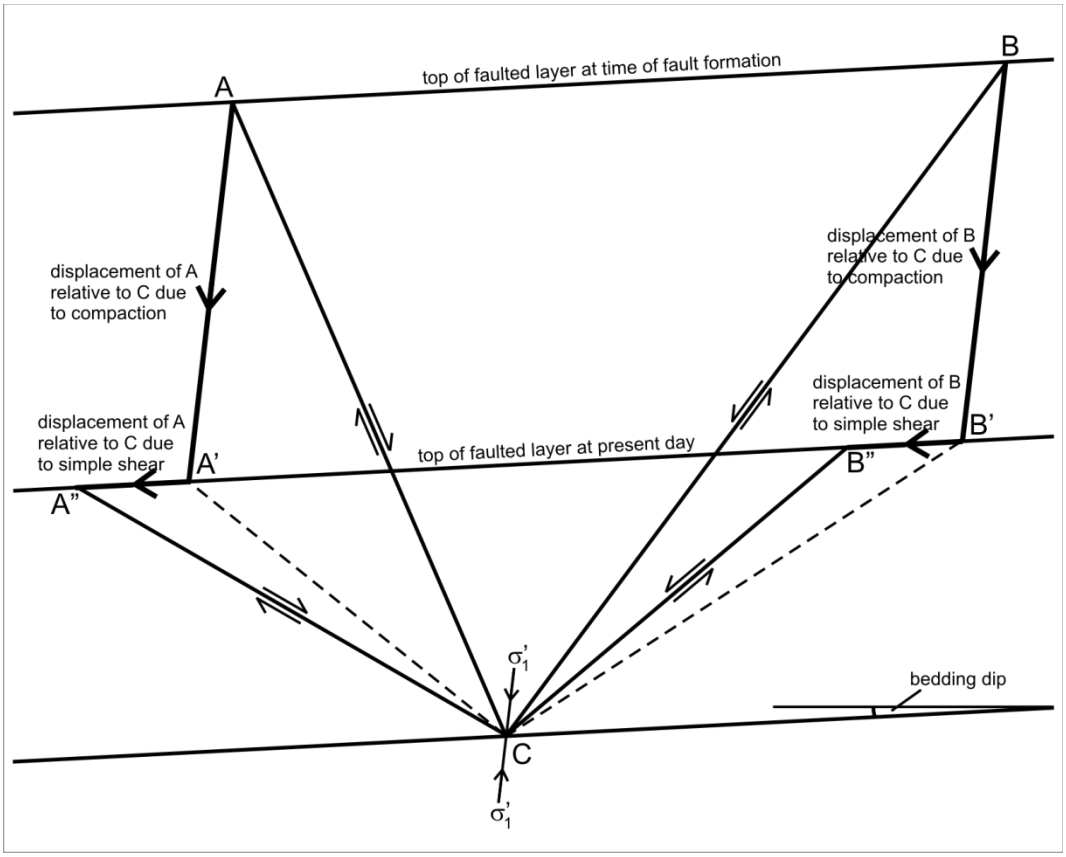

Fig. 5.15 Graphical illustration of the simple shear that has taken place across the faulted layer within Canyon III. Planar antithetic and synthetic faults are shown in vertical section, with bottom tips coincident at point C. In this diagram, the bedding plane through C is fixed. AC and BC are the original fault planes, inclined at angles of 30° to the direction of σ'_1 at the time of fault formation. A'C and B'C are the locations the fault planes would have had after compaction in the direction of σ'_1, which is parallel to lines AA' and BB', without simple shear. A"C and B"C are the fault planes at the present day: A"C dips at 30° from the horizontal, the observed average dip of antithetic faults; and B"C dips at 40°, the observed average dip of synthetic faults. Compaction is assumed to take place without any strain on bedding planes, so AB = A'B' = A"B". The lateral displacement across the faulted layer due to simple shear is estimated as the distance A"A' = B"B' ≈ 125 m, given that the present-day thickness of the faulted layer is ~300 m, so the amount of simple shear is ~23°.

5.8 DISCUSSION AND CONCLUSIONS

The relationship between the canyons and the patterns of layer-bound compaction faulting on the Mauritanian continental margin is very clear (Figs. 5.8–5.11), with abrupt changes from polygonal arrays to linear arrays, which begs the question why such abrupt variations have not

been reported before. A possible explanation lies in the relative sizes of fault spacing and canyon widths. The canyon widths on the Mauritanian continental margin are exceptionally large. On other margins, canyon widths may be less than the average fault length (e.g. Gay *et al.,* 2004), and therefore would not be expected to exert a significant influence on fault patterns. It is not possible to date the precise timing of the shearing which the layer has been subject to. But given the presence of many slides and mass transport complexes throughout the Neogene succession (Fig 5.6) it seems reasonable to infer that not only has the layer hosting the fault systems here undergone shearing, but also the overburdern above to some degree, but this cannot be quantified.

Layer-bound faults show strong alignment in regions where the bedding dip is greater than the average regional dip. Where they are aligned, the dip direction is largely controlled by the nature of the substrate. If the substrate is ductile and acts as a detachment, synthetic faulting is possible. Where the substrate is more rigid, the lower fault tips are pinned so that, kinematically, only antithetic faults can develop seismically resolvable throws. Mandl (1988) suggested that in the case of a sediment wedge, with a dipping upper surface and planar lower surface, that the orientation of σ'_1 will change with depth, rotating towards the pole to bedding near the base, favouring the development of antithetic faults towards the base. We discount this as a viable mechanism for the alignments reported here because the deformed unit is not a wedge but of uniform thickness and the entire sedimentary interval dips.

Where the bedding dip is 1–3°, the fault dips are not as would be expected considering the rotation of the principal stresses caused by the effect of downslope gravity traction. The dips of the antithetic faults dipping shelfwards are gentler than those of the synthetic faults dipping basinwards. We have interpreted the cause to be simple shear of around 20° or more, with the top of the layer hosting the polygonal faults having moved downslope by ~100 m or more relative to the bottom of the layer. This conclusion has potential implications for assessing the stability of continental margins. Systems of layer-bound compaction faults are not ubiquitous, but they are not the only possible strain markers available in seismic data for estimating simple shear. Fluid-escape features such as the pipes described by Berndt et al. (2005) are widespread across some parts of continental margins. If pipes have been active over long periods of geological time while sediments were being deposited, it may be possible to use their inclinations to estimate the amount of downslope simple shear that has taken place across different beds since their deposition.

6 THICK SLIDES DOMINATED BY REGULAR WAVELENGTH FOLDS AND THRUSTS IN BIOSILICEOUS SEDIMENT ON THE VEMA DOME OFFSHORE NORWAY

ABSTRACT

Three-dimensional seismic reflection data image four submarine slides on the flanks of the Vema Dome in the Vøring Basin. Each one covers an area of about 30 km^2, is several hundred metres thick, and is located in biosiliceous sediments. The surface topography of each slide consists of a series of regular-wavelength arcuate ridges and troughs, perpendicular to the dip of the slope, that correspond to internal fold and thrust structures. Thrusts probably propagated retrogressively based upon the observation that fold amplitudes decrease upslope. The slides lack clearly defined head-scarps, and the magnitude of shortening accommodated by the folding indicates short transport distances. The spatial location of the slides on the flanks of the Vema Dome suggests that they formed due to increased dip on the flanks of the dome cause by differential uplift during the Late Miocene (6 – 8 My). These slides have three particularly unusual characteristics in comparison to other submarine slides: a relatively low ratio of length to thickness, regular high amplitude folds, and short translational distances. We attribute these characteristics to deep detachments that resulted from the inherent ability of biosiliceous sediments to maintain a cohesive framework and resist failure during early burial (burial depths <75 m).

6.1 INTRODUCTION

The mass movement of sediments can range from turbulent flow of fluidised grains to the relatively slow movement of coherent masses with discrete internal structural deformation (e.g. Martinsen, 1994). Such movements on submarine slopes range from less than a metre thick up to hundreds of metres thick (Butler and Turner, 2010). Submarine slope failure is an important mechanism in transporting large volumes of sediment on continental margins (Kenyon, 1987) and the collection of well and seismic reflection data for oil and gas exploration has led to the identification of many such events on margins around the world (Posamentier *et al.,* 2007).

Assessing the morphology and internal structure of submarine slope failures is important for understanding the style and kinematics of deformation. The internal structure of large-scale gravitational failures such as deep-water fold and thrust belts on continental margins are well documented, but there have been fewer attempts to resolve the structure within smaller scale gravitational failures (Butler and Turner, 2010). Recent studies have identified internal structuring in mass transport deposits (Bull *et al.,* 2009; Gafeira *et al.,* 2010; Ker *et al.,* 2010), implying that the structural integrity of sediments which have undergone gravity-driven deformation at all scales may be far greater than generally assumed (Butler and Turner, 2010). Over the past two decades, there has also been significant focus on understanding the triggering mechanisms and preconditions for slope failure (e.g. Dugan and Flemings, 2000; Maslin *et al.,* 2004; Leynaud *et al.,* 2009).

Submarine slides are commonly characterised by a headwall scarp, an extensional domain, a translational domain, and a compressive domain (see Martinsen, 1994; Bull *et al.,* 2009). The term ‘slide’ describes a particular form of slope failure, where there is movement of a coherent mass of sediment bounded by distinct failure planes (Masson *et al.,* 2006). Here we describe four submarine slides occurring in Neogene biosiliceous sediments which are a poorly documented end member of slope failures, using three-dimensional (3-D) seismic reflection data from the Vema Dome, Vøring Basin, offshore Norway (Fig. 1). The failures are entirely dominated by compressional structures, with unusually low ratios of length to thickness and relatively short translation distances. Internally, they comprise blocks of folded sediment bounded by thrust faults; hence, we term them ‘blocky slides’.

The Norwegian margin has been the focus of numerous studies on slope instabilities (Elverhøi *et al.,* 1997; Gee *et al.,* 2005; Lawrence and Cartwright, 2009; Micallef *et al.,* 2009), not least because it is host to the Storegga slide, one of the largest documented submarine slope failures identified to date (e.g. Kvalstad *et al.,* 2005). An interesting aspect of the blocky slides described here is their similarity to the style of deformation recently described in siliceous

sediments that have undergone mass movement elsewhere (Volpi *et al.,* 2003; Davies and Clark, 2006; Kristoffersen *et al.,* 2007). We propose that their unusual geometries are due to the inherent characteristics of siliceous sediments which cause the detachments to be relatively deep.

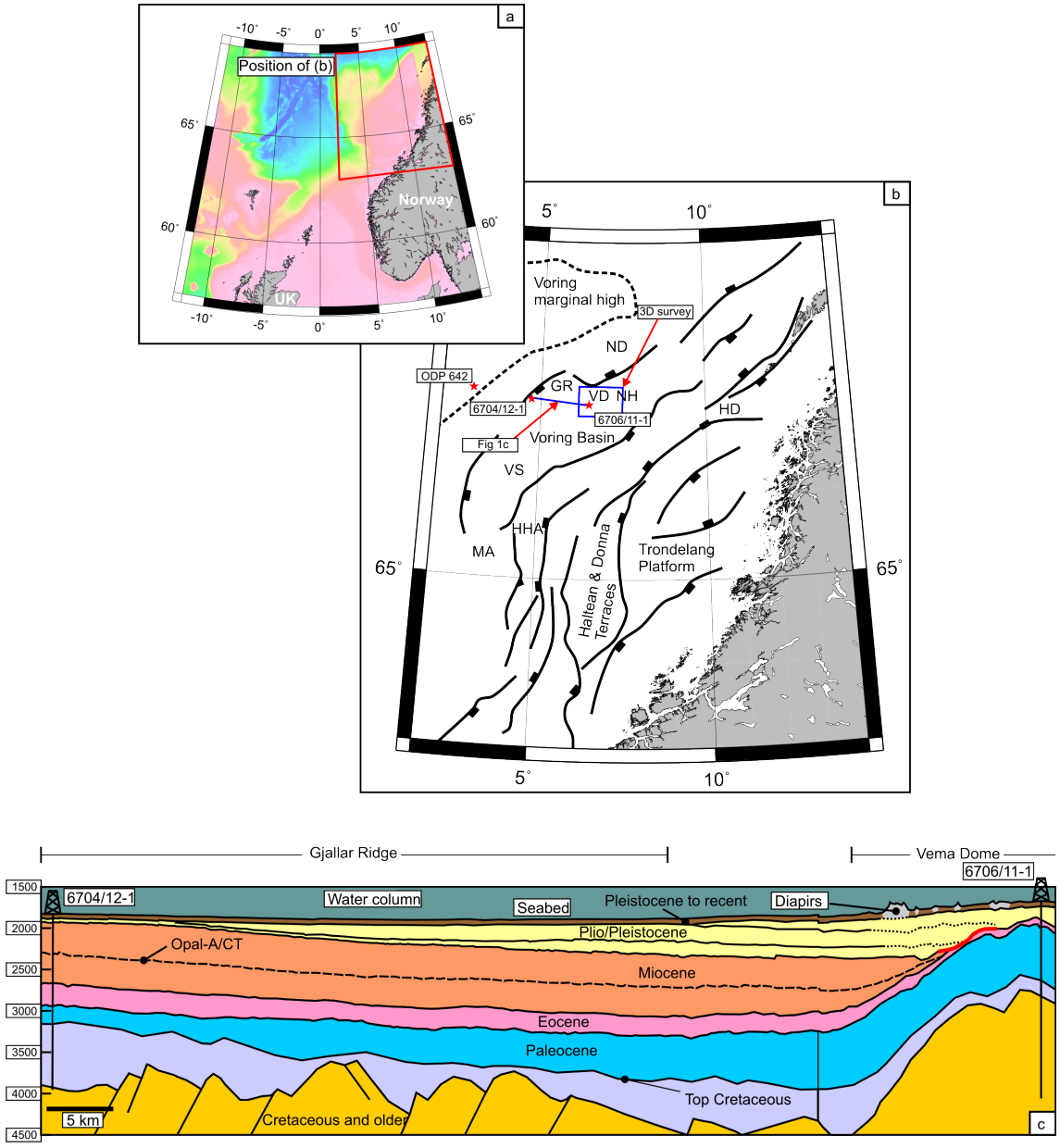

Fig. 6.1 (a) Map of the North Atlantic margin, location of part (b) outline in red, with coloured bathymetry, pink shallowest, blue deepest (from NOAA). (b) Simplified structural map of the mid-Norwegian margin (after Doré *et al.,* 2008). VD – Vema Dome, GR – Gjallar Ridge, NH – Nyk High, HHA – Helland Hansen Arch, MA - Modgunn Arch; ND - Naglfar Dome; VS – Vigrid Syncline. Blue square shows approximate outline of 3-D seismic survey. (c) Geo-seismic profile across from the Gjallar Ridge to the Vema Dome, showing the key structural elements and stratigraphic units. The bold red line indicates the relative position of the detachment surfaces of failures to the structure.

6.2 DATA AND METHODOLOGY

3-D seismic reflection data have been interpreted from a time-migrated merged volume that covers an area of ~1600 km^2. These data have a trace spacing of 25 m by 25 m and have been processed using a standard sequence of steps including post-stack time migration and multiple suppression. The dominant frequency at the depth of interest in the upper 1 s two way time (TWT) is 50 Hz, and the data have a vertical resolution of ~10 m equivalent to one quarter of the wavelength at the dominant frequency, and a horizontal resolution of ~25 m. In the seismic sections shown here a black-red reflection event represents a downward increase in acoustic impedance, and a red-black reflection event a downward decrease in acoustic impedance. Regions of poor reflectivity above the failures are mostly the result of the scattering of energy due to the shallow diapiric structures (Hovland *et al.,* 1998). Information relating to physical properties, lithology and stratigraphic ages have been constrained using three wells; 6704/12-1, 6706/11-1, ODP 642 (Fig. 6.1). Apart from their intrinsic importance as slides, these particular failures cause problems for prestack depth migration due to their complex internal structure combined with the anomalously low velocity of the sediments.

6.3 GEOLOGICAL SETTING

The Vema Dome is located on the western margin of the Vøring Basin, 350 km offshore Norway (Fig. 6.1). The Vema Dome is a structural high which sits between the Gjallar Ridge and the Nyk High. The Nyk High and Gjallar Ridge are complexes of tilted fault blocks (Fig. 6.1c) that trend parallel to each other, with the Helland Hansen Arch to the south and the Naglfar Dome and Någrind Syncline towards the north and north-east. The Mid-Norway continental margin has been subject to a series of extensional phases from the Devonian through to the early Eocene, with the rift axis migrating from east to west (Brekke, 2000; Doré *et al.,* 1999). The Vema Dome area was one of three significant depocentres prior to the Cenozoic, the others being the Træna Basin and Någrind Syncline, which formed as a result of activity on normal faults associated with the Nyk High (Gomez *et al.,* 2004).

The tectonic evolution of the outer Vøring Basin is complex (Ren *et al.,* 2003; Moy, 2010) but its early development can be divided into two main stages. There was a Late Cretaceous rift phase (85 to 65 Ma) when extension was predominantly accommodated by upper crustal faulting. It was followed in the Palaeocene (65 to 55 Ma) by depth-dependent lithospheric extension (Kusznir *et al.,* 2005), synchronous with normal fault reactivation, regional uplift and erosion of the structural highs. The rifting culminated in continental break-

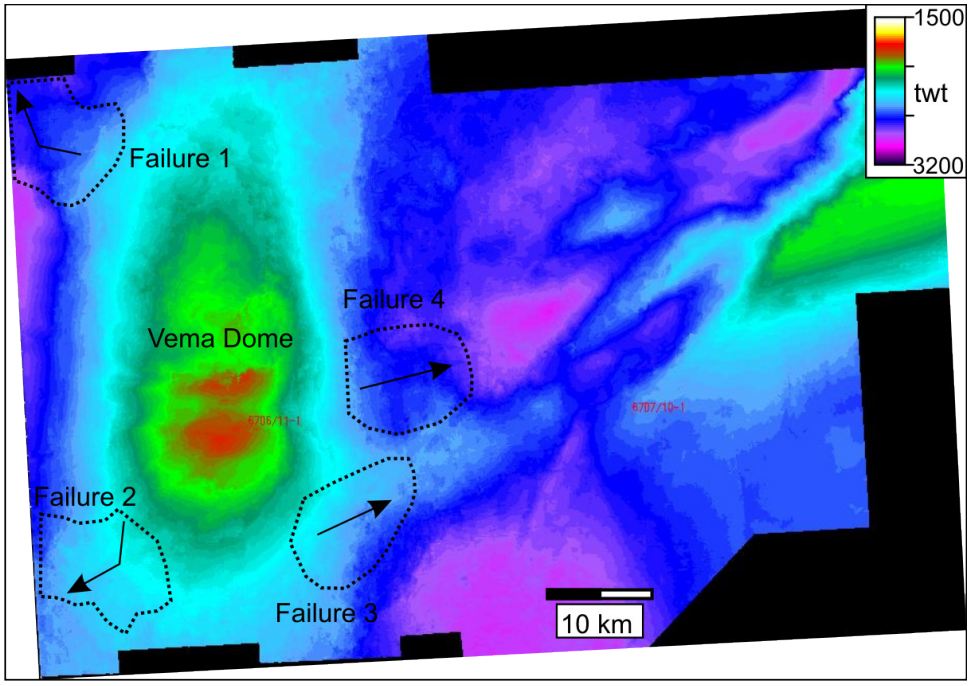

Fig. 6.2 Time-structure map of the top Oligocene showing the Vema Dome and the approximate outlines of the submarine failures described in the text.

up close to the Palaeocene–Eocene transition (~55 Ma). Rifting was associated with the widespread deposition of volcanic units and intrusion of sills and dykes, over a period of 1 Myr (Planke *et al.,* 2005). The Vema Dome was uplifted during the Oligo-Miocene and significantly influenced the latest stage of basin evolution (Doré *et al.,* 2008). Several mechanisms have been proposed for the formation of the Vema Dome and other domal structures on the Atlantic margin (Lundin and Doré, 2002; Mosar *et al.,* 2002; Mjelde *et al.,* 2003). One proposed mechanism is that they developed preferentially where the basement was hotter, weaker and therefore more prone to shearing at the relatively low stress levels, with the primary agent generating the force being development of the Iceland Insular Margin (Doré *et al.,* 2008).

The interval which hosts the failures lies in the approximate depth range 200 to 800 m below the present day seafloor, in the Pliocene to Miocene, the Kai Formation (Fig. 6.1). During the late Miocene to early Pliocene, sedimentation was dominated by hemipelagic sedimentation (Rise *et al.,* 2005) (also see Chapter 3, Fig 3.8). Since ~2.7 Ma, large quantities of glacially-derived material were transported westwards from the Norwegian mainland areas and inner shelf and deposited mainly as prograding sediment wedges into the basins offshore Mid Norway (Rise *et al.,* 2005).

6.4 SEISMIC OBSERVATIONS

6.4.1 GENERAL CHARACTERISTICS OF SUCCESSION AND STRUCTURES

The present-day water depth is 1100 – 1600 m, generally deepening northwards. The typically planer-parallel reflections that characterise the hemipelagic sediments of the Neogene succession observed across much of the Vøring Basin (e.g. Rise *et al.,* 2005; e.g. Laberg *et al.,* 2005; Ireland *et al.,* 2010) are highly disturbed locally above and surrounding the Vema Dome (Fig. 6.1c and Fig. 6.3). Complexity arises from the presence of kilometre-scale subsurface sediment remobilization features near the seabed (Hovland *et al.,* 1998; Hjelstuen *et al.,* 1997) (Fig. 3). We have examined the 3-D geometry and seismic characteristics of four units which exhibit characteristics of submarine failures on the flanks of the Vema Dome, within the Miocene to Pliocene sediments. In general, the failures comprise a ridge-trough topography at their upper surface. This is the key characteristic that distinguish the failures from the shallower, near–seabed, diapiric structures above the Vema Dome (Fig. 6.3) (Hovland *et al.,* 1998).

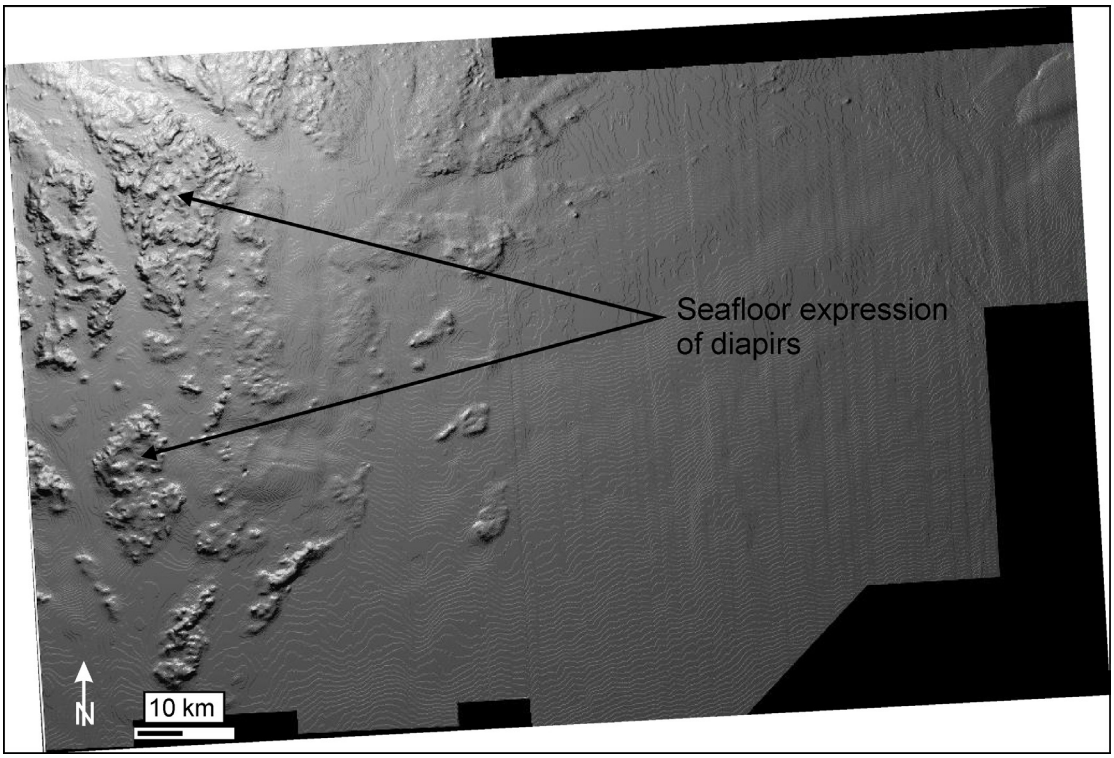

Fig. 6.3 Shaded relief map of the present day seafloor lit from the NW, in which the irregular mounded diapirs can be identified.

6.4.2 RIDGE - TROUGH STRUCTURES

The ridge–trough topography of the upper surface of each failure always has a negative reflection coefficient. Overlying planar reflections commonly terminate against the flanks of the folded upper surface (onlap). The upper surface typically has a regular wavelength of folding, ~400 m. The internal seismic character of the failures can be divided into two units, an upper high-to-medium reflectivity portion with some coherent reflections, and a lower poor reflectivity section with chaotic to semi-coherent reflection events (Fig 6.4a). The base of the failed unit is marked by a very strong positive reflection coefficient. It is generally non-planar and irregular, with evidence of truncation of surrounding reflections (Fig. 6.4). In the interpretations here, the top of each slide is refered to as Horizon A, an internal reflection as Horizon B and the base of the slide as Horizon C.

6.4.2.1 Slide 1

Slide 1 is located on the north-western edge of the Vema Dome (Fig. 6.2). Horizon A (Fig. 6.4) is the upper surface and has a complex 3-D topography, consisting of an approximately radial pattern of ridges and troughs rotating from an approximately N-S trend to E-W (Fig. 6.4c). The ridges and troughs themselves are generally asymmetrical with the downslope limb steeper than the upslope limb, and have wavelengths of ~400 m. Towards the edge of these data, the downslope limbs become poorly imaged (Fig. 6.4a). The maximum ridge height, from the base of trough (T – Fig. 6.4a) to crest of ridge (R – Fig. 6.4a) is 80 ms (~144 m assuming 1800 m s^{-1} interval velocity, a typical value from the three wells). Reflections terminate against the steeply dipping flanks of the ridges and troughs (Fig. 4a). In a section parallel to the ridges, the unit is thickest close to the margins, and has influenced the seafloor topography through to the present day (Fig. 6.4b). The unit consists of two clearly distinguishable seismic packages which are both relatively low reflectivity and seismically transparent, separated by Horizon B. Within these units, seismic reflections are not continuous: they are broken and disturbed. Horizon B itself is a discontinuous reflection, and has a positive reflection coefficient. It can be seen to approximately mirror the topography of Horizon A, the upper surface, in some places (Fig. 6.4). Horizon C demarcates a change from broken and disturbed seismic reflections to plane-parallel reflections below. It is irregular and truncates seismic reflections below it (Fig. 6.4). The difference in two-way time between Horizons A and C is 150 to 500 ms (~180 to 700 m thick). The mapped areal extent of the structure is 32 km^2, and its volume is about 16 km^3.

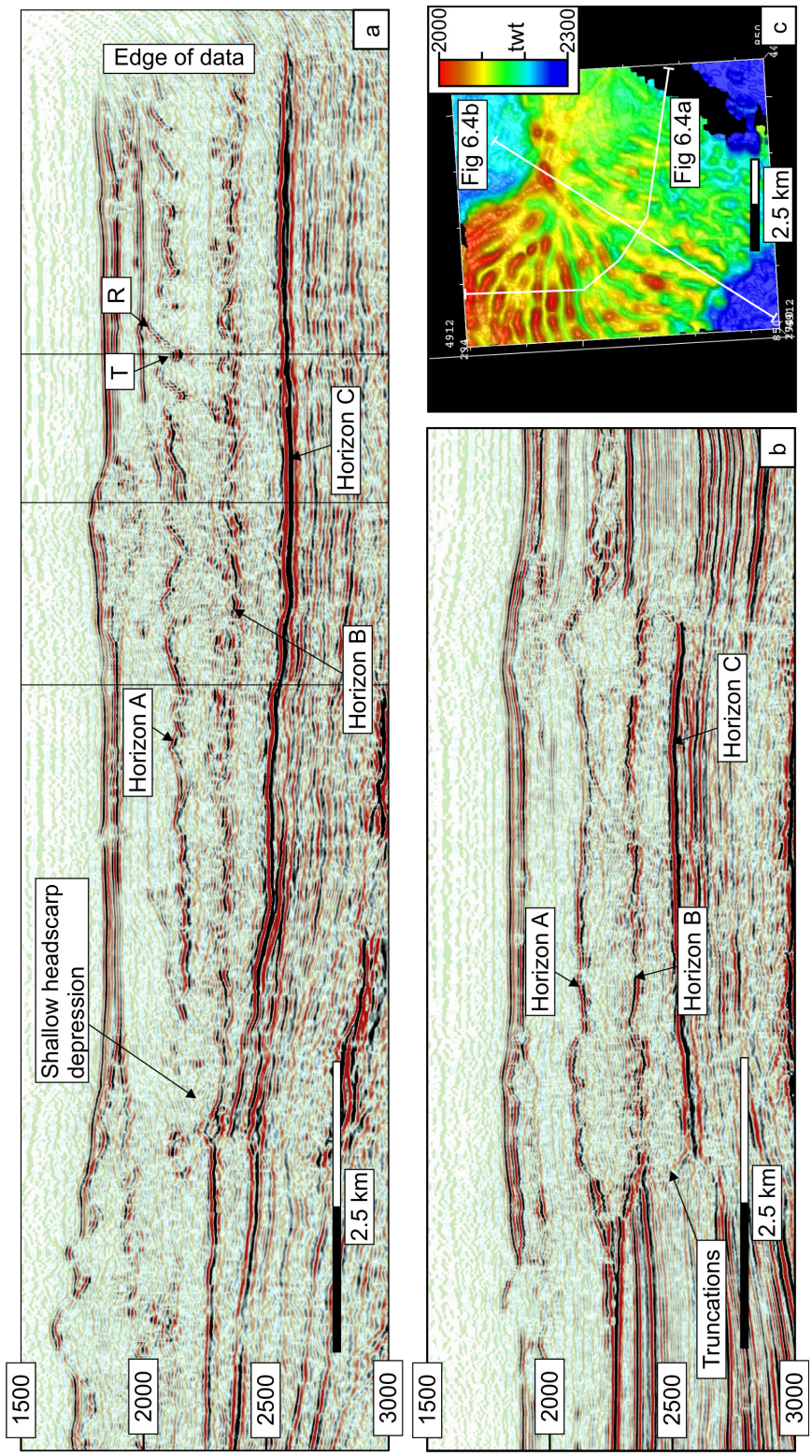

Fig. 6.4 (a) Seismic section along dip of failure 1. (b) Seismic section perpendicular to failure direction. (c) Time-structure map of the upper surface of failure 1.

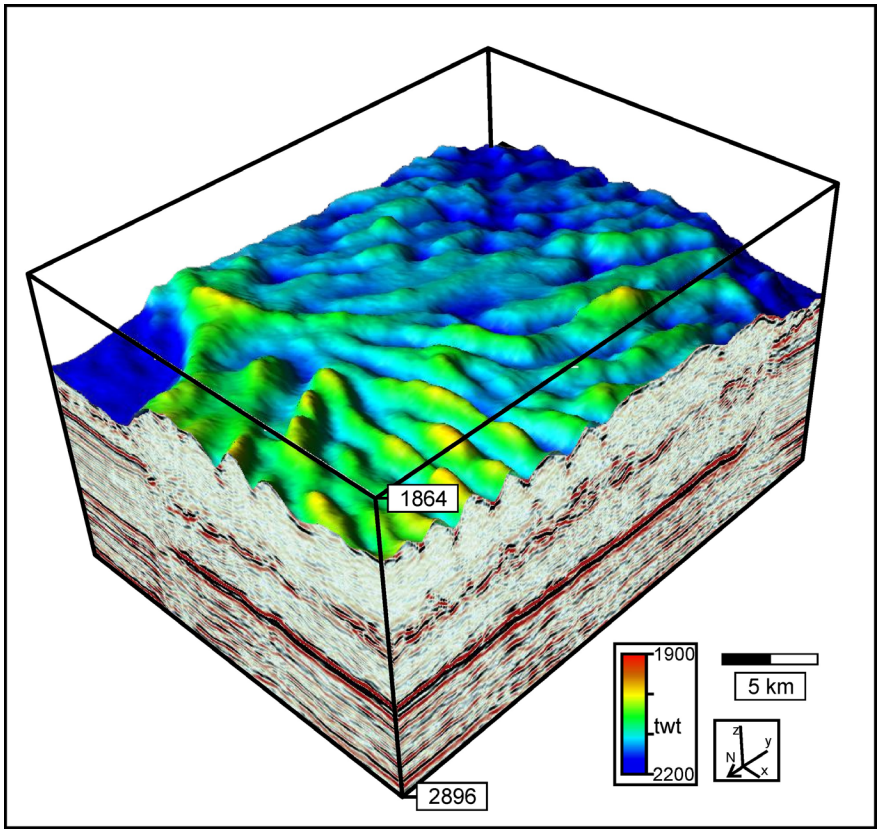

Fig. 6.5 . 3-D visualization of failure 1, showing the ridge–trough topography of the upper surface, interpreted as thrust propagation folds.

6.4.2.2 Slide 2

Slide 2 is located on the south western edge of the Vema Dome. Horizon D marks the top of the failed unit (Fig. 6.6a). The topography of this upper surface has a less clearly defined ridge–trough topography. The topography can be seen to consist of a series of small ridges, troughs and mounds, and a single large elongate ridge which is 5 km long and 80 ms (100 m) high trending NNW–SSE (Fig. 6.6c). Below Horizon A, there is a region of low seismic reflectivity with broken and disturbed seismic reflections separated by Horizon B. Horizon B has a positive reflection coefficient and is often broken and disturbed. Horizon C, which is around 200 ms below Horizon B, has a negative reflection coefficient. It is generally neither broken nor offset, but does exhibit some shallow synclinal shapes of limited lateral extent. In some places it truncates surrounding seismic reflections (Fig. 6.6). The two-way time interval between Horizons D and F is ~400 ms, corresponding to a thickness of ~500 m, and generally increases in the downslope direction. Below Horizon C, seismic reflection events are plane-parallel. The mapped extent of the unit covers an area of 43 km^2, and it has a volume of 20 km^3. The single large elongate ridge on the upper surface coincides with a significant step down to the west of

Horizon C, which is at the upper tip of a reactivated deeper Mesozoic fault (labelled F on Fig. 6.6a).

6.4.2.3 Slide 3

Slide 3 is located on the south-east flank of the Vema Dome (Fig. 6.2) and has an upper surface, Horizon A, which is characterised by a ridge – trough topography (Fig. 6.7a). The ridges are generally asymmetrical with widths around 400 m and a maximum ridge height, from the base of trough (T – Fig. 6.7) to crest of ridge (R – Fig. 6.7), of 80 ms (~100 m). In map view the ridges can be seen to be arcuate and elongate (Fig. 6.7c), convex in the downslope direction and 0.5 – 5 km in length. The unit covers an area of 25 km^2, elongated in the NE-SW directions, and has a volume of 12 km^3. The unit between Horizons G and I can broadly be divided into an upper high reflectivity section and a lower poorly reflective section, separated by Horizon B. Below Horizon C, which has a positive reflection coefficient, reflections are undisturbed and plane-parallel. Downslope, at the north-eastern edge of the arcuate ridges, there is a frontal boundary between deformed and undeformed seismic reflections (Fig. 6.7), marked by a dipping reflection. Steeply dipping reflections, with a broadly listric geometry,that do not parallel the stratigraphy, can be observed behind this frontal reflection with dips between 30 and 40° (Fig. 6.7d). The upper unit of higher reflectivity can be seen to continue beyond the sharp boundary, but with a much lower relief (~50 m), and instead of prominent ridges at its upper surface, there are smaller individual mounds (Fig. 6.7c). The thickness of the unit between Horizons G and I generally increases downdip from 100 to 400 ms (~180 to 720 m). Horizon C is a continuous event, but has an irregular topography and in some places broadly mirrors Horizon A.

6.4.2.4 Slide 4

Slide 4 is located on the eastern edge of the Vema Dome (Fig. 6.2). The ridge – trough topography of the upper surface, Horizon A, forms a semi-circular region of arcuate ridges convex in the down-slope direction (Fig. 6.8). The ridges are asymmetrical, with widths around 400 m, and are 0.5 – 3 km long. Ridges have a maximum height of 80 ms (100 m) from the base of an adjacent trough to the crest of the ridge. A lower boundary which demarcates the return to plane-parallel reflections is difficult to identify with confidence. It is tentatively placed where Horizon C is marked (Fig. 6.8).

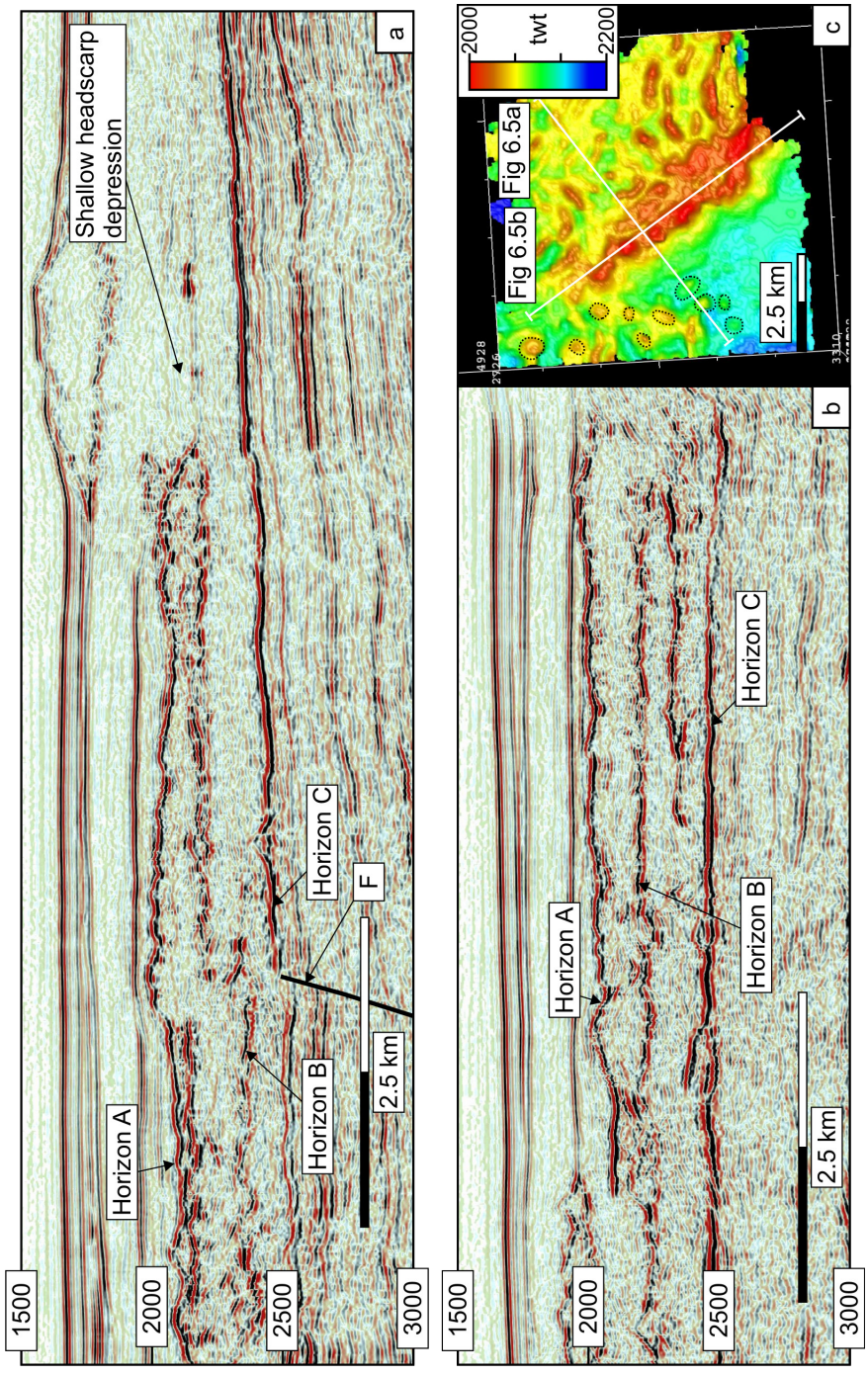

Fig. 6.6 (a) Seismic section along dip of failure 2. (b) Seismic section perpendicular to failure direction. (c) Time-structure map of the upper surface of failure 2. Dashed circles highlight individual mounds ahead of frontal boundary – see text for description.

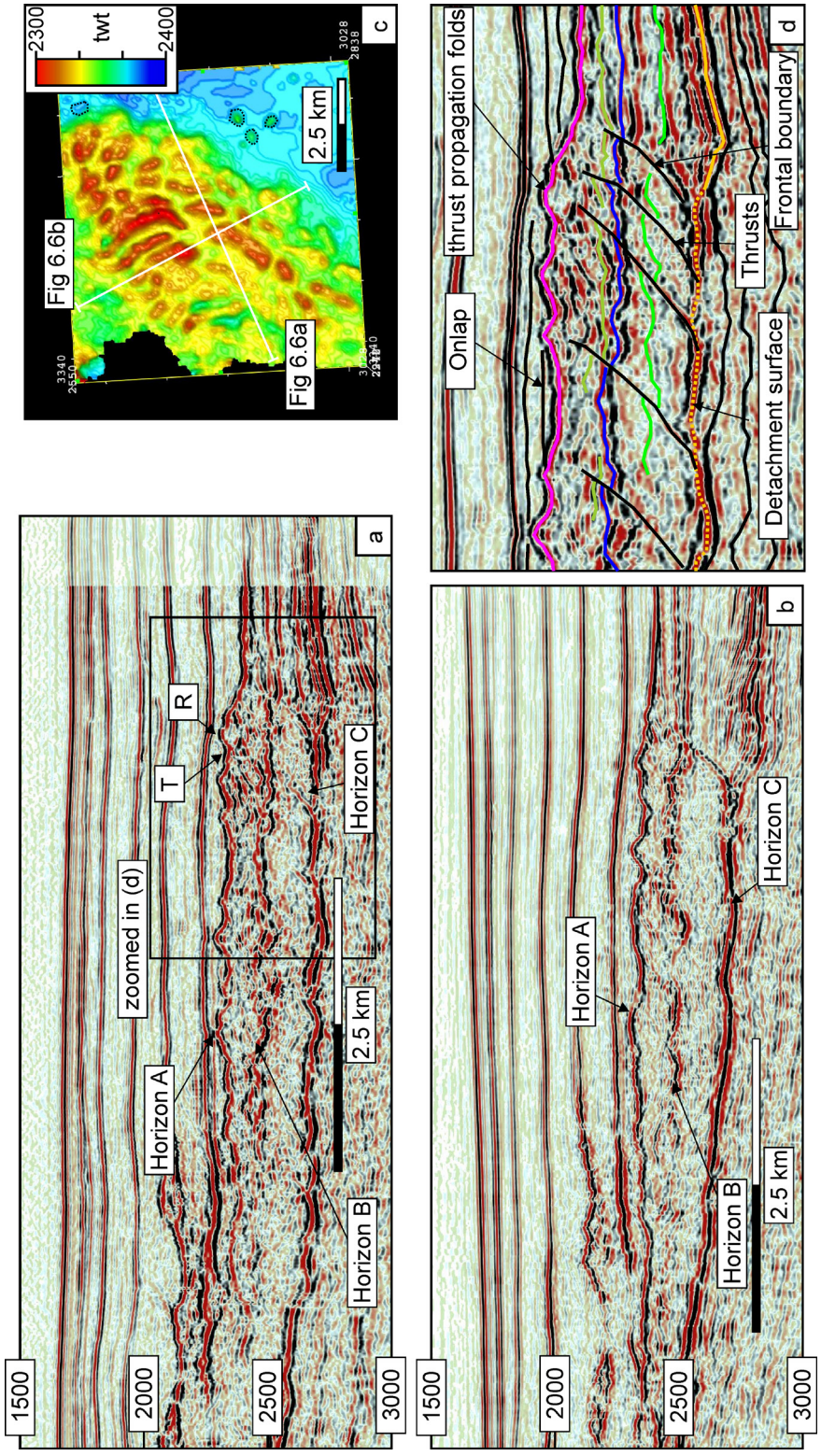

Fig. 6.7 (a) Seismic section along dip of failure 3. (b) Seismic section perpendicular to failure direction. (c) time-structure of the upper surface of failure 3. Dashed circles highlight individual mounds ahead of frontal boundary – see text for description. (d)

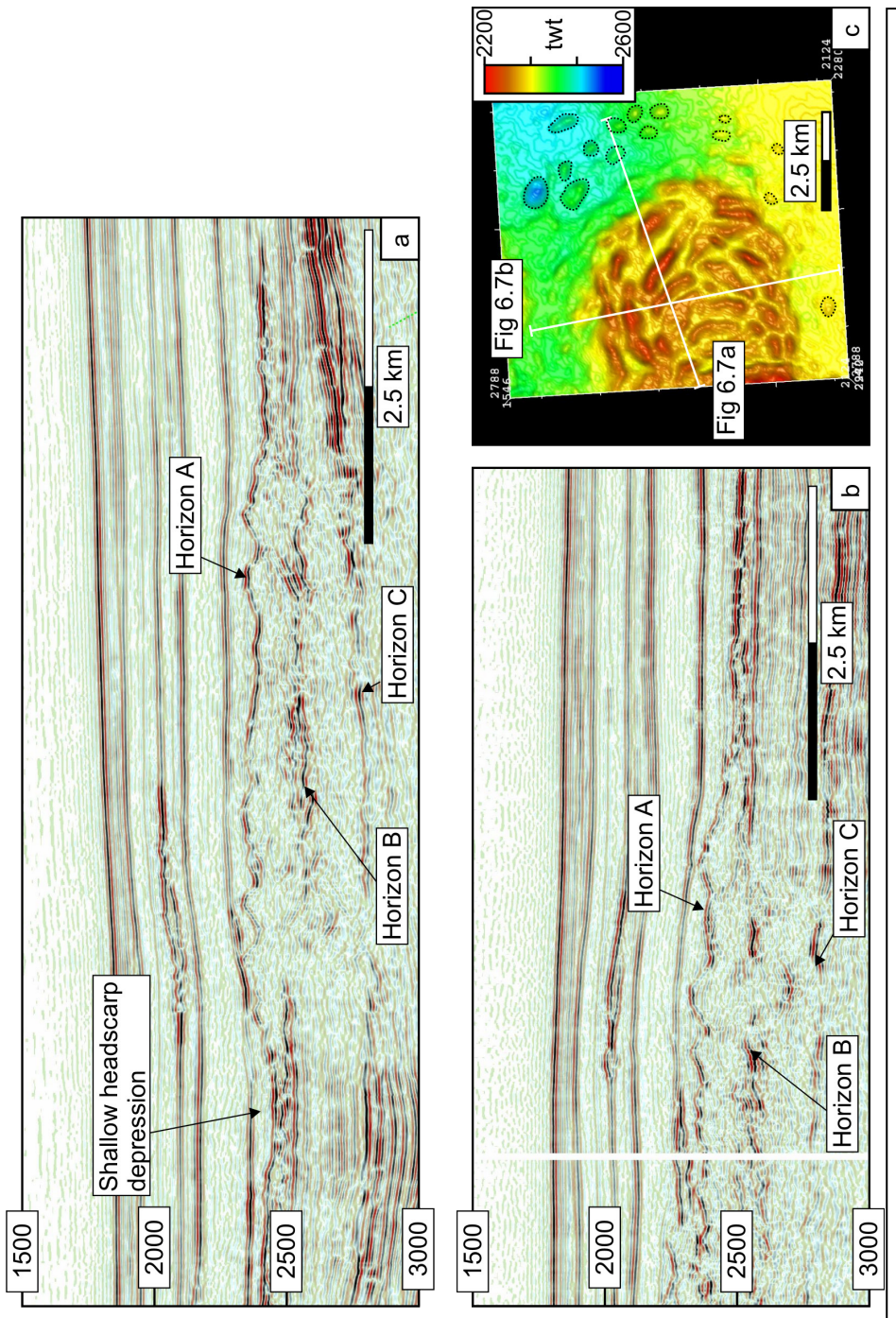

Fig. 6.8 (a) Seismic section along dip of failure 4. (b) Seismic section perpendicular to failure direction. (c) Time-structure of the upper surface of failure 4. Dashed circles highlight individual mounds ahead of frontal boundary – see text for description.

The unit between Horizons A and C can again be divided, by Horizon B, into upper and lower units. The two-way time between Horizons A and C is between 200 and 400 ms. The slide covers an area of ~30 km^2, with a volume of ~15 km^3. Downdip, at the eastern edge of the arcuate ridges, there is a frontal boundary between deformed and undeformed seismic reflections (Fig. 6.8), marked by a dipping reflection. The upper unit between Horizons A and B can be seen to continue ahead of the sharp boundary, but with a much lower relief (~50 m), and instead of prominent ridges at its upper surface, there are smaller individual mounds (Fig. 6.8).

	Area (km^2)	Volume (km^3)	Maximum thickness (m)	Length (km)	Ratio length:max thickness
Slide 1	32	16	700	9.3	13.3
Slide 2	43	20	500	8.4	16.8
Slide 3	25	12	720	6.6	9.2
Slide 4	30	15	720	6.9	9.6

Table 6.1 Comparison of the dimensions of the four slides from the Vema Dome.

6.4.3 LITHOLOGY, SEISMIC CORRELATION AND PHYSICAL PROPERTIES

Here we give an overview of the sediment composition, physical properties and ages of the sedimentary section which has failed around the Vema Dome. Lithological and stratigraphic information about the Neogene succession which host the slides has been taken from Laberg et al. (2005), using regional 2D seismic sections and the correlations from the Gjallar Ridge made by Ireland et al. (in press) (Chapter 3). In addition, limited data available from the shallow part of well 6706/7-1 on the Vema Dome are incorporated (Fig. 6.1).

The uppermost sediments in the region can be correlated to the Naust Formation, of late Pliocene to Pleistocene age (Fig. 6.1). These sediments mainly comprise glacial sediments. Above the Vema Dome the section is disturbed by kilometre-scale subsurface sediment remobilisation features (Fig. 6.1c and Fig. 6.3). The section was penetrated by DSDP 339 and

340, and allocthonous blocks of Eocene and Miocene oozes were identified within the depth range of the Naust Formation, indicating mobilised blocks (Talwani *et al.,* 1976)

Below the Naust Formation lie the Miocene to Pliocene sediments of the Kai Formation (Fig. 6.1a). These are siliceous sediments of very low density (e.g. Ireland *et al.,* in press, Chapter 3). The Kai Formation is absent immediately above the crest of the Vema Dome in 6706/11-1 (Fig. 6.1c) (see Appendix C). The sediments of the Kai Formation on the outer edge of the Vøring Basin (Gjallar Ridge, Nyk High, Vema Dome region in Fig. 6.1b) consist of nannofossil oozes, diatom oozes, siliceous oozes, siliceous muds and mudstones (Eldholm and Thiede, 1987). The exact boundary between the Naust Formation and the Kai Formation on the Vema Dome is extremely hard to identify, hence in Fig. 6.1c units are defined by approximate ages.

At the neighbouring Gjallar Ridge, seismic and well data indicate the transformation of opal-A to opal-CT, in the Kai Formation and subsequently opal-CT to quartz in the Brygge Formation (Ireland *et al.,* 2010, Chapter 3). The opal-A to opal-CT transformation boundary can be traced on seismic sections onto the flanks of the Vema Dome, but terminates well below the slides around the dome (Fig. 6.1c). During the Mid-Miocene there was widespread coeval uplift and erosion in the deepwater of the Vøring Basin (Scheck-Wenderoth *et al.,* 2007) which probably resulted in erosion of the some of the Kai Formation and the underlying Brygge Formation. The Eocene to Oligocene sediments of the Brygge Formation comprise diatomaceous sediments and muds in varying proportions. In general, the Brygge Formation has a larger percentage of mud grains than the overlying Kai Formation. In both the Kai and Brygge formations diatom oozes at ODP Site 642 have a biogenic silica content of up to 75% (Eldholm *et al.,* 1987b).

The Cenozoic diatomaceous sediments have a significant component of biogenic silica grains, and such sediments have been shown to not follow typical compaction trends (e.g. Compton, 1991). Petrophysical data reveal that both the Kai and Brygge formations are characterised by low sonic velocity values, in the range 1500 – 1800 m s^{-1}, consistent with the low saturated bulk densities measured at ODP 642 and the seismic interval velocities calculated from the checkshot survey of 6704/12-1 (Ireland *et al.,* in press, Chapter 3). The Kai Formation is characterised by low densities around 1.4 g cm^{-3}, with an increase below the opal-A to opal-CT transformation boundary of about 0.2 g cm^{-3} as a result of the silica phase transformations (Ireland *et al.,* 2010). Sediments may be underconsolidated, which suggests an increase in pore pressure with increasing depth (Eldholm *et al.,* 1987b). Shear strengths measured for the Neogene succession at ODP 642 vary between 4.5 and 203 kPa, depending on composition, depth and other factors unidentifiable from the available ODP data (Fig. 6.9). In addition, data

from ODP 112 are shown to compare the strength of sediments with a significant biogenic silica component in the upper 100 m.

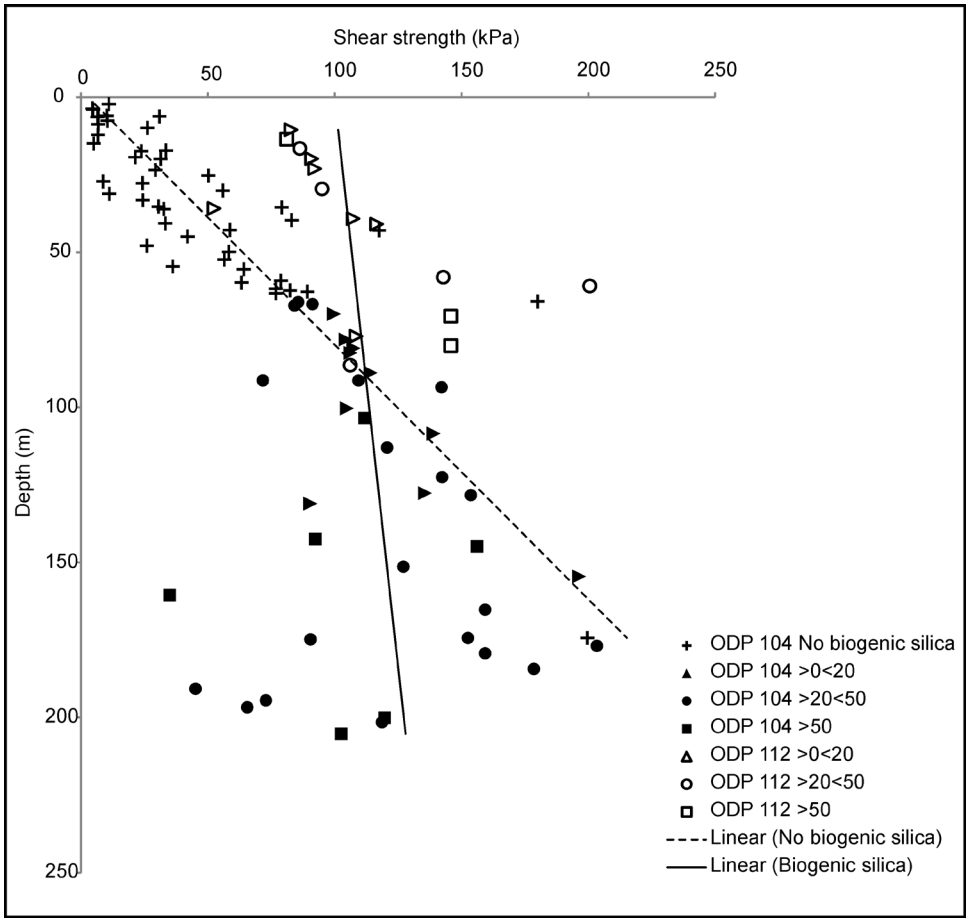

Fig. 6.9 Shear strength vs depth scatter plot for ODP 104 site 642 and ODP 112 site 358. Shear strength was measured by torvane (see Pittenger *et al.*, 1989 for details)

6.5 INTERPRETATION

The blocky slides described here exhibit a number of common characteristics. Key observations are: (a) a ridge–trough topography at the upper surface, (b) a shallow head scarp region, (c) a sharp downslope frontal boundary between disturbed seismic reflections and adjacent plane-parallel reflections, (d) seismic reflections onlapping the upper surface, (e) a sharp basal contact, and (f) the presence of individual blocks ahead of the frontal boundary. The Vema Dome structure has resulted in increased stratal dips of the Miocene to Pliocene section, up to 10°. The slides and the style of deformation are described in the following sections.

The ridge–trough topography of the upper surface together with the listric reflections that cross-cut stratigraphy which have reverse offsets are interpreted as a series of thrust faults

and thrust propagation folds (Fig. 6.10). The varying geometry of the ridges (elongate, semi-circular, radial) are interpreted as due to variations in transport directions and shear at the lateral margins. The onlap observed at the upper surface of all the slides indicates that the surfaces of the slides were exposed at the seabed. The folding of the upper surface accommodates horizontal shortening above the upper tips of thrusts, with each ridge representing the propagation of a single thrust (cf. Twiss and Moores, 2007). The thickness of the low reflectivity unit which extends from the upper surfaces (Horizon A in Fig. 6.4, 6.6, 6.7 and 6.8) to the lower surfaces (Horizon C in Fig. 6.4, 6.6, 6.7 and 6.8) generally increases with distance downslope, which is consistent with slide development as a result of gravity-driven deformation where the front of the slide is confined. The sharp frontal boundary clearly indicates frontal confinement (e.g. Frey-Martínez *et al.,* 2006). Thickening downslope rules out gravity spreading as that generally results in thinning downslope (Schultz-Ela, 2001). Slides are not restricted to being either frontally confined or emergent. Ahead of the frontal boundary between deformed and undeformed sediments, the upper surface (Horizon A in Fig. 6.7 and 6.8) continues downslope, but comprises a thinner unit. We interpret this thinner unit as small (<50 m) blocks or rafts of sediment transported by gliding or hydroplaning, known as frontally emergent behaviour (cf. Frey-Martínez *et al.,* 2006). The location of the frontal deformation boundary was probably controlled by a reduced dip of the detachment surface, reducing the shear stress acting on that surface due to gravity. We infer that the formation of thrusts was retrogressive based on the updip decrease in amplitude of thrust propagation folds (Fig. 6.4).

Frontally confined failures are more likely to occur if a translation occurs over a deeper detachment surface relative to its length since this results in a lower centre of gravity relative to the seabed (e.g. Mandl and Crans, 1981) and therefore greater energy would be required for the slide to emerge onto the seabed at the frontal ramp (Frey-Martínez *et al.,* 2006). Some of the poor reflectivity in the parts of the slides beyond the frontal ramp may be attributed to steep bedding dips and metre-scale deformation below seismic resolution. In sections parallel to the strike of the slope, sharp lateral boundaries between undeformed and deformed sediments are locations of strong shear deformation, and the arcuate shape of the ridges (Fig 6.7 and Fig 6.8) indicates frictional resistance to the movement of the slides at the margins. We suggest that the characteristics described favour interpretation as gravity driven deformation structure, as opposed to other processes that have been known to result in similar geometry structures, such as subsurface sediment mobilization, buckle folding of a viscous layer, or tectonic compression.

The distinct change in seismic character between the upper and lower sections of the slides can be related to the seismic character of the section adjacent to the slides. The undeformed sedimentary succession adjacent to the slides consists of an upper unit with three

prominent seismic reflections of high amplitude overlying a unit of lower reflectivity. Ignoring thickness changes due to folding and thrust development within the slides, the same reflection events can be tracked from the undeformed section into the slides.

At the updip end of the slides the headwall scarp region is relatively shallow and lacks any clear evidence of extensional structures. The absence of indicators for extension has been noted previously for slides in siliceous sediments (Davies and Clark, 2006), and was attributed to relatively short translation distances. That interpretation is consistent with the characteristics of the blocky slides described here. The shallow head-scarp region is particularly unusual for submarine slides. Four possible hypotheses have previously been made to explain such structures: detachment and movement as a consequence of bedding plane sliding of the entire stratigraphic section surrounding the slide (e.g Mosher *et al.,* 2004; Richardson *et al.,* in review); extensional structures are obscured by poor seismic imaging; a low-angle detachment that is covered by subsequent sedimentation and thus not possible to distinguishable the head-scarp from the overlying sediments; or loading from the prograding or overlying sediments, resulting in gravity spreading, so no detachment (e.g. Schultz-Ela, 2001).

It is very likely that some extensional structures do exist in the head-scarp region but are obscured, but in addition we also favour the hypothesis of the detachment and movement of entire stratigraphic section because: 1) gravity spreading is ruled out due to downslope thickening; 2) the approximate coincidence of the detachment surface and the base of the sediment wedge (Fig. 6.1). The horizontal shortening which has taken place is estimated by comparing the length of the folded upper surface to the length of a planar stratigraphic reflection below the slide. The difference in length is ~300 m, which can be taken as a first order approximation of the shortening which has taken place, amounting to ~5% shortening.

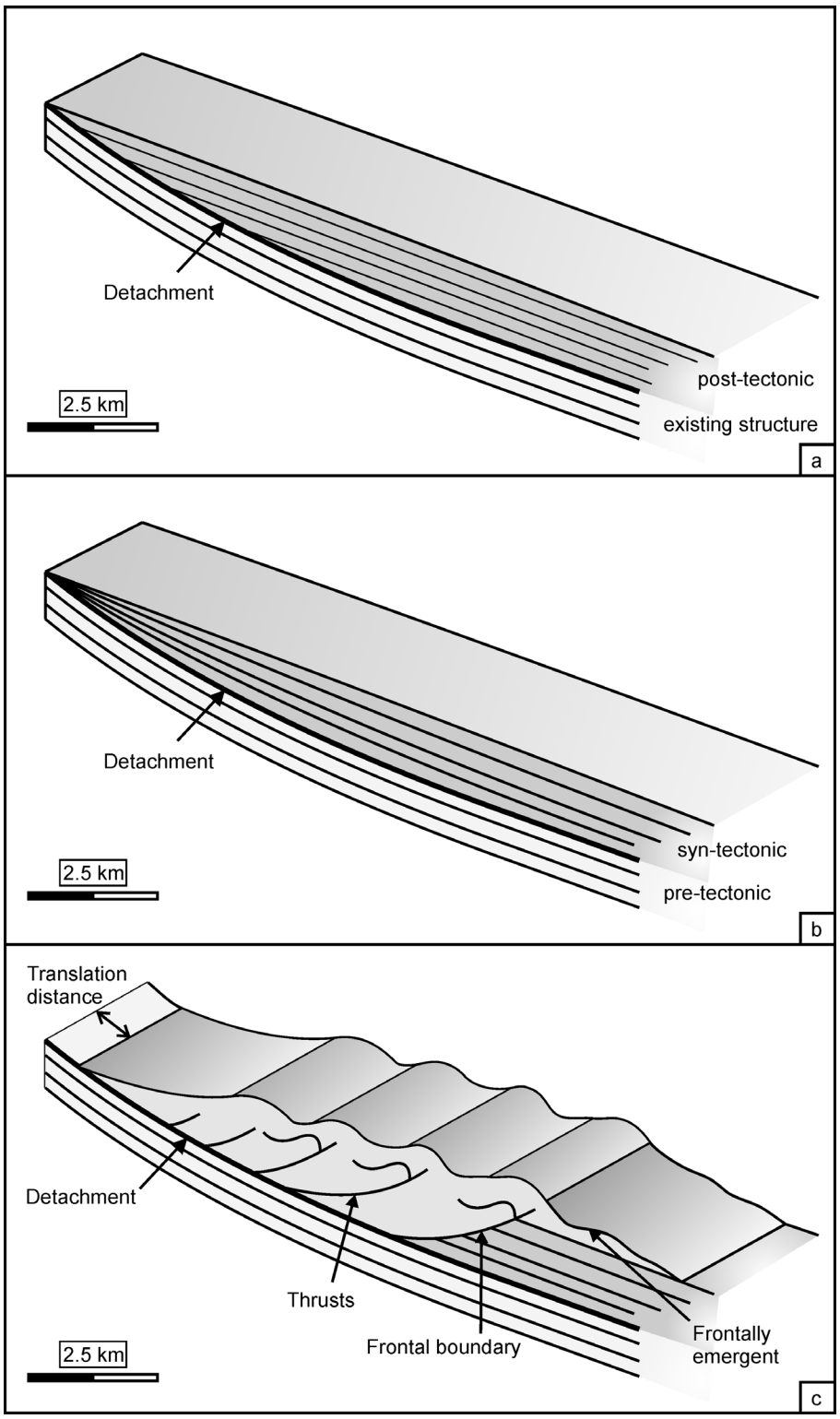

Fig. 6.10 Cartoon model for the development and detachment of a sediment wedge, with two different starting configurations: (a) onlapping wedge onto an existing structure, and (b) a syn-tectonic sediment wedge. (c) Final configuration after slide initiation and thrust propagation. Modified after (Frey-Martínez *et al.*, 2006).

6.6 DISCUSSION

6.6.1 NATURE OF DETACHMENT

The position of the detachment surface has been described as the point where the pore pressure approaches or balances the normal stress induced by the weight of the overburden, and reduces the shearing resistance along the surface (Martinsen, 1994). The slides described here all have average thickness of 300 m, with a minimum thickness of 30 m and maximum thickness of 600 m. Thickness increases rapidly at the slide margins, so the depth from the top of the slide to the detachment for ~90 % of their length is >400 m. This thickness is similar to the depths of the detachments documented in the Faroe Shetland Basin (Davies and Clark, 2006). Given the limited well data available, the lithology around the level of detachment layer cannot be identified, but it probably coincides with a sudden change in lithology, most likely into a muddier, lower permeability fine-grained lithology at the base of the biosiliceous ooze. The upward flow of pressured fluids, such as water and hydrocarbons, may significantly reduce slope stability and enhance the potential for gravitational sliding along such a layer (Sultan *et al.,* 2004). Translation distance must be in part controlled by the dynamic friction on the detachment.

Frey Martinez et al. (2006) identified that the depth to detachment of submarine landslides is important in governing the development of frontally confined landslides, that the slides here can be classed as. We expand on this with reference to these blocky slides, suggesting that two factors contribute to deep detachments. The first factor is that the sediment needs to have sufficient shear strength to avoid shear failure under normally pressured conditions during shallow burial of <75 m (see next section). The second factor is the continued increase in shear stress with depth in the presence of overpressure, despite effective stress increasing more slowly below the top of the overpressure. In the presence of overpressure the shear stress on bedding planes due to the downslope component of gravity continues to increase with burial depth, whereas the frictional resistance to sliding barely increases because the normal effective stress acting on bedding planes increases only slowly with increasing burial depth. No direct measurements of pore pressure are available as evidence that overpressure is present, but a number of geological phenomena on the outer Vøring Basin, such as mud volcanoes and fluid expulsion features (Hansen *et al.,* 2005), pock marks (Ireland *et al.,* 2010b) and subsurface sediment remobilization (Hovland *et al.,* 1998), indicate that sediments have probably experienced transient increases in pore fluid pressure during the Cenozoic. In addition, ODP 642 identified sediments that were not normally consolidated for their burial depth, suggesting elevated pore pressures (Eldholm *et al.,* 1987b). Disequilibrium compaction

is the most likely mechanism to generate significant overpressure within the uppermost 1000 m of sediment (Swarbrick *et al.,* 2002).

6.6.2 SEDIMENT STRENGTH

A number of studies make links between the style of macro-scale deformation and the micro-structural behaviour of siliceous sediments (e.g. Grimm and Orange, 1997; Tanaka and Locat, 1999; Fredrich *et al.,* 2000; Davies, 2005). Sediments rich in siliceous microfossils (in particular diatoms) have unique physical properties (e.g. Tanaka and Locat, 1999). They do not follow typical clastic compaction trends because the silica frustules form a relatively incompressible framework and maintain a high porosity relative to detrital, organic, and calcareous components of the rock (e.g. Compton, 1991). Measurements from DSDP, ODP and IODP indicate a wide range of in-situ shear strengths (Fig. 6.9), with some data suggesting that sediments have low shear strengths and are close to the liquid and plastic limits compared to terrigenous sediments (Bryant *et al.,* 1981; Pittenger *et al.,* 1989) while other data indicate they have high shear strengths compared to terrigenous sediments (Hill and Marsters, 1990). The cohesion of sediment is a critical factor in stabilizing sediments near the seafloor and increasing the overall stability of a margin (Dugan and Flemings, 2002), preventing failures from evolving into large mass movements or debris flows (Iverson, 1997). We suggest that siliceous sediments are unlikely to fail during very shallow burial (within 75 m of the seafloor) because of their ability to maintain a cohesive framework during early burial. Non-biogenic sediments from ODP leg 104 site 642 (Fig. 6.9) display a trend of increasing shear strength with depth, and generally those sediments with a biogenic component tend to display a different trend from the terrigenous sediments. There may be some errors in the measured shear strengths as a result of fracturing of the sediment due to coring (Eldholm and Thiede, 1987). ODP 112 measurements show that at shallow depths (<100 m) biosiliceous sediments have higher shear strengths than typical terrigenous sediments (Fig. 6.9).

The recognition of similar thrust structures in other sediment types (e.g. Frey-Martínez *et al.,* 2006) indicate that such structures are not exclusive to siliceous sediments, but a common characteristic is the relatively deep (>300 m) depth to the detachment layer that could result from the ability of sediments to a resist failure during early burial.

6.6.3 PRIMERS AND TRIGGERS

Triggering mechanisms are the external stimuli that initiate slope instability (Sultan *et al.,* 2004). Primers can be considered those processes which act as an early stimulus, such as increases in pore pressure (e.g. Davies and Clark, 2006), before the final 'trigger'. Adjacent sections of the sedimentary section with similar slope gradients, show no evidence of slope failure, so failure must have involved a localized combination of critical factors (cf. Gardner *et al.,* 1999). Backstripping reveals that the Vema Dome has changed from a low relief structural high in Palaeocene-Oligocene times to a much higher and narrower feature from the Miocene to the present (Hjelstuen *et al.,* 1997). Given the approximate age placed on the blocky slides and the coincidence with sediment packages (Fig. 6.1c), it seems highly likely that the uplift of the Vema Dome was key to triggering the slope failures. Whether uplift was synchronous with failure or the failure occurred after deposition of sediment on a steep slope, the seismic data do not allow us to differentiate. Either stratigraphic configuration explains the observed shallow head-scarp (Fig. 6.10). While other mechanisms may contribute, such as development of transient excess pore pressure due to earthquake shaking and gas hydrate dissociation, the simplest and most apparent evidence is that the slides are approximately synchronous with the late stage of uplift of the Vema Dome. The explicit trigger, as in most other cases, cannot be determined.

6.6.4 COMPARISON WITH OTHER FAILURES

While a number of slope failures on the North Atlantic margin have been described that cover much greater areas, and therefore have greater total volumes of sediment associated with them, such as the Storegga slide (Haflidason *et al.,* 2004), the Hinlopen slide (Vanneste *et al.,* 2006) and the Tampen slide (Sejrup *et al.,* 1996), the ratio of length to thickness and also the translation distances involved in the blocky slides described here are unusual. Three recent studies (Volpi *et al.,* 2003; Davies and Clark, 2006; Kristoffersen *et al.,* 2007) that have identified evidence of mass movements within siliceous sediments interestingly exhibit a number of similar deformational characteristics to the slides described here (Fig. 6.11a). It is suggested that the style of deformation of all failures in siliceous sediments results from the inherent characteristics of the sediments and relatively deep detachments. The three other slope instabilities in siliceous sediments (Fig. 6.11b, c and d) are all interpreted as having coherent structural deformation, comprising fault-bounded blocks with preserved bedding. The example from Volpi *et al.,* (2003) (Fig. 6.11d) is slightly different from the other two, as creep is a different process to sliding, associated with low strain rates (Martinsen, 1994), but the

deformation is compatible with the hypothesis that cohesive siliceous sediments result in deep detachments on slopes where mass movements take place. Table 6.2 compares the dimensions of the slides from the Vema Dome, Faroe Shetland Basin and Lomonsov Ridge. Note the slides have comparable volumes and thicknesses.

	Length	Area	Max thickness	Approximate volume	Dominant sediment type	Ratio length:max thickness
Slide 2, (this study)	8.4 km	43 km^2	500 m	20 km^3	Siliceous	**16.8**
Faroe Shetland Basin (Davies & Clark, 2006)	13 km	110 km^2	620 m	25 km^3	Siliceous	**21**
Lomonsov Ridge (Kristoffen et al., 2007)	**10 km**	**60 km^2**	**400 m**	**10 km^3**	**Siliceous**	**25**

Table 6.2 Comparison of characteristics of submarine slides in siliceous sediments.

Such coherent deformation suggests that the slides did not form geological instantaneously, like sudden catastrophic debris avalanche type failures (e.g. Iverson, 1997) and therefore are less likely to be responsible for tsunami generation. These failures may be considered to be frontally confined, with their compressional toe regions buttressed by the ramp separating their main body from the undeformed 'foreland' (Frey-Martínez *et al.,* 2006).

6.7 CONCLUSIONS

Four discrete submarine slides have been identified, which in total cover an area of more than 120km^2. The style of deformation appears to have been greatly influenced by the depth to the detachment. Blocky slides initially develop as frontally confined systems with significant

bathymetric expression, later developing minor frontally emergent toes. They have shallow head-scarps akin to failures that involve an entire sediment wedge. They are relatively thick and short, with coherent structures, and two factors that are the key to their development are the resistance of sediments to shear failure at shallow burial depths (<75 m), and the presence of overpressure which means that shear stress on bedding planes due to the downslope component of gravity continues to increase with burial depth, whereas the frictional resistance to sliding barely increases because the normal effective stress acting on bedding planes increases only slowly with increasing burial depth. Local tectonic uplift of the Vema Dome was fundamental to the development of the four blocky slides described here.

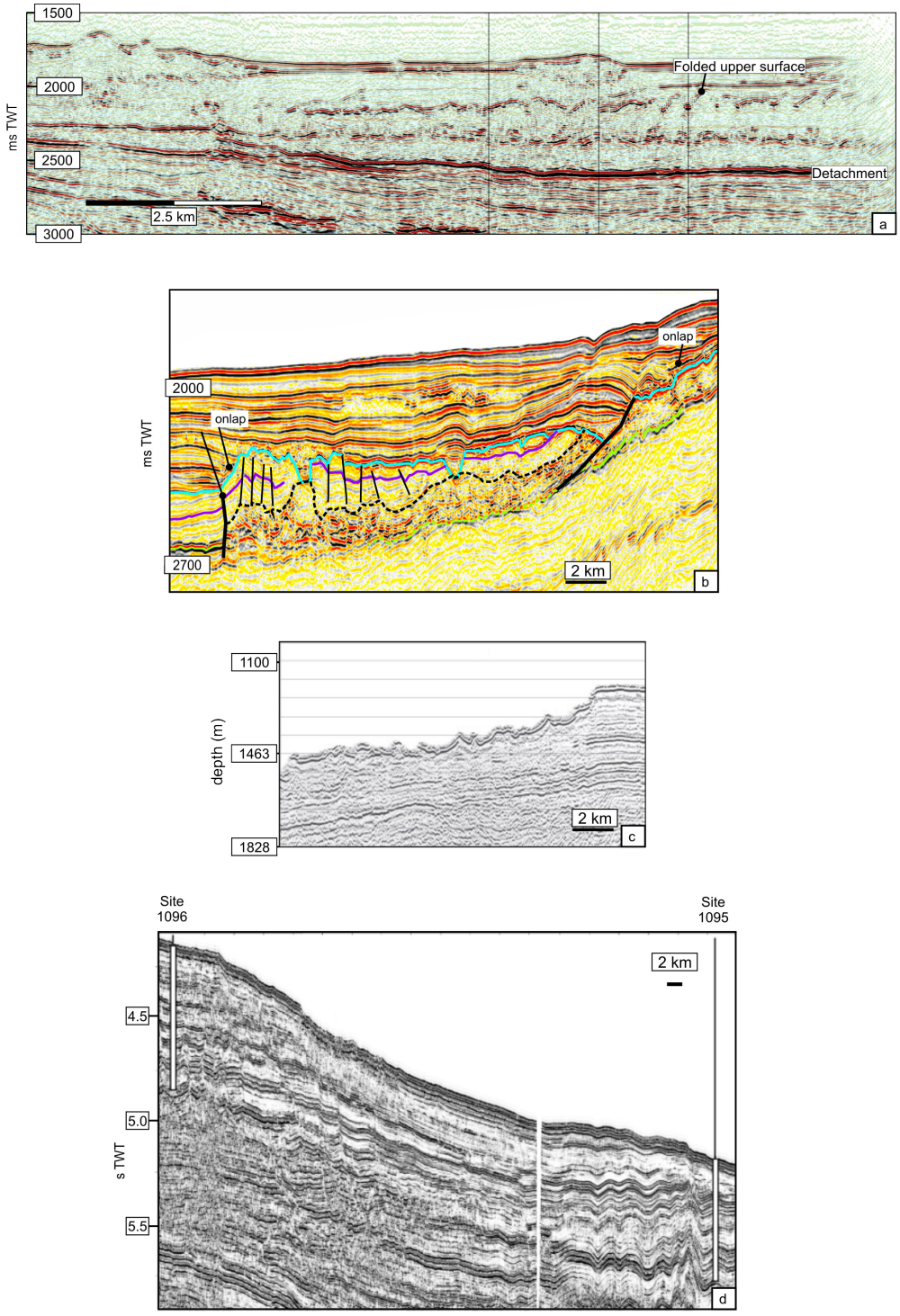

Fig. 6.11 **Seismic sections of submarine slope failures in siliceous sediments: (a) Vema Dome, this study; (b) Faroe Shetland Basin from Davies & Clark (2006); (c) Lomonsov Ridge, Arctic, from Kristoffeson (2005), and d) Antarctica Peninsula from Volpi et al. (2003). Note that (a) and (c) both have coherent internal structure, are thick (>200 m) and relatively short.**

7 DISCUSSION & CONCLUSIONS

This chapter summarizes the principal findings and discusses some of the uncertainties and implications of them as well highlighting some avenues for further research.

7.1 PRINCIPAL FINDINGS

3-D seismic data offer a novel method for the investigation of diagenesis and shallow deformation across large tracts of sedimentary basins (e.g. Cartwright, 2007). This thesis reports the investigations of the diagenesis of siliceous sediments, their compaction, their susceptibility to simple shear as evidenced by the geometry of layer-bound faults, and the characteristics of slides within them.

Chapter 3 examined the seismic expression of the structure of a silica diagenetic transformation zone, at a scale of tens to hundreds of metres thickness, in Cenozoic sediments from the Gjallar Ridge, offshore Norway. Supported by the integration of well data, it provides the first recognition, using 3-D seismic, that silica diagenetic transformations are not simply narrow boundaries represented by single cross-cutting reflection events, but can be heterogeneous and hundreds of metres in thickness. Chapter 4 hypothesises that the chemistry of formation water expelled transiently through polygonal faults is a key control on the formation of topographic highs at the transformation boundary and on lateral variations within the underlying transformation zone.

Chapter 5 describes the internal strains evidenced by a layer-bound fault system on the Mauritanian continental margin. The observed fault dips are unexpected given the stress conditions that result from the presence of dipping stratigraphy. It is hypothesised that the layer hosting the faults has been subjected to simple shear, with the top of the layer displaced downdip relative to its base, resulting in rotation of the fault planes.

Chapter 6 describes four blocky submarine slides form the flanks of the Vema Dome, offshore Norway located in siliceous sediments. These slides have three distinguishing characteristics in comparison to other submarine slides: a relatively low ratio of length to thickness, folds and thrusts of a regular wavelength, and short translational

distances. These characteristics are attributed to deep detachments that resulted from the high cohesion of siliceous sediments and, consequently, their resistance to shear failure during early burial (<75 m).

The work presented in Chapters 3, 4, 5 and 6 has examined the seismic expression of diagenesis and the style, kinematics and cause of deformation in Cenozoic siliceous sediments on the Eastern Atlantic Margin. Though each chapter examines a different geological phenomenon, the inherent properties of siliceous sediments and the processes involved in each may all be intrinsically linked. The unique properties of biogenic silica mean that exponentially decaying porosity trends (e.g. Hurley and Hempel, 1990) do not apply. In siliceous sediments compaction occurs abruptly at the diagenetic transformation boundaries (Compton, 1991). Prior to the opal-A to opal-CT diagenetic transformation, siliceous sediments may have an increased cohesion compared to terrigenous sediments (Chapter 6) as a result of this framework. Subsequently diagenesis modifies the mineralogy, porosity and shear strength of the sediment (Chapter 3). Since the diagenesis of siliceous sediments is non-uniform with significant lateral variability (Chapters 3 and 4), so may the subsequent compaction (e.g. Davies, 2005). The complexity in diagenetic transformation may arise from the effects of regional scale structure and variations in subsidence, sedimentation rate, and geothermal gradient. These may be coupled with local interactions between pore water chemistry and fluid flow through faults (Chapter 4) as well as local variations in sediment composition. The deformation of siliceous sediments on continental margins may be strongly affected by the stress imposed by dipping stratigraphy, the result of geological structures at a range of scales (entire continental margins, regional local structural highs and canyons). Variations in substrate, which may act as local detachments (Chapters 5 and 6) and the presence of overpressure (Chapter 6) may also be an important control on the kinematics of deformation. The style of deformation observed in siliceous sediment may reflect their unique physical properties and the complex influence of diagenesis during burial.

7.2 SUBSURFACE UNCERTAINTIES

Key to the work presented in this thesis is the high resolution of seismic reflection data in the shallow subsurface (<1000 mbsf), where data generally have the highest frequency content. This high resolution allows subsurface structures to be resolved to a scale of tens of metres, which highlights diagenetic and structural and complexities in siliceous sediments.

The investigation of these processes has also benefited from the availability of high end seismic technologies, in particular volume based attributes and 3-D visualization, which helpimprove the accuracy to which features can be mapped and delineated (e.g. Brown, 2005b).

As with any study based on the interpretation of seismic reflection data, it is important to be acutely aware of the uncertainties and possible pitfalls. The high resolution of the data reduces some of the uncertainty and increases confidence in the interpretations. Despite this, well data are required to ground truth interpretations and, where available, have been correlated to the 3-D seismic reflection data (Chapter 3, 4 and 6). Chapter 4 presents a hypothesis for the mechanism of preferential transformation of opal-A to opal-CT which is based solely on seismic observations and the present understanding of the chemical systems involved in silica diagenesis. To ground truth the model presented will require additional data, in particular detailed sampling and analysis of pore water chemistry. The extensive work on the redistribution and transport of silica during cementation in sandstones (e.g. Worden and Morad, 2000) may help constrain further this mechanism.

Chapter 5 focuses on the geometry of a fault system, and is again solely based on seismic interpretation. The work could benefit from well data to provide information on the physical properties of the sediments, present day stress orientations from borehole data and in-situ pore pressures. Despite the absence of well data, the study is still robust, as discussed further in section 7.2.3. In Chapter 6 the shallow section is relatively well imaged and, given that there are a number of existing scientific boreholes nearby, this has allowed the integration of some measurements of physical properties which support the interpretations. The slides have not been directly penetrated by any well to date; however, such data could improve the seismic imaging of the slides because it would allow accurate interval velocities to be incorporated into reprocessing the seismic data. Below a number of more specific uncertainties are discussed.

7.2.1 Quantification of silica phases

XRD and XRDP data have been integrated from two wells in Chapter 3, but neither is within the limits of the 3-D seismic data. Though this precludes a high resolution correlation of the proportions of silica phases to reflection events, the data do indicate that the transformation of silica phases occurs within the sedimentary succession and the depth range over which

this takes place. Studies which provide compositional data to demonstrate and prove the presence of the silica transformation in the subsurface from seismic reflection data are limited (Hein *et al.,* 1978; Pegrum *et al.,* 2001). Unfortunately no higher resolution correlation is likely in the near future, due the lack of core, cuttings and samples from seismically imaged diagenetic transformation zones.

7.2.2 Rate and timing of silica diagenesis

The structure and heterogeneity of the silica diagenetic transformation zone on the Gjallar Ridge indicate that the transformation of silica phases in non-uniform, and that the rate of transformation is probably not dependent on a single factor. The most commonly cited influences are temperature, time and the composition of both the host sediments and the pore fluids (Kastner *et al.,* 1977). It was speculated in Chapter 4 that that the chemistry of pore water expelled through polygonal fault systems may be key in the preferential transformation of opal-A to opal-CT. There is a lack of geochemical data to support this interpretation, but it has previously been suggested that transient pore water chemistry profiles may be important in the formation of chert spheroids in the Monterey Formation (Behl, 2010) and as an explanation for the varying oxygen isotope ratios of opal-CT in sediments offshore Peru (Behl and Smith, 1992).

Across much of the Norwegian margin, where the silica diagenetic transformation has been mapped out using 2-D and 3-D seismic reflection data, there are significant variations in the depth of the transformation boundary below the present day seafloor (see Neagu *et al.,* 2010b). A tendency for the transformation boundary to parallel unconformities has also been noted (Davies and Cartwright, 2002; Meadows and Davies, 2007). To date the exact cause of this variation in depth has not been properly explained, and only two hypotheses currently exist in the literature: changes in geothermal gradient (Davies and Cartwright, 2002) and variations in pore water chemistry (Ireland *et al.,* 2010a, Chapter 4). Whatever the cause, the variation across an entire continental margin (tens to hundreds of kilometres) coupled with local (tens to hundreds of metres) variations indicate a highly dynamic chemical system.

7.2.3 PHYSICAL PROPERTIES OF SILICEOUS SEDIMENTS

The burial, compaction and deformation history of sediments are determined by the physical properties of the sediment, along with the stress regime and pore fluid pressure (e.g. Maltman, 1994) and these three factors are not independent of each other. It is well documented from the Monterey Formation that siliceous sediments compact at a different rate to terrigenous sediments under the same burial conditions (e.g. Compton, 1991).

In Chapter 3 the sonic log used to create the synthetic seismic trace produced a good match despite being relatively lacking in any significant events (see Fig 3.2). The consistency of the sonic log response is surprising, given the significant variations in density at the two silica transformation boundaries where the density steps up (see Fig 3.2). A possible explanation for this log response is that despite undergoing compaction and diagenesis at the two stages of silica transformation, the overall rigidity does not change significantly at either of these stages. The velocity of a P-wave, V_p through a medium can be defined by:

$$V_p = \sqrt{\frac{K_b + \frac{4\mu}{3}}{\rho}} \qquad \textbf{Eq. 7.1}$$

where K_b is the bulk modulus, μ is the shear modulus and ρ is density. According to equation 7.1, the compressional wave velocity depends on the bulk moduli, density and the shear modulus. Changes in mineralogy result in changes to these parameters, as do changes in porosity. However, since opal-A dominated sediments have a remarkably different micro structure to typical terrigenous sediments, (described in Chapters 1 and 6) it could be hypothesised that the sonic log response is related to the elastic moduli. Using equation 7.1, it can be seen that for an increase in density, and no change in elastic moduli that the sonic velocity would be reduced. But essentially the sonic velocity does not change at the opal-A to opal-CT transformation boundary, which means that, $K_b + \frac{4\mu}{3}$ must increase by exactly the same factor as the density. This is in contrast to most sediment, where in general, $K_b + \frac{4\mu}{3}$ increases faster than density. Opal-CT dominated sediments would be predicted to have a significantly higher bulk modulus than opal-A-rich sediment because of the decrease in porosity, and increase in grain density, so it can be speculated that μ is lower in opal-CT-rich sediment that in opal-A-rich, which partially offsets the greater bulk modulus. This

hypothesis could be tested if sufficient reliable measurements of V_p and V_s could be collated from well logs, core and rock samples.

In Chapter 5, the geometry of a layer-bound fault system is described. In the absence of faulting when the horizontal strains are zero, the ratio of horizontal and vertical effective stresses is known as the coefficient of earth pressure at rest, K_0 (Maltman, 1994). If $K_0 = 1$ then sediments are subject to hydrostatic stress and undergo isotropic consolidation (Maltman, 1994). This is unrealistic, and the more likely situation is for the horizontal stress to be just sufficient to prevent lateral strain, and under these conditions consolidation induces anisotropy in the sediments (Maltman, 1994). No direct direct measurements of K_0 are available for the sediment layer affected by the faults. A value of 0.7 was used in Chapter 5 based upon the measurements by Bishop *et al.,* (1971) and there is no reason to doubt that this value for fine grained sediments where similar measurements have been recorded by others (e.g. Mayne and Kulhawy, 1982). However, if other values of K_0 are substituted into the equations in Chapter 5, then the stress tensor will still be rotated. For example, given a stratigraphic dip of 3°, and $K_0 = 0.5$ (which is probably an underestimate for fine grained sediments) then the maximum principal effective stress would plunge basinwards at 87° (as opposed to 83° as quoted in Chapter 5, when $K_0 = 0.7$). This means that if K_0 was underestimated, the amount of simple shear that has occurred was also underestimated.

In Chapter 6 the unusual geometry of four submarine slides were described. It was proposed that the key to the development of a deep detachment was the inherent ability of biosiliceous sediments to maintain a cohesive framework and resist failure during early burial (burial depths <75 m). It has been shown (Dugan and Flemings, 2002) that if a modest and reasonable cohesion value is used in slope stability analysis, then stable conditions are predicted in contrast to when a zero value is used and instabilities predicted. Although generally for near surface sediments the contribution of cohesion to their strength is negligible (Maltman, 1994), recent accumulations of biogenic silica on the seafloor show evidence of flocculation immediately after deposition and centimetre-thick sediment structures consisting of a meshwork of delicate siliceous tests apparently formed at the sea floor by resuspension and aggregation of a fine siliceous matrix (Reimers and Waldo Wakefield, 1989). ODP data indicate that at shallow depths siliceous sediments have higher shear strength than typical terrigenous sediments (see Chapter 6). There are very few values for the cohesion of sediment, probably because of the difficult in quantifying it. This work highlights the importance of cohesion to the development and style of submarine slope

failures and that it should not be ignored when developing models of submarine slope stability analysis.

7.2.4 FLUID EXPULSION AND PORE PRESSURE

The expulsion and flow of pore water across sedimentary basins is likely to occur in siliceous sediments during shallow burial (e.g. Davies *et al.,* 2008), and may be intrinsically linked to several subsurface processes. The effect of compaction, porosity loss and expulsion of fluid is likely to contribute an increased amount of fluid compared to terrigenous fine grained sediments (e.g. Davies *et al.,* 2008). Using 3-D seismic reflection data, a number of features have been interpreted as direct evidence of fluid expulsion (for example Fig 4.5). Pore water is probably expelled episodically and therefore changes in pore pressure are likely to be transient in the shallow section. There are no direct measurements of pore pressure, but it is possible that sediments have experienced periods of overpressure on the Norwegian margin and the Mauritania margin. The role of overpressure in the initiation of submarine slides was discussed in Chapter 6. In addition the geometry of a layer-bound fault system, such as described in Chapter 5 could also be affected by the presence of overpressure, where it could increase the magnitude of rotation of the stress tensor due to stratigraphic dip, compared with normally pressured sediment (e.g. Mourgues and Cobbold, 2006). The physical explanation for this is the same as that for the development of a deep detachment as described in Chapter 6. Shear stress continues to increase with depth in the presence of overpressure, but the effective stress increases more slowly below the top of the overpressure.

7.2.5 CHEMICAL AND MECHANICAL INTERACTION

Diagenetic processes and structural deformation have been investigated independently in this thesis. When sediments are between depths of 300 to 1000 m (temperatures ~15 to 56°C, for a geothermal gradient of 52°C as estimated at the Gjallar Ridge, Chapter 3) both chemical and mechanical processes could interact. Such interactions represent a newly emerging area of study which could be increasingly prevalent and central to an understanding of fluid flow, geological storage and other processes in basins (Laubach *et al.,* 2010).

From the Monterey Formation, extensive studies of the chemical systems involved in diagenesis, the brittle deformation and fluid migration have highlighted the interaction among these processes (Eichhubl and Behl, 1998). Though not explicitly investigated in this thesis, the findings in Chapters 3 and 4 identify heterogeneities in the silica diagenetic transformation zone that could influence the initiation and propagation of polygonal faults in siliceous successions (Davies and Ireland, in review). Previous authors have speculated that the transformation of opal-A to opal-CT could be involved in the formation of polygonal faults (Brekke *et al.,* 1999; Volpi *et al.,* 2003). A direct link between silica diagenesis and deformation from seismic reflection data was made by Davies (2005) and subsequently evidence has been presented demonstrating that transformation of opal-A to opal-CT and associated differential compaction is a viable mechanism for the formation of some polygonal faults (Davies *et al.,* 2009). Differential subsidence, which imposes sufficient shear stress for failure to occur is a viable mechanism for fault development in siliceous sediments (Davies and Ireland in review). At the grain scale, modelling of shear fractures has shown that mineral dissolution could be a viable mechanism for the initiation of polygonal faults (Shin *et al.,* 2008, 2010), but such models need to be verified with outcrop (or borehole) evidence of the processes.

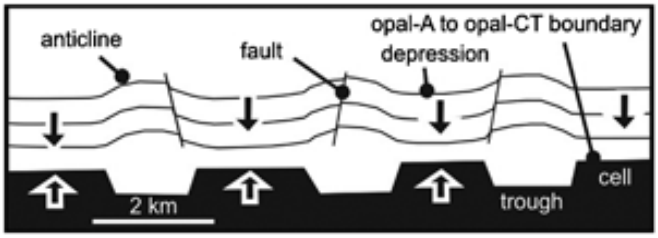

Fig. 7.1 Schematic figure showing an opal-A to opal-CT diagenetic boundary that has undergone differential advancement. Faults are located on the margins and crests of the anticlines in the overburden. Arrows indicate subsidence occurring above upward-advancing cell. From Davies *et al.,* (2009).

7.3 SILICEOUS SEDIMENTS – OUTCROP ANALOGUES

This thesis has investigated processes, both chemical and mechanical occurring in siliceous sediments on the Atlantic margin using 3-D seismic reflection data. Below a brief comparison of the processes from seismic reflection data are made with siliceous sediments in outcrop.

7.3.1 MONTEREY FORMATION

The Monterey Formation which outcrops in California has been used as an analogue for some of the processes occurring in siliceous sediments in both this thesis and in the literature (e.g. Davies and Cartwright, 2002, 2007; Davies, 2005; Davies *et al.,* 2009). The formation provides the best documented analogue for the siliceous sediments offshore the Atlantic margin. However, due to the significant differences in the scale of investigations, it is difficult to compare the structural deformation and the proposed models for diagenetic transformation across large tracts of sedimentary basins. This difficulty is best demonstrated by the contrast in differential compaction that is observed at each location. Differential compaction described from 3-D seismic reflection data indicates greater compaction within cells (regions preferential transformation) than outside them at the same stratigraphic interval (Fig. 7.2a). Above chert bodies formed by silicification along faults within the Monterey Formation, the exact opposite compaction pattern is observed because the chert is relatively incompressible compared to the surrounding diatomite and with burial the diatomite is compressed around the rigid chert (Fig. 7.2b) (e.g. Behl, 2010).

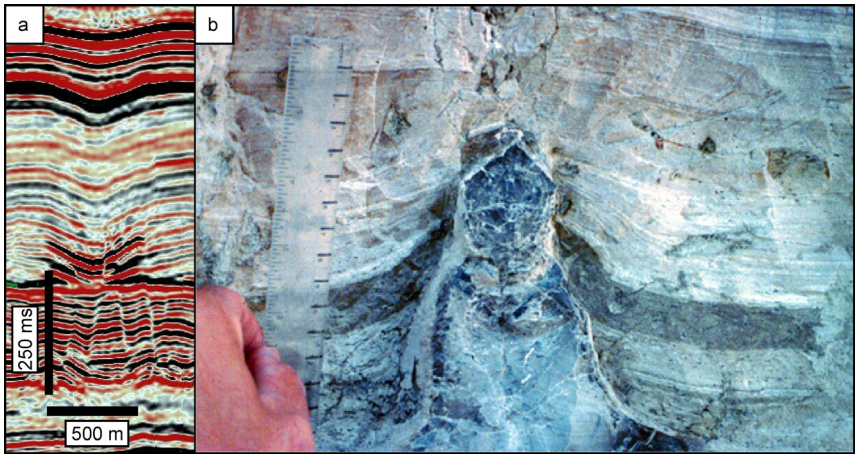

Fig. 7.2 Example of differential compaction (a) above diagenetic cell, from the Gjallar Ridge offshore Norway and (b) around a chert nodule in the Monterey Formation (photo courtesy of Rick Behl, UCLB). See text for explanation.

Seismic reflection data from offshore Norway indicate variations in diagenetic transformations at a range of scales from sub-seismic resolution variations indicated by XRPD (Fig 3.9) to kilometre scale variations (Fig 3.4). Understanding the precise chemical processes that occur across such a range of scale is difficult from seismic reflection data alone. In addition, identifying the kilometre scale variations from outcrops is difficult, and

even identifying a prominent transformation boundary, as observed in seismic reflection, is difficult (see Fig 1.6). Scale is a limiting factor in both seismic and outcrop investigations. Seismic reflection data, supported by XRPD indicate that the transformation of opal-A to opal-CT takes place across a ~20 m zone, with further complexities in the transformation occurring within a wider zone some 300 m across (see Chapter 3). From a single outcrop such a zone would be almost impossible to identify. Testing if the same mechanisms that result in local variations in diagenetic transformations in the Monterey Formation operate across large tracts of sedimentary basins is difficult with only limited borehole calibration.

7.3.2 EGYPT

The increasing availability of high resolution satellite imagery of the Earth has been an invaluable tool in identifying kilometre scale geological structures (Haxby *et al.,* 1983). Tewksbury et al. (2009) identified a 'bubble wrap' structure using satellite imagery in Egypt similar to that described by Davies (2005) using 3-D seismic reflection data from the Faroe Shetland Basin (Fig. 7.3).

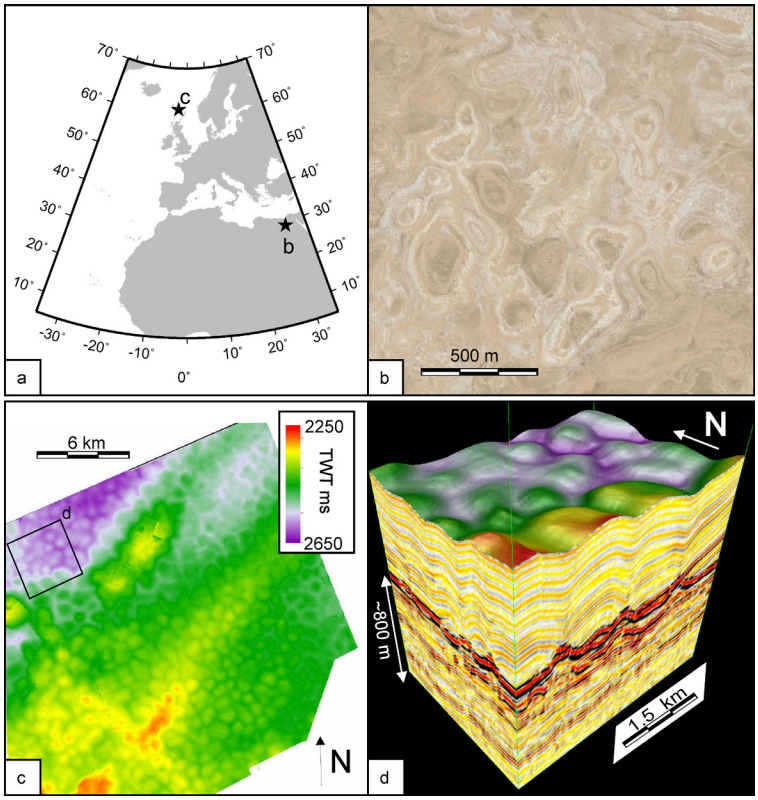

Fig. 7.3 Comparison of differential compaction due to silica diagenesis from the Faroe Shetland Basin (Davies, 2005) and the similar 'bubble wrap' texture from Egypt (Tewksbury *et al.*, 2009).

(a) Location of (b) and (c). (b) Google Earth image of bubble wrap texture, © 2010 Cnes/Spot Image, © Google Earth. (c) Time-structure map of folded overburden above irregular opal-A to opal-CT transformation boundary. (d) 3-D visualization of folded overburden.

They suggested based on initial observations that these feature may be analogous to the deformation observed from the Faroe Shetland Basin caused by the differential compaction of sediments above a diagenetic transformation boundary (Davies, 2005). Field based studies over the coming years will ground truth the observations and hypothesis (Tewskbury, pers. comm.). These structures may provide an opportunity to study the kilometre scale interaction of silica diagenesis and deformation onshore.

7.4 IMPLICATIONS OF FINDINGS

The findings from this thesis should be of broad interest those studying siliceous successions. Given the extensive distribution of siliceous sediments both globally and in geological time, understanding their burial history should be important to understanding the evolution of many sedimentary basins.

3-D seismic investigation of silica diagenesis indicates a dynamic and complex system. The findings open up the possibility that such scales of variations and complexities may exist in other diagenetic systems (e.g. Morton, 1985). They contribute to the field of study termed 'seismic diagenesis' by Davies & Cartwright (2007) which, with improving seismic technologies and an increased understanding of diagenesis across large tracts of sedimentary basins, will advance rapidly as a subject. Understanding the timing, rate and distribution of diagenesis and related processes such as porosity reduction, compaction and faulting, is important in sedimentary basin analysis (Meadows and Davies, 2008).

Recognising precursory phenomena in submarine slope stability is difficult due to their often transient nature (cf. Integrated Ocean Drilling Program, 2001). It has been identified here (Chapter 6) that the inherent properties of siliceous sediments may be important as a pre-conditioner to the style of deformation in submarine slides. Previously it is has also been demonstrated that enhanced fluid flow as a result of the silica diagenetic transformation is important in understanding submarine slope failure (Davies and Clark, 2006). By using the geometry of a layer-bound fault system, the approximate magnitude of

downslope movement that part of a continental margin has undergone can be estimated by comparing predicted fault geometries with the observed. A similar methodology could be applied using layer-bound fault systems elsewhere and potentially other geological structures, such blow out pipes which have been noted to be sub-vertical (e.g. Løseth *et al.,* in press).

This thesis has again highlighted that given nature of 3-D seismic data significant findings can be made by adopting a more exploratory approach using basic mapping and curiosity-driven analysis to exploit seismic reflection data sets (Cartwright, 2007).

7.5 FUTURE RESEARCH

Though a number of definitive conclusions have been made about the diagenesis and deformation of siliceous sediments, there are still a number of unknowns. Subsurface uncertainties have been discussed earlier; here areas for future research which would make significant contributions to our understanding of the diagenesis and deformation of siliceous sediments are described.

Within this thesis available well data from scientific drilling projects have been integrated. ODP Leg 104 on the Norwegian Margin is in close proximity to the 3-D seismic data, but other scientific drilling sites (ODP 112, DSDP 12), have been used in addition which have information pertaining to siliceous sediments. There are a vast number of scientific drill sites which have penetrated siliceous sections and it is not within the scope of this study to provide a comparison to them all. A problem with this current database, however, is to date no project has explicitly set out with the primary objective to investigate the diagenesis and deformation of siliceous sediments, therefore key information may not be available.

In October 2009 a proposal was submitted to the Integrated Ocean Drilling Program (Davies *et al.,* 2009), which identified 3 sites on the Gjallar Ridge to ground truth the seismic observations of a silica diagenetic transformation zone. The following objectives would be key to an improved understanding of the processes:

1) Identify the differences in sediment composition and properties, and fluid composition in regions of preferential diagenetic transformation and immediately adjacent to.

2) Determine the dominant control on the formation of regions of preferential diagenetic transformation and the role of external controls on, such as temperature and pore water composition.
3) Characterize the extent of fracturing within the diagenetic transformation zone and its implications for the development of chemical and mechanical interactions.
4) Quantify the extent of transformation through a 'the diagenetic transformation zone and in particular regions of preferential transformation, in terms of % wt. of silica polymorphs and relate it to bulk sediment and pore fluid composition.

Achieving the above would require drilling, coring and collection of additional data, such as pore water sampling, and would represent a unique opportunity to provide a high resolution petrophyisical correlation of sediment undergoing diageneis to a high resolution 3-D seismic reflection dataset. In the absence of scientific drilling, hydrocarbon exploration drilling has potential to retrieve the required samples for the above objectives, but it is unlikely that such an expensive drilling program will be carried out by any operator in the near future. An alternative to expensive drilling operations could be to revisit existing DSDP, ODP and IODP data, carrying out additional analysis on core samples but this would be disadvantaged because of the lack of 3-D seismic coverage at most existing drill sites.

Future work on the deformation of siliceous sediments should include examining additional 3-D seismic reflection datasets. A comparison of layer-bound fault systems from different areas across a continental slope with extensive 3-D seismic coverage would provide a unique opportunity to investigate the distribution of stress and strain across a large area and could be used to reconstruct palaeo-stresses (e.g. Cartwright, 2009). Submarine slope failures have been widely studied and documented but despite this a number of uncertainties remain. Understanding the kinematics of structural deformation within slope failure deposits should improve our understanding of the mechanisms involved in their failure, and should encompass both seismic reflection and outcrop approaches.

REFERENCES

A

Allen, J.R.L., 1982. *Sedimentary structures 1*. Elsevier Scientific, Amsterdam.

Antobreh, A.A., Krastel, S., 2007. Mauritania Slide Complex: morphology, seismic characterisation and processes of formation. *International Journal of Earth Sciences* **96**, 451-472.

B

Bacon, M., Simm, R., Redshaw, T., 2007. *3-D Seismic Interpretation*. Cambridge University Press.

Bahorich, M., Farmer, S., 1995. 3-D seismic discontinuity for faults and stratigraphic features: The coherence cube. *The Leading Edge* **14**, 1053-1058.

Baron, J.A., 1986. Paleoceanographic and tectonic controls on the deposition of the Monterey formation and related siliceous rocks in California. *Paleogeography, Paleoclimatology, Paleoecology* **53**, 27-45.

Behl, R.J., Garrison, R.E., 1994. The origin of chert in the Monterey Formation of California (USA), in: *Proceedings of the 29th International Geological Congress: Siliceous, phosphatic and clauconitic sediments of the Tertiary and Mesozoic*, 101.

Behl, R.J., 2010. Chert spheroids of the Monterey Formation, California (USA): early-diagenetic structures of bedded siliceous deposits. *Sedimentology*. **58**, 325-351.

Behl, R.J., Smith, B.M., 1992. Silicification of deep-sea sediments and the oxygen isotope composition of diagenetic siliceous rocks from the western Pacific, Pigafetta and East Mariana basins, *In*: Larson, R.L., Lancelot, Y., Fisher, A. *et al., (eds), Proceedings Ocean Drilling Program, Scientific Results, 129*. Ocean Drilling Program, College Station, TX, 81–117.

Berndt, C., Bunz, S., Mienert, J., 2003. Polygonal fault systems on the mid-Norwegian margin: a long-term source for fluid flow. *In*: Van Rensbergen, P., Hillis, R.R., Maltman, A.J. & Morley, C.K. (eds) *Subsurface Sediment Mobilization*. .Geological Society, London, Special Publications **216**, 283-290.

Berndt, C., Bunz, S., Clayton, T., Mienert, J., Saunders, M., 2004. Seismic character of bottom simulating reflectors: examples from the mid-Norwegian margin. *Marine and Petroleum Geology* **21**, 723-733.

Berndt, C., 2005. Focused fluid flow in passive continental margins. *Philosophical Transactions of*

the Royal Society A: Mathematical, Physical and Engineering Sciences **363**, 2855-2871.

Berner, R.A., 1980. *Early diagenesis*. Princeton University Press.

Bishop, A.W., Green, G.E., Garga, V.K., Andresen, A., Brown, J.D., 1971. A new ring shear apparatus and its application to the measurement of residual strength. *Geotechnique* **21**, 273-328.

Bjørlykke, K., Høeg, K., 1997. Effects of burial diagenesis on stresses, compaction and fluid flow in sedimentary basins. *Marine and Petroleum Geology* **14**, 267-276.

Bonatti, E., 1976. Serpentinite protrusions in the oceanic crust. *Earth and Planetary Science Letters* **32**, 107-113.

Bouma, A.H., 2004. Key controls on the characteristics of turbidite systems. *In* Lomas, S.A., Joseph, P. (ed.) *Confined Turbidite Systems*. Geological Society, London, Special Publications **222**, 9-22.

Bramlette, M.N., 1946. The Monterey Formation of California and the origin of its siliceous rocks. *US Geological Survey Professional Paper* **212**, 57.

Brand, U., Veizer, J., 1980. Chemical diagenesis of a multicomponent carbonate system. 1. Trace elements. *Journal of Sedimentary Petrology* **50**, 1219-1236.

Brekke, H., Dahlgren, K.I.T., Nyland, B., Magnus, C., 1999. The prospectivity of the Vøring and Møre basins on the Norwegian Sea continental margin. Geological Society, London, *Petroleum Geology Conference Series* **5**, 261 -274.

Brekke, H., 2000. The tectonic evolution of the Norwegian Sea Continental Margin with emphasis on the Vøring and Møre Basins. *Dynamics of the Norwegian Margin.* Geological Society London, Special Publications **167**, 327.

Brown, A.R, 2005a. *Interpretation of Three-Dimensional Seismic Data*, AAPG Memoir. AAPG and SEG.

Brown, A.R., 2005b. Pitfalls in 3D seismic interpretation. *The Leading Edge* **24**, 716-717.

Bryant, W.R., Bennett, R., Katerman, C., 1981. Shear strength, consolodation, porosity and permability of oceanic sediments, in: *The Sea*. John Wiley & Sons, New York, pp. 1555 - 1616.

Bull, S., Cartwright, J.A., Huuse, M., 2009. A review of kinematic indicators from mass-transport complexes using 3D seismic data. *Marine and Petroleum Geology* **26**, 1132-1151.

Butler, R., Turner, J., 2010. Gravitational collapse at continental margins: products and processes; an introduction. *Journal of the Geological Society, London* **167**, 569-570.

C

Carr, R.M., Fyfe, W.S., 1958. Some observations on the crystallization of amorphous silica. *American*

Mineralogist **43**, 908-916.

Cartwright, J.A., 1994. Episodic basin-wide fluid expulsion from geopressured shale sequences in the North Sea basin. *Geology* **22**, 447-450.

Cartwright, J.A., Lonergan, L., 1996. Volumetric contraction during the compaction of mudrocks: a mechanism for the development of regional-scale polygonal fault systems. *Basin Research* **8**, 183-193.

Cartwright, J.A., Dewhurst, D.N., 1998. Layer-bound compaction faults in fine-grained sediments. *Geological Society of America Bulletin* **110**, 1242.

Cartwright, J.A., Huuse, M., 2005. 3D seismic technology: the geological 'Hubble'. *Basin Research* **17**, 1-20.

Cartwright, J.A., 2007. The impact of 3D seismic data on the understanding of compaction, fluid flow and diagenesis in sedimentary basins. *Journal of the Geological Society, London* **164**, 881.

Cartwright, J.A., 2009. Palaeostress reconstruction using polygonal faults, in: Presented at the merican Geophysical Union, Fall Meeting.

Carver, R.E., 1968. Differential compaction as a cause of regional contemporaneous faults. *AAPG Bulletin* **52**, 414-419.

Chilingar, G.V., Wolf, K.H., 1988. Diagenesis*, Developments in sedimentology*. Elsevier, Amsterdam.

Clausen, J.A., Gabrielsen, R.H., Reksnes, P.A., Nysæther, E., 1999. Development of intraformational (Oligocene-Miocene) faults in the northern North Sea: influence of remote stresses and doming of Fennoscandia. *Journal of Structural Geology* **21**, 1457-1475.

Compton, J.S., 1991. Porosity reduction and burial history of siliceous rocks from the Monterey and Sisquoc Formations, Point Pedernales area, California. *Geological Society of America Bulletin* **103**, 625-636.

Cosgrove, J.W., 1999. Forced folds and fractures: An introduction. *Forced Folds and Fractures* Geological Society, London, Special Publications **169**, 1-6.

Crans, W., Mandl, G., Haremboure, J., 1980. On the Theory of Growth Faulting: A Geomechanical Delta Model Based on Gravity Sliding. *Journal of Petroleum Geology* **2**, 265-307.

D

Davies, R.J., 2005. Differential compaction and subsidence in sedimentary basins due to silica diagenesis: A case study. *Geological Society of America Bulletin* **117**, 1146-1155.

Davies, R.J., Cartwright, J.A., 2002. A fossilized Opal A to Opal C/T transformation on the northeast Atlantic margin: support for a significantly elevated Palaeogeothermal gradient during the Neogene? *Basin Research* **14**, 467-486.

Davies, R.J., Cartwright, J.A., 2007. Kilometer-scale chemical reaction boundary patterns and

deformation in sedimentary rocks. *Earth and Planetary Science Letters* **262**, 125-137.

Davies, R.J., Clark, I.R., 2006. Submarine slope failure primed and triggered by silica and its diagenesis. *Basin Research* **18**, 339-350.

Davies, R.J., Goulty, N.R., Meadows, D., 2008. Fluid flow due to the advance of basin-scale silica reaction zones. *Geological Society of America Bulletin* **120**, 195.

Davies, R.J., Goulty, N.R., Ireland, M.T., 2009. Silica diagenesis – investigating kilometer scale diagenetic patterns through three-dimensional seismic reflection data and scientific drilling [WWW Document]. IODP - Active proposals. URL http://www.iodp.org/index.php?option=com_docman&task=doc_download&gid=2833

Davies, R.J., Huuse, M., Hirst, P., Cartwright, J.A., Yang, Y., 2006. Giant clastic intrusions primed by silica diagenesis. *Geology* **34**, 917-920.

Davies, R.J., Ireland, M.T., Cartwright, J.A., 2009. Differential compaction due to the irregular topology of a diagenetic reaction boundary: a new mechanism for the formation of polygonal faults. *Basin Research* **21**, 354-359.

Davies, R.J., Ireland, M.T., in review. Thermal triggering and propagation of polygonal fault arrays by volume reduction reactions in siliceous sediments. *Marine Geology*.

Davies, R.J., Posamentier, H.W., 2005. Geologic processes in sedimentary basins inferred from three-dimensional seismic imaging. *GSA Today* **15**, 4-9.

Doré, A.G., Lundin, E.R., Jensen, L.N., Birkeland, Ø., Eliassen, P.E., Fichler, C., 1999. Principal tectonic events in the evolution of the northwest European Atlantic margin. Geological Society, London, *Petroleum Geology Conference Series* **5**, 41-61.

Doré, A.G., Lundin, E.R., Kusznir, N.J., Pascal, C., 2008. Potential mechanisms for the genesis of Cenozoic domal structures on the NE Atlantic margin: pros, cons and some new ideas. *Nature and Origin of Compression in Passive Margins.* Geological Society, London, Special Publications **306**, 1-26.

Dugan, B., Flemings, P.B., 2000. Overpressure and Fluid Flow in the New Jersey Continental Slope: Implications for Slope Failure and Cold Seeps. *Science* **289**, 288-291.

Dugan, B., Flemings, P.B., 2002. Fluid flow and stability of the US continental slope offshore New Jersey from the Pleistocene to the present. *Geofluids* **2**, 137-146.

Durham, L.S., 2010. Monterey shale gets new look. AAPG Explorer, **31**, 11.

E

Eichhubl, P., Behl, R.J., 1998. Diagenesis, Deformation, and Fluid Flow in the Miocene Monterey Formation, in: *Diagenesis, Deformation, and Fluid Flow in the Miocene Monterey Formation*, Special Publication of the Pacific Section Society of Economic Paleontologists

and Mineralogists. Society for Sedimentary Geology.

Eichhubl, P., Boles, J.R., 2000a. Focused fluid flow along faults in the Monterey Formation, coastal California. *Bulletin of the Geological Society of America* **112**, 1667-1679.

Eichhubl, P., Boles, J.R., 2000b. Rates of fluid flow in fault systems; evidence for episodic rapid fluid flow in the Miocene Monterey Formation, coastal California. *American Journal of Science* **300**, 571-600.

Eldholm, O., Thiede, J., 1987. Site 642: Norwegian Sea, in: Eldholm, O., Thiede, J., Aharonov, E., Barton, C., Bjørklund, K., Bleil, U. (Eds.), *In*: Eldholm, O., Thiede, J., Taylor, E.*et al*. (eds) *Proceedings of the Ocean Drilling Program, Initial Reports, 104.*Ocean Drilling Program, College Station, TX, 455-615.

Eldholm, O., Thiede, J. & Taylor, E. 1987a. Evolution of the Norwegian continental margins: background and objectives. *In*: Eldholm, O., Thiede, J., Taylor, E.*et al*. (eds) *Proceedings of the Ocean Drilling Program, Initial Reports, 104.*Ocean Drilling Program, College Station, TX, 5–25.

Eldholm, O., Theide, J., Taylor, E., Shipboard Scientific Party, 1987b. Summary and preliminary conclusions, ODP Leg 104, in: Eldholm, O., Thiede, J., Aharonov, E., Barton, C., Bjørklund, K., Bleil, U. (Eds.), *In*: Eldholm, O., Thiede, J., Taylor, E.*et al*. (eds) *Proceedings of the Ocean Drilling Program, Initial Reports, 104.*Ocean Drilling Program, College Station, TX.

Elvebakk, G., Hunt, D.W., Stemmerik, L., 2002. From isolated buildups to buildup mosaics: 3D seismic sheds new light on upper Carboniferous-Permian fault controlled carbonate buildups, Norwegian Barents Sea. *Sedimentary Geology* **152**, 7-17.

Elverhøi, A., Norem, H., Andersen, E.S., Dowdeswell, J.A., Fossen, I., Haflidason, H., Kenyon, N.H., Laberg, J.S., King, E.L., Sejrup, H.P., others, 1997. On the origin and flow behavior of submarine slides on deep-sea fans along the Norwegian–Barents Sea continental margin. *Geo-Marine Letters* **17**, 119–125.

Emery, D., Myers, K., Bertram, G.T., 1996. *Sequence stratigraphy*. Blackwell Science, Oxford; Cambridge, Mass.

Engelder, T., 1993. *Stress regimes in the lithosphere*. Princeton University Press, Princeton, New Jersey.

Exon, N.F., Lafoy, Y., Hill, P.J., Dickens, G.R., Pecher, I., 2007. Geology and petroleum potential of the Fairway Basin in the Tasman Sea. *Australian Journal of Earth Sciences* **54**, 629-645.

F

Ferrill, D.A., Morris, A.P., Jones, S.M., Stamatakos, J.A., 1998. Extensional layer-parallel shear and normal faulting. *Journal of Structural Geology* **20**, 355–362.

Fredrich, J.T., Arguello, J.G., Deitrick, G.L., Rouffignac, E.P., 2000. Geomechanical modeling of reservoir compaction, surface subsidence, and casing damage at the Belridge diatomite field. *SPE Reservoir Evaluation and Engineering* **3**, 348-359.

Freed, R., Peacor, D., 1989. Variability in temperature of the smectite/illite reaction in Gulf Coast sediments. *Clay Mineral* **24**, 171-180.

Frey-Martínez, J., Cartwright, J.A., James, D., 2006. Frontally confined versus frontally emergent submarine landslides: A 3D seismic characterisation. *Marine and Petroleum Geology* **23**, 585-604.

G

Gafeira, J., Long, D., Scrutton, R., Evans, D., 2010. 3D seismic evidence of internal structure within Tampen Slide deposits on the North Sea Fan: are chaotic deposits that chaotic? *Journal of the Geological Society London* **167**, 605-616.

Gallinari, M., Ragueneau, O., Corrin, L., DeMaster, D.J., Treguer, P., 2002. The importance of water column processes on the dissolution properties of biogenic silica in deep-sea sediments I. Solubility. *Geochimica et Cosmochimica Acta* **66**, 2701-2717.

Gardner, J.V., Prior, D.B., Field, M.E., 1999. Humboldt Slide -- a large shear-dominated retrogressive slope failure. *Marine Geology* **154**, 323-338.

Gay, A., Lopez, M., Cochonat, P., Sermondadaz, G., 2004. Polygonal faults-furrows system related to early stages of compaction - upper Miocene to recent sediments of the Lower Congo Basin. *Basin Research* **16**, 101-116.

Gay, A., Berndt, C., 2007. Cessation/reactivation of polygonal faulting and effects on fluid flow in the Voring Basin, Norwegian Margin. *Journal of the Geological Society London* **164**, 129.

Gee, M., Gawthorpe, R., Friedmann, J., 2005. Giant striations at the base of a submarine landslide. *Marine Geology* **214**, 287-294.

Gomez, M., Verges, J., Fernandez, M., Torne, M., Ayala, C., Wheeler, W., Karpuz, R., 2004. Extensional geometry of the Mid Norwegian Margin before Early Tertiary continental breakup. *Marine and Petroleum Geology* **21**, 177-194.

Gonzalez, R.C., Woods, R.E., 2008. Image Segmentation, in: *Digital image processing*. Pearson Prentice Hall, Upper Saddle River, N.J.

Goulty, N.R., 2001. Polygonal fault networks in fine-grained sediments-an alternative to the syneresis mechanism. *First Break* **19**, 69-73.

Goulty, N.R., 2002. Mechanics of layer-bound polygonal faulting in fine-grained sediments. *Journal of the Geological Society London* **159**, 239-246.

Goulty, N.R., 2008. Geomechanics of polygonal fault systems: a review. *Petroleum Geoscience* **14**, 389.

Goulty, N.R., Swarbrick, R.E., 2005. Development of polygonal fault systems: a test of hypotheses. *Journal of the Geological Society London* **162**, 587-590.

Graham, S.A., Williams, L.A., 1985. Tectonic, depositional, and diagenetic history of Monterey

Formation (Miocene), central San Joaquin basin, California. *AAPG Bulletin* **69**, 385.

Grimm, K.A., Orange, D.L., 1997. Synsedimentary fracturing, fluid migration, and subaqueous mass wasting; intrastratal microfractured zones in laminated diatomaceous sediments, Miocene Monterey Formation, California, U.S.A. *Journal of Sedimentary Research* **67**, 601-613.

Gross, M.R., Gutiérrez-Alonso, G., Bai, T., Wacker, M.A., Collinsworth, K.B., Behl, R.J., 1997. Influence of mechanical stratigraphy and kinematics on fault scaling relations. *Journal of Structural Geology* **19**, 171-183.

Guerin, G., Goldberg, D., 1996. Acoustic and elastic properties of calcareous sediments across a siliceous diagenetic front on the eastern U.S. continental slope. *Geophysical Research Letters* **23**, 2697–2700.

H

Haflidason, H., Sejrup, H.P., Nygard, A., Mienert, J., Bryn, P., Lien, R., Forsberg, C.F., Berg, K., Masson, D.G., 2004. The Storegga Slide: architecture, geometry and slide development. *Marine Geology* **213**, 201-234.

Hamilton, E.L., 1976. Variations of density and porosity with depth in deep-sea sediments. *Journal of Sedimentary Research* **46**, 280-300.

Hansen, J.P.V., Cartwright, J.A., Huuse, M., Clausen, O.R., 2005. 3D seismic expression of fluid migration and mud remobilization on the Gjallar Ridge, offshore mid-Norway. *Basin Research* **17**, 123-139.

Hansen, D.M., Shimeld, J.W., Williamson, M.A., Lykke-Andersen, H., 2004. Development of a major polygonal fault system in Upper Cretaceous chalk and Cenozoic mudrocks of the Sable Subbasin, Canadian Atlantic margin. *Marine and Petroleum Geology* **21**, 1205–1219.

Haxby, W.F., Labrecque, J.L., Weissel, J.K., Karner, G.D., 1983. Digital images of combined oceanic and continental data sets and their use in tectonic studies. *EOS Transactions* **64**, 995-1004.

Hein, J., Scholl, D., Barron, J., Jones, M.G., Miller, J., 1978. Diagenesis of late Cenozoic diatomaceous deposits and formation of the bottom simulating reflector in the southern Bering Sea. *Sedimentology* **25**, 155-181.

Hempel, P., Mayer, L., Taylor, E., Bohrmann, G., Pittenger, A., 1989. The influence of biogenic silica on seismic lithostratigraphy at ODP sites 642 and 643, eastern Norwegian sea, in: *Proceedings of Ocean Drilling Program*. Ocean Drilling Program, College Station, TX.

Henrich, R., 1987. Diagenetic environments of authigenic carbonates and opal-ct crystallization in Lower Miocene to Upper Oligocene Deposits of the Norwegian Sea (ODP Site 643, Leg 104), in: *Proceedings of the Ocean Drilling Program*. pp. 233–248.

Herman, Y., 1972. Origin of Deep Sea Cherts in the North Atlantic. *Nature* **283**, 392-393.

Higgs, W.G., McClay, K.R., 1993. Analogue sandbox modelling of Miocene extensional faulting in the Outer Moray Firth. *Tectonics and Seismic Sequence Stratigraphy*. Geological Society,

London, Special Publications **71**, 141-162.

Hill, P.R., Marsters, J.C., 1990. Controls on physical properties of Peru continental margin sediments and their relationship to deformation styles, in: Suess, E., von Huene, R. (Eds.), *Proceeding of the Ocean Drilling Program, Scientific Results, 112*. Ocean Drilling Program, College Station, TX, pp. 407-409.

Hjelstuen, B.O., Eldholm, O., Skogseid, J., 1997. Vøring Plateau diapir fields and their structural and depositional settings. *Marine Geology* **144**, 33-57.

Hjelstuen, B.O., Eldholm, O., Skogseid, J., 1999. Cenozoic evolution of the northern Vøring margin. *Geological Society of America Bulletin* **111**, 1792 -1807.

Hovland, M., Judd, A., 1988. *Seabed Pockmarks and Seepages: Impact on Geology, Biology and the Marine Environment*. Graham and Trotman Ltd., London.

Hovland, M., Nygaard, E., Thorbjornsen, S., 1998. Piercement shale diapirism in the deep-water Vema Dome area, Voring basin, offshore Norway. *Marine and Petroleum Geology* **15**, 191-201.

Hovland, M., Svensen, H., Forsberg, C.F., Johansen, H., Fichler, C., Fosså, J.H., Jonsson, R., Rueslåtten, H., 2005. Complex pockmarks with carbonate-ridges off mid-Norway: Products of sediment degassing. *Marine Geology* **218**, 191–206.

Huang, Z., Gradstein, F.M., 1990. Depth-porosity relationship from deep sea sediments. *In:* Scientific Drilling, **1**, 157-162.

Hurley, M.T., Hempel, P., 1990. Porosity and velocity vs. depth and effective stress in carbonate sediments. *In:* Duncan, R.A., Backman, J., Peterson, L.C., et al., *Proceedings of the Ocean Drilling Program, Scientific Results,*115: College Station, TX (Ocean Drilling Program), 773–777.

Hustoft, S., Mienert, J., Bunz, S., Nouzé, H., 2007. High-resolution 3D-seismic data indicate focussed fluid migration pathways above polygonal fault systems of the mid-Norwegian margin. *Marine Geology* **245**, 89-106.

I

Integrated Ocean Drilling Program, 2001. Earth, Oceans and Life. Scientific Investigation of the Earth System. Using Mulltiple Drilling Platforms and New Technologies. Initial Science Plan.

Integrated Ocean Drilling Program, 2010. *Data and core samples* [Online]. Available from: http://www.iodp-usio.org/Data_Samples/default.html [Accessed: 3 Decemeber 2010]

Ireland, M.T., Goulty, N.R., Davies, R.J., 2010. Influence of pore water chemistry on silica diagenesis: evidence from the interaction of diagenetic reaction zones with polygonal fault systems. *Journal of the Geological Society, London* **167**, 273-279.

Ireland, M.T., Davies, R.J., Goulty, N.R., Carruthers, T.D., 2011. Structure of a silica diagenetic

transformation zone: the Gjallar Ridge, offshore Norway. *Sedimentology* **58,** 424-441.

Isaacs, C.M., 1981. Porosity reduction during diagenesis of the Monterey Formation, Santa Barbara coastal area, California, in: The Monterey Formation and related siliceous rocks of California: proceedings of an SEPM Research Symposium dedicated to examine the paleontology, sedimentology, depositional environments, and diagenesis of the Monterey Formation. Pacific Section, Society of Economic Paleontologists and Mineralogists, p. 257.

Isaacs, C.M., 1982. Influence of rock composition on kinetics of silica phase-changes in the Monterey Formation, Santa-Barbara area, California. *Geology* **10**, 304-308.

Iverson, R., 1997. The physics of debris flows. *Reviews of Geophysics* **35**, 245-296.

J

Jones, B., Renaut, R.W., 2004. Water Content of Opal-A: Implications for the Origin of Laminae in Geyserite and Sinter. *Journal of Sedimentary Research* **74**, 117-128.

Jones, J.B., Segnit, E.R., 1971. The nature of opal I. nomenclature and constituent phases. *Journal of the Geological Society of Australia* **18**, 57-68.

K

Kastner, M., Keene, J., Gieskes, J., 1977. Diagenesis of siliceous oozes .1. Chemical controls on rate of opal-A to opal-CT transformation - experimental study. *Geochimica et Cosmochimica Acta* **41**, 1041-&.

Kastner, M., Elderfield, H., Martin, J.B., 1991. Fluids in Convergent Margins: What do We Know about their Composition, Origin, Role in Diagenesis and Importance for Oceanic Chemical Fluxes? *Philosophical Transactions: Physical Sciences and Engineering* **335**, 243-259.

Kenyon, N.H., 1987. Mass-wasting features on the continental slope of Northwest Europe. *Marine Geology* **74**, 57-77.

Keller, G., Barron, J.A., 1983. Paleoceanographic implications of Miocene deep-sea hiatuses. *Geological Society of America Bulletin* **94**, 590-613.

Keller, M., Isaacs, C., 1985. An evaluation of temperature scales for silica diagenesis in diatomaceous sequences including a new approach based on the Miocene Monterey Formation, California. *Geo-Marine Letters* **5**, 31-35.

Ker, S., Marsset, B., Garziglia, S., Le Gonidec, Y., Gibert, D., Voisset, M., Adamy, J., 2010. High-resolution seismic imaging in deep sea from a joint deep-towed/OBH reflection experiment: application to a Mass Transport Complex offshore Nigeria. *Geophysical Journal International* **182**, 1524-1542.

Kim, G.Y., Yoo, D.G., Lee, H.Y., Lee, Y.J., Kim, D.C., 2007. The relationship between silica diagenesis and physical properties in the East/Japan Sea: ODP Legs 127/128. *Journal of*

Asian Earth Sciences **30**, 448-456.

Kobayashi, K., Nakanishi, M., Tamaki, K., Ogawa, Y., 1998. Outer slope faulting associated with the western Kuril and Japan trenches. *Geophysical Journal International* **134**, 356-372.

Kristoffersen, Y., Coakley, B.J., Hall, J.K., Edwards, M., 2007. Mass wasting on the submarine Lomonosov Ridge, central Arctic Ocean. *Marine Geology* **243**, 132-142.

Kusznir, N.J., Hunsdale, R., Roberts, A.M., 2005. Timing and magnitude of depth-dependent lithosphere stretching on the southern Lofoten and northern Vøring continental margins offshore mid-Norway: implications for subsidence and hydrocarbon maturation at volcanic rifted margins, in: *Petroleum Geology Conference series*. Geological Society of London, p. 767.

Kvalstad, T.J., Andresen, L., Forsberg, C.F., Berg, K., Bryn, P., Wangen, M., 2005. The Storegga slide: evaluation of triggering sources and slide mechanics. *Marine and Petroleum Geology* **22**, 245-256.

Kusznir, N.J., Hunsdale, R., Roberts, A.M., 2005. Timing and magnitude of depth-dependent lithosphere stretching on the southern Lofoten and northern Vøring continental margins offshore mid-Norway: implications for subsidence and hydrocarbon maturation at volcanic rifted margins, in: *Petroleum Geology Conference series.* Geological Society of London, p. 767.

L

Laberg, J.S., Dahlgren, K.I.T., Vorren, T.O., 2005. The Eocene–late Pliocene paleoenvironment in the Vøring Plateau area, Norwegian Sea—paleoceanographic implications. *Marine Geology* **214**, 269–285.

Lade, P.V., Overton, D.D., 1989. Cementation Effects in Frictional Materials. *Journal of Geotechnical Engineering* **115**, 1373 - 1387.

Landmark, 2005. SeisWorks/3D Horizon Interpretation, in: *Landmark Users Manuals*. Landmark Graphics Corporation.

Landmark, 2006. GeoProbe User Manual, in: *Landmark Users Manuals*. Landmark Graphics Corporation.

Lansley, M., 2000. 3D seismic survey design: a solution: 3D Seismic surveys: design, tests and experience. *First break* **18**, 162-166.

Laubach, S., Eichhubl, P., Hilgers, C., Lander, R., 2010. Structural diagenesis. *Journal of Structural Geology* **32**, 1866-1872.

Laventer, A., 2009. Diatoms, in: Gornitz, V. (Ed.), *Encylopedia of Paleoclimate and Ancient Environments*. Springer, Berlin, pp. 279–280.

Lawrence, G.W., Cartwright, J.A., 2009. The initiation of sliding on the mid Norway margin in the Møre Basin. *Marine Geology* **259**, 21–35.

Leynaud, D., Mienert, J., Vanneste, M., 2009. Submarine mass movements on glaciated and non-glaciated European continental margins: A review of triggering mechanisms and preconditions to failure. *Marine and Petroleum Geology* **26**, 618-632.

Lisitzin, E., 1972. Water volume in oceans and seas. In: Second International Congress on the history of Oceanography – 1. *Proceedings of the Royal Society of Edinburgh Section B-Biology* **72**, 429.

Lonergan, L., Cartwright, J., Jolly, R., 1998. The geometry of polygonal fault systems in Tertiary mudrocks of the North Sea. *Journal of Structural Geology* **20**, 529-548.

Lonergan, L., Cartwright, J.A., 1999. Polygonal faults and their influence on deep-water sandstone reservoir geometries, Alba Field, United Kingdom central North Sea. *AAPG Bulletin* **83**, 410-432.

Løseth, H., Wensaas, L., Arntsen, B., Hanken, N., Basire, C., Graue, K., n.d. 1000 m Long Gas Blow-Out Pipes. *Marine and Petroleum Geology* **In Press**.

Lundin, E.R., Doré, A.G., 1997. A tectonic model for the Norwegian passive margin with implications for the NE Atlantic; Early Cretaceous to break-up. *Journal of the Geological Society, London* **154**, 545-550.

Lundin, E.R., Doré, A.G., 2002. Mid-Cenozoic post-breakup deformation in the `passive' margins bordering the Norwegian-Greenland Sea. *Marine and Petroleum Geology* **19**, 79-93.

M

Maltman, A., 1994. *The Geological Deformation of Sediments*. Chapman and Hall.

Mandl, G., 1988. *Mechanics of tectonic faulting : models and basic concepts, Developments in structural geology, 1*. Elsevier ; Distributors for the U.S. and Canada, Elsevier Science Pub. Co., Amsterdam; New York; New York, NY, U.S.A.

Mandl, G., Crans, W., 1981. Gravitational gliding in deltas. *Mechanics of Thrusts and Nappes*. Geological Society, London, Special Publications **9**, 41-54.

Martinsen, O.J., 1994. Mass movements, in: The *Geological Deformation of Sediments*. Chapman and Hall, pp. 127-164.

Maslin, M., Owen, M., Day, S., Long, D., 2004. Linking continental-slope failures and climate change: Testing the clathrate gun hypothesis. *Geology* **32**, 53 -56.

Masson, D.G., Harbitz, C., Wynn, R., Pedersen, G., Løvholt, F., 2006. Submarine landslides: processes, triggers and hazard prediction. *Philosophical Transactions of the Royal Society A: Mathematical, Physical and Engineering Sciences* **364**, 2009 -2039.

Mayne, P.W., Kulhawy, F.H., 1982. K0-OCR relationships in soil. *Journal of the Geotechnical Engineering* **108**, 851-872.

McCrory, P. A., Wilson, D. S., Ingle, J. C. Jr., Stanley, R. G., 1995. Neogene Geohistory Analysis of

Santa Maria Basin, California, and Its Relationship to Transfer of Central California to the Pacific Plate: *U.S. Geological Survey Bulletin* **J**.

Meadows, D., Davies, R.J., 2007. Morphological development of basin-scale silica diagenetic fronts revealed with 2D seismic reflection data: offshore Sakhalin, Russian Far East. *Journal of the Geological Society, London* **164**, 1193.

Meadows, D., Davies, R.J., 2009. Predicting porosity reduction due to silica diagenesis using seismic reflection data. *Marine and Petroleum Geology* **26**, 1543-1553.

Micallef, A., Masson, D.G., Berndt, C., Stow, D.A., 2009. Development and mass movement processes of the north-eastern Storegga Slide. *Quaternary Science Reviews* **28**, 433–448.

Miyashiro, A., Shido, F., Ewing, M., 1969. Composition and origin of serpentinites from the Mid-Atlantic Ridge near 24° and 30° North Latitude. *Contributions to Mineralogy and Petrology* **23**, 117-127.

Mjelde, R., Shimamura, H., Kanazawa, T., Kodaira, S., Raum, T., Shiobara, H., 2003. Crustal lineaments, distribution of lower crustal intrusives and structural evolution of the Vøring Margin, NE Atlantic; new insight from wide-angle seismic models. *Tectonophysics* **369**, 199-218.

Morton, J.P., 1985. Rb-Sr evidence for punctuated illite/smectite diagenesis in the Oligocene Frio Formation, Texas Gulf Coast. *Geological Society of America Bulletin* **96**, 114 -122.

Morley, C.K., Guerin, G., 1996. Comparison of gravity-driven deformation styles and behavior associated with mobile shales and salt. *Tectonics* **15**, 1154-1170.

Mosar, J., Lewis, G., Torsvik, T., 2002. North Atlantic sea-floor spreading rates: implications for the Tertiary development of inversion structures of the Norwegian-Greenland Sea. *Journal of the Geological Society, London* **159**, 503-515.

Mosher, D., Shipp, C., Moscardelli, L., 2010. *Submarine Mass Movements and Their Consequences. Springer*, Dordrecht.

Mosher, D.C., Piper, D.J.W., Calvin Campbell, D., Jenner, K.A., 2004. Near-surface geology and sediment-failure geohazards of the central Scotian Slope. *AAPG Bulletin* **88**, 703-723.

Mourgues, R., Cobbold, P., 2006. Sandbox experiments on gravitational spreading and gliding in the presence of fluid overpressures. *Journal of Structural Geology* **28**, 887-901.

Moy, D.J., 2010. The architecture, growth and tectono-stratigraphic significance of rift-oblique lineaments on the NE Atlantic Margin (Unpublished PhD thesis, Durham University).

Murata, K.J., Larson, R.R., 1975. Diagenesis of Miocene siliceous shales, Temblor Range, California. *Journal of Research US Geological Survey* **3**, 553-566.

N

Neagu, R.C., Cartwright, J., Davies, R.J., 2010a. Measurement of diagenetic compaction strain from

quantitative analysis of fault plane dip. *Journal of Structural Geology* **32**, 641-655.

Neagu, R.C., Cartwright, J., Davies, R.J., Jensen, L., 2010b. Fossilisation of a silica diagenesis reaction front on the mid-Norwegian margin. *Marine and Petroleum Geology* **27**, 2141-2155.

Nelson, D.M., Tréguer, P., Brzezinski, M.A., Leynaert, A., Quéguiner, B., 1995. Production and Dissolution of Biogenic Silica in the Ocean: Revised Global Estimates, Comparison With Regional Data and Relationship to Biogenic Sedimentation. *Global Biogeochemical Cycles* **9,** 359-372.

Nobes, D.C., Murry, R.W., Kuramoto, S., Pisciotto, K.A., 1992. Impact of silica diagenesis on physical properties variations. *In*: Kensaku, T., Pisciotto, K., Allan, J., *et al.* (eds) *Proceedings of the Ocean Drilling Program Scientific Results*, *127/128*. Ocean Drilling Program, College Station, TX, Scientific Results. 3-31.

Norwegian Petroleum Directorate, 2009. The NPD's fact-pages. WDSS 6704/12-1. [WWW Document]. URL http://www.npd.no/engelsk/cwi/pbl/en/well/all/3759.htm

Norwegian Petroleum Directorate, 2010. The NPD's fact-pages. WDSS 6302/6-1. [WWW Document]. URL http://www.npd.no/engelsk/cwi/pbl/en/well/all/5086.htm

O

Ortoleva, P.J., 1994. Geochemical Self-organization. Oxford University Press.

P

Pegrum, R.M., Odegard, T., Bonde, K., Hamann, N.E., 2001. Exploration in the Fylla Area, SW Greenland, in: . Presented at the AAPG Regional Conference, St. Petersburg, Russia.

Pittenger, A., Taylor, E., Bryant, W.R., 1989. The influence of biogenic silica on the geotechnical stratigraphy of the Vøring Plateau, Norwegian Sea, in: Proceedings of the Ocean Drilling Program, Scientific Results. College Station, TX, pp. 923 - 940.

Pisciotto, K., 1981. Diagenetic trends in the siliceous facies of the Monterey Shale in the Santa Maria region, California. *Sedimentology* **28**, 547-571.

Planke, S., Rasmussen, T., Rey, S.S., Myklebust, R., 2005. Seismic characteristics and distribution of volcanic intrusions and hydrothermal vent complexes in the Vøring and Møre basins, in: *Petroleum Geology Conference series*. Geological Society of London, p. 833.

Posamentier, H.W., Davies, R.J., Cartwright, J.A., Wood, L., 2007. Seismic geomorphology - an overview. In: *Seismic Geomorphology*, Geological Society, London, Special Publications **277**, 1-14.

R

Reading, H.G., 1998. *Sedimentary environments : processes, facies, and stratigraphy*. Blackwell Science, Oxford [u.a.].

Reimers, C.E., Waldo Wakefield, W., 1989. Flocculation of siliceous detritus on the sea floor of a deep Pacific seamount. *Deep Sea Research Part A. Oceanographic Research Papers* **36**, 1841-1861.

Ren, S., Faleide, J.I., Eldholm, O., Skogseid, J., Gradstein, F., 2003. Late Cretaceous-Paleocene tectonic development of the NW Vøring Basin. *Marine and Petroleum Geology* **20**, 177-206.

Richardson, S., Allen, M.B., Davies, R.J., Grant, S.,Structure and evolution of mass transport complexes in the South Caspian Basin, Azerbaijan. *Basin Research*. **In review**

Riech, V., Roesch, H., 1977. Silica diagenesis in continental margin sediments off Northwest Africa, *In*: Gardner, J., Herring, J., *(eds). Initial Reports of the Deep Sea Drilling Project 41*. Ocean Drilling Program, College Station, TX, 879-905.

Rise, L., Ottesen, D., Berg, K., Lundin, E.R., 2005. Large-scale development of the mid-Norwegian margin during the last 3 million years. *Marine and Petroleum Geology* **22**, 33-44.

S

Santos, R.A., 2000. Adaptive visualization of deepwater turbidite systems in Campos Basin using 3-D seismic. *The Leading Edge* **19**, 512.

Scheck-Wenderoth, M., Raum, T., Faleide, J., Mjelde, R., Horsfield, B., 2007. The transition from the continent to the ocean: a deeper view on the Norwegian margin. *Journal of the Geological Society, London* **164**, 855-868.

Schieber, J., Krinsley, D., Riciputi, L., 2000. Diagenetic origin of quartz silt in mudstones and implications for silica cycling. *Nature* **406**, 981-985.

Schrader, H.J., Fenner, J., 1976. Norwegian Sea Cenozoic diatom biostratigraphy and taxonomy. *In: Initial Reports of the Deep Sea Drilling Project 38*. Ocean Drilling Program, College Station, TX, 921-962.

Schultz-Ela, D.D., 2001. Excursus on gravity gliding and gravity spreading. *Journal of Structural Geology* **23**, 725-731.

Schwab, A.M., Tremblay, S., Hurst, A., 2007. Seismic expression of turbidity-current and bottom-current processes on the Northern Mauritanian continental slope. *Seismic Geomorphology,* Geological Society, London, Special Publications **277**, 237-252.

Sejrup, H.P., King, E.L., Aarseth, I., Haflidason, H., Elverhoi, A., 1996. Quaternary erosion and depositional processes: western Norwegian fjords, Norwegian Channel and North Sea Fan. *In* De Batist, M., Jacobs, P. (Ed) *Geology of Siliciclastic Shelf Seas.* Geological Society London Special Publications **117**, 187.

Sheriff, R.E., Geldart, L.P., 1995. *Exploration seismology*. Cambridge University Press., Cambridge, Angleterre.

Sheriff, R.E., 2002. Encyclopedic dictionary of applied geophysics. Society of Exploration Geophysicists.

Shin, H., Santamarina, J.C., Cartwright, J.A., 2008. Contraction-driven shear failure in compacting uncemented sediments. *Geology* **36**, 931.

Shin, H., Santamarina, J.C., Cartwright, J.A., 2010. Displacement field in contraction-driven faults. *Journal of Geophysical Research* **115**, 1-13

Shipley, T.H., Houston, M.H., Buffler, R.T., Shaub, F.J., McMillen, K.J., Ladd, J.W., Worzel, J.L., 1979. Seismic evidence for widespread possible gas hydrate horizons on continental slopes and rises. *AAPG Bullitin* **63**, 2204–2213.

Statoil internal report. 2008. Report on the Quantitative Analysis of Fifty-One Shale Samples, by X-ray Powder Diffraction

Steefel, C.I., Van Cappellen, P., 1990. A new kinetic approach to modeling water-rock interaction: The role of nucleation, precursors, and Ostwald ripening. *Geochimica et Cosmochimica Acta* **54**, 2657–2677.

Stewart, S.A., Argent, J.D., 2000. Relationship between polarity of extensional fault arrays and presence of detachments. *Journal of Structural Geology* **22**, 693–711.

Stewart, S., 2006. Implications of passive salt diapir kinematics for reservoir segmentation by radial and concentric faults. *Marine and Petroleum Geology* **23**, 843-853.

Stroud, K.A., Booth, D.J., 2007. Engineering mathematics. Industrial Press, New York.

Sultan, N., Cochonat, P., Canals, M., Cattaneo, A., Dennielou, B., Haflidason, H., Laberg, J.S., Long, D., Mienert, J., Trincardi, F., Urgeles, R., Vorren, T., Wilson, C., 2004. Triggering mechanisms of slope instability processes and sediment failures on continental margins: a geotechnical approach. *Marine Geology* **213**, 291-321.

Swarbrick, R.E., Osborne, M.J., Yardley, G.S., 2002. Comparison of overpressure magnitude resulting from the main generating mechanisms. *Memoirs American Association of Petroleum Geologists* **76**, 1-12.

T

Tada, R., Iijima, A., 1983. Petrology and diagenetic changes of Neogene siliceous rocks in northern Japan. *Journal of Sedimentary Research* **53**, 911-930.

Tada, R., 1991. Compaction and cementation in siliceous rocks and their possible effect on bedding enhancement., in: Cycles and Events in *Stratigraphy*. pp. 480–491.

Talwani, M., Udintsev, G.B., Bjoerklund, K., Caston, V.N.D., Faas, R.W., van Hinte, J.E., Kharin, G.N., Morris, D.A., Mueller, C., Nilsen, T.H., Warnke, D.A., White, S.M., Manum, S.B.,

Raschka, H., Eckhardt, F., Schrader, H., 1976. Sites 338-343. Initial Reports of the Deep Sea Drilling Project 38, 151-387.

Tanaka, H., Locat, J., 1999. A microstructural investigation of Osaka Bay clay : the impact of microfossils on its mechanical behaviour. *Canadian Geotechnical Journal* **36**, 493-508.

Tewksbury, B., Abdelsalam, M.G., Tewksbury-Christle, C., Hogan, J., Jerris, T.J., Pandey, A., 2009. Reconnaissance study of domes and basins in Tertiary sedimentary rocks in the western desert of Egypt using high resolution satellite imagery, in: . Presented at the GSA Annual Meeting, Portland, USA.

Terzaghi, K., 1943. *Theoretical Soil Mechanics,* John Wiley and Sons, New York.

Trabant, P., 1977. Synthesis of physical properties data from DSDP Leg 41. *In:* Gardner, J., Herring, J., *Initial Reports of the Deep Sea Drilling Project 41*, Ocean Drilling Program, College Station, TX, United States1199-1213.

Treguer, P., Nelson, D.M., Van Bennekom, A.J., DeMaster, D.J., Leynaert, A., Queguiner, B., 1995. The Silica Balance in the World Ocean: A Reestimate. *Science* **268**, 375-379.

Tucholke, B., 1978. Relationships between acoustic stratigraphy and lithostratigraphy in the western North Atlantic basin, *In*: Tucholke, B.E., Vogt, P.R., Murdmaa, I.O., *et al*., *Initial Reports of the Deep Sea Drilling Project 43*. Ocean Drilling Program, College Station, TX, United States. 827-846.

Twiss, R.J., Moores, E.M., 2007. *Structural geology*. W.H. Freeman, New York, NY.

V

Vail, P., Mitchum, R., Todd, R., Widmier, J., Thompson, S., Sangree, J., Bubb, J., Hatleilid, W., 1977. Seismic stratigraphy and global changes of sea level, in: Payton, C. (Ed.), Seismic Stratigraphy-Applications to Hydrocarbon Exploration, *American Association of Petroleum. Geologists Memoirs*. pp. 49 - 212.

Vanderborght, J.P., Wollast, R., Billen, G., 1977. Kinetic models of diagenesis in disturbed sediments. Part 1. Mass transfer properties and silica diagenesis. *Limnology and Oceanography* **22**, 787-793.

Vanneste, M., Mienert, J., Bunz, S., 2006. The Hinlopen Slide: A giant, submarine slope failure on the northern Svalbard margin, Arctic Ocean. *Earth and Planetary Science Letters* **245**, 373-388.

Vear, A., 2005. Deep-water plays of the Mauritanian continental margin. Geological Society, London, Petroleum Geology Conference series **6**, 1217-1232.

Victor, P., Moretti, I., 2006. Polygonal fault systems and channel boudinage: 3D analysis of multidirectional extension in analogue sandbox experiments. *Marine and Petroleum Geology* **23**, 777–789.

Volpi, V., Camerlenghi, A., Hillenbrand, C.D., Rebesco, M., Ivaldi, R., 2003. Effects of biogenic silica on sediment compaction and slope stability on the Pacific margin of the Antarctic

Peninsula. *Basin Research* **15**, 339-363.

W

Watterson, J., Walsh, J., Nicol, A., Nell, P., Bretan, P., 2000. Geometry and origin of a polygonal fault system. *Journal of the Geological Society, London* **157**, 151-162.

White, R., 1980. Partial coherence matching of synthetic seismograms with seismic traces. *Geophysical Prospecting* **28**, 333-358.

Williams, L., Parks, G., Crerar, D., 1985. Silica diagenesis: I. Solubility controls. *Journal of Sedimentary Research* **55**, 301-311.

Williams, L., Crerar, D., 1985. Silica diagenesis: II. General mechanisms. *Journal of Sedimentary Research* **55**, 312-321.

Wolf-Welling, T.C.W., Brenner, W., Mienert, J., Theide, J., 1997. Synatlab database tars. DSDP Sites 338 and 343 age-depth models. [WWW Document]. URL http://www.geomar.de/ twolf

Worden, R.H., Morad, S., 2000. *Quartz cementation in sandstones*. Blackwell Science, Malden, MA.

Y

Yilmaz, Ö., Doherty, S.M., 1987. *Seismic data processing*. Society of Exploration Geophysicists, Tulsa, OK.

NOTE ON APPENDIX

Appendices which contain large tables of data and well logs are supplied in electronic format on the CD-ROM included with this thesis. Also included on this CD-ROM is an Adobe Acrobat PDF of the thesis in its entirety, PDF copies of journal articles by or co-authored by the author of this thesis. Electronic versions of all the figures are also included. A full list of electronic files is provided in Appendix C.

APPENDIX A - GLOSSARY OF TERMS

2-D – two dimensional, referring to a single plane in either the x,y direction, or x,z, or y,z. In this thesis, often refers to seismic reflection data and a single line of data in the x,z plane

3-D – three-dimensional, referring to a feature or data which can be described in terms of x,y,z co-ordinates. In this thesis, often refers to seismic reflection data

Amorphous – refers to a disordered non-crystalline structure in material sciences.

Acoustic impedance – product of seismic velocity and density of material, determines the proportion of seismic wave energy transmitted across geological interfaces.

Biogenic – refers to component of sediment which has formed as a result of primary productivity.

Cristobalite – a quartz polymorph which commonly has a diagenetic origin, it is only stable above temperature of 1470 celcius, below this it is unstable. Metling point 1710°C, boiling point 2590°C, density 2.27 g cm3

Crossline - One of the two sequentially numbered orthogonal reference coordinates for 3-D seismic surveys the other being the inline.

Diatom –Phytoplankton organism which are common in oceanic and lake settings, their cell walls are comprised of silica (SiO2)

Dip – Referring to the seismic attribute, the calculation for dip is:

$$\text{Dip} = \sqrt{\left[\left(\frac{dt}{dx}\right)^2 + \left(\frac{dt}{dy}\right)^2\right]} \times 1000$$

where: dt/dx is the dip in the x direction, and dt/dy is the dip in the y direction, with x and y as real-world coordinates.

Diffraction hyperbola – geometric description of the arrival of a wavefront in seismic reflection data due to a point source

Edge detection – Referring to the edge detection seismic attribute. Calculated by:

$$x = (C + 2F + K) - (A + 2D + G)$$

$$y = (A + 2B + C) - (G + 2H + K)$$

$$edge = \sqrt{x^2} + y^2$$

where A – K are sample points on seismic horizon.

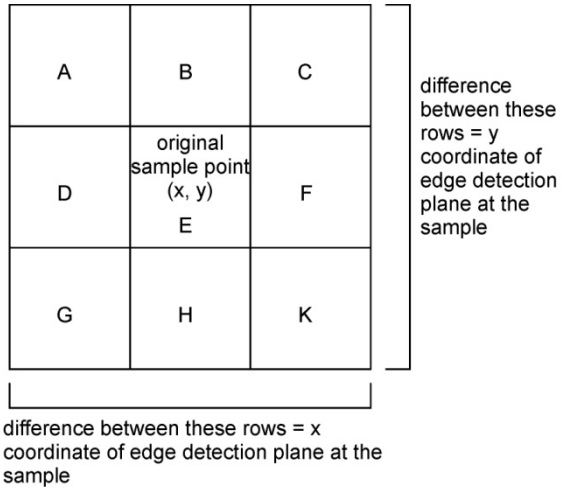

Elastic constants – Constants that define the elastic properties of an isotropic medium and which control the seismic wave velocity of the medium.

Fresnel zone – area surrounding any point on the reflector from which reflected energy arrives at the receiver more or less in phase and thus contributing to the signal at that reflection point. For 2-D data the Fresnel zone is reduced to an ellipse after migration, and for 3-D data a circle.

Horizon — refers to a tracked seismic reflection, corresponding to a geologically significant event or feature, for instance the seabed or an unconformity.

In-line - One of the two sequentially numbered orthogonal reference coordinates for 3-D seismic surveys the other being the crossline.

K_0 –The lateral coefficient of Earth pressure at rest, which can be defined as the pressure which soil, or sediments exert in the horizontal plane.

mbsf – abbreviation of metres below seafloor.

Normal incidence - raypath impinging on an interface at right angles.

Ocean productivity – relates to the production of organic material from the Earth's oceans, primarily as a result of photosynthesis.

Opal – A – refers to amorphous (see separate entry) silica

Opal – CT – refers to cristobolite/tridymite (see separate entries)

P-wave – called pressure waves, are longitudinal waves, i.e., the oscillation occurs parallel to the travel direction of the propagating wave. The restoring force for P-waves is provided by the medium's bulk modulus.

Polymorph – refers to different crystal forms of materials with the same given chemistry.

Quartz – the most stable form of silica, with a formula of SiO2. Melting point 1427°C, boiling point 2230°C, density 2.634 g cm3.

Radiolarians – a protozoa that can produce intricate siliceous skeletons.

Reflection coefficient - The ratio of the amplitude of the displacement of a reflected wave to that of the incident wave.

S–wave – shear wave, where the restoring force for a wave in an elastic medium is provided by shear. S-waves are divergenceless

Silica – Common name for silicon dioxide (SiO2). Silica is the most abundant mineral on Earth.

Silicoflagellates – group of unicellular alage found in marine settings, which produce a siliceous skeleton.

Structure cube – seismic discontinuity (D) attribute, the mathematics of which can be simplified to:

$$D = 100\left(1 - \frac{1}{E}\sum_{i=1}^{M}(x_i \times x_a)^2\right)$$

where E, is total energy in set of traces (which is the sum of the squares of the amplitudes in a wavelet) M, xa is unit vector of average trace, xi represents unit vector trace. Discontinuity varies from 0 for perfectly continuous data to 100 for perfectly discontinuous data.

Tridymite – a silica polymorph, which may have a diagenetic origin, melting point 1610°C, boiling point 2230°C, density 2.6 g cm3.

Unix – computer operating system

XRD – X-ray diffraction

XRDP – X-ray powder diffraction

APPENDIX B – ADDITIONAL SEISMIC DATA

HORIZON MAPS – GJALLAR RIDGE

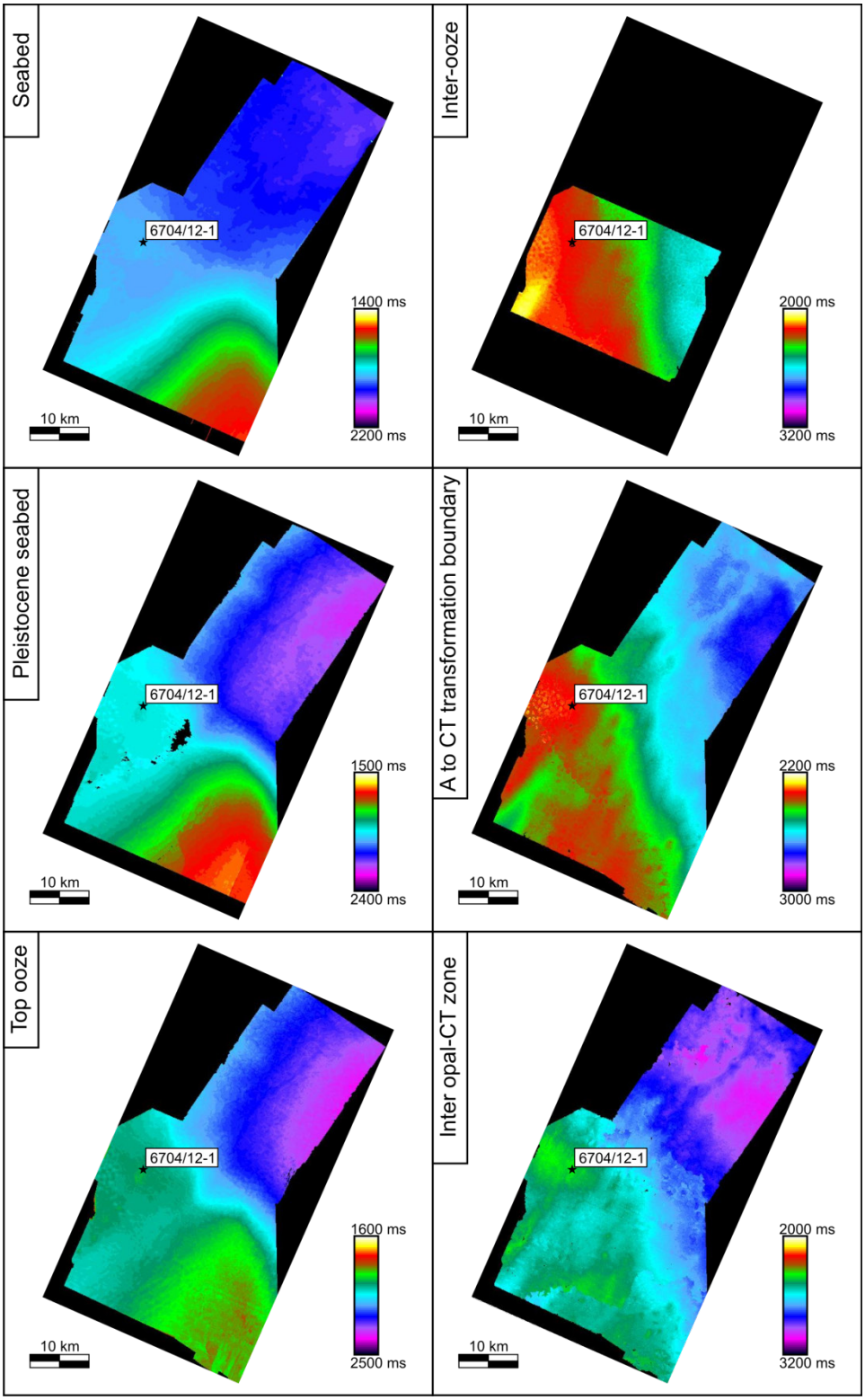

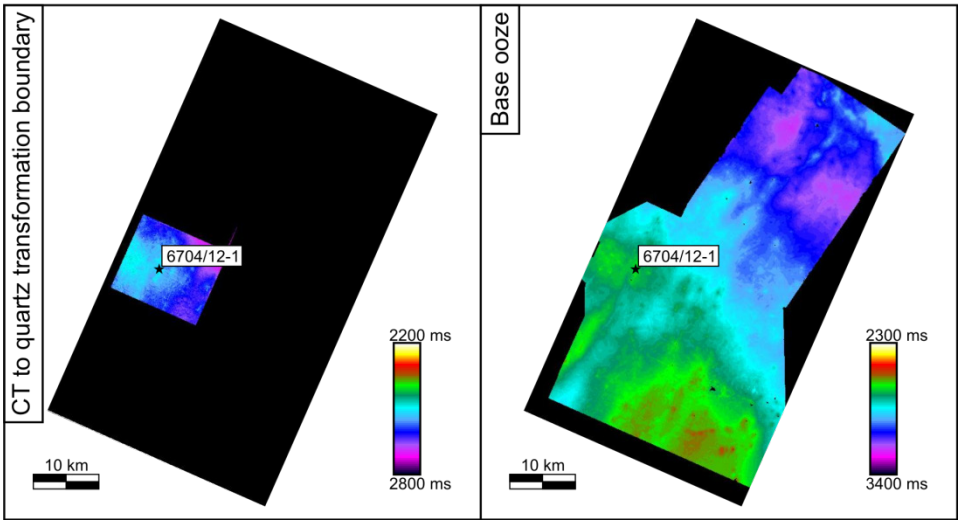

Alternative horizon names used in text:

A to CT transformation boundary - Horizon 1 (Chapter 3) and reflection A (Chapter 4)

CT to quartz transformation boundary – Horizon 2 (Chapter 3)

Inter opal-CT zone – Horizon 1a (Chapter 3) and reflection D (Chapter 4)

HORIZON MAPS – VEMA DOME

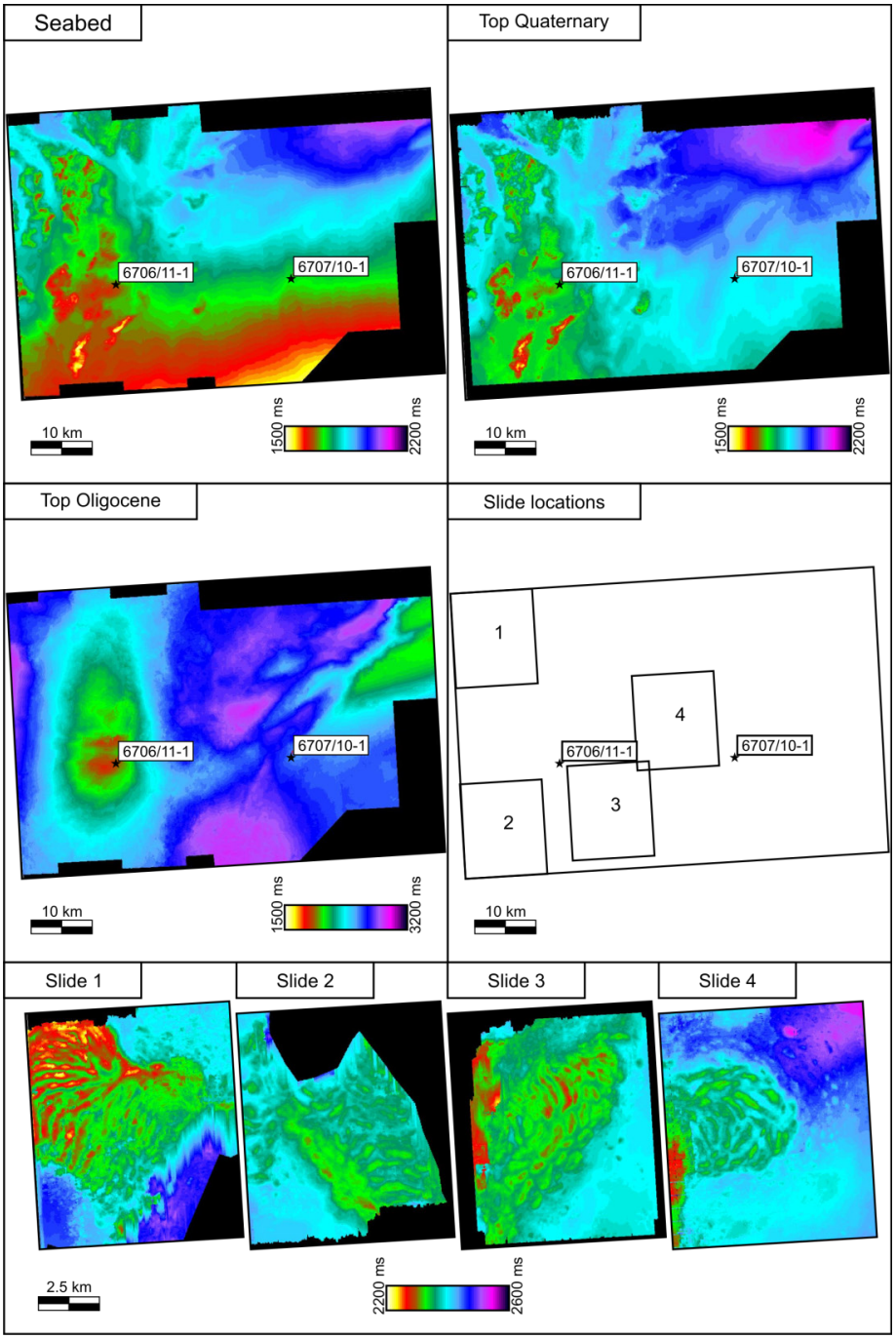

Alternative horizon names used in text:

Slide 1 – Reflection A (Chapter 6)

Slide 2 – Reflection D (Chatper 6)

Slide 3 – Reflection G (Chapter 6)

Slide 4 – Reflection J – (Chapter 6)

HORIZON MAPS – MAURITANIA BASIN

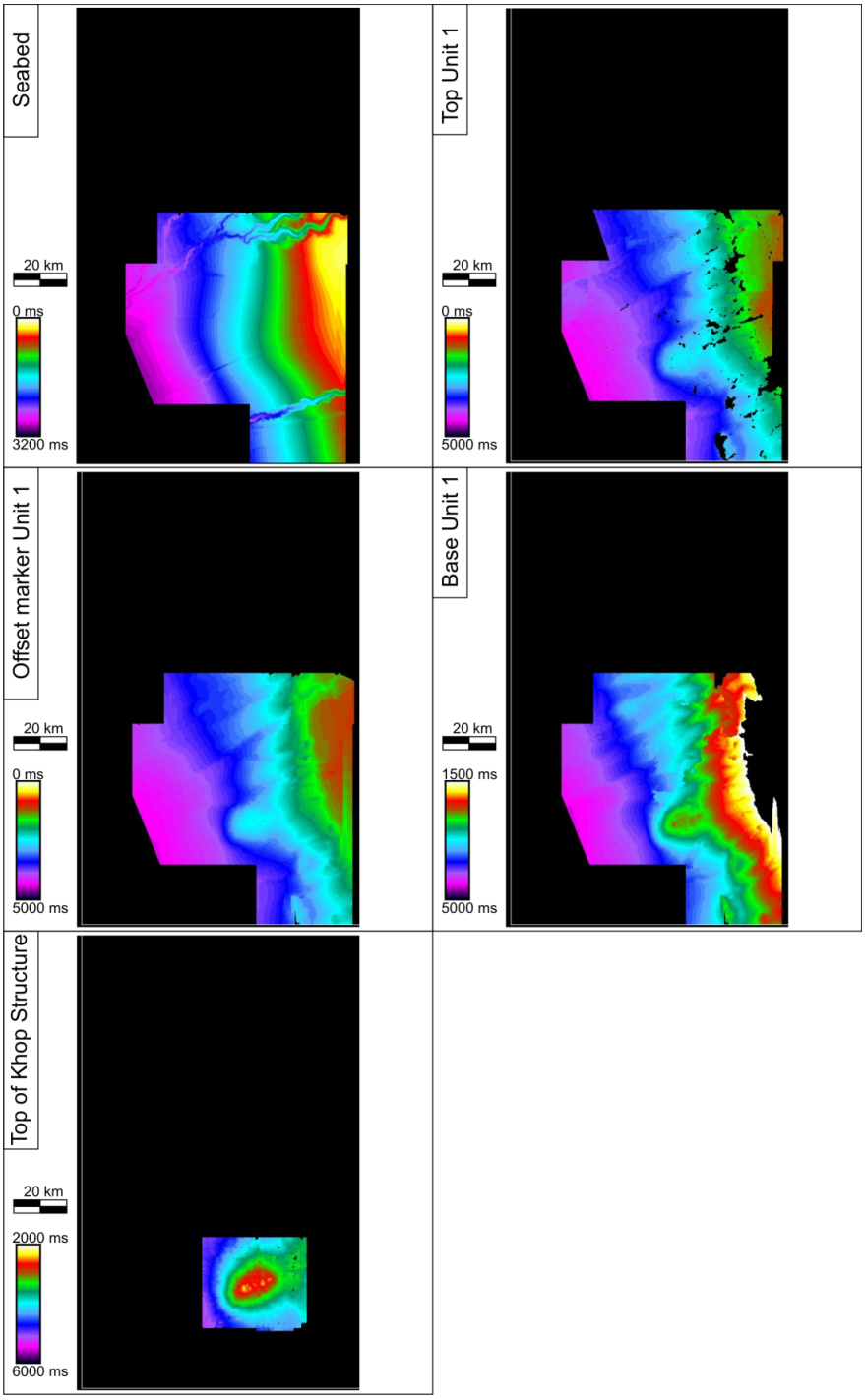

Alternative horizon names used in text:

Top Unit 1 – Horizon C (Chapter 5)

Offset marker Unit 1 – Horizon A (Chapter 5)

Base Unit 1 – Horizon B (Chapter 5)

SEISMIC SECTION – GJALLAR RIDGE TO VEMA DOME 2-D LINE TIE.

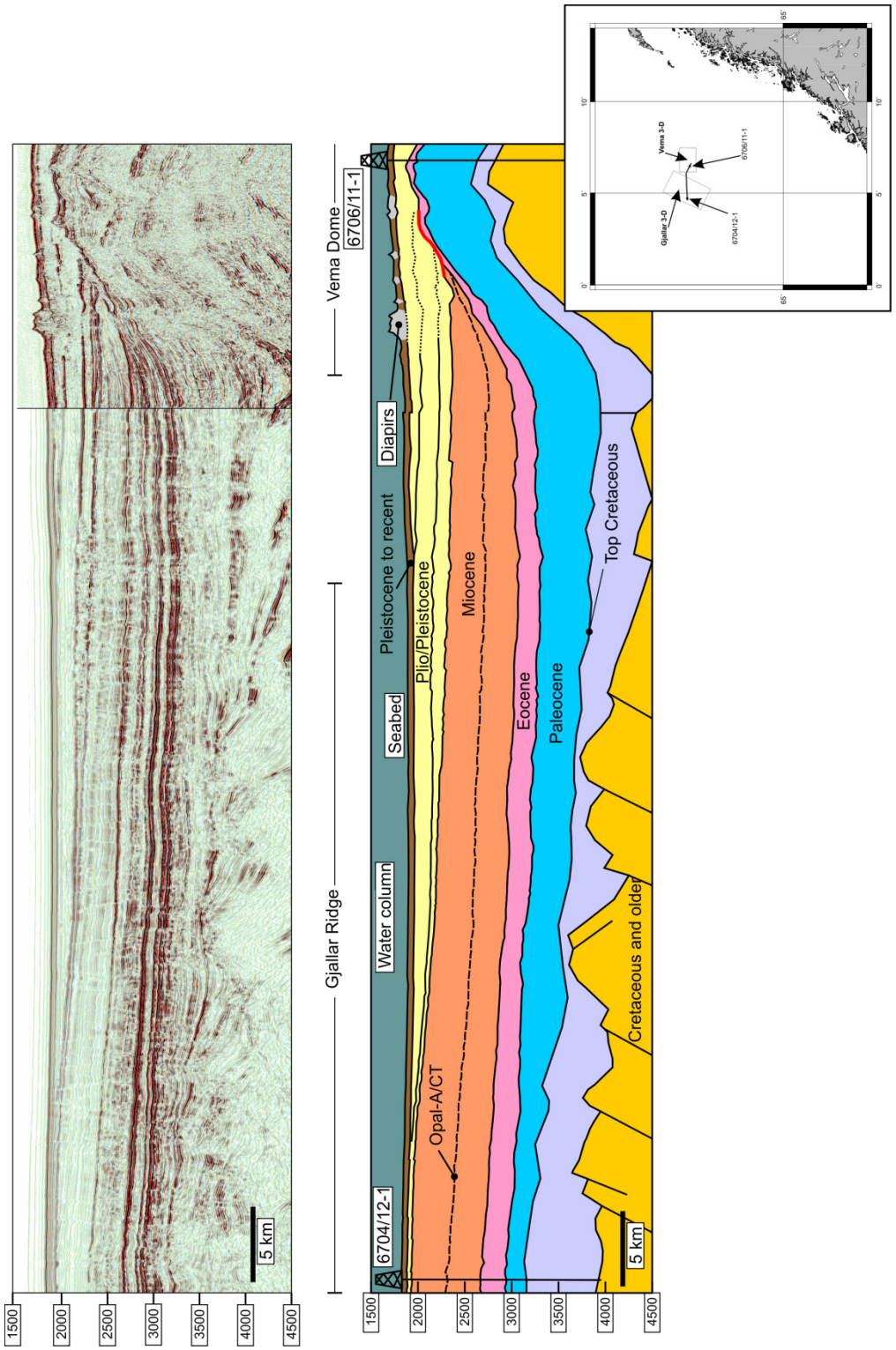

APPENDIX C – LIST OF MATERIALS ON CD-ROM

- Well log of 6706/11-1 from Norwegian Petroleum Directorate (file name – 6706_11_1.pdf)
- Well log of 6704/12-1 from Norwegian Petroleum Directorate (file name – 6704/12-1)
- Naust, Brygge and Kai Formation thicknesses on the Norwegian Margin, from the Norwegian Petroleum Directorate (file name 'Formation_thicknesses_NPD.xlsx')
- Measured physical properties from ODP Leg 104, Site 643 (file name – 'ODP_643.xlsx)
- Shear strength measurements of Neogene sediments related to the Norwegian margin (file name 'ODP_shear_strength_Norway.xlsx)
- XRPD data of silica phases from well 6302/6-1 (file name – XRPD_6302_6_1.xlsx)
- Fault dips from layer-bound faults offshore Mauritania (file name – Fault_dips_Mauritania.xlsx)
- Representative scanning electron microscope images of different silica phases, examples from the Monterey Formation (file name – SEM_images.docx)

In the folder '*Figures*', electronic copies of all the figures in this thesis are provided in either .jpg or .png format. They follow the naming convention Fig.[Chapter number].[Figure number]. For example Fig 3.2.png refers to Fig. 3.2, the second figure in Chapter 3.

In the folder '*Journal articles*', PDF copies of the following journal articles can be found:

- Davies, R.J., Ireland, M.T., Cartwright, J.A., 2009. Differential compaction due to the irregular topology of a diagenetic reaction boundary: a new mechanism for the formation of polygonal faults. *Basin Research* **21**, 354-359. (file name 'davies_ireland_cartwright_BASIN_RESEARCH_2010.pdf')
- Ireland, M.T., Goulty, N.R., Davies, R.J., 2010. Influence of pore water chemistry on silica diagenesis: evidence from the interaction of diagenetic reaction zones with polygonal fault systems. *Journal of the Geological Society, London* **167**, 273-279. (file name 'ireland_goulty_davies_JGSL_2010')

- Ireland, M.T., Davies, R.J., Goulty, N.R., Carruthers, T.D., 2011. Structure of a silica diagenetic transformation zone: the Gjallar Ridge, offshore Norway. *Sedimentology* **58**, 424-441. (file name 'ireland_davies_goulty_carruthers_SEDIMENTOLOGY_2011')
- Ireland, M.T., Goulty, N.R., Davies, R.J., Influence of stratigraphic setting and simple shear on layer-bound compaction faults from offshore Mauritania. *Journal of Structural Geology* **33**, 487-499**.** (file name 'ireland_goulty_davies_JSG_2011')